

Evaluation of Glass Fiber Reinforced Polymer (GFRP) Spirals in Corrosion Resistant Concrete Piles

Contract Number: BVD-30-977-27 and BED-30-977-12

FSU Project ID: 042924

Submitted to:

Florida Department of Transportation

Research Center
605 Suwannee Street
Tallahassee, Florida 32399-0450



Project Managers:

Christina Freeman	FDOT Structures Research Center
Ge Wan	FDOT Structures Design Office
Rodrigo Herrera	FDOT Structures Design Office



**FAMU-FSU
Engineering**

Prepared by:

Olayiwola Adegbulugbe	Graduate Research Assistant
Sungmoon Jung	Principal Investigator
Raphael Kampmann	Co-Principal Investigator

Department of Civil and Environmental Engineering
FAMU-FSU College of Engineering
2525 Pottsdamer St., Tallahassee, FL. 32310.

**December 2023
FINAL REPORT**

DISCLAIMER

The opinions, findings, and conclusions expressed in this publication are those of the authors, and not necessarily those of the State of Florida Department of Transportation

UNIT CONVERSION CHART

Approximate conversion to SI units

Symbol	When you know	Multiply by	To find	Symbol
Length				
in.	inches	25.4	millimeters	mm
ft.	feet	0.305	meters	m
yd	yards	0.914	meters	m
mi	miles	1.61	kilometers	km
Area				
in. ²	square inches	645.2	square millimeters	mm ²
ft. ²	square feet	0.093	square meters	m ²
yd ²	square yard	0.836	square meters	m ²
ac	acres	0.405	hectares	ha
mi ²	square miles	2.59	square kilometers	km ²
Volume				
fl oz	fluid ounces	29.57	milliliters	mL
gal	gallons	3.785	liters	L
ft ³	cubic feet	0.028	cubic meters	m ³
yd ³	cubic yards	0.765	cubic meters	m ³
Mass				
oz	ounces	28.35	grams	g
lb	pounds	0.454	kilograms	kg
T	short tons (2000 lbs)	0.907	megagrams	Mg
Temperature				
°F	Fahrenheit	$\frac{5}{9}(F - 32)$	Celsius	°C
Illumination				
fc	foot-candles	10.76	lux	lx
fl	foot-Lamberts	3.426	$\frac{\text{candela}}{\text{m}^2}$	$\frac{\text{cand}}{\text{m}^2}$
Force/Stress/Pressure				
lbf	poundforce	4.45	newtons	N
k	kips	4.45	kilonewtons	kN
$\frac{\text{lbf}}{\text{in.}^2}$ (psi)	$\frac{\text{poundforce}}{\text{square inch}}$	6.89	kilopascals	kPa
$\frac{\text{k}}{\text{in.}^2}$ (ksi)	$\frac{\text{kips}}{\text{square inch}}$	6.89	megapascals	MPa

Approximate conversion to imperial units

Symbol	When you know	Multiply by	To find	Symbol
Length				
mm	millimeters	0.039	inches	in.
m	meters	3.28	feet	ft.
m	meters	1.09	yards	yd
km	kilometers	0.621	miles	mi
Area				
mm ²	square millimeters	0.0016	square inches	in. ²
m ²	square meters	10.764	square feet	ft. ²
m ²	square meters	1.195	square yard	yd ²
Ha	hectares	2.47	acres	ac
km ²	square kilometers	0.386	square miles	mi ²
Volume				
mL	milliliters	0.034	fluid ounces	fl oz
L	liters	0.264	gallons	gal
m ³	cubic meters	35.314	cubic feet	ft ³
m ³	cubic meters	1.307	cubic yards	yd ³
Mass				
g	grams	0.035	ounces	oz
kg	kilograms	2.202	pounds	lb
Mg	megagrams	1.103	short tons (2000 lbs)	T
Temperature				
°C	Celsius	$\frac{9}{5}(C + 32)$	Fahrenheit	°F
Illumination				
lx	lux	0.0929	foot-candles	fc
$\frac{\text{cand}}{\text{m}^2}$	$\frac{\text{candela}}{\text{m}^2}$	0.2919	foot-Lamberts	fl
Force/Stress/Pressure				
N	newtons	0.225	poundforce	lbf
kN	kilonewtons	0.225	kips	k
kPa	kilopascals	0.145	$\frac{\text{poundforce}}{\text{square inch}}$	$\frac{\text{lbf}}{\text{in.}^2}$ (psi)
MPa	megapascals	0.145	$\frac{\text{kips}}{\text{square inch}}$	$\frac{\text{k}}{\text{in.}^2}$ (ksi)

TECHNICAL REPORT DOCUMENTATION PAGE

1. Report No.	2. Government Accession No.	3. Recipient's Catalog No.	
4. Title and Subtitle Evaluation of GFRP Spirals in Corrosion Resistant Concrete Piles		5. Report Date December 2023	
		6. Performing Organization Code	
7. Author(s) Olayiwola Adegbulugbe, Sungmoon Jung, Raphael Kampmann		8. Performing Organization Report No. BDV-30-977-27 and BED-30-977-12	
9. Performing Organization Name and Address FAMU-FSU College of Engineering Department of Civil and Environmental Engineering 2525 Pottsdamer St. Rm. A129 Tallahassee, FL 32310-6046		10. Work Unit No. (TRAIS)	
		11. Contract or Grant No.	
12. Sponsoring Agency Name and Address Florida Department of Transportation 605 Suwannee Street, MS 30 Tallahassee, FL 32399-0450		13. Type of Report and Period Covered Final Report November 2018 – December 2023	
		14. Sponsoring Agency Code	
15. Supplementary Notes			
16. Abstract <p>Corrosion of steel in concrete has long been a significant factor contributing to the deterioration of reinforced concrete structures, particularly in aggressive environments. In Florida, where many piles are situated in marine or similarly harsh conditions, the susceptibility of reinforcing steel in concrete piles to corrosion is a critical concern, as it can substantially diminish the lifespan of these structures.</p> <p>The Florida Department of Transportation (FDOT) has recognized the need to address this issue by permitting the use of Carbon Fiber Reinforced Polymer (CFRP) spirals and prestressing strands as corrosion-resistant alternatives to enhance the durability of concrete piles. However, the relatively high cost of CFRP material has limited their widespread implementation. Consequently, this project aims to assess the feasibility of employing a more cost-effective, non-corrosive material for the lateral (spiral) reinforcement of piles.</p> <p>To achieve this objective, the behavior of piles with Glass Fiber Reinforced Polymer (GFRP) spirals was investigated through two distinct phases. Phase 1 involved a series of impact, flexural, and pile cutting tests, wherein GFRP spirals were utilized in conjunction with steel strands to reinforce test piles. In contrast, Phase 2 focused exclusively on impact tests, evaluating the performance of corrosion-resistant piles reinforced with GFRP spirals in combination with CFRP/CFCC prestressing strands.</p> <p>The test results demonstrate that piles featuring GFRP spirals exhibit performance comparable to those reinforced with steel or CFRP spirals. Therefore, it is evident that prestressed concrete piles can be effectively confined using GFRP spirals, all while maintaining their load-carrying capacity. Furthermore, the implementation of corrosion-resistant piles incorporating GFRP spirals for bridge foundations, especially in harsh environmental conditions, offers the potential to reduce construction costs, decrease maintenance requirements, and extend the lifespan of bridges—a promising and cost-effective solution for the future.</p>			
17. Key Word Corrosion resistant prestressed concrete piles, GFRP spiral, pendulum impact testing, finite element (FE) analysis with ABAQUS.		18. Distribution Statement No restrictions	
19. Security Classif. (of this report) Unclassified	20. Security Classif. (of this page) Unclassified	21. No. of Pages 294	22. Price

ACKNOWLEDGEMENT

The authors express their sincere gratitude to the Florida Department of Transportation (FDOT) for providing the funding that made this research project possible. In addition, the invaluable technical input and guidance offered by Christina Freeman, Ge Wan, Rodrigo Herrera, and Steve Nolan are deeply acknowledged and greatly appreciated.

Furthermore, it is important to recognize that the dedicated efforts of the FDOT Structures Research Center staff played a pivotal role in the successful completion of this project. Steve Eudy, Justin Robertson, Paul Tighe, Ben Allen, Miguel Ramirez, and Michael Waters all made exceptional contributions to this research endeavor. Their expertise in testing, instrumentation, and the fabrication of test apparatus proved to be invaluable, allowing for the smooth progression of the project.

Special thanks are extended to Dr. Kim Mingu and Meek Casyn at Terracon Consultants Inc. for their provision of pile driving analyzer (PDA) services.

EXECUTIVE SUMMARY

Piles in Florida are often installed in marine environments or in other environmentally aggressive regions. Under such conditions and without sufficient cover, reinforcing steel in concrete piles is vulnerable to corrosion, and the lifespan of support structures can be reduced. FDOT Standard Plans allow carbon fiber reinforced polymer (CFRP) as a corrosion-resistant alternative to improve durability. While these materials are effective, the high costs are a hindrance and prevent widespread implementation. This project investigated replacing the CFRP spirals with glass fiber reinforced polymers (GFRP) spirals, because of their strength, ease of production, and economic benefits. The scope of the project was the spirals only, which provided pile reinforcement in combination with CFRP (or CFCC: carbon fiber composite cables) prestressing strands.

The roles of the spiral ties are to resist impact loading when the pile is installed and to maintain the position of the strands under high loads. To test if the GFRP spirals could provide these mechanisms, the project began by designing and constructing an apparatus to replicate the impact loading on pile specimens. The apparatus utilized the pendulum facility of the FDOT Structures Research Center. It was designed to be able to exert at least 5 ksi stress on a 24" × 24" pile, a condition that such a pile may experience during installation. The test setup also included supports where the pile specimen was placed laterally and large blocks at the pile toe to prevent excessive movement upon the impact loading.

The tests were conducted in two phases. The first phase involved testing four prestressed concrete piles, each measuring 28 feet in length and having a cross-sectional dimension of 24" × 24". The first pile was the control specimen with steel strands and steel spirals, adhering to the FDOT's standard specifications for a 24" × 24" prestressed concrete pile. The subsequent two piles were reinforced with steel strands and GFRP spirals. The GFRP spiral design was similar to the FDOT's standard specifications for steel spirals but with size necessary to resist the impact and modification to accommodate the larger cross-sectional area of the GFRP spirals. Steel strands were used in phase 1 to save the cost of experiment. Additionally, one pile with CFRP strands and spirals, sourced from a prior project, was also tested.

The experimental testing showed that the performance of the GFRP spirals was comparable to the control specimen and CFRP-only specimen. The GFRP spiral did not show failure nor excessive strain, but the localized spalling of concrete was observed under high (>5 ksi) impact loading.

Minor concrete cracks throughout the specimen were also observed, but the pile specimen remained intact until the end. Flexural testing of the pile of one specimen was also conducted, showing satisfactory performance. Finally, a pile-cutting test was also performed, mimicking a condition in the real-world installation where piles are typically cut after driving to a certain elevation. The pile cutting testing showed a very small change in strain (<50 microstrains) indicating no issues.

After completing the phase 1 testing, analytical and finite element models were developed to explain the experimental observations. The analytical model was based on force equilibrium, whereas the finite element model was based on explicit numerical simulation. After obtaining these models, additional plots were produced complementing phase 1 experiment. Next, GFRP spiral designs were produced that used the CFRP strands.

The second phase testing involved two 24" × 24" CFRP prestressed concrete piles, with two different GFRP spiral configurations. Both specimens had #3 GFRP spirals but with a different number of spiral turns at pile ends. Testing of both specimens was satisfactory, showing largely the same behavior as the phase 1 specimens. The project ended by providing drawings for 14", 18", 24", and 30" square concrete piles reinforced with GFRP spirals and CFRP strands. The necessary size of the spirals was based on the analytical model prediction explained earlier. The spiral scheme followed the 24" spirals that were tested experimentally.

This project demonstrated the feasibility and potential cost savings of corrosion-resistant prestressed concrete piles with GFRP ties. More options will lead to more competition in the market and to less expensive products. The project provided the proposed GFRP spiral designs and drawings, which could be used by FDOT in the future as a less expensive alternative.

TABLE OF CONTENTS

DISCLAIMER	ii
UNIT CONVERSION CHART	iii
TECHNICAL REPORT DOCUMENTATION PAGE	v
ACKNOWLEDGEMENT	vi
EXECUTIVE SUMMARY	vii
LIST OF TABLES	xvii
LIST OF FIGURES	xviii
CHAPTER 1. INTRODUCTION	1
1.1 Introduction	1
1.2 Problem Statement	2
1.3 Research Objectives	2
1.4 Report Organization	3
CHAPTER 2. BACKGROUND	4
2.1 Pile Driving System	4
2.1.1 Impact Hammers	4
2.1.2 Vibratory Hammers	9
2.1.3 Resonant Hammers	10
2.2 Pile Driving Process Energy and Stresses	10
2.3 Dynamic Response of Piles during Testing	15
2.4 Soil Resistance	20
2.5 FDOT Impact Pendulum Test Facility	21
2.6 Experimental Apparatus to Simulate Pile Driving	23
2.7 Field Pile Testing	26

2.8	Confinement by Transverse Reinforcement in Concrete	29
2.9	Pile Axial Load.....	34
2.10	Spiral Area and Pitch Requirements	35
2.11	GFRP Stirrups and Spirals as Confinement during Pile Driving – Lesson Learned.....	36
2.12	Properties of Fiber-Reinforced Polymer	37
CHAPTER 3. IMPACTOR AND SPIRAL DESIGN.....		39
3.1	Introduction	39
3.2	Design Requirements and Preferences for Impactor and Test Setup.....	39
3.3	Impact Test Concept.....	40
3.4	Design of Impactor and Test Setup	41
3.4.1	Estimation of Test Setup Performance (Analytical Calculation).....	41
3.4.2	Estimation of Test Setup Performance (Finite Element Analysis)	45
3.5	Specification for GFRP Spirals	49
3.6	Design Calculations for the GFRP Spiral Size	51
3.6.1	Size of GFRP and CFRP Spirals Based on Equivalent Steel Spiral Tensile Capacity and FRP Strain Limit.....	51
3.6.2	Size of CFRP and GFRP Spiral Based on Equivalent Steel Spiral Shear Capacity	53
3.7	Other Design-Related Parameters	54
3.7.1	Prestress Loss.....	54
3.7.2	Moment Capacity.....	54
3.7.3	Driving Stress Limits and Axial Capacity	55
CHAPTER 4. PHASE 1 EXPERIMENTS		56
4.1	Introduction	56
4.2	Specimen Description	56
4.3	Materials for Phase 1 Test Piles	58

4.3.1	Prestressing Strands and Spirals	58
4.3.2	Concrete	58
4.3.3	Plywood Cushion	59
4.4	Instrumentation (Phase 1 Test Piles).....	59
4.4.1	Strain Gauges	59
4.4.2	Deflection Gauges.....	60
4.4.3	Accelerometers	60
4.4.4	Pile Driving Analyzer® (PDA).....	60
4.4.5	Infrared Optical Break Beam Sensors.....	61
4.4.6	High-Speed Cameras	61
4.5	Construction of Test Piles	62
4.5.1	Preparation and Instrumentation of Spirals.....	62
4.5.2	Casting Bed Layout.....	62
4.5.3	Spiral/Strand Installation and Stressing of Strands.....	63
4.5.4	Spiral Splicing.....	63
4.5.5	Concrete Pouring	64
4.5.6	Strand Stress Release	65
4.6	Testing Procedure.....	65
4.6.1	Impact Test Procedure	65
4.6.2	Procedure for Flexural Test	67
4.7	Test Results for Phase 1 Test Piles	67
4.7.1	Impactor Velocity and Acceleration	68
4.7.2	Pile Driving Analyzer (PDA) Measurements	69
4.7.3	Spiral Strain	78
4.7.4	Failure of Pile under Impact	84

4.7.5	Pile Cutting Test	86
4.7.6	Flexural Test (PSG2)	88
CHAPTER 5. DISCUSSION AND FE ANALYSIS BASED ON PHASE 1 EXPERIMENTS ...		92
5.1	Comparison of Spiral Design Strength to Test Results.....	92
5.1.1	Introduction.....	92
5.1.2	GFRP Spiral Design Summary and Prediction of Spiral Stress	92
5.1.3	Observed Spiral Force from Impact Tests vs. Predicted Force and Design Tensile Capacity	93
5.1.4	Prediction Using the Concrete Core Behavior.....	94
5.1.5	Limitations of the Analytical Model.....	95
5.2	Finite Element Model Prediction	95
5.2.1	Background.....	95
5.2.2	General Model Details	95
5.2.3	Concrete Material Model	99
5.2.4	Concrete Stress-Strain Curve.....	101
5.2.5	Prestressing Strand, Steel Wire, and GFRP Material Model.....	103
5.2.6	Plywood Material Model	106
5.3	Comparison of Test Results to FE Model Results	106
CHAPTER 6. PHASE 2 EXPERIMENTS		112
6.1	Updated Spiral Design (Utilized in Phase 2 Piles).....	112
6.2	Design Calculations, Specifications, and Construction Plans.....	112
6.2.1	Analytical Calculation	112
6.2.2	Finite Element Analysis.....	113
6.3	Construction of Test Piles (Phase 2)	119
6.3.1	Specimen Description and Design Configuration (Phase2).....	119

6.3.2	Preparation and Instrumentation of Spirals (Phase 2).....	121
6.3.3	Strand and Spiral Installation.....	121
6.3.4	Concrete Pouring	121
6.4	Phase 2 Impact Testing Procedure	121
6.5	Impact Test Results for Phase 2 Test Piles	122
6.5.1	Impactor Velocity and Acceleration (Phase 2).....	122
6.5.2	Pile Driving Analyzer (PDA) measurements (Phase 2).....	123
6.6	Spiral Strain Measurements	133
6.6.1	Spiral Strain Profile along Pile Length	133
6.6.2	Maximum Spiral Strain vs. Drop Height	137
6.6.3	A Stepped Simplification of Spiral Behavior Relative to the Spiral Spacing.....	138
6.7	Failure of Pile under Impact.....	140
CHAPTER 7. SUMMARY, DISCUSSION, and RECOMENDATIONS		144
7.1	Summary	144
7.2	Discussion from Impact Test.....	144
7.3	Recommendations for Different Pile Sizes	145
7.3.1	Introduction.....	145
7.3.2	Selection of GFRP Spiral Size.....	145
7.3.3	Spiral Size Check for Stainless Steel and CFRP Spirals	146
7.3.4	#3 GFRP Bent Portion Strength Check	147
7.3.5	Corrosion Resistant Pile Details and GFRP Spiral Patterns	148
7.4	Recommendations for Pile Driving and Testing	149
REFERENCES		150
APPENDICES		156
Appendix A. Impact Test Setup (Impactor, Restraining Blocks, and Support) Drawing		156

Appendix B. Spiral Size, Shear Capacity, Prestress Loss, Moment Capacity, and Driving Stress Limit Calculations.	187
B.1. Size of CFRP and GFRP Spiral Based on Force Equilibrium	187
B.2. Prestress Loss Calculations	188
B.3. Moment Capacity Calculations	193
B.4. Calculations for Axial Capacities and Compression Driving Stress Limits	195
B.5. Calculations for Shear Capacity of Transverse Reinforcement	197
Appendix C. Pile Information, Instrumentation Plan, and Numbering.....	204
C.1. Pile Information	204
C.2. Tests and Sensors Monitored	205
C.3. Internal (Spiral) Strain Gauge and Fiber Optic Gauge Instrumentation for PSS.....	210
C.4. Internal (Spiral) Strain Gauge and Fiber Optic Gauge Instrumentation for PSG1	211
C.5. Internal (Spiral) Strain Gauge, Fiber Optic Gauge, and Vibrating Wire Instrumentation for PSG2	212
C.6. Flexural Test Setup and Instrumentation	214
C.7. Cable Routing for Internal Instrumentation	216
C.8. PDA Instrumentation	217
Appendix D. Data Sheet for EGCS-D5 Accelerometer	218
Appendix E. PDA Measurements (Phase 1 Impact Tests).....	222
E.1. PDA Strain Gauge Measurements	222
E.1.1. PDA Strain Gauge Measurement (PSS).....	222
E.1.2. PDA Strain Gauge Measurements (PSG1)	222
E.1.3. PDA Strain Gauge Measurements (PCC)	224
E.2. PDA Acceleration Measurements	227
E.2.1. PDA Acceleration Measurement (PSS)	227
E.2.2. PDA Acceleration Measurements (PSG1)	227

E.2.3. PDA Acceleration Measurements (PCC).....	229
E.3. Pile Force Traces from PDA	232
E.3.1. Pile Force Traces from PDA (PSS).....	232
E.3.2. Pile Force Traces from PDA (PSG1)	232
E.3.3. Pile Force Traces from PDA (PCC).....	234
E.4. Peak Tensile Stress (TSX) and Its Location along the Pile.	237
E.4.1. Peak Tensile Stress (TSX) and its Location along the Pile (PSS)	237
E.4.2. Peak Tensile Stress (TSX) and its Location along the Pile (PSG1).....	237
E.4.3. Peak Tensile Stress (TSX) and its Location along the Pile (PCC)	239
E.5. Spiral Strain under Impact Loading	242
E.5.1. Spiral Strain (PSS)	242
E.5.2. Spiral Strain (PSG1).....	242
E.6. Summary of All Test Results	244
Appendix F. Construction Documents from CDS Manufacturing Inc. for Phase 2 Test Piles	245
Appendix G. As-built Drawing of Phase 2 Test Piles.....	249
Appendix H. PDA Measurements (Phase 2 Impact Tests)	250
H.1. PDA Measurements (PCG1).....	250
H.1.1. PDA Strain Gauge Measurement (PCG1)	250
H.1.2. PDA Acceleration Measurement (PCG1).....	251
H.2. PDA Measurements (PCG2).....	253
H.2.1. PDA Strain Gauge Measurement (PCG2)	253
H.2.1. PDA Acceleration Measurement (PCG2).....	254
H.3. Pile Force Traces from PDA.....	256
H.3.1. Pile Force Traces from PDA (PCG1)	256
H.3.2. Pile Force Traces from PDA (PCG1)	257

H.4. Peak Tensile Stress (TSX) and Its Location along the Pile	259
H.4.1. Peak Tensile Stress (TSX) and its Location along the Pile (PCG1).....	259
H.4.2. Peak Tensile Stress (TSX) and its Location along the Pile (PCG1).....	260
H.5. Spiral Strain under Impact Loading.....	262
H.5.1. Spiral Strain (PCG1).....	262
H.5.2. Spiral Strain (PCG2).....	263
H.6. Summary of All Test Results.....	264
Appendix I. Final Drawings for Piles with CFRP Strands and GFRP Spirals.....	265

LIST OF TABLES

Table 2.1: Pile hammer characteristics	12
Table 2.2: Typical tensile properties of reinforcement	37
Table 3.1: Summary of FE model	47
Table 3.2: Material properties used in the analysis.....	47
Table 3.3: Physical and mechanical property requirements for GFRP spirals	49
Table 3.4: Geometric and mechanical properties requirement for GFRP bars	50
Table 3.5: Required area of transverse reinforcements and the prescribed area.....	53
Table 3.6: Comparison of the shear capacity of transverse reinforcement	54
Table 4.1: Pile nomenclature and test matrix for phase 1 test piles	56
Table 4.2: Distinguishing characteristics of strain gauges used	59
Table 4.3: Summary of impactor velocity and acceleration readings	69
Table 4.4: Peak strain, acceleration, and stresses (PSS)	72
Table 4.5: Peak top strain, acceleration, and stress (PSG1).....	74
Table 4.6: Peak top strain, acceleration, and stress (PCC)	78
Table 4.7: Experimental vs. Theoretical moment capacity.....	91
Table 5.1: Axial pile force and corresponding maximum spiral stress (PSS)	93
Table 5.2: Axial pile force and corresponding maximum spiral stress (PSG1).....	94
Table 5.3: Reduction factor for estimating energy-equivalent velocity in FE.....	98
Table 5.4: Concrete damaged plasticity (CDP) model parameters	101
Table 5.5: Mechanical properties of concrete	103
Table 5.6: Mechanical properties of reinforcement	105
Table 5.7: Mechanical properties of plywood	106
Table 6.1: Pile nomenclature (updated design).....	112
Table 6.2: FE specimens for stress comparison.....	113
Table 6.3: Mechanical properties of CFRP strand.....	115
Table 6.4: Summary of impactor velocity and acceleration readings	123
Table 6.5: Acceleration, peak concrete strain and stress (PCG1).....	131
Table 6.6: Acceleration, peak concrete strain and stress (PCG2).....	132
Table 7.1: Required area and recommended area of GFRP spirals compared to steel spirals.....	146
Table 7.2: SS and CFRP spiral size check.....	147

LIST OF FIGURES

Figure 1.1: Pile corrosion zones (left photo: source unknown, right figure: drawn by the author).....	1
Figure 2.1: Operation of a single-acting air/steam hammer (Hannigan et al., 2016a).....	6
Figure 2.2: Schematic of a single-acting hydraulic hammer (Hannigan et al., 2016a).....	7
Figure 2.3: Operation of an open-end diesel hammer (Hannigan et al., 2016a).....	8
Figure 2.4: Schematic representation of the various energies involved in the process of driving a pile (So & Ng, 2010).....	14
Figure 2.5: Wave equation model (Lee et al., 1988).....	15
Figure 2.6: Pile driving analyzer (PDA).....	16
Figure 2.7: FDOT impact pendulum test facility with steel towers and strong floor.....	22
Figure 2.8: Pile driving apparatus (McVay et al., 2009).....	23
Figure 2.9: Centrifuge pile driving apparatus (McVay et al., 1994).....	24
Figure 2.10: Centrifuge pile driving apparatus (McVay et al., 2000).....	25
Figure 2.11: (a) Model pile; (b) Vertical cross section of test apparatus (El-Garhy et al., 2013).....	26
Figure 2.12: Pile details (Fam et al., 2003).....	27
Figure 2.13: Instrumentation of test piles (Fam et al., 2003).....	28
Figure 2.14: Confining action of spirals.....	30
Figure 2.15: Comparison of the stress-strain curve for steel and FRPs.....	38
Figure 3.1: Illustration of the block-based design.....	40
Figure 3.2: Impact velocity and impact energy of the impactor.....	42
Figure 3.3: Schematic diagram of the variable involved with the test setup.....	43
Figure 3.4: Estimated movement of the restraining blocks.....	45
Figure 3.5: Simulated impact on the pile using LS-Dyna.....	46
Figure 3.6: Von Mises stress for the impactor test ($V=11.46$ m/s (37.63 ft/s)) for two different time steps showing largest stresses.....	48
Figure 3.7: Maximum von Mises stress at the beginning and end of the concrete pile ($V=11.46$ m/s (37.63 ft/s)).....	48
Figure 3.8: Maximum x-stress at the beginning and end of the concrete pile ($V=11.46$ m/s (37.63 ft/s)).....	49
Figure 4.1: Pile with steel strand and steel spirals (PSS).....	57
Figure 4.2: Pile with steel strand and GFRP spirals (PSG1 and PSG2).....	58
Figure 4.3: Location of break beams (elevation).....	61

Figure 4.4: Strain gauge installation	62
Figure 4.5: Casting bed layout	62
Figure 4.6: Strand stressing sequence	63
Figure 4.7: Spiral splicing: (a) PSG2, (b) PSG1	64
Figure 4.8: Pile casting	64
Figure 4.9: Strand cutting sequence	65
Figure 4.10: Pile impact test setup drawing	66
Figure 4.11: Pile cushion with screw eyes and its placement	66
Figure 4.12: Pile orientation	67
Figure 4.13: Impactor velocity	68
Figure 4.14: Top and tip strains from PDA strain gauges at impact drop height of 15 ft (PSS)	70
Figure 4.15: PDA measured acceleration at pile top and tip at a drop height of 15 ft (PSS)	71
Figure 4.16: Pile force traces from PDA resulting from impact drop height of 15 ft (PSS). (Compressive force is positive in this figure which was produced by Terracon)	71
Figure 4.17: Peak tensile stress (TSX) resulting from impact drop height of 15 ft (PSS) and its location along the pile. (This figure was produced by Terracon)	72
Figure 4.18: Top and tip strains from PDA strain gauges at impact drop height of 20 ft (PSG1)	73
Figure 4.19: PDA measured acceleration at pile top and tip at a drop height of 20 ft (PSG1)	74
Figure 4.20: Pile force traces from PDA resulting from impact drop height of 20 ft (PSG1) (Compressive force is positive in this figure which was produced by Terracon)	75
Figure 4.21: Peak tensile stress (TSX) resulting from impact drop height of 20 ft (PSG1) and its location along the pile. (This figure was produced by Terracon)	75
Figure 4.22: Top and tip strains from PDA strain gauges at impact drop height of 20 ft (PCC)	76
Figure 4.23: PDA measured acceleration at pile top and tip at a drop height of 20 ft (PCC)	77
Figure 4.24: Pile force traces from PDA resulting from impact drop height of 20 ft (PCC) (Compressive force is positive in this figure which was produced by Terracon)	77
Figure 4.25: Peak tensile stress (TSX) resulting from impact drop height of 20 ft (PCC) and its location along the pile. (This figure was produced by Terracon)	78
Figure 4.26: Steel spiral strain PSS (15-ft drop height)	79
Figure 4.27: GFRP spiral strain PSG1 (20-ft drop height)	79
Figure 4.28: Maximum spiral tensile strain vs. drop height (PSS)	80
Figure 4.29: Maximum spiral tensile strain vs. drop height (PSG1)	81
Figure 4.30: Spiral tensile strain at pile center and pile tip region vs. drop height (PSS)	81

Figure 4.31: Spiral tensile strain at pile center and pile tip region vs. drop height (PSG1).....	82
Figure 4.32: Average strains along pile (PSS) length resulting from impact from (a) 7-ft drop height, and (b) 15-ft drop height	82
Figure 4.33: Average strains along pile (PSG1) length resulting from impact from (a) 4-ft, (b) 7-ft, (c) 10-ft, (d) 15-ft, and (e) 20-ft drop heights.....	83
Figure 4.34: Crack pattern after final impact for PSS.....	84
Figure 4.35: Failure at top and tip after final impact for PSS and PSG1	85
Figure 4.36: Crack pattern after final impact for PSG1	85
Figure 4.37: Failure at top and tip after final impact for PCC	86
Figure 4.38: Crack pattern after final impact for PCC.....	86
Figure 4.39: Pile cutting process.....	87
Figure 4.40: PSS pile cut	87
Figure 4.41: PSG1 pile cut.....	88
Figure 4.42: Load-deflection curve from flexural test.....	89
Figure 4.43: Deflection along the length of the pile	89
Figure 4.44: Load-strain curve from flexural test	90
Figure 4.45: Concrete crushed in the compression zone	90
Figure 4.46: Spiral rupture in the compression zone	91
Figure 5.1: (a) Test setup assembly in ABAQUS; (b) Reinforcement embedded in pile model	97
Figure 5.2: Stress-strain curve of concrete in (a) compression and (b) tension for the CDP model....	99
Figure 5.3: Concrete stress-strain curve in compression utilized in FE.....	102
Figure 5.4: Concrete stress-strain curve in tension utilized in FE	103
Figure 5.5: Stress-strain curve for prestressing steel strands	104
Figure 5.6: Stress-strain curve for steel wire spiral	105
Figure 5.7: Stress propagation after impact, the PSS pile, 15-ft drop height. (a), (b), (c) forward propagation (t = 0.0026, 0.0034, and 0.0050 sec), and (d) reflection and backward propagation (t = 0.0075 sec).....	107
Figure 5.8: Stress at the pile top, the PSS pile, 15 ft drop height. (a) t = 0.003 sec, (b) t = 0.004 sec	107
Figure 5.9: Stress at the pile top, the PSG1 pile, 20-ft drop height. (a) t = 0.003 sec, (b) t = 0.004 sec	107
Figure 5.10: PSS FE stress plot (concrete stress on the surface, 4 ft from the top)	108
Figure 5.11: PSG1 FE stress plot (concrete stress on the surface, 4 ft from the top)	109

Figure 5.12: Comparison of experimental pile stress results to FE stress results (PSS).....	109
Figure 5.13: Comparison of test pile stress results to FE stress results (PSG1)	110
Figure 5.14: Test vs. FE steel spiral strain for PSS (15-ft drop height).....	111
Figure 5.15: Test vs. FE steel spiral strain for PSG1 (20-ft drop height)	111
Figure 6.1: PSS-test vs. PSS -FE stress plot using 0.75 in. top plywood cushion (7-ft drop)	114
Figure 6.2: PSS-test vs. PSS -FE stress plot using 0.75 in. top plywood cushion (15-ft drop)	114
Figure 6.3: PSS' FE stress plot corrected for 1.5 in. top plywood cushion (concrete stress on the surface, 4 ft from the top)	115
Figure 6.4: PSG1 FE stress plot (concrete stress on the surface, 4 ft from the top)	116
Figure 6.5: PCG1 FE stress plot (concrete stress on the surface, 4 ft from the top)	116
Figure 6.6: PCG2 FE stress plot (concrete stress on the surface, 4 ft from the top)	117
Figure 6.7: PCG3 FE stress plot (concrete stress on the surface, 4 ft from the top)	117
Figure 6.8: Pile head stress, 20-ft drop, $t = 0.003$ sec, (a) PCG1, (b) PCG2, (c) PCG3	118
Figure 6.9: FE GFRP spiral strain comparison for PSG, PCG1 and PCG2 (20-ft drop height).....	119
Figure 6.10: PCG1	120
Figure 6.11: PCG2	120
Figure 6.12: Pile cross-section and GFRP spiral bending details	120
Figure 6.13: Impactor velocity.....	122
Figure 6.14: Top and tip concrete strains from PDA strain gauges at impact drop height of 20 ft (PCG1)	124
Figure 6.15: Top and tip concrete strains from PDA strain gauges at impact drop height of 20 ft (PCG2)	124
Figure 6.16: Top and tip concrete strains from PDA strain gauges at impact drop height of 25 ft (PCG1)	125
Figure 6.17: Top and tip concrete strains from PDA strain gauges at impact drop height of 25 ft (PCG2)	125
Figure 6.18: PDA measured acceleration at pile top and tip at a drop height of 20 ft (PCG1)	126
Figure 6.19: PDA measured acceleration at pile top and tip at a drop height of 20 ft (PCG2)	127
Figure 6.20: PDA measured acceleration at pile top and tip at a drop height of 25 ft (PCG1)	127
Figure 6.21: PDA measured acceleration at pile top and tip at a drop height of 25 ft (PCG2)	128
Figure 6.22: Pile force traces from PDA resulting from impact drop height of 20 ft (PCG1). (Compressive force is positive in this figure which was produced by Terracon)	129

Figure 6.23: Pile force traces from PDA resulting from impact drop height of 20 ft (PCG2). (Compressive force is positive in this figure which was produced by Terracon)	130
Figure 6.24: Pile force traces from PDA resulting from impact drop height of 25 ft (PCG1). (Compressive force is positive in this figure which was produced by Terracon)	130
Figure 6.25: Pile force traces from PDA resulting from impact drop height of 25 ft (PCG2). (Compressive force is positive in this figure which was produced by Terracon)	131
Figure 6.26: Peak tensile stress (TSX) resulting from impact drop height of 20 ft (PCG1) and its location along the pile. (This figure was produced by Terracon)	132
Figure 6.27: Peak tensile stress (TSX) resulting from impact drop height of 20 ft (PCG2) and its location along the pile. (This figure was produced by Terracon)	132
Figure 6.28: Peak tensile stress (TSX) resulting from impact drop height of 25 ft (PCG1) and its location along the pile. (This figure was produced by Terracon)	133
Figure 6.29: Peak tensile stress (TSX) resulting from impact drop height of 25 ft (PCG2) and its location along the pile. (This figure was produced by Terracon)	133
Figure 6.30: PCG1 spiral strain (15-ft drop height).....	134
Figure 6.31: PCG2 spiral strain (15-ft drop height).....	135
Figure 6.32: PCG1 spiral strain (20-ft drop height).....	135
Figure 6.33: PCG2 spiral strain (20-ft drop height).....	136
Figure 6.34: PCG1 spiral strain (25-ft drop height).....	136
Figure 6.35: PCG2 spiral strain (25-ft drop height).....	137
Figure 6.36: Maximum spiral tensile strain vs. drop height (PCG1 and PCG2)	137
Figure 6.37: Average strains along pile (PCG1) length resulting from impact from (a) 5-ft (b) 10-ft (c) 15-ft (d) 20-ft, and (e) 25-ft drop heights.....	138
Figure 6.38: Average strains along pile (PCG2) length resulting from impact from (a) 5-ft (b) 10-ft (c) 15-ft (d) 20-ft, and (e) 25-ft drop heights.....	139
Figure 6.39: Failure at top and tip after final impact for PCG1	141
Figure 6.40: Failure at top and tip after final impact for PCG2	142
Figure 6.41: Crack pattern after final impact for PCG1	142
Figure 6.42: Crack pattern after final impact for PCG2	143
Figure 6.43: Bond slippage (PCG1).....	143
Figure E.1: Top and tip strains from PDA strain gauges at impact drop height of 7 ft (PSS)	222
Figure E.2: Top and tip strains from PDA strain gauges at impact drop height of 4 ft (PSG1)	222

Figure E.3: Top and tip strains from PDA strain gauges at impact drop height of 7 ft (PSG1)	223
Figure E.4: Top and tip strains from PDA strain gauges at impact drop height of 10 ft (PSG1)	223
Figure E.5: Top and tip strains from PDA strain gauges at impact drop height of 15 ft (PSG1)	224
Figure E.6: Top and tip strains from PDA strain gauges at impact drop height of 4 ft (PCC)	224
Figure E.7: Top and tip strains from PDA strain gauges at impact drop height of 7 ft (PCC)	225
Figure E.8: Top and tip strains from PDA strain gauges at impact drop height of 10 ft (PCC)	225
Figure E.9: Top and tip strains from PDA strain gauges at impact drop height of 15 ft (PCC)	226
Figure E.10: Top and tip strains from PDA strain gauges at impact drop height of 25 ft (PCC)	226
Figure E.11: PDA measured acceleration at pile top and tip at a drop height of 7 ft (PSS)	227
Figure E.12: PDA measured acceleration at pile top and tip at a drop height of 4 ft (PSG1)	227
Figure E.13: PDA measured acceleration at pile top and tip at a drop height of 7 ft (PSG1)	228
Figure E.14: PDA measured acceleration at pile top and tip at a drop height of 10 ft (PSG1)	228
Figure E.15: PDA measured acceleration at pile top and tip at a drop height of 15 ft (PSG1)	229
Figure E.16: PDA measured acceleration at pile top and tip at a drop height of 4 ft (PCC)	229
Figure E.17: PDA measured acceleration at pile top and tip at a drop height of 7 ft (PCC)	230
Figure E.18: PDA measured acceleration at pile top and tip at a drop height of 10 ft (PCC)	230
Figure E.19: PDA measured acceleration at pile top and tip at a drop height of 15 ft (PCC)	231
Figure E.20: PDA measured acceleration at pile top and tip at a drop height of 25 ft (PCC)	231
Figure E.21: Pile force traces from PDA resulting from impact drop height of 7 ft (PSS)	232
Figure E.22: Pile force traces from PDA resulting from impact drop height of 4 ft (PSG1)	232
Figure E.23: Pile force traces from PDA resulting from impact drop height of 7 ft (PSG1)	233
Figure E.24: Pile force traces from PDA resulting from impact drop height of 10 ft (PSG1)	233
Figure E.25: Pile force traces from PDA resulting from impact drop height of 15 ft (PSG1)	234
Figure E.26: Pile force traces from PDA resulting from impact drop height of 4 ft (PCC)	234
Figure E.27: Pile force traces from PDA resulting from impact drop height of 7 ft (PCC)	235
Figure E.28: Pile force traces from PDA resulting from impact drop height of 10 ft (PCC)	235
Figure E.29: Pile force traces from PDA resulting from impact drop height of 15 ft (PCC)	236
Figure E.30: Pile force traces from PDA resulting from impact drop height of 25 ft (PCC)	236
Figure E.31: Peak tensile stress (TSX) resulting from impact drop height of 7 ft (PSS) and its location along the pile	237
Figure E.32: Peak tensile stress (TSX) resulting from impact drop height of 4 ft (PSG1) and its location along the pile	237

Figure E.33: Peak tensile stress (TSX) resulting from impact drop height of 7 ft (PSG1) and its location along the pile.....	238
Figure E.34: Peak tensile stress (TSX) resulting from impact drop height of 10 ft (PSG1) and its location along the pile.....	238
Figure E.35: Peak tensile stress (TSX) resulting from impact drop height of 15 ft (PSG1) and its location along the pile.....	239
Figure E.36: Peak tensile stress (TSX) resulting from impact drop height of 4 ft (PCC) and its location along the pile.....	239
Figure E.37: Peak tensile stress (TSX) resulting from impact drop height of 7 ft (PCC) and its location along the pile.....	240
Figure E.38: Peak tensile stress (TSX) resulting from impact drop height of 10 ft (PCC) and its location along the pile.....	240
Figure E.39: Peak tensile stress (TSX) resulting from impact drop height of 15 ft (PCC) and its location along the pile.....	241
Figure E.40: Peak tensile stress (TSX) resulting from impact drop height of 25 ft (PCC) and its location along the pile.....	241
Figure E.41: Steel spiral strain PSS (7-ft drop height)	242
Figure E.42: GFRP spiral strain PSG1 (4-ft drop height).....	242
Figure E.43: GFRP spiral strain PSG1 (7-ft drop height).....	243
Figure E.44: GFRP spiral strain PSG1 (10-ft drop height).....	243
Figure H.1: Top and tip strains from PDA strain gauges at impact drop height of 5 ft (PCG1)	250
Figure H.2: Top and tip strains from PDA strain gauges at impact drop height of 10 ft (PCG1)	250
Figure H.3: Top and tip strains from PDA strain gauges at impact drop height of 15 ft (PCG1)	251
Figure H.4: PDA measured acceleration at pile top and tip at a drop height of 5 ft (PCG1)	251
Figure H.5: PDA measured acceleration at pile top and tip at a drop height of 10 ft (PCG1)	252
Figure H.6: PDA measured acceleration at pile top and tip at a drop height of 15 ft (PCG1)	252
Figure H.7: Top and tip strains from PDA strain gauges at impact drop height of 5 ft (PCG2)	253
Figure H.8: PDA measured acceleration at pile top and tip at a drop height of 10 ft (PCG2)	253
Figure H.9: PDA measured acceleration at pile top and tip at a drop height of 15 ft (PCG2)	254
Figure H.10: PDA measured acceleration at pile top and tip at a drop height of 5 ft (PCG2)	254
Figure H.11: PDA measured acceleration at pile top and tip at a drop height of 10 ft (PCG2).....	255
Figure H.12: PDA measured acceleration at pile top and tip at a drop height of 15 ft (PCG2).....	255

Figure H.13: Pile force traces from PDA resulting from impact drop height of 5 ft (PCG1). (Compressive force is positive in this figure which was produced by Terracon)	256
Figure H.14: Pile force traces from PDA resulting from impact drop height of 10 ft (PCG1). (Compressive force is positive in this figure which was produced by Terracon)	256
Figure H.15: Pile force traces from PDA resulting from impact drop height of 15 ft (PCG1). (Compressive force is positive in this figure which was produced by Terracon)	257
Figure H.16: Pile force traces from PDA resulting from impact drop height of 5 ft (PCG2). (Compressive force is positive in this figure which was produced by Terracon)	257
Figure H.17: Pile force traces from PDA resulting from impact drop height of 10 ft (PCG2). (Compressive force is positive in this figure which was produced by Terracon)	258
Figure H.18: Pile force traces from PDA resulting from impact drop height of 15 ft (PCG2). (Compressive force is positive in this figure which was produced by Terracon)	258
Figure H.19: Peak tensile stress (TSX) resulting from impact drop height of 5 ft (PCG1) and its location along the pile. (This figure was produced by Terracon)	259
Figure H.20: Peak tensile stress (TSX) resulting from impact drop height of 10 ft (PCG1) and its location along the pile. (This figure was produced by Terracon)	259
Figure H.21: Peak tensile stress (TSX) resulting from impact drop height of 15 ft (PCG1) and its location along the pile. (This figure was produced by Terracon)	260
Figure H.22: Peak tensile stress (TSX) resulting from impact drop height of 5 ft (PCG2) and its location along the pile. (This figure was produced by Terracon)	260
Figure H.23: Peak tensile stress (TSX) resulting from impact drop height of 10 ft (PCG2) and its location along the pile. (This figure was produced by Terracon)	261
Figure H.24: Peak tensile stress (TSX) resulting from impact drop height of 15 ft (PCG2) and its location along the pile. (This figure was produced by Terracon)	261
Figure H.25: PCG1 spiral strain (5-ft drop height)	262
Figure H.26: PCG1 spiral strain (10-ft drop height)	262
Figure H.27: PCG2 spiral strain (5-ft drop height)	263
Figure H.28: PCG2 spiral strain (10-ft drop height)	263

CHAPTER 1. INTRODUCTION

1.1 Introduction

Piles in Florida are often installed in marine environments or in other environmentally aggressive regions. Corrosion occurs across four zones for piles in these environments as shown in Figure 1.1. Most especially, the tidal zone and splash zone are often subjected to salt deposits and several wet and dry cycles. Under such conditions and without sufficient cover, steel reinforcements in concrete piles are vulnerable to corrosion and the lifespan of support structures can be reduced.

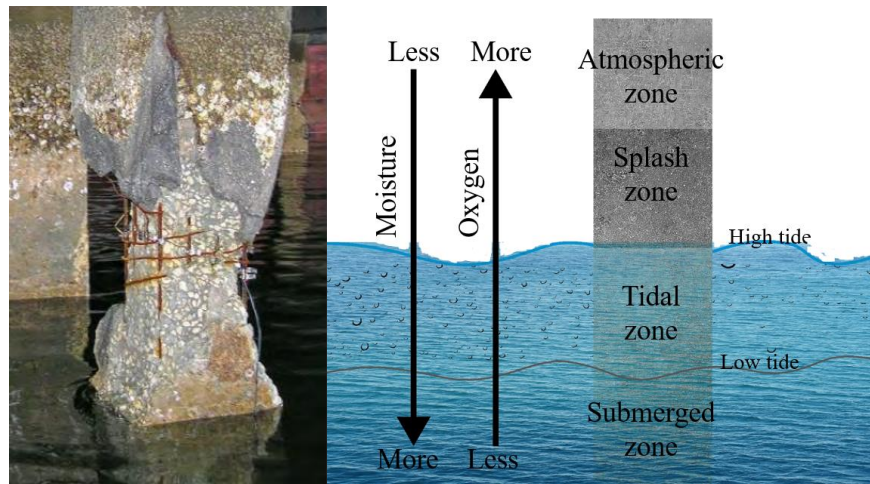


Figure 1.1: Pile corrosion zones (left photo: source unknown, right figure: drawn by the author)

In the United States, the cost of repairing and replacing the piling system in bridges is measured in billions of dollars. Therefore, government agencies and infrastructure owners are actively seeking cost-effective solutions that offer longer lasting and more durable structures. Prestressed concrete (PC) piles remain a favored choice for deep bridge foundations, therefore, incorporating non-corroding fiber-reinforced polymer (FRP) reinforcements in PC piles exposed to corrosive environments can be an economically advantageous option due to the extended lifespan of these piles.

FRP reinforcing bars have become a material of choice world-wide in recent years because of their success and practicality (ACI 440.1R-15). In addition to their non-corroding properties, FRP bars, when compared to steel, have a density that is one fourth to one fifth the density of steel and a high tensile strength (ACI 440.1R-15). These properties mean structures reinforced with FRP bars can be lighter than if they were reinforced with steel.

Confinement in precast piles is generally provided by spirals. In addition to restraining the lateral expansion of the concrete core, the spirals maintain the position of the longitudinal reinforcement under high loads, provide increased ductility, enhance the load carrying capacity of the pile, and sustain impact forces during pile driving. According to Hartt et al. (2007) spiral design can be performance based such that the confining action provided by the spiral compensates for losses in the pile's load capacity resulting from concrete spalling. Also, they stated that spiral design can be prescriptive, especially for piles that are not installed in moderate to high seismic regions. For example, the spiral design for piles in the FDOT standard for bridge construction is prescriptive based on years of successful practice.

1.2 Problem Statement

The Florida Department of Transportation (FDOT) offers corrosion-resistant alternatives like carbon fiber reinforced polymer (CFRP) and stainless steel (SS) in their standard plans for concrete piles to enhance their durability. These materials serve as both longitudinal and lateral (spiral) reinforcements. However, their high costs have limited widespread adoption. Given that glass fiber reinforced polymer (GFRP) is a widely used and cost-effective FRP reinforcement due to its strength, ease of production, and economic advantages, employing GFRP spirals as lateral reinforcements in corrosion-resistant PC piles can help reduce support structure costs in aggressive environments.

Past studies on GFRP lateral reinforcement were conducted primarily for axial and bending loading on reinforced concrete (RC) piles or columns (Ahmed, El-Salakawy, & Benmokrane, 2010; Ali, Mohamed, & Benmokrane, 2016; De Luca, Matta, & Nanni, 2010; El-Mogy, El-Ragaby, & El-Salakawy, 2011; Lotfy, 2010; Tobbi, Farghaly, & Benmokrane, 2012). However, the structural performance and drivability of prestressed piles with GFRP spirals have not been experimentally evaluated. These studies are crucial for establishing standards and enabling the use of corrosion-resistant piles with GFRP spirals in FDOT projects.

1.3 Research Objectives

The goal of this study was to evaluate the feasibility and potential cost savings of corrosion-resistant prestressed concrete piles with GFRP spirals. More options provide more competition in the market and can lead to less expensive products.

To achieve the goal of this research, specific objectives are as follows:

1. Develop impactor and test setup that simulate pile driving impact load and extends the capabilities of the FDOT Structures Research Center pendulum facility.
2. Experimentally evaluate the response of piles with steel, GFRP, CFRP spirals under impact loading and bending.
3. Experimentally evaluate the confinement behavior at a pile cut-off location.
4. Develop numerical models to explain the observed behavior, to provide guidelines for piles that are not experimentally tested.
5. Design GFRP spiral ties that meet the loading requirements.
6. Implement GFRP spiral design in prestressed concrete piles with CFRP strands, to make them corrosion resistant.

1.4 Report Organization

This report is organized into distinct chapters, each serving a specific purpose. Following the introductory chapter, Chapter 2 delves into topics such as pile driving systems, the dynamic behavior of piles during installation, and the significance of spiral confinement in piles. In Chapter 3, details pertaining to the design of the test apparatus and the creation of test specimens for phase 1 experiments are expounded upon. The subsequent chapter, Chapter 4, provides a comprehensive account of phase 1 experiments, including the construction process of the test piles, material used, test instrumentation and test results. The focal point then shifts to a subsequent discussion and analysis of phase 1 results, including a comparison with the finite element simulations, in Chapter 5. Additionally, Chapter 6 provides an account of phase 2 experiments. Finally, Chapter 7 discusses comparison of phase 1 and phase 2 experiments and provides final design drawings recommendation for corrosion-resistant piles.

CHAPTER 2. BACKGROUND

2.1 Pile Driving System

Piles can be driven by a variety of hammers, each having its advantages and disadvantages. To select a hammer, the project needs, and the economy of the hammers are important considerations. Also, factors such as soil properties, pile type, driving depth and installation procedure influence the magnitude of force needed to drive a pile to the desired depth. It is therefore imperative to select the most suitable and cost-effective equipment not only for a specific soil condition, but also for the pile material. In addition, a pile driving system can also serve as a mechanism for evaluating the geotechnical resistance of a pile.

Piles can be installed using different types of hammers, each with its own set of pros and cons. The choice of hammer should align with project requirements and cost considerations. Broadly, pile driving methods can be categorized into impact and vibration. Impact hammers are evaluated based on energy, whereas vibratory hammers are assessed based on power.

2.1.1 Impact Hammers

Impact hammers work by creating a downward velocity in the ram or drop weight to drive piles into the ground. When the ram makes contact with the pile, it generates enough force to gradually advance it into the ground. Impact hammers are typically classified as either external combustion or internal combustion. External combustion hammers receive their power from sources external to the hammer itself, such as cranes, air compressors, steam boilers, or hydraulic power packs. In contrast, internal combustion hammers use fuel contained within the hammer cylinder as their energy source.

When an impact hammer is used to drive a pile, it completes a cycle of loading and unloading. This results in a short-duration force/velocity pulse being transmitted to the driven pile. The impact itself is brief compared to the intervals between hammer blows, during which both the pile and the surrounding soil remain at rest.

2.1.1.1 Drop (Gravity) Hammers

Drop hammers, among the oldest pile driving hammers still in use, function by hoisting a ram or drop weight using a crane-mounted winch. When the winch brake is released, the ram falls due to

its own weight, impacting the pile. However, energy is lost during this process as the falling ram must overcome the rotational inertia of the winch cable or hoist line. Consequently, the stroke of the hammer is often inconsistent and challenging to control precisely.

Ideally, the winch brake should be engaged immediately after impact. Premature application of the brake, typically done by the operator to prevent cable spooling, can reduce the hammer's impact energy and efficiency. The number of blows delivered per minute by a drop hammer is relatively slow and depends on the operator's experience and the chosen fall height. It's crucial to operate these hammers with care to prevent over-stressing and damaging the pile. The maximum stroke should be carefully adjusted to avoid pile damage.

Energy losses in drop hammers are attributed to various factors, including friction, inaccuracies in drop height, rotational inertia of the winch cable, premature brake application, and misalignment. As a result up to 50% of the hammer's potential energy can be lost in the process (Rausche, 2000). These hammers are not highly efficient compared to other hammer types and are commonly used for sheet pile installation where pile resistance is not a primary concern.

2.1.1.2 Air/Steam Hammers

Powered by pressurized fluid (either air or steam) within the hammer cylinder, they were originally designed to run on steam but are now predominantly powered by compressed air. These hammers offer consistent stroke height with each blow once adjusted and come in three varieties: single-acting, double-acting, and differential-acting.

A single-acting air/steam hammer is depicted in Figure 2.1. During the upstroke cycle, pressurized air, or steam acts against a piston, pushing the ram upward. In the downstroke cycle, the fluid valve is closed, allowing the ram to fall freely and deliver an impact. Just before impact, the pressure valve is activated, allowing pressure to re-enter the cylinder and initiate a new cycle.

For wave equation analyses, these hammers are generally assumed to have an efficiency of 67% (Rausche, 2000). However, it's worth noting that hammer efficiency can be increased for wave equation analysis, especially for short stroke hammers. At the end of driving, energy transfer efficiency averages around 55% for steel piles and 40% for concrete and timber piles (Rausche, 2000).

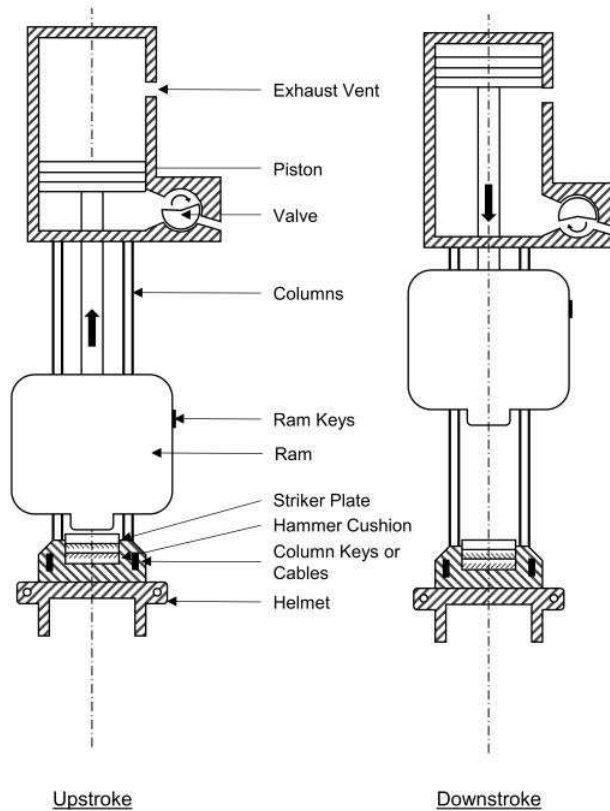


Figure 2.1: Operation of a single-acting air/steam hammer (Hannigan et al., 2016a)

Single-acting air/steam hammers, although heavier than drop hammers, are simple to operate and cost-effective. They can drive various pile types, especially large steel, and concrete piles, and are suitable for all soil conditions, particularly heavy clay. However, they cannot be used for pile extraction.

Double-acting air/steam hammers function similarly to single-acting ones, but they provide downward active pressure in addition to raising the ram. This shorter stroke results in higher operational speeds and blow rates, even with the same ram weight as single-acting hammers. However, they are generally slightly less efficient compared to equivalently rated single hammers.

Differential-acting air/steam hammers feature two pistons with different surface areas, creating a net upward force during the upstroke. During the downstroke, the ram falls faster than free fall due to the fluid below the piston flowing to the top. These hammers operate at half the stroke and twice the speed of single-acting hammers but have lower efficiency.

To ensure acceptable final bearing for piles driven by air-steam hammers, the hammer must operate within 10% of the manufacturer's rated speed, unless specified otherwise (FDOT, 2015).

2.1.1.3 Hydraulic Hammers

Hydraulic fluid under pressure from an external power pack is applied to the piston to set the ram in motion. They can be single acting or double acting. In single-acting hydraulic hammers, pressurized fluid raises the ram to a predetermined height, then the ram is allowed to fall freely or as freely as the escaping fluid permits. After impact, the ram is raised again by the hydraulic system to begin a new cycle. Figure 2.2 shows a diagram of a single acting hydraulic hammer.

A pendant on the hydraulic power pack controls the volume of fluid supplied to raise the ram. The pendant controls and continuously adjusts the stroke and blow rate of the hydraulic hammer. The hammer short stroke can be set to as small as 6 inches to prevent pile run during easy driving. Hard driving can be achieved at higher strokes. The stroke can be visually estimated on several single acting hydraulic hammers. In newer single acting hydraulic hammers, the ram velocity just before impact can be observed from an inbuilt monitoring system. The stroke and kinetic energy of the hammer can be calculated from the measured ram velocity.

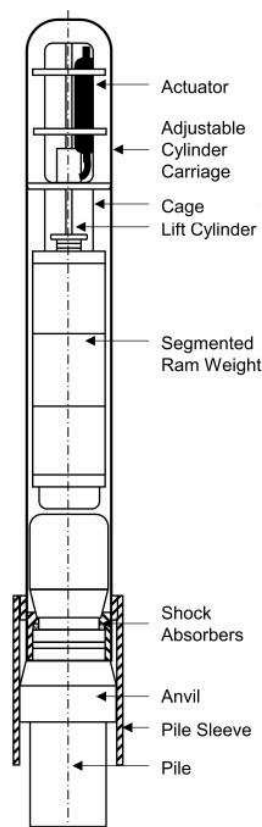


Figure 2.2: Schematic of a single-acting hydraulic hammer (Hannigan et al., 2016a)

2.1.1.4 Diesel hammers

These are the only type of internal combustion hammer within the impact hammer group. They generate energy for driving the hammer through the combustion of diesel fuel within the hammer's combustion chamber. Diesel hammers come in two main types: open-end and closed-end.

Figure 2.3 illustrates the operation of an open-end (single-acting) diesel hammer. A hoist or starting device initially raises the ram, which is then released to fall under gravity. As the ram descends and passes the exhaust port located on the side of the hammer cylinder, air trapped in the lower part of the cylinder gets compressed. Just before the bottom of the ram exits through the exhaust port, fuel is injected into the compressed air within the cylinder. At the end of the downstroke, the initially compressed air becomes highly pressurized in a small volume. When the ram strikes the anvil, this increased pressure, combined with a rise in temperature, triggers combustion. This combustion drives the ram upward and transmits the driving force to the pile. As the ram rises during the upstroke, spent gases are expelled through the exhaust port. This cycle repeats until fuel is no longer supplied.

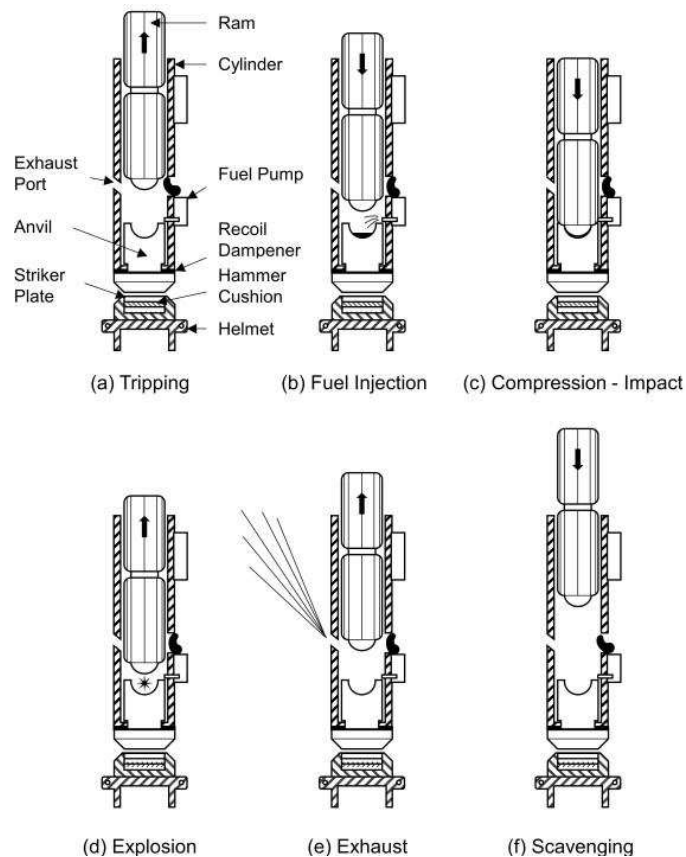


Figure 2.3: Operation of an open-end diesel hammer (Hannigan et al., 2016a)

Closed-end (double-acting) diesel hammers differ from open-end hammers in that they have a closed top cylinder. The initial starting process is like open-end hammers. During the upstroke, air gets compressed in the upper part of the hammer cylinder, known as the bounce chamber or compression chamber. The compressed air in the bounce chamber reduces the ram stroke and increases the blow rate. Pressurized air exits the bounce chamber through the bounce chamber port during the downstroke.

2.1.2 Vibratory Hammers

Vibratory hammers operate by using hydraulic power packs to apply a rapidly alternating force for driving piles into the ground. They consist of pairs of hydraulic motors equipped with counter-rotating eccentric weights. These eccentric motors work in a way that their axial force components add together while their lateral centrifugal force components cancel each other out, preventing lateral whip. This mechanism produces a sinusoidal axial force at a frequency matching the motors' rotation speed. Some vibratory machines may have multiple pairs of smaller eccentrics that achieve the same result as a single large pair. The maximum downward dynamic force produced is calculated as:

$$F_F = (2\pi f)^2 M_E \quad (2.1)$$

where:

F_F is the dynamic force, f is the hammer frequency and M_E is the summation of all eccentric moments.

Hydraulically activated clamps connect the hammer to the pile, and static weights positioned above and isolated from the vibrators provide the hammer with enough mass for driving. These hammers operate at a frequency that excites the soil, moving it aside to allow the pile to penetrate under its self-weight and the hammer's weight. Vibratory hammers are not rated by the impact energy delivered per blow but rather by the frequency of energy developed per second and/or the force delivered to the pile.

To assess pile bearing capacity, a blow count criterion is usually required, necessitating the use of an impact hammer at the end of the driving process. Vibratory hammers are generally unsuitable for installing prestressed concrete piles due to the potential for tensile and bending stresses that could damage the piles. They are commonly used for driving and extracting sheet piles and

installing non-displacement piles. However, they are less suitable for installing closed-end pipes and other displacement piles, particularly when it comes to laterally displacing soil at the pile toe. Vibratory hammers perform best in granular soils, especially in submerged conditions, but are not recommended for stiff to hard clays.

2.1.3 Resonant Hammers

Resonant hammers are essentially advanced vibratory hammers that operate at even higher frequencies. They use high-frequency vibrations generated by a hydraulic piston-cylinder system to induce resonance responses in piles. A valve controls the supply of hydraulic oil to alternate sides of the piston, allowing adjustment of the amplitude and magnitude of the oscillating force produced by the hammer. These hammers can reach operating frequencies of up to 180 Hz.

When driving piles with resonant hammers, it's crucial to match the machine's frequency range properly with the length of the pile. However, it's important to note that resonant hammers cannot be used to determine the bearing capacity of a pile. Therefore, a conventional impact hammer must be used after the installation process with the resonant hammer is complete to assess the bearing capacity of the pile.

2.2 Pile Driving Process Energy and Stresses

In summary, hammers that rely solely on gravity are typically rated by their potential energy, which is the product of the ram weight and the stroke. This category includes drop hammers, single-acting air/steam hammers, single-acting hydraulic hammers, and open-end diesel hammers. However, some hammers may use alternative energy rating principles depending on the manufacturer. Double-acting hammers have an increased equivalent stroke due to higher pressure compared to free fall, resulting in shorter blow cycles. The equivalent stroke of a double-acting hammer is the stroke of a corresponding single-acting hammer that produces the same impact velocity.

The drivability of a pile is influenced by several factors, including the energy transmitted by the hammer, soil resistance, pile strength, and the pile's ability to transfer stresses from top to bottom. When a hammer falls under gravity, its potential energy gradually transforms into kinetic energy. Upon impacting the pile head, typically cushioned, there is some energy loss. The impact force at the pile head is assumed to cause the pile to behave like an elastic bar. This impact force travels

down the pile as a stress wave, its velocity being contingent on the pile's elastic modulus. As this stress wave moves down the pile, some energy dissipates into the soil along the pile's shaft and at its tip. With sufficient driving force, the pile advances into the underlying soil.

The drivability of a pile is influenced by several factors, including the energy transmitted by the hammer, soil resistance, pile strength, and the pile's ability to transfer stresses from top to bottom. When a hammer falls under gravity, its potential energy gradually transforms into kinetic energy. Upon impacting the pile head, typically cushioned, there is some energy loss. The impact force at the pile head is assumed to cause the pile to behave like an elastic bar. This impact force travels down the pile as a stress wave, its velocity being contingent on the pile's elastic modulus. As this stress wave moves down the pile, some energy dissipates into the soil along the pile's shaft and at its tip. With sufficient driving force, the pile advances into the underlying soil.

Table 2.1 provides a range of energy, impact velocity, and blow rates for different hammer types, and detailed specifications for various hammers can be found from (Hannigan et al., 2016b).

Equation (2.2) shows the impact velocity, V_i , calculated from the maximum stroke.

$$V_i = (2gh)^{1/2} \quad (2.2)$$

where

V_i is the impact velocity, g is acceleration due to gravity and h is the ram stroke.

The kinetic energy delivered by hammers is typically lower than their potential energy due to various energy losses such as friction, misalignment, residual fluid pressure, preignition, etc. Additionally, energy is dissipated in the hammer cushion, helmet, pile cushion, and inelastic collision at the pile top. The calculation of kinetic energy is expressed in Equation (2.3).

$$KE = \frac{1}{2}mV_i^2 \quad (2.3)$$

where

m is the ram mass

To determine the energy transferred to the pile top, the integral of the force and velocity response of the pile is used, as shown in Equation (2.4).

$$E_t(t) = \int_0^t F(t)V(t)dt \quad (2.4)$$

where

E_t is the transferred energy to the pile, V is the particle velocity of pile and F is the average pile force and given by

$$F = \varepsilon EA \quad (2.5)$$

where

ε is the pile strain, E is the elastic modulus of the pile and A is the cross-sectional area of the pile (2.4)

The drivability of a pile is influenced by several factors, including the energy transmitted by the hammer, soil resistance, pile strength, and the pile's ability to transfer stresses from top to bottom. When a hammer falls under gravity, its potential energy gradually transforms into kinetic energy. Upon impacting the pile head, typically cushioned, there is some energy loss. The impact force at the pile head is assumed to cause the pile to behave like an elastic bar. This impact force travels down the pile as a stress wave, its velocity being contingent on the pile's elastic modulus. As this stress wave moves down the pile, some energy dissipates into the soil along the pile's shaft and at its tip. With sufficient driving force, the pile advances into the underlying soil.

Table 2.1: Pile hammer characteristics

Hammer type	Rated energy (ft-kips)	Impact velocity (ft/s)	Blow rate (blows/min)	Energy (per blow)
Drop (Gravity) Hammers	7 to 60	23 to 33	4 to 8	Ram weight \times height of fall
Single Acting Air/Steam Hammers	7 to 1800	8 to 16.5	35 to 60	Ram weight \times height of fall
Double Acting Air/Steam Hammers	1 to 21	15 to 20	95 to 300	(Ram weight + effective piston head area \times effective fluid pressure) \times stroke

Table 2.1: Pile hammer characteristics – continued

Hammer type	Rated energy (ft-kips)	Impact velocity (ft/s)	Blow rate (blows/min)	Energy (per blow)
Differential Acting Air/Steam Hammers	15 to 50	13 to 15	98 to 300	(Ram weight + effective piston head area × effective fluid pressure) × stroke
Single Acting Hydraulic Hammers	25 to 2162	5 to 18	30 to 50	Ram weight × height of fall
Double Acting Hydraulic Hammers	25 to 2581	5 to 23	40 to 90	(Ram weight + effective piston head area × effective fluid pressure) × stroke
Open-end Diesel Hammers	9 to 1620	10 to 16.5	40 to 60	Ram weight × height of fall
Closed-end Diesel Hammers	5 to 73	8 to 16.5	80 to 105	(Ram weight + effective piston head area × effective fluid pressure) × stroke
Vibratory Hammers	—	—	750 to 2400 vibrations/m in	—
Resonant Hammers	—	—	up to 10,800 vibrations/m in	—

Before employing the wave equation to analyze piles, the dynamic equation utilizing the energy principles outlined in Figure 2.4 was utilized.

Equation (2.6) represents the pile driving process using the principle of energy balance.

$$E_t = E_c + E_v + E_{pen} \quad (2.6)$$

where

E_c is the strained energy stored in the pile and soil temporarily, E_v is the energy lost to pile vibration, and E_{pen} is the energy used to penetrate the soil.

The hammer's performance is assessed by measuring the transferred energy, which is typically less than the kinetic energy of the hammer due to energy losses. In Figure 2.4, it's assumed that R represents the force at the bottom of the pile. However, this assumption doesn't account for changing skin friction resistance and end bearing resistance as the pile moves (Rajapakse, 2008). The dynamic equation ($WhH= RS$) doesn't consider factors like stress distribution in the pile, pile diameter, or pile type. Additionally, it assumes the pile to be rigid, whereas in reality, the pile experiences recoil and rebound during driving. Smith (1960) developed a pile driving analysis model known as the wave equation analysis. This analysis treats the pile as a series of small, interconnected segments with pile springs, representing side friction and pile toe resistance with additional springs and dashpots (Figure 2.5).

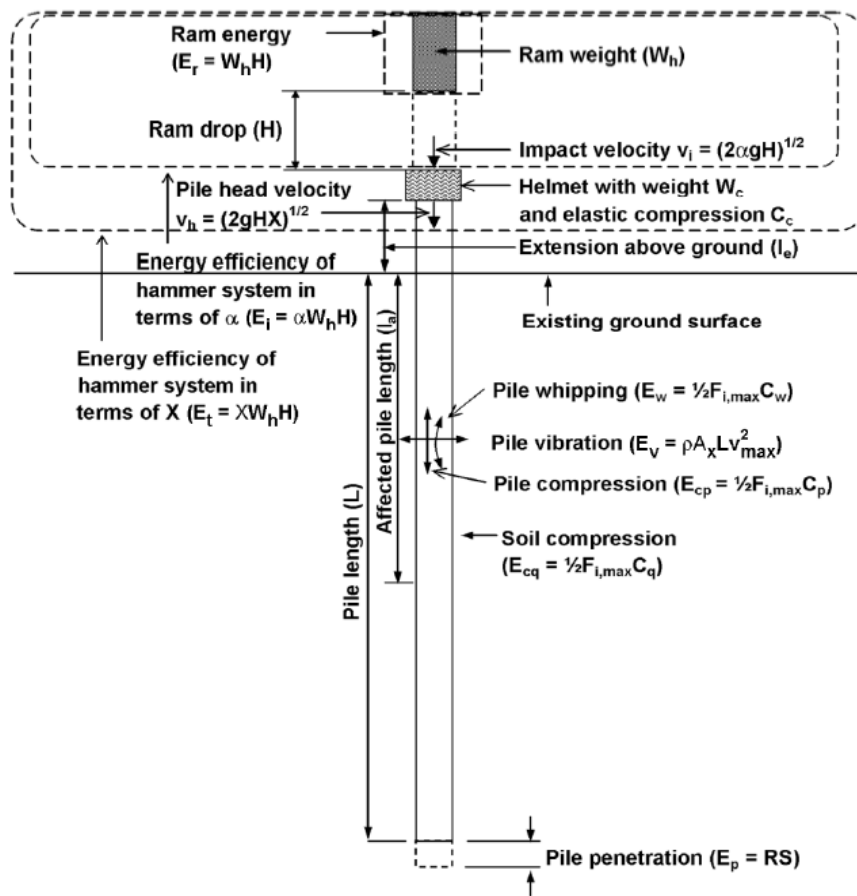


Figure 2.4: Schematic representation of the various energies involved in the process of driving a pile (So & Ng, 2010)

It views the pile as an elastic bar where only axial stress waves propagate, providing insight into the pile's dynamic response to driving. The one-dimensional wave analysis calculates the axial wave speed (c) of the traveling waves as follows:

$$c = \sqrt{E/\rho} \quad (2.7)$$

where

E is the modulus of elasticity and ρ is mass density of the pile material.

Furthermore, changes in the interaction of the pile with its immediate surroundings (i.e., materials at the pile top, along the shaft, and at the toe) and alterations in the pile's cross-sectional shape contribute to the complexity and the quantity of waves propagating along the pile (Holeyman, 1992).

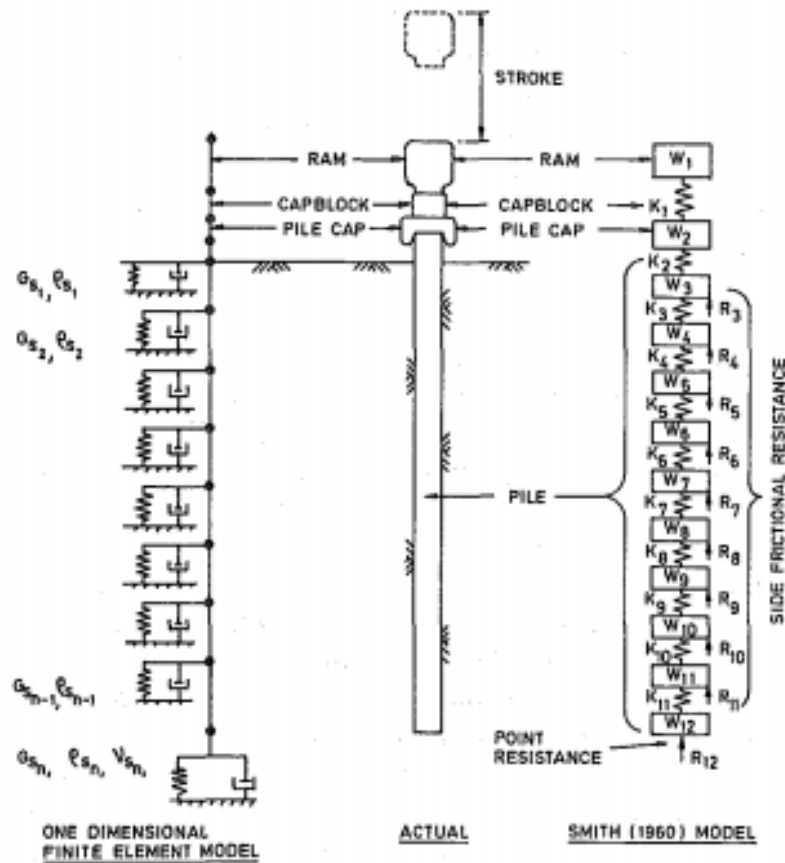


Figure 2.5: Wave equation model (Lee et al., 1988)

2.3 Dynamic Response of Piles during Testing

Piles undergo inspection using static load tests and dynamic tests. Static load testing involves applying a large surcharge load, is time-consuming, and is typically applicable to a limited number of piles. Dynamic tests, on the other hand, are more cost-effective, reliable, quicker to conduct,

and provide enhanced quality control (Ding, Liu, Liu, & Chen, 2011; Likins, 1984). The following description pertains to high strain dynamic testing.

Dynamic pile testing aids in understanding the relationship between the surrounding soil and a driven pile during or after installation. Early practitioners estimated pile capacity from blow counts using dynamic formulas and subjected test piles to static tests for final proof (Likins, Rausche, & Goble, 2000). The one-dimensional wave equation analysis program (WEAP) was developed to analyze and process test data from the field. It provided a realistic approach to modeling the hammer, driving system, pile, and soil, as well as simulating the pile driving process (Bullock, 2012; Rausche, 2000). However, WEAP analysis performed prior to pile driving relies on certain assumptions due to limited information on soil and hammer parameters.

Modern dynamic pile testing is based on measurements obtained from a pile driving analyzer (PDA). The PDA test is a popular dynamic test procedure used to evaluate bearing capacity, driving stresses, hammer performance, and the integrity of driven piles during initial driving and restriking. When a hammer impacts a pile, it produces strain and acceleration, which are measured by strain gauges and accelerometers located near the pile's top. Data collected from these sensors are transmitted via a cable to the PDA (Figure 2.6), which processes the data to display a plot of force and velocity. Penetration resistance is another crucial component of dynamic testing required to analyze pile capacity.



Figure 2.6: Pile driving analyzer (PDA)

The dynamic response of the pile to a suddenly applied axial load can be explained by the propagation of a stress wave (Clough & Penzien, 1993). To elucidate the stress amplification at the pile tip, consider that the impact magnitude is F , and the pile tip has a fixed boundary condition. After the impact at the pile top, a force wave with an amplitude of F_d travels downward. According to wave propagation theory, the reflection of this force wave at the tip causes it to double in magnitude near the rigid support. Conversely, the reflection at the pile top (free end) results in a negative reflection, reducing the force and generating a tension wave that travels up the pile. The downward force traveling along the pile is related to the particle velocity as follows:

$$F_d = ZV \quad (2.8)$$

where

F_d is in the pile and Z is the pile impedance given by Equation (2.9):

$$Z = \frac{EA}{c} = \rho Ac \quad (2.9)$$

The impedance of the pile dictates the amount of hammer energy transmitted through the pile into the soil. The greater the impedance of the pile the greater the energy transmitted through the pile into the soil (Ashford & Jakrapiyanun, 2001; Guades et al., 2012). Also, c can be determined from the time ($2L/c$) taken by the wave to travel down and up the pile length, L , considering the instrumentation is located near the pile head.

Dynamic resistance is tied to pile velocity, while static resistance relies on the movement required to mobilize the ultimate static resistance. To obtain the static resistance of a pile, one subtracts the dynamic component, expressed as the product of a selected damping factor and the pile tip's velocity, from the total resistance (Bullock, 2012). The pile capacity determined from a dynamic test reflects the properties of the pile-soil system only at the time of testing. Real-time data processing from the PDA yields results for evaluating hammer performance, compression, and tension stresses during pile driving, pile structural integrity, distribution of soil resistance, and the static load-bearing capacity of the pile (Hussein & Goble, 2004; Hussein, Woerner, Sharp, & Hwang, 2006).

Post-testing analysis of PDA data can be conducted using a signal matching computer algorithm called the Case Pile Wave Analysis Program (CAPWAP). CAPWAP extracts active soil parameters during impact from PDA measurements, taking the downward wave as input and

iteratively estimating the resistance model to calculate the upward wave. The calculated upward wave validates the measured upward wave. CAPWAP results include static resistance along the pile shaft (skin friction), static resistance at the pile tip (end bearing), soil quake, damping values in friction and end bearing, and a simulated static load versus movement graph (Bullock, 2012; Hussein et al., 2006; Rausche, Hussein, Likins, & Thendean, 1994; Rausche, Likins, Liang, & Hussein, 2010).

More recently, McVay, Alvarez, Zhang, Perez, & Gibsen (2002) collaborated with FDOT to develop the Embedded Data Collector (EDC) system. This system aims to calculate real-time static resistance by using damping values obtained during pile driving as an alternative to the PDA-CAPWAP system. PDA-CAPWAP assumed a constant damping factor throughout the driving process, typically based on experience with a similar soil condition. Thus, CAPWAP results are not unique solutions, as different personnel may obtain different results based on their experience.

The EDC system comprises accelerometers and strain transducers near both ends of the pile (pile top and tip). An antenna connected to the embedded instrumentation is positioned at the face of the pile. A field receiver collects and analyzes data transmitted from the antenna, providing real-time estimates of static capacity, pile stresses, and energy transferred to the pile for each hammer blow. This information is crucial for evaluating the driving system and soil resistance (Herrera et al., 2009). According to Herrera et al. (2009), EDC's total static resistance estimates are typically within 15% of the PDA-CAPWAP estimates on average.

In addition, prestressed concrete piles are engineered and manufactured to withstand various stresses, including handling, service loads, and driving forces, as outlined in ACI 543R. When a pile is subjected to impact forces from a pile driving hammer, these forces travel through the pile as compressive waves. Upon reaching the pile tip, these waves are reflected, either as compression waves (when the pile tip encounters a hard layer) or tension waves (when the pile tip is in contact with a soft layer). These waves then return to the pile top, where they are reflected again. Generally, pile driving imposes the most significant stresses on a pile. The dynamic compressive stresses generated during pile driving typically exceed the static compressive stresses from service loads (ACI, 2012). Consequently, a pile must possess sufficient structural strength to resist these driving stresses to prevent damage.

Furthermore, the minimum compressive strength, denoted as f'_c , for a prestressed concrete pile should be at least 5000 psi or higher, as required at the time of driving (ACI 543R-12; PCI bridge design manual, 2003). It's worth noting that most pile materials exhibit greater strength under dynamic loading than under static conditions (Crapps, 2004).

As per the recommendations outlined in the PCI bridge design manual (2003) and ACI 543R,, the allowable driving stresses for a pile must not exceed the specified limits. According to the AASHTO (2017), these stress limits for a concrete pile are determined by Equations (2.10) to (2.12). Equation (2.10) represents the compression stress limit, Equation (2.11) outlines the tension stress limit (in ksi), and Equation (2.12) provides the tension stress limit for severe environments as recommended by AASHTO.

$$s_{apc} = 0.85f'_c - f_{pe} \quad (2.10)$$

$$S_{apt} = 0.095\sqrt{f'_c} + f_{pe} \quad (2.11)$$

$$S_{apt} = f_{pe} \quad (2.12)$$

However, according to FDOT (2019), the maximum allowable pile driving stresses are determined using the following equations: Equation (2.13) provides the compression stress limit (in psi), Equation (2.14) specifies the tension stress limit for piles less than 50 ft in length (in psi), and Equation (2.15) outlines the tension stress limit for piles that are 50 ft and longer (in psi), as recommended by FDOT.

$$s_{apc} = 0.7f'_c - 0.75f_{pe} \quad (2.13)$$

$$s_{apt} = 6.5(f'_c)^{0.5} + 1.05f_{pe} \quad (2.14)$$

$$s_{apt} = 3.25(f'_c)^{0.5} + 1.05f_{pe} \quad (2.15)$$

where

f_{pe} is the effective prestress (after all losses) at the time of driving, taken as 0.8 times the initial prestress force divided by the minimum net concrete cross-sectional area of the pile, and f'_c is the compressive strength of concrete (or specified minimum compressive strength of concrete according to FDOT).

FDOT Structures Design Guidelines (2018) require that the maximum driving resistance of a 24-inch pile must not exceed 450 tons (900 kip) unless justifiable reasons for exceeding this value is provided. This pile driving resistance corresponds to the required nominal bearing resistance of

the pile. It should be noted that the maximum pile driving resistance does not represent a default value for design as subsoil conditions may require using a lesser value. The maximum driving resistance requirements for piles of other dimensions can be obtained from Table 3.5.12-1 of the FDOT Structures Design Guidelines.

2.4 Soil Resistance

The resistance experienced by a pile during installation is a result of its interaction with the surrounding soil. This resistance comprises side friction, distributed along the pile shaft, and end bearing, which acts at the pile's toe. Side friction depends on the embedded pile length, while end bearing uses the cross-sectional area of the pile as the effective gross area (Guades et al., 2012). The total (ultimate) capacity Q_{total} of a pile is the sum of side friction resistance Q_{sL} and the end bearing resistance Q_b , as shown in Equation (2.16).

$$Q_{total} = Q_{sL} + Q_b \quad (2.16)$$

$$Q_{sL} = \sum_{i=1}^n q_{sLi} A_{si} \quad (2.17)$$

$$Q_b = q_b A_b \quad (2.18)$$

here:

Q_{sL} is the unit shaft resistance for each soil layer, A_{si} is the pile shaft area interfacing with layer i , Q_b is the unit base resistance, and A_b is the area of the pile base.

In saturated cohesive soils, driven piles create strain fields near the pile toe and along the pile shaft. Soil around the pile is radially compressed outward during installation, resulting in high pore water pressure around the shaft due to increased stresses. This temporarily reduces soil shear strength and resistance, affecting the blow count or pile penetration resistance. As high pore water pressure dissipates radially after installation, the soil begins to reconsolidate, increasing both its shear strength and pile resistance. This process is known as "setup," with a significant increase in side shear strength observed within the first 24 hours after pile installation, particularly in cohesive soils (Bullock et al., 2005).

However, in partially saturated soils, setup is not significant as high pore water pressure is not generated during installation.

On the other hand, in loose to medium dense noncohesive soils, pile installation increases the relative density of the soil due to lateral soil displacement, subsequently enhancing pile resistance. In contrast, dense cohesionless soils may experience a temporary negative pore pressure during installation, causing a transient increase in pile resistance along the shaft and below the pile toe. This phenomenon is known as "relaxation," and it occurs as high pore pressure dissipates, reducing the built-up stress and resistance along the pile shaft and toe.

Dynamic and static tests conducted on prestressed concrete piles at various Florida bridge sites (Buckman Bridge, Aucilla River Bridge, Vilano Bridge and Seabreeze Bridge) reported by Bullock et al. (2005) revealed differences in pile resistance and setup behavior depending on the soil type. Their findings can be found in the paper by Bullock et al. (2005).

2.5 FDOT Impact Pendulum Test Facility

The pendulum-impact facility at the Florida Department of Transportation (FDOT) Marcus H. Ansley Structures Research Center in Tallahassee, Florida, consists of three standalone 50 ft galvanized steel towers and a robust concrete foundation for the anchor system as shown in Figure 2.7. Each pylon is supported by a 19 ft-long, 4 ft diameter drilled shaft foundation. These pylons incorporate three 12 in. diameter steel piles with various $L5 \times 5 \times 5/16$ steel angles (Consolazio, Bui, & Walters, 2012).

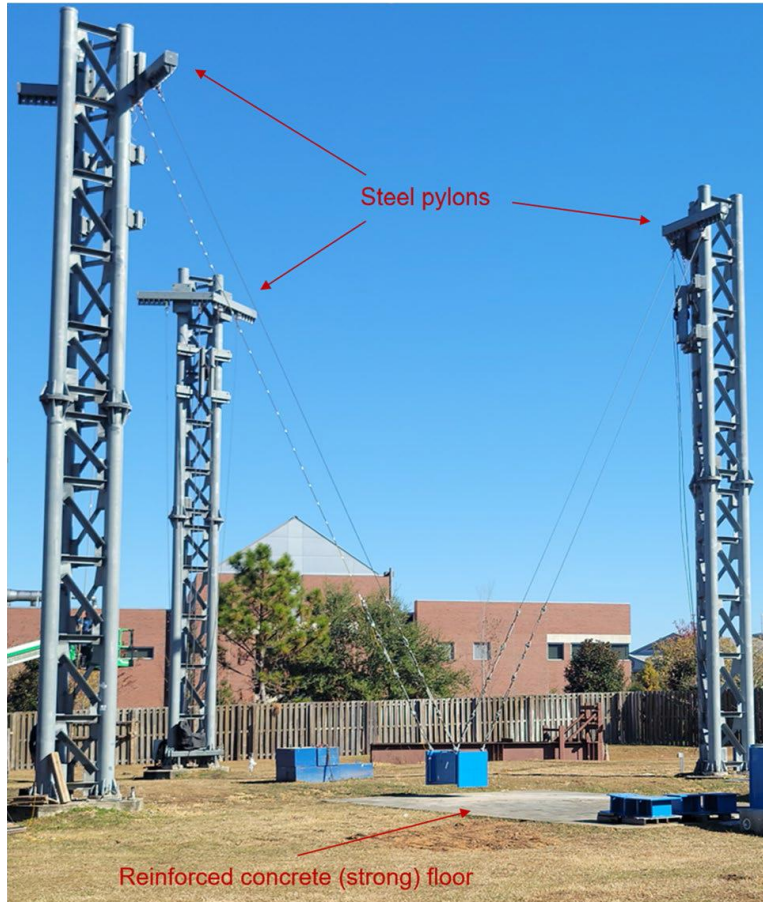


Figure 2.7: FDOT impact pendulum test facility with steel towers and strong floor

The drop height of an attached pendulum mass is adjustable via a steel cable, pulley, and winch system mounted on one of the pylons. The other two pylons are interconnected by four cables that support the pendulum mass's swinging motion during operation. This pendulum support structure can handle impact masses weighing up to 9020 lbs. (4090 kg) dropped from a height of 35 ft. The FDOT pendulum can deliver impact energies of approximately 315 kip-ft (427 kJ). The reinforced concrete foundation for the anchor system measures 34 ft in length, 20 ft in width, and 3 ft in depth.

Accelerometers are commonly installed on the impact mass to record time-varying deceleration. These accelerometers can be oriented in the direction of impact as well as in the vertical direction (Kantrales et al., 2016). Data collected from these accelerometers are used to quantify the time-varying impact force.

2.6 Experimental Apparatus to Simulate Pile Driving

McVay et al. (2009) conducted experiments to study the propagation of waves in typical FDOT full-scale piles under different conditions. In one experiment conducted without soil, they used an 18 in. \times 18 in. \times 180 in. pile equipped with EDC sensors near the top and bottom. The pile was supported by 6 ft long cargo straps suspended from two steel frames. A cylindrical steel pipe hammer filled with concrete, weighing 1000 lbs., was suspended from a 28 ft tall forklift frame. To apply blows to the pile, the hammer was pulled backward to the required height and then released to fall freely. Additional instrumentation on the test pile included PDA accelerometers and strain gauges, as well as UF accelerometers and strain gauges. Figure 2.8 provides a schematic of this experimental setup. In another test aimed at investigating soil-pile interaction, the same pile dimensions were used, but the pile was placed horizontally in a 150 cubic yard Florida silty-sand soil. The soil had an initial moisture content of 11 % and a dry unit weight of 110 pcf. This soil was compacted using walk-behind compactors, and 20 ft of the pile length was buried into the compacted soil. EDC sensors were again placed near the top and bottom of the embedded pile. External instrumentation included piezo-resistant accelerometers at the bottom of the pile and piezo-electric accelerometers at the top. The same hammer as described earlier was used, suspended as a pendulum by a 20 ft steel channel connected to a large forklift. The hammer's strike distance was controlled between 4 ft to 6 ft chord length (equivalent to a drop height of 1 ft) and 14 ft to 16 ft chord length (equivalent to a drop height of 6 ft).

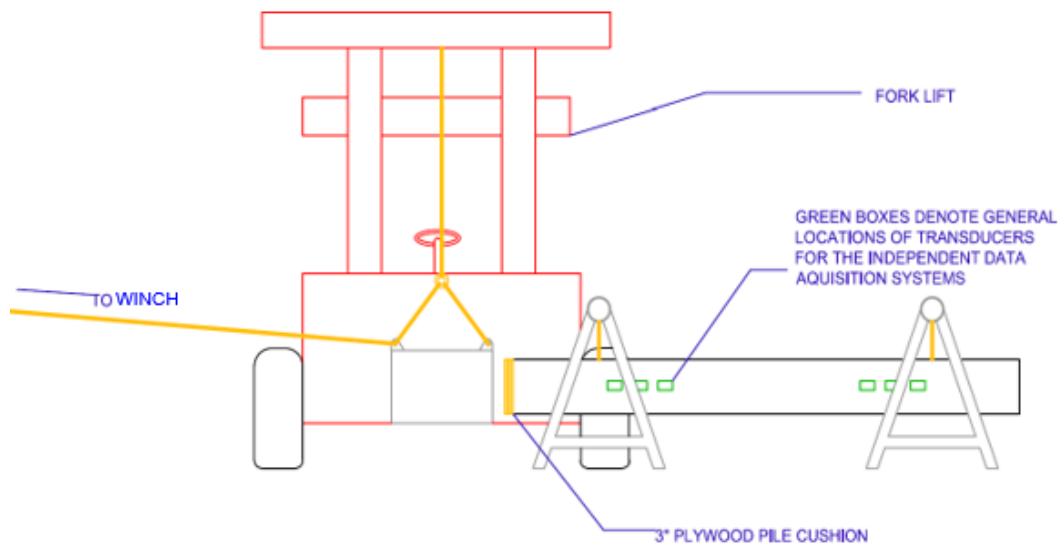


Figure 2.8: Pile driving apparatus (McVay et al., 2009)

McVay, Bloomquist, Vanderlinde, & Clausen (1994) developed an innovative centrifuge modeling apparatus designed for driving scaled model piles within a laboratory environment. This unique apparatus not only had the capability to drive these model piles but also subjected them to lateral loading, all while the centrifuge was in motion. The apparatus itself was intricately designed and connected to a computer system. It consisted of several components, including a soil container, a top beam that housed the pile driving mechanism, and a pile driving sequencer plate, among other features detailed in the author's description. The computer played a central role in initiating and controlling the pile driving process. For lateral loading, a 1200 lbs. air cylinder (denoted as "R") was employed as shown in Figure 2.9. A 0.25 in. range LVDT (Linear Variable Differential Transformer) was used to precisely measure lateral movement. The computer, equipped with specialized software, not only controlled the raising and lowering of the pile driving mechanism but also documented the entire process, recording the results obtained during testing. Model piles were made of high strength aluminum tubing that was 11 inches in length from the bottom of the pile cap and had an outer and inner diameter of 0.375 in. and 0.305 in. respectively. This simulated open-ended piles that had a diameter of 18 in., a length of 44 ft and a flexural stiffness (EI) of 28.98×10^8 lbs. in.². Pile models were driven at 48 times the normal gravitational field (48 g). The author conducted the experiment using the Reid-Bedford sand because the research was concerned with ship impacts in Florida and 90 % of usable waterways in Florida are on sand or silty sand. Also, the properties of the selected soil were widely published.

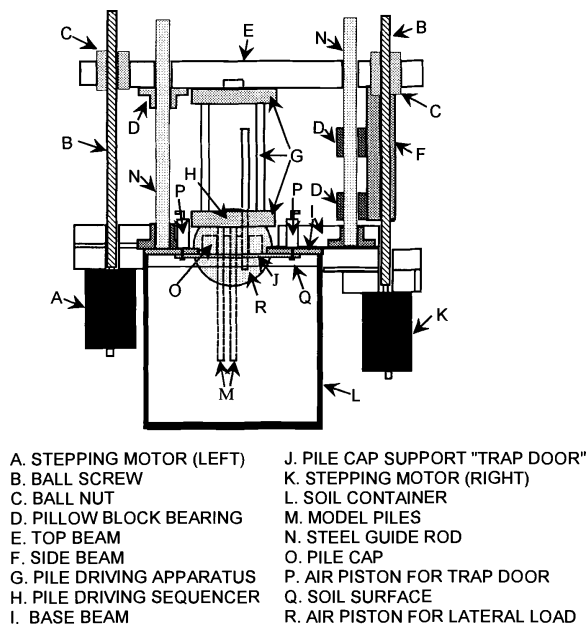


Figure 2.9: Centrifuge pile driving apparatus (McVay et al., 1994)

In another centrifugal test, McVay, Zhang, Han, & Lai (2000) examined the impact of pile cap placement on large deflections. They considered four different pile cap locations in this study, using a centrifuge with a 12.5 g-ton payload capacity. The specimen platform was positioned 1.6 meters from the center of rotation. To replicate real-world stress conditions, model piles were driven during flight at 45 g. Lateral loads were applied to groups of model piles by an air piston rated at 125 psi, capable of delivering a maximum lateral load of 1200 lbs. (equivalent to 1215 tons in real terms). Lateral displacements were measured using an LVDT. The model piles, mimicking 17-inch prototype piles, were constructed from solid square aluminum (6061 alloy) bars, with dimensions of 3/8 inch in width and lengths of 11.54, 9.53, 8.50, and 7.52 inches, corresponding to prototype lengths of 43.31, 35.76, 31.82, and 28.22 feet, respectively. The sand used in the tests was obtained from the Edgar, Florida sand mine and had a gradation like that of Reid-Bedford sand. Further apparatus details (see Figure 2.10) are provided by McVay, Zhang, Molnit, & Peterlai (1998).

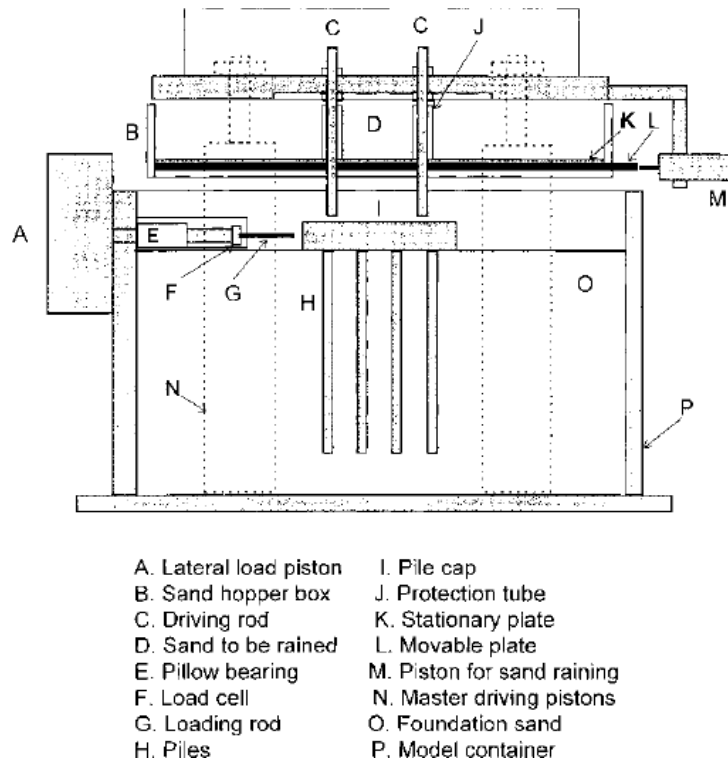


Figure 2.10: Centrifuge pile driving apparatus (McVay et al., 2000)

El-Garhy, Galil, Youssef, & Raia (2013) conducted model tests involving a single pile, unpiled rafts, and central piled rafts. The experiment utilized poorly graded dry sand as the soil material,

characterized by a unit weight of 15.5 kN/m³ and an angle of friction of 33 degrees. Steel hollow piles with an outer diameter of 10 mm and a thickness of 1.5 mm were employed as model piles (see Figure 2.11(a)). Various pile lengths were tested, including 200 mm, 300 mm, and 500 mm, with the steel pipe's modulus of elasticity set at 2.1×10^8 kPa. Pile shoes were affixed to the pile tips, and the pile tops featured bolts for connection with the pile cap. The soil was contained within a steel tank measuring 1 m in depth, 1 m in length, and 1 m in width. Loads were applied via a hydraulic jack connected to the top of a steel frame positioned over the tank, as depicted in Figure 2.11(b).

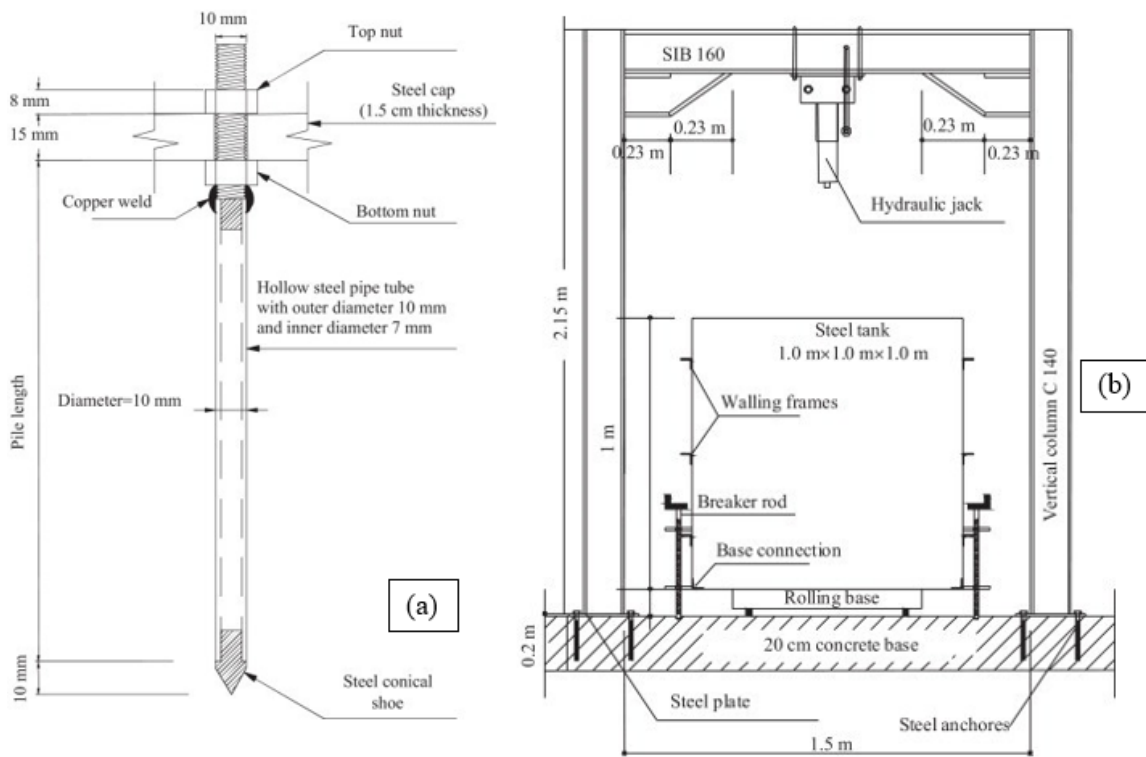


Figure 2.11: (a) Model pile; (b) Vertical cross section of test apparatus (El-Garhy et al., 2013)

2.7 Field Pile Testing

Fam et al. (2003) conducted full-scale field tests on two types of piles: a conventional square prestressed concrete pile and a circular precast composite pile, as illustrated in Figure 2.12. The square pile measured 20 inches by 20 inches by 516 inches and was prestressed using fourteen 0.5-inch diameter seven-wired strands of prestressing steel with an ultimate strength of 270 ksi. The prestressing produced a level of 0.809 ksi. Lateral reinforcement was provided by a No. 5 gauge spiral wire, and the specified compressive strength of concrete was 5.8 ksi. The circular precast

composite pile consisted of a GFRP tube with an outer diameter of 24.6 inches and a structural wall thickness of 0.213 inches, filled with concrete containing a shrinkage-reducing admixture. The specified compressive strength of the concrete was 6 ksi. The composite pile had a length of 516 inches. Both piles were instrumented, as shown in Figure 2.13. The estimated axial load capacities for the prestressed and composite piles, based on the concrete compressive strengths, properties of steel reinforcement, and GFRP tubes, were 2071 kips and 2812 kips, respectively. A hydraulic impact hammer, the ICE Model 160S with a ram weight of 16,000 lbs., was used to drive both piles. To prevent damage to the pile head from the high impact mass, a 7.5-inch-thick plywood cushion was employed. The piles were driven to a depth of 33.5 ft below ground level. During driving, the prestressed concrete pile experienced four blows per inch, while the composite pile experienced six blows per inch. Details regarding the soil properties in the vicinity were not provided.

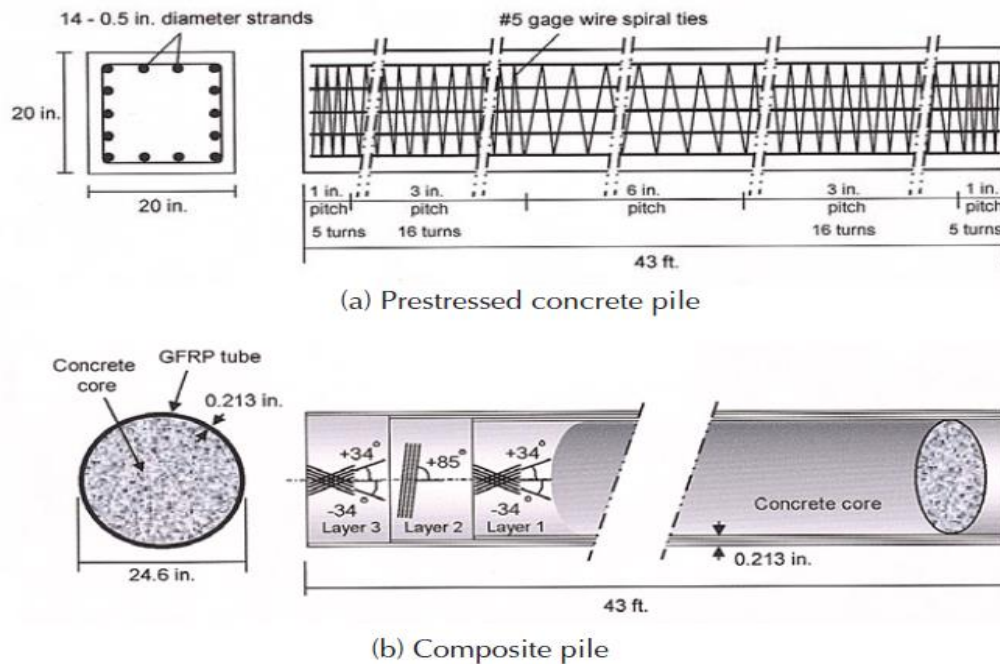


Figure 2.12: Pile details (Fam et al., 2003)

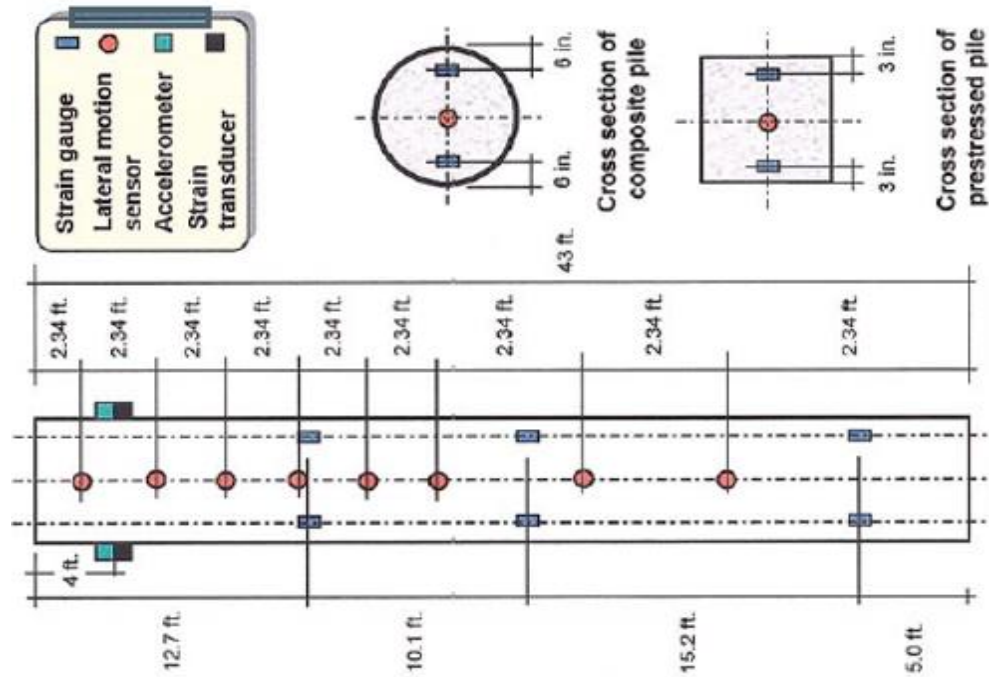


Figure 2.13: Instrumentation of test piles (Fam et al., 2003)

Measurements obtained for the prestressed pile during driving showed a wave speed of 12,150 ft/s. Maximum compressive strength and tensile stress were 2.55 ksi and 0.75 ksi, well below allowable limits of 4.5 ksi in compression and 1.02 ksi in tension. For the composite pile, measurements indicated a wave speed of 11,840 ft/s. Maximum compressive and tensile stresses were 2.78 ksi and 0.42 ksi. These results demonstrated similar driving performance for both piles.

In a study by Rausche et al. (2008) the relationship between ram weight, pile penetration, and stresses in various pile types was investigated. It was found that compression stresses in piles were mainly influenced by ram weight and cushion properties. A heavier ram reduced tension stresses, which could occur when resistance is very low. For a square prestressed concrete pile tested, measuring 85.58 ft (27 m) in length, with a cross-sectional area of 387.50 in² (0.25 m²), and a weight of 35.74 kip (158 kN), the ram-to-pile weight ratio was 0.94. The results showed a tension stress of 0.52 ksi (3.6 MPa) and a compression stress of 3.62 ksi (25 MPa) in the pile.

Roddenberry et al. (2014) conducted a study involving two 24-inch square CFRP prestressed concrete piles as part of the Deer Crossing Bridge project. Both piles were 100 feet long and longitudinally reinforced with twenty 0.6-inch diameter CFRP prestressing strands. Additionally, the CFRP spirals used had a diameter of 0.2 inches. In the study, the first pile was initially driven

normally, and later subjected to hard driving during the latter stage of installation. The second pile, on the other hand, was continuously subjected to hard driving throughout the installation process. Stresses in both piles were monitored and measured using embedded data collectors (EDC), which included strain transducers and accelerometers embedded within the piles. Furthermore, a Pile Driving Analyzer was employed, which utilized accelerometers and strain transducers attached to the surface of the piles to measure forces and velocities. Notably, the authors reported measured stresses of up to 4.0 ksi during the study.

2.8 Confinement by Transverse Reinforcement in Concrete

Confinement in precast piles is generally provided by spirals or ties. In addition to restraining the lateral expansion of the concrete core, the spirals maintain the position of the longitudinal reinforcement under high loads, provide increased ductility, enhance the load-carrying capacity of the pile, and sustain impact forces during pile driving. Spirals are designed such that the confining action they provide would compensate for load capacity losses resulting from concrete spalling.

The confining action of transverse reinforcement is activated by lateral pressure generated by the expansion of concrete under axial compression, at stresses close to the unconfined strength of concrete. In addition to confining the concrete within the core of the pile, confinement reinforcement controls longitudinal cracks resulting from handling, driving, or the design load. Longitudinal spacing between pile turns (spiral pitch) are more closely spaced at the pile top and pile tip for energy absorption and to resist splitting stresses that could result from pile driving activities.

Under compressive loads, concrete experiences longitudinal shortening but also lateral expansion due to Poisson's effect and microcracking. When concrete is confined by steel spirals, this lateral expansion is restricted by the spirals, leading to lateral tensile stresses in the spirals and, in turn, lateral compressive stresses in the concrete core. As a result, the concrete element within the core is subjected to triaxial compression, which enhances both its strength and ductility.

Martinez, Nilson & Slate (1984) and Pantelides, Gibbons & Reavely (2013) have provided a formula to calculate the confined compressive strength of normal weight reinforced concrete, denoted as f'_{cc} , for columns confined by steel spirals. This formula is given by Equation (2.19).

$$f'_{cc} = 0.85f'_c + 4.0f_l \left(1 - \frac{s}{d_c}\right) \quad (2.19)$$

where

f_l is the confining lateral compressive strength produce by the steel spiral, f'_c is unconfined concrete strength, and $\left(1 - \frac{s}{d_c}\right)$ represents the confinement effective stress factor, which shows that the confinement becomes less effective as the spiral pitch, s , increases and approaches the core diameter, d_c . It should be noted that $0.85f'_c$ in Equation (2.19) represents the in-place concrete strength.

Also, the confining lateral compressive strength produced by the circular steel spirals, as depicted in Figure 2.14, is provided by Equation (2.20).

$$f_l = \frac{2A_{sp}f_{sp}}{sd_c} \quad (2.20)$$

where

A_{sp} is the cross-sectional area of the spiral and f_{sp} is the stress in the spiral at maximum load.

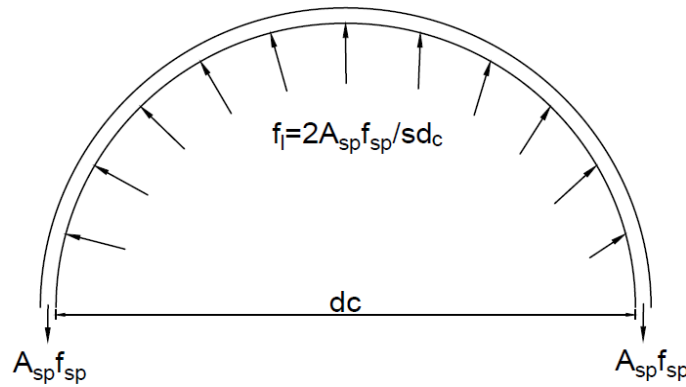


Figure 2.14: Confining action of spirals

Also, Mander, Priestley, & Park (1988) provided a comprehensive model for the confined compressive strength of concrete reinforced with steel spirals as seen in Equation (2.21).

$$f'_{cc} = 0.85f'_c \left(-1.254 + 2.254 \sqrt{1 + 7.94 \frac{f'_l}{0.85f'_c}} - 2 \frac{f'_l}{0.85f'_c} \right) \quad (2.21)$$

where the effective lateral confining compressive strength f'_l for steel spirals is

$$f'_l = k_e \frac{2A_{sp}f_{yh}}{sd_c} \quad (2.22)$$

On the other hand, Afifi, Mohamed, & Benmokrane (2015) and Mousa, Mohamed, & Benmokrane (2018) stated the confined concrete strength for concrete reinforced with circular GFRP spirals as Equation (2.23) and Equation (2.24), respectively.

$$f'_{cc} = 0.85f'_c \left(1 + 4.547 \left(\frac{f'_l}{0.85f'_c} \right)^{0.723} \right) \quad (2.23)$$

$$f'_{cc} = 0.85f'_c \left(0.85 + \sqrt{0.17 + 6.43 \frac{f'_l}{0.85f'_c} - 2 \frac{f'_l}{0.85f'_c}} \right) \quad (2.24)$$

where the effective lateral confining compressive strength f'_l for GFRP spirals is

$$f'_l = k_e \frac{2A_{sp}f_{fb}}{sd_c} \quad (2.25)$$

and the confinement effectiveness coefficient k_e is

$$k_e = \frac{1 - (s'/2d_c)}{1 - \rho_{cc}} \quad (2.26)$$

where

f_{fb} is the bend strength of spirals recommended in ACI 440.1R as

$$f_{fb} = \left(0.05 \frac{r_b}{d_b} + 0.3 \right) f_{fu} \leq f_{fu} \quad (2.27)$$

where

r_b is the inner radius of the spirals; d_b is the diameter of the spiral bars; and f_{fu} is the ultimate tensile strength of the straight FRP bars.

Section 932-3.3.1 of the FDOT (2019) standard specifications for road and bridge construction requires that the minimum strength of bent bars (90° bends), be no less than 60% of the straight bar strength.

The ACI specification for spiral reinforcement aims to ensure that it enhances the core's capacity by an amount equal to the shell's capacity. This is done to maintain capacity in case the shell

becomes damaged or spalls off. According to the ACI specifications (ACI 318; ACI 543), the required transverse reinforcement ratio for a pile reinforced with spirals must be

$$\rho_s = 0.45 \left(\frac{A_g}{A_c} - 1 \right) \frac{f'_c}{f_{yh}} \quad (2.28)$$

or,

$$\rho_s = 0.12 \frac{f'_c}{f_{yh}} \quad (2.29)$$

whichever is greater

where

ρ_s is the ratio of the volume of spiral reinforcement to the volume of concrete core (out-to-out of spiral), i.e. $4A_{sp}/sd_c$, A_g is the gross area of the pile, A_c is the area of pile core (out-to-out of spiral), f_{yh} is the yield strength of spiral reinforcement, and f'_c is the specified compressive strength of concrete.

Equations (2.28) and (2.29) were derived specifically for circular spirals. However, ACI 318 also offers empirical equations for square or rectangular transverse reinforcement as follows:

$$A_{sh} = 0.3sh_c \left(\frac{A_g}{A_c} - 1 \right) \frac{f'_c}{f_{yh}} \quad (2.30)$$

or,

$$A_{sh} = 0.12sh_c \frac{f'_c}{f_{yh}} \quad (2.31)$$

whichever is greater

where

A_{sh} is the total cross-sectional area of transverse reinforcement in the direction considered, s is the spacing of tie sets in the longitudinal direction, and h_c is the width of the core in the direction considered.

The ACI spiral equations are not generally applicable to piles; therefore, these equations were adjusted for piles in seismic regions. PCI recommendation for transverse reinforcement in prestressed concrete piles in regions of low to medium seismic risk is:

$$\rho_s = 0.12 \left(\frac{f'_c}{f_{yh}} \right) \geq 0.007 \quad (2.32)$$

where

$$f'_c \leq 6000 \text{ psi (40 MPa) and } f_y \leq 85,000 \text{ psi (585 MPa).}$$

In regions of high seismic risks, the PCI recommendation for minimum amount of transverse reinforcement for prestressed concrete pile with circular ties or spirals is

$$\rho_s = 0.45 \left(\frac{f'_c}{f_{yh}} \right) \left(\frac{A_g}{A_c} - 1 \right) \left[0.5 + 1.4 \frac{P_u}{f'_c A_g} \right] \quad (2.33)$$

but not less than

$$\rho_s = 0.12 \left(\frac{f'_c}{f_{yh}} \right) \left[0.5 + 1.4 \frac{P_u}{f'_c A_g} \right] \quad (2.34)$$

where

P_u is the maximum factored axial compressive load on the pile, $f'_c \leq 6000$ psi (40 MPa) and f_y is the yield strength of transverse reinforcement $\leq 85,000$ psi (585 MPa).

In regions of high seismic risks, the PCI recommendation for total area of transverse reinforcement, A_{sh} , in the direction considered for prestressed concrete pile with square spirals or ties is:

$$A_{sh} = 0.3sh_c \frac{f'_c}{f_y} \left(\frac{A_g}{A_c} - 1 \right) \left[0.5 + 1.4 \frac{P_u}{f'_c A_g} \right] \quad (2.35)$$

but not less than

$$A_{sh} = 0.12sh_c \frac{f'_c}{f_y} \left[0.5 + 1.4 \frac{P_u}{f'_c A_g} \right] \quad (2.36)$$

where

h_c is the cross-sectional dimension of pile core measured center-to-center of spiral or tie reinforcement and $f_y \leq 70,000$ psi (480 MPa).

Mohamed, Afifi, & Benmokrane (2014) tested fourteen (14) full-scale circular column specimens under concentric axial load. Six (6) specimens each were reinforced with GFRP and another six (6) were reinforced with CFRP rebars. The other two reference columns were plain and steel RC specimens. All specimens had diameter of 300 mm and measured 1500 mm in length. Test parameters were confinement configuration (spirals versus hoops), hoop lap length, volumetric ratio, and FRP reinforcement type (GFRP versus CFRP). FRP Spiral reinforcements were designed

according to clause 8.4.3.13 of the Canadian Standards Association (2012) code requirements. It stipulates that spiral reinforcement shall have a minimum diameter of 6 mm, distance between spiral turns shall not exceed 1/6 of the core diameter, clear spacing between successive spiral turns shall not be less than 25 mm or exceed 75 mm, and the minimum volumetric ratio of spirals is given by

$$\rho_{Fs} = \frac{f'_c}{f_{Fh}} \left(\frac{A_g}{A_c} - 1 \right) \left(\frac{P}{P_o} \right) \quad (2.37)$$

where

$$\left(\frac{P}{P_o} \right) \geq 0.2 \quad (2.38)$$

$$\left(\frac{A_g}{A_c} \right) \geq 0.3 \quad (2.39)$$

where

f'_c is the specified concrete compressive strength; f_{Fh} is the least of $\phi_{FRP} f_{fu}$, or the stress equivalent to a strain of $0.006E_f$ in the FRP, or the stress corresponding to the local failure of corners, hooks, bends, and laps; ϕ_{FRP} is the resistance factor for FRP reinforcement; P is the applied concentrated load which is assumed to be 0.65 times the nominal axial load capacity of the designed column, P_o .

According to Mohamed et al. (2014), the ratio f'_{cc}/f'_{co} , where f'_{cc} is the confined concrete strength and f'_{co} is the in-place compressive strength of the unconfined concrete in the column ($0.85f'_c$) indicates the strength enhancement of the concrete core by the confining FRP spirals and hoops. The ratio of f'_{cc}/f'_{co} obtained for the FRP RC columns ranged from 1.38 to 1.81, and ductility ranged from 1.63 to 2.53. This shows the ductility enhancement capabilities of the confining FRP reinforcements even when the concrete cover has spalled.

2.9 Pile Axial Load

According to PCI Design Handbook (1999), for a prestressed concrete compression member P_o is given by:

$$P_o = (0.85f'_c - 0.6f_{pe})A_g \quad (2.40)$$

However, when considering service loads, the allowable axial capacity (N) for prestressed concrete piles that are fully supported laterally by soil and primarily subjected to axial load is determined as follows:

$$N = (0.33f'_c - 0.27f_{pe})A_g \quad (2.41)$$

A factor of safety, P_o/N , between 2.0 and 3.0 is usually sufficient for short column piles (PCI Design Handbook, 1999).

2.10 Spiral Area and Pitch Requirements

Additional requirements for confinement reinforcement in terms of the cross-sectional area, pitch, and number of turns according to PCI are provided below. It's important to note that these are minimum requirements and are applicable when a significant portion of the pile's length is laterally supported by soil and when minimal lateral loads are applied to the pile. These specifications, designed for steel spirals, are prescriptive and suitable for piles installed in regions with low or negligible seismic activity. The requirements are as follows:

- For piles with nominal sizes equal to or less than 24 in., minimum spiral cross-sectional area, A_{sp} , is 0.034 in². Spiral pitch at both ends of the pile are 1 in. for 5 turns, followed by a pitch of 3 in. for 16 turns, and then a spiral pitch of 6 in. for the remaining portion along the pile length.
- For piles with nominal sizes greater than 24 in., minimum spiral cross-sectional area, A_{sp} , is 0.04 in². Spiral pitch at both ends of the pile are 1.5 in. for 4 turns, followed by a pitch of 2 in. for 16 turns, and then a spiral pitch of 4 in. for the remaining portion along the pile length.

However, Benmokrane, Mohamed, ElSafty, & Nolan (2018) designed No. 5 GFRP spirals to provide confinement for the concrete core of 60-ft-long 24-in. square non-prestressed concrete piles. Spiral pitch at both ends of the piles were 2 in. for 5 turns, followed by 3 in. for 16 turns, and then a spiral pitch of 6 in. for the remaining portion of the pile length.

2.11 GFRP Stirrups and Spirals as Confinement during Pile Driving – Lesson Learned

Vicaria et al. (2014) conducted an analysis of results obtained from driving and high-strain dynamic tests performed on 400 mm (15.7 in.) square GFRP-reinforced piles. These piles had a length of 12 m (39.3 ft) and were longitudinally reinforced with 12 GFRP bars (3 at each corner), each having a diameter of 20 mm. Additionally, the piles were transversely reinforced with 10 mm GFRP stirrups. During the handling of these GFRP-reinforced piles, the authors reported an average crack width of 0.30 mm (0.01 in.), which was attributed to the lower axial stiffness of the GFRP bars. For driving these piles to refusal, a hammer with a ram weight of 9 tons and a constant drop height of 0.40 m was utilized. Subsequently, the drop height was increased to 1.20 m for the dynamic load tests. The results indicated that although significant tensile stresses exceeding 15 MPa were generated in the GFRP piles during pile driving, no damage occurred because of the dynamic testing of the piles.

Benmokrane, Mohamed, ElSafty, & Nolan (2018) conducted a field test on two 60 ft long, 24-inch square piles that were reinforced longitudinally with GFRP bars and transversely with GFRP spirals. In the case of Pile 1, 20 No. 8 GFRP bars were utilized as longitudinal reinforcement, while for Pile 2, 12 No. 8 GFRP bars were used for longitudinal reinforcement. Both piles were reinforced with No. 5 GFRP spiral reinforcement in the transverse direction, resulting in reinforcement ratios of 2.7% for Pile 1 and 1.6% for Pile 2. The spiral pitch at both ends of the piles was 2 inches for 5 turns, followed by a pitch of 3 inches for 16 turns, and then a spiral pitch of 6 inches for the remaining portion along the pile length. Without prestressing involved, the maximum allowable pile compressive stress was estimated using the first term of Equation (2.13), which is $0.7f'_c$. Although the piles were 60 ft long, the maximum tensile stress was estimated using the first term of Equation (2.14), which is $6.5(f'_c)^{0.5}$. The test results indicated that the maximum compressive stresses measured in Pile 1 were within the allowable limit of 5.95 ksi. However, for Pile 2, the tensile stresses at the end-of-drive exceeded the allowable limit of 0.6 ksi, with values reaching up to 1.6 ksi. Overall, the test demonstrated that the concrete core of the piles was effectively confined by GFRP spirals, with no cover spalling observed. Additionally, no cracks were detected, and there was no significant pile damage resulting from compression loading.

2.12 Properties of Fiber-Reinforced Polymer

FRPs consist of fibers embedded within a polymeric resin matrix. Different types of FRPs include AFRP (Aramid Fiber Reinforced Polymer), BFRP (Basalt Fiber Reinforced Polymer), CFRP, and GFRP. These FRP materials offer a corrosion-resistant alternative to steel. They also possess desirable properties such as electromagnetic transparency in the case of GFRP, high stiffness-to-weight ratios, and high strength-to-weight ratios when compared to steel. These characteristics make FRP reinforcements attractive for use in concrete structures (Correia, Branco, & Ferreira, 2007; Robert & Benmokrane, 2013).

In FRP reinforcements, the fibers bear a significant portion of the applied load, while the polymeric resin matrix facilitates stress transfer among the fibers (Cantwell & Morton, 1991). FRPs exhibit anisotropic behavior and maintain linear elastic behavior until failure, whereas steel is isotropic and undergoes significant yielding before failure. Table 2.2 summarizes the typical tensile properties of reinforcements of AFRP, BFRP, CFRP, GFRP, and steel materials. Additionally, Figure 2.15 illustrates that steel demonstrates greater ductility compared to FRPs.

Table 2.2: Typical tensile properties of reinforcement

	AFRP	BFRP	CFRP	GRFP	Steel
Nominal yield stress, ksi (MPa)	NA	NA	NA	NA	40 – 75 (276 – 517)
Tensile strength, ksi (MPa)	250 – 386 (1720 – 2540)	150 – 240 (1035 – 1650)	87 – 535 (600 – 3690)	70 – 230 (483 – 1600)	70 – 100 (483 – 690)
Elastic Modulus, ksi (GPa)	6000 – 18200 (41 – 125)	6500 – 8500 (45 – 59)	15900 – 84000 (120 – 580)	6500 – 8700 (45 – 60)	29000 (200)
Yield strain, percent	NA	NA	NA	NA	0.14 – 0.25
Rupture strain, percent	1.9 – 4.4	1.6 – 3.0	0.5 – 1.7	1.2 – 3.1	6 – 12

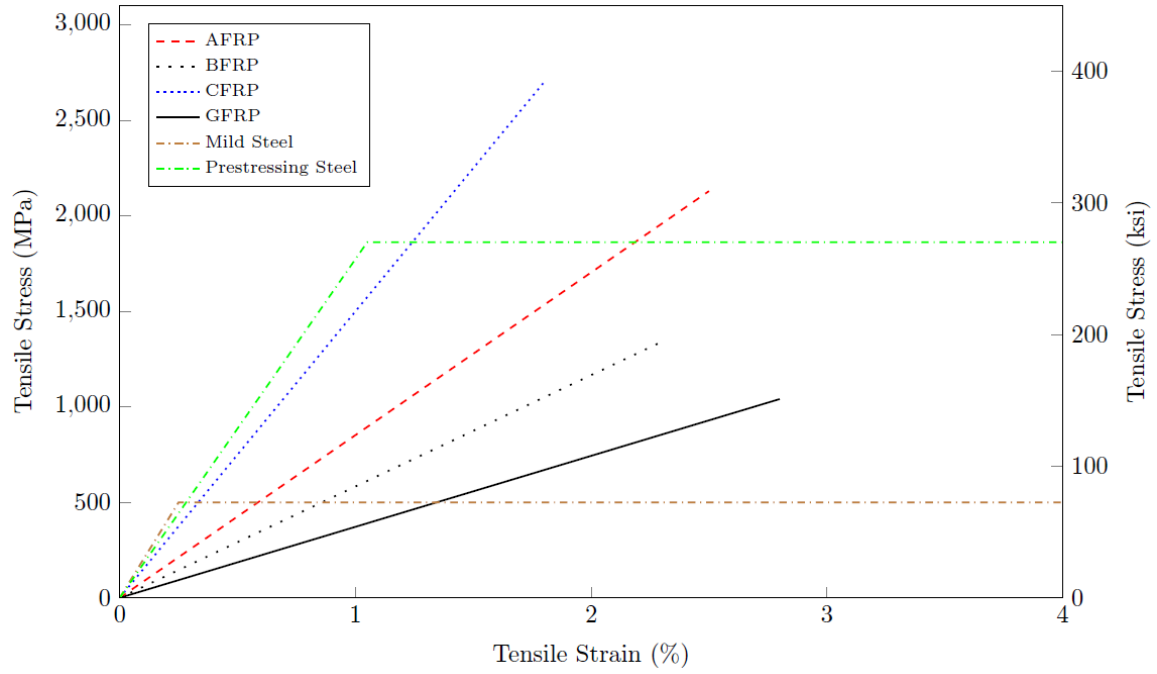


Figure 2.15: Comparison of the stress-strain curve for steel and FRPs

CHAPTER 3. IMPACTOR AND SPIRAL DESIGN

3.1 Introduction

In the previous chapter (Chapter 2), we reviewed various pile hammer types and their specifications. It was observed that the impact velocity of these hammers typically ranged from about 5 ft/s to 33 ft/s. In contrast, the rated energy of these hammers had a wide range, varying from about 5 kip-ft to over 2000 kip-ft.

For the purposes of our research, the experimental apparatus designed to replicate the impact loading on pile specimens was based on the specifications we discussed earlier. This apparatus was constructed to operate within the constraints of the current pendulum facility stated in Section 2.5.

3.2 Design Requirements and Preferences for Impactor and Test Setup

Incorporating the ability to replicate typical pile driving hammer impact velocity and energy, the apparatus was purposefully designed to exert compressive stress equal to or greater than the recommended concrete pile limit. The maximum allowable pile stresses, as outlined in the Florida Department of Transportation Standard Specifications 455-5.12.2 (FDOT, 2018), are defined by Equation (2.13).

For commonly produced piles with a minimum 28-day concrete strength of f'_c at 6000 psi and an initial prestress of 1000 psi before losses, the calculated maximum allowable compressive stress (s_{apc}) is $[0.7(6000 \text{ psi}) - 0.75(0.8 \times 1000 \text{ psi})] / 1000$, resulting in 3.6 ksi. Depending on the specific properties of the piles being driven in the field, the allowable maximum compressive stress during driving may exceed this value.

As a result, the design criteria for both the impactor and the impact test setup are summarized as follows:

- 1 Attainable impact velocity of 30 ft/s and higher.
- 2 Achievable impact energy of 120 kip-ft and above, considering the capabilities of the pendulum facility.
- 3 Realization of a pile top stress of 5 ksi.

The first two requirements pertain solely to the impactor, while the third condition (pile top stress) relies on both the impactor and the pile restraint. Additionally, other test requirements considered encompass:

- Impactor drop height, which should be less than 30 ft to deliver the desired pile top stress.
- Ensuring that displacement of the restraining block remains within acceptable limits.
- Striving for minimum or no utilization of soil to streamline test preparation.

Ensuring that the displacement of the restraining blocks was not excessive meant the blocks were not always repositioned after each impact. Likewise, minimizing or eliminating the use of soil was aimed at optimizing test preparation time.

3.3 Impact Test Concept

As illustrated in Figure 3.1, the pile specimen was positioned atop supports that permitted movement along the direction of the impact force without constraint. It's essential to note that this arrangement differs from an actual pile installation, where the pile penetrates the soil, resulting in energy dissipation into the surrounding soil through the sides of the pile. However, it's crucial to emphasize that the experiment's primary objective does not encompass simulating actual soil conditions because the objective of the testing was to cause large stress to the spiral efficiently. In addition, replicating such conditions is not only challenging but would also significantly prolong the experiment's duration.

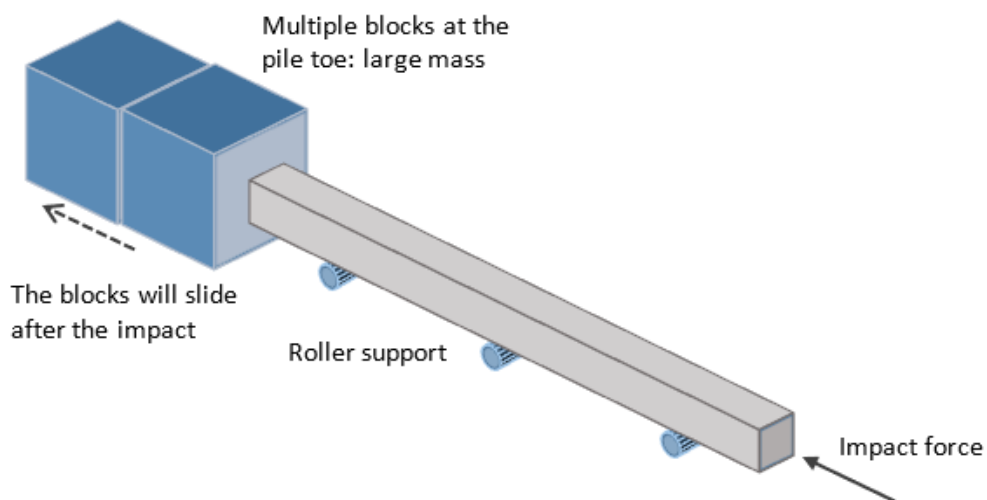


Figure 3.1: Illustration of the block-based design

Within this testing setup, several blocks were positioned adjacent to the pile tip. Following the impact, both the pile and the blocks experienced a degree of sliding motion. This motion occurred because the potential energy generated by the impactor was transformed into kinetic energy, affecting both the pile and the blocks. However, it's noteworthy that the blocks eventually came to a halt due to the frictional resistance between the blocks and the ground.

3.4 Design of Impactor and Test Setup

Analytical equations and finite element analyses played a central role in the design of both the impactor and the pile restraint. While the process was iterative, we have presented the final process here for clarity and conciseness. The primary objective was to ensure that the design requirements could be achieved for a specific drop height without causing any damage to the experimental apparatus. During the actual experiment, a progressive increase in the drop height was employed to gather additional data for the same specimen. This approach was chosen because predicting the impact stress with high certainty is challenging. By incrementally increasing the drop height, we aimed to study the pile's behavior both before and after failure. It's important to note that the major sources of uncertainty in this context are the frictional forces between the pile restraint and the soil, as well as the presence of plywood cushions at both the pile's top and tip. Nevertheless, the impact stress could be readily adjusted during the experiment by either increasing or decreasing the drop height. In the initial design phase, we deliberately selected a target drop height that could be easily adjusted, rather than opting for extremely low or high drop heights that would prove challenging to modify.

3.4.1 Estimation of Test Setup Performance (Analytical Calculation)

If we have the mass of the impactor as m_a , the drop height as h , and the velocity of the impactor immediately before hitting the pile (after the drop) as v_{ai} , and we consider that energy loss due to the swing of the impactor is negligible, we can calculate the impact energy based on the potential energy E_p of the impactor.

$$E_p = m_a g h \quad (3.1)$$

The kinetic energy of the impactor just before it hits the pile can be calculated using the formula:

$$E_k = \frac{1}{2} m_a v_{ai}^2 \quad (3.2)$$

The impact velocity for different drop heights can be determined using the principle of conservation of energy, that is, the potential energy E_p of the impactor at a certain height is equal to the kinetic energy E_k of the impactor just before it hits the pile. The plot in Figure 3.2 shows how the impact velocity changes with varying drop heights for an impactor mass m_a of 6000 lbm (2700 kg).

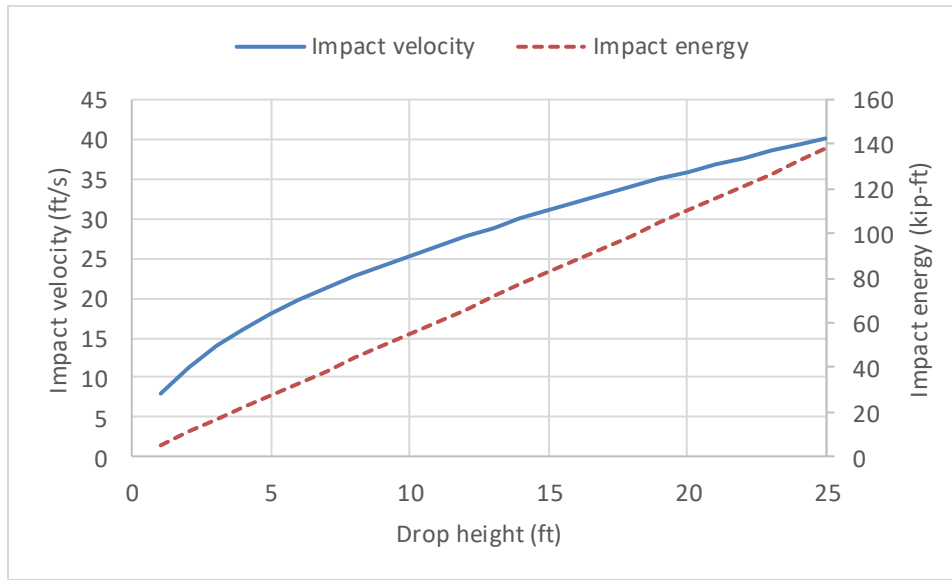


Figure 3.2: Impact velocity and impact energy of the impactor

The indicates that at a 14-ft drop height, the impactor achieves an impact velocity of 30 ft/s, resulting in an impact energy of 77 kip-ft. To reach higher impact energies of 120 kip-ft and above, the drop height needs to be increased to at least 22 ft.

In the schematic diagram presented in Figure 3.3, several key variables are introduced for further discussions; d is the displacement of the pile restraining blocks after the impact m_b and m_c are the mass of the pile and pile restraining blocks, respectively. v_{ai} , v_{af} , $v_{bi} = 0$, and v_{bf} are the velocity of the impactor just before the impact, velocity of the impactor after the impact, velocity of the pile restraint before the impact, and velocity of the pile restraint after the impact, respectively. The friction between the pile restraints and the soil depends on m_c , gravity g , and friction coefficient μ . Finally, the coefficient of restitution C_R is assumed to be 0.5.

The primary goal of this analysis is twofold. Firstly, it aims to comprehend the underlying physics to improve the design of both the impactor and the pile restraint. Secondly, it seeks to derive initial estimates that will be valuable for subsequent finite element analysis. In this analytical calculation, an isolated system was assumed. Although the process involved iterations, this discussion will focus on the most pertinent scenarios. For a more precise estimation, we would need to turn to the finite element analysis.

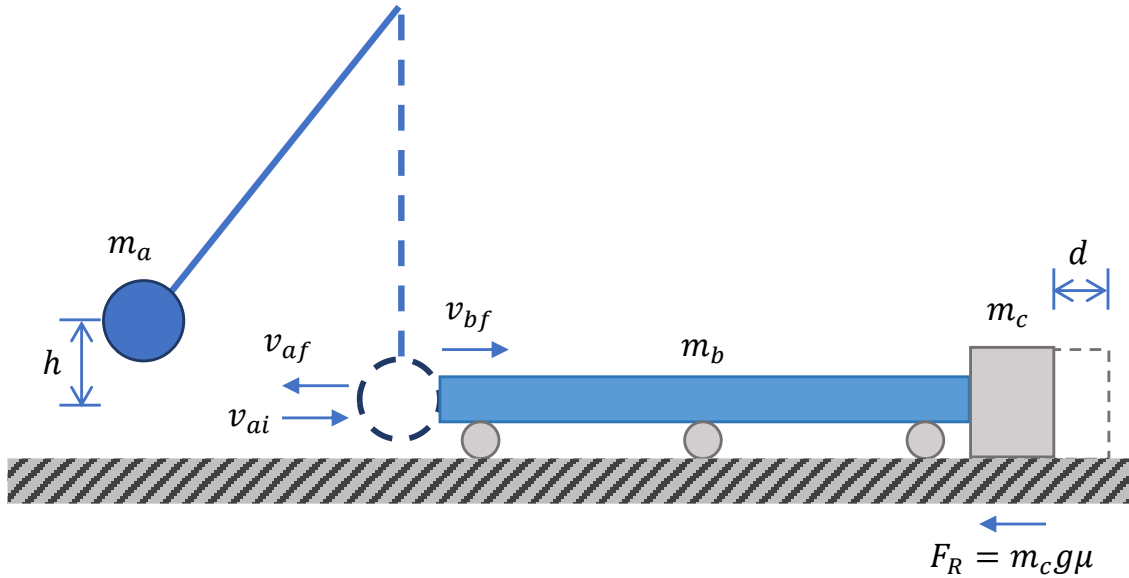


Figure 3.3: Schematic diagram of the variable involved with the test setup

In the context of the setup, as per the velocities indicated in Figure 3.3, the conservation of momentum is described by the equation:

$$m_a v_{ai} = (m_b + m_c) v_{bf} - m_a v_{af} \quad (3.3)$$

Utilizing the definition of the coefficient of restitution:

$$C_R = \frac{v_{bf} + v_{af}}{v_{ai}} \quad (3.4)$$

The masses are assigned as follows: The mass of the pile m_b was assumed to be 7700 kg (17,000 lbs) based on the concrete pile's dimensions of 2 ft \times 2 ft \times 28 ft. However, m_a and m_c were selected during the design process.

The primary design requirement is to apply a 5 ksi stress at the pile's top, which corresponds to a force of 2880 kips for the 2 ft \times 2 ft pile cross-section. While an accurate calculation of the peak

impact force is not possible analytically, an average impact force can be estimated using the impulse-momentum theorem:

$$F_{avg}t = (m_b + m_c)v_{bf} \quad (3.5)$$

A rough estimate of the impact time t was derived from a quarter of the sine wave, that is, the response of the pile under the impulse F_{avg} . Here, it is assumed that the impactor bounces backwards after reaching the peak displacement (compression) of the pile. The pile is assumed to be an axial “spring.” Then, the impact time is:

$$t = \frac{T_n}{4} = \left(\frac{2\pi}{\omega_n}\right)\left(\frac{1}{4}\right) \quad (3.6)$$

By solving the partial differential equation of an axially loaded member, the natural frequency can be obtained as:

$$\omega_n = \frac{\pi}{2L} \sqrt{\frac{EA}{m_b/L}} \quad (3.7)$$

Here, L represents the length of the pile, and E was assumed as 6178 ksi (taken from Roddenberry et al. 2014). This results in $t = 0.00217$ seconds, which is used as the impact time to estimate the average impact force (not the time of peak stress – which cannot be obtained analytically).

During the design process, the mass of the restraining blocks m_c was considered in the range of 22,046 lbm (10,000 kg) to 88,184 lbm (40,000 kg). The maximum average impact force F_{avg} was estimated to range from 3121 kips to 3375 kips, indicating that the desired 5 ksi top stress was attainable. However, the drop height can be increased to further enhance the impact energy if necessary. This analysis verifies that the design objective is achievable.

It is important to note that this estimate of F_{avg} was quite rough, as it did not account for factors like sliding and the presence of plywood, both commonly encountered in pile installation. These factors can affect the impact force.

In addition, the displacement of the restraining blocks can be estimated using the conservation of energy:

$$\frac{1}{2}(m_b + m_c)v_{bf}^2 = F_R d \quad (3.8)$$

The friction force (F_R) depends on the friction coefficient (μ). A design preference is to minimize the displacement of the restraining blocks because excessive displacement significantly increases the experiment time because of the need to move the blocks with a crane even after an impact from a low drop height impact. Figure 3.4 illustrates the estimated movement of the restraining blocks using the earlier equations and Equation (3.8), assuming μ as 0.45.

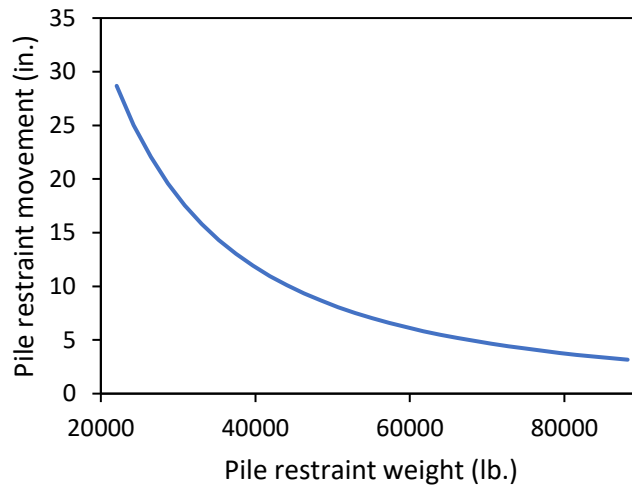


Figure 3.4: Estimated movement of the restraining blocks

To provide the weights that restrict pile movement at the tip, two 4 ft × 4 ft × 6 ft steel blocks composed of 0.75-inch-thick plates filled with concrete were designed. Detailed drawings can be found in Appendix A. These blocks have an estimated mass of 16,900 lb (7,666 kg) each. Additionally, four extra concrete blocks measuring 8 ft × 7 ft × 4 ft were supplied by FDOT as additional restraining blocks. The mass of these blocks was estimated at 25,200 lb (11,431 kg) each. Increasing the number of blocks and thus the total mass of restraining blocks can help reduce the displacement of both the pile and the restraining blocks.

3.4.2 Estimation of Test Setup Performance (Finite Element Analysis)

This section primarily employs SI units for its parameters as they were used in the FE analysis. However, U.S. customary units are provided in parenthesis where necessary. The simulated components of the impact tests are illustrated in Figure 3.5 using LS-Dyna software.

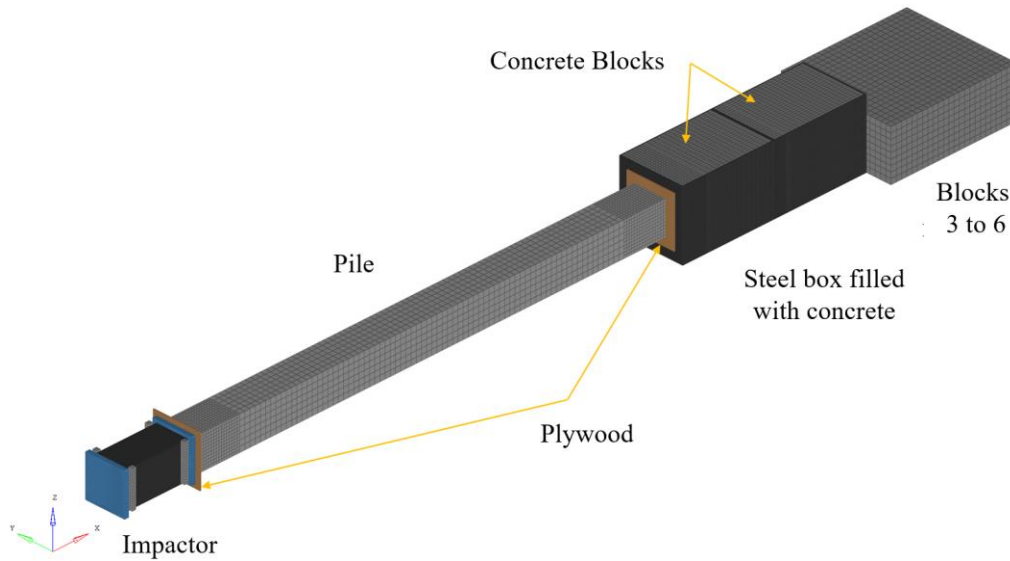


Figure 3.5: Simulated impact on the pile using LS-Dyna

The explicit finite element solver was employed to conduct the impact test analysis. The simulation utilized 3D solid elements with a full integration formulation (ELEFORM 2) to represent all the components involved. Beam elements (1D) were used to describe the welding connections in the steel parts. For the concrete pile, a fine mesh size was applied at both ends, while the middle section used a coarser mesh. Additionally, two sheets of 3/4 inch-thick (19 mm) plywood were included at two contact points where the pile interacts with the impactor and the restraining blocks. Two different contact algorithms, "node to surface" and "automatic single surface," were employed to model interactions between different parts of the simulation.

Table 3.1 provides an overview of the components utilized in the Finite Element (FE) model, while Table 3.2 details the material properties of each component. In this model, all the steel components were represented using piecewise linear plasticity with an isotropic MAT 24 formulation. The steel was considered to transition to a perfectly plastic state at 500 MPa. To account for the influence of strain rate, a viscoplastic formulation with VP=1, as per Škrlec and Klemenc (2016), was integrated into the simulation.

Table 3.1: Summary of FE model

Component	Material	Total mass	Element size (min, max)
		Kg (lb.)	mm (in.)
Impactor	Steel (elastic-plastic)	2700 (6000)	10, 20 (0.4,0.8)
Pile	Concrete (elastic)	7700 (17000)	100 (4)
Steel box	Steel (elastic-plastic)	1350 (2976)	5, 20 (0.2, 0.8)
Concrete block	Concrete (elastic)	7481 (16493)	25 (1)
Plywood	Wood (elastic-plastic)	21 (46)	5 (0.2)
Extra concrete blocks	Concrete (elastic)	11793 (25999)	100 (4)

Table 3.2: Material properties used in the analysis

Material	Density	Module of elasticity	Yield stress	Poisson's ratio
	kg/m ³ (lb./ft ³)	GPa (ksi)	MPa (ksi)	
Steel (impactor)	7850 (490)	210 (3×10^4)	345 (50)	0.3
Steel (blocks)	7850 (490)	210 (3×10^4)	345 (50)	0.3
Concrete (pile)	2430(151)	42.5 (6.2×10^3)	70 (10.)	0.3
Concrete (blocks)	2400(150)	26.3 (3.8×10^3)	50 (7)	0.3
Wood	673(42)	$E_L=16.7 (2.4 \times 10^3)$	42 (6)	0.15
		(Longitudinal)	(tensile)	
		$E_T= 0.1 (14.5)$	54 (7.8)	
		(Transverse)	(compressive)	

To optimize computational efficiency, an elastic material model was applied to the concrete component. This decision was made as the primary focus here did not involve an intricate analysis of concrete failure, but rather centered on defining the shapes and dimensions of the steel components, following insights from Murray (2007a). Furthermore, it is worth noting that most of the concrete elements remained within the yield stress limit. To replicate the failure mechanisms

in the plywood, the MAT_143 WOOD model was employed, taking into consideration a 10% moisture content (Murray, 2007b).

At a drop height of 22 ft, the finite element analyses confirmed that the required impact stress was successfully achieved for the pile specimen. Nonetheless, acknowledging the uncertainties related to the modeling of plywood and friction, as well as any potential unidentified issues, practical testing may necessitate adjustments in the drop height of the impactor. The subsequent discussion delves into the implications of utilizing a 22-ft drop height. This height corresponds to an impact velocity of 37.63 ft/s (11.46 m/s). As displayed in Figure 3.6, the impactor remained within the yield stress parameters, with the exception of localized high stresses observed at the corners of the box, which spanned less than one element in size, approximately 5mm. Additionally, Figure 3.8 and Figure 3.8 illustrate the stress distribution in the pile, which surpasses 5 ksi.

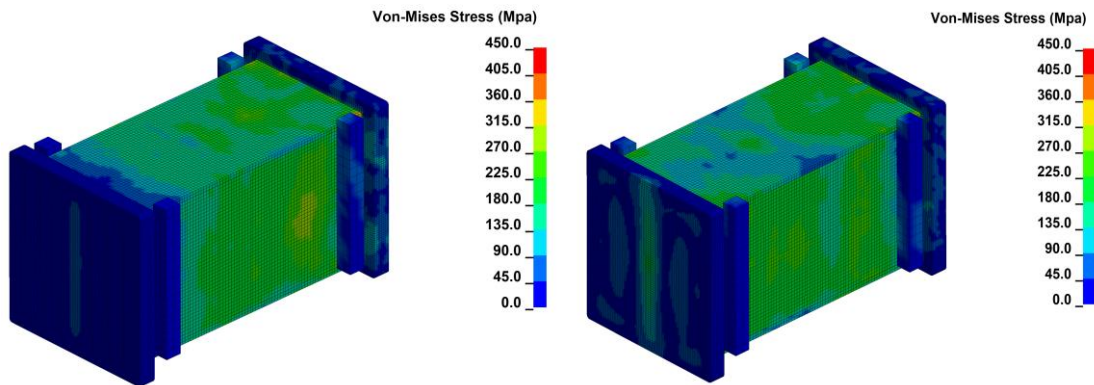


Figure 3.6: Von Mises stress for the impactor test ($V=11.46$ m/s (37.63 ft/s)) for two different time steps showing largest stresses

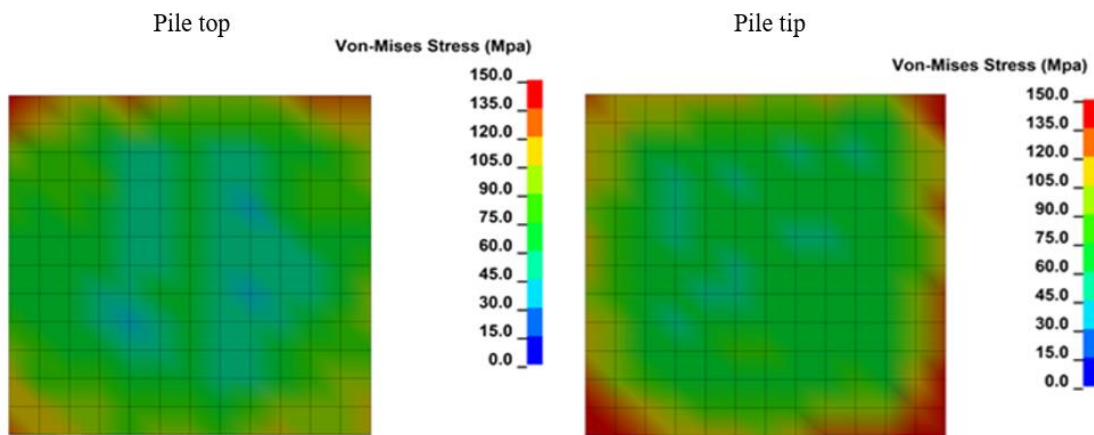


Figure 3.7: Maximum von Mises stress at the beginning and end of the concrete pile ($V=11.46$ m/s (37.63 ft/s))

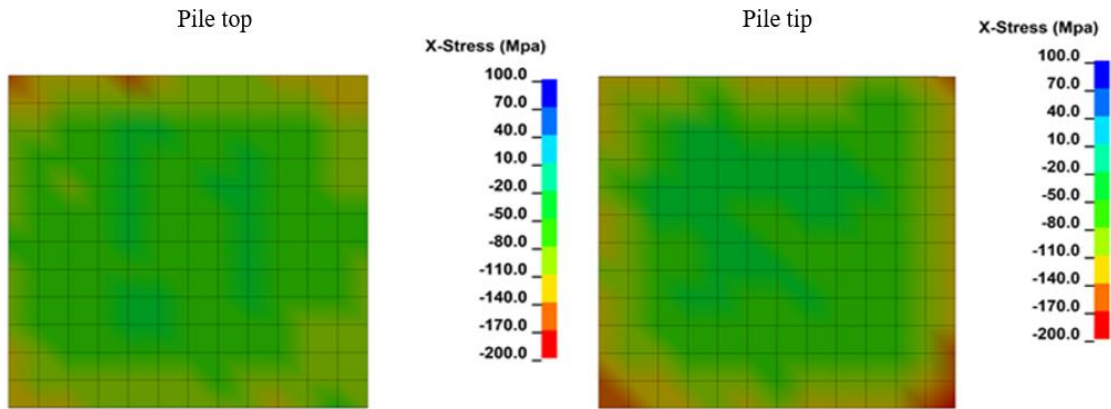


Figure 3.8: Maximum x-stress at the beginning and end of the concrete pile ($V=11.46$ m/s (37.63 ft/s))

3.5 Specification for GFRP Spirals

GFRP spirals for reinforcing in concrete piling must meet the requirements specified in ASTM D7957. Table 3.3 provides an overview of the physical and mechanical property requirements for GFRP spirals. The geometric and mechanical properties for GFRP bars are detailed in Table 3.4. These standards help ensure that GFRP spirals meet the necessary criteria for safe and effective use in concrete piling applications.

Table 3.3: Physical and mechanical property requirements for GFRP spirals

Property	Test method	Requirement
Fiber mass fraction	ASTM D2584 or ASTM D3171	≥ 70 %
Short-term moisture absorption	ASTM D570, subsection 7.4; 24 hours immersion at 122°F	≤ 0.25 %
Long-term moisture absorption	ASTM D570, subsection 7.4; immersion to full saturation at 122°F	≤ 1.0 %
Glass transition temperature (T_g)	ASTM E1356	Midpoint temperature 212 °F
Degree of cure	≥ 95 %	ASTM E2160
Measured cross sectional area	ASTM D7205/D7205M, subsection 11.2.5.1	Table 3.4

Table 3.3: Physical and mechanical property requirements for GFRP spirals - continued

Property	Test method	Requirement
Ultimate tensile strength (UTS)	ASTM D7205/D7205M	Table 3.4
Tensile modulus of elasticity	ASTM D7205/D7205M	$\geq 6,500$ ksi
Ultimate tensile strain	ASTM D7205/D7205M	≥ 1.1 %
Alkali resistance with load	ASTM D7705/D7705M, procedure A. 90 days test duration at 140 °F.	Tensile strength retention ≥ 80 % of UTS
Strength of bends	ASTM D7914/D7914M	≥ 60 % of the values in Table 3.4

Table 3.4: Geometric and mechanical properties requirement for GFRP bars

Bar Size designation	Nominal bar diameter in.	Nominal cross-sectional area in. ²	Measured cross-sectional area in. ² Min. – Max.	Min. guaranteed tensile load kips
2	0.250	0.049	0.046 – 0.085	6.1
3	0.375	0.11	0.104 – 0.161	13.2
4	0.500	0.20	0.185 – 0.263	21.6
5	0.625	0.31	0.288 – 0.388	29.1
6	0.750	0.44	0.415 – 0.539	40.9
7	0.875	0.60	0.565 – 0.713	54.1
8	1.000	0.79	0.738 – 0.913	66.8
9	1.128	1.00	0.934 – 1.137	82.0
10	1.270	1.27	1.154 – 1.385	98.2

3.6 Design Calculations for the GFRP Spiral Size

The existing FDOT design specifications for steel spirals in prestressed concrete piles rely on established practice rather than analytical calculations. Therefore, the methods discussed aim to determine the appropriate size of GFRP spirals that match the performance of proven steel spirals with a history of success.

To select the correct GFRP spiral size, two different approaches are utilized, as outlined in Sections 3.6.1 and 3.6.2. These same approaches were also used to select CFRP spiral size for the purpose of comparing the obtained size with the standardized CFRP spiral in FDOT's CFRP prestressed concrete piles.

Again, the proposed design is to select a GFRP spiral size that matches the performance of the successful steel spiral provided by FDOT. Therefore, we are not following Article 5.6.4.6 of AASHTO (2017), because it is too conservative for piles. It is too conservative because it assumes complete failure/spalling of the outer concrete while maintaining the load carrying capacity of the pile using the core of the concrete alone. Also, compression members designed as piles follow specifications for non-pile compression members. This is because piles might be required to protrude from the soil. Also, when fully embedded in the soil, it is uncertain that the surrounding soil will sufficiently support the entire length of the pile to prevent lateral buckling (Graybeal & Pessiki, 1998). For reference purposes, this conservative approach is given in Appendix B.

3.6.1 Size of GFRP and CFRP Spirals Based on Equivalent Steel Spiral Tensile Capacity and FRP Strain Limit

The first approach in determining the required area of FRP spiral is to compare the tensile capacity of steel spiral to the tensile capacity of FRP transverse reinforcement. The initial step in this approach involves calculating the tensile capacity of the steel spiral by multiplying its yield stress by the area. The properties of the steel spiral used in FDOT's design for a 24-inch square prestressed concrete pile are as follows: area of steel spiral, A_s , of 0.034 in.², minimum tensile stress, f_u of 80 ksi and a minimum yield stress, f_{yh} of 70 ksi (ASTM A1064-18a). Therefore, the tensile capacity of the steel spiral is

$$F_{\text{steel}} = A_s f_{yh} \quad (3.9)$$

$$F_{\text{steel}} = 70 \text{ ksi} (0.034 \text{ in.}^2) = 2.38 \text{ kips}$$

The next step involves calculating the required area of the FRP spiral using the concept of force equivalency. Unlike steel, FRP does not have a clearly defined yield stress, and it should not reach its ultimate stress to avoid brittle failure. Instead of using the stress value directly, it is computed using the elastic modulus and a strain limit. According to ACI 440.1R-15, the effective strain in FRP reinforcement should not exceed 0.004 to prevent aggregate interlock degradation, control shear crack widths, and avoid concrete shear failure. However, the aim here is to provide confinement with the end spirals and not for transverse shear, therefore, a higher strain limit of 0.006 is used, as recommended by CSA-806.

With this strain limit and the elastic modulus of the FRP, the area of the FRP rebar required to provide a tensile capacity equivalent to that of the standard steel spiral is calculated as follows:

Modulus of Elasticity of GFRP, $E_{\text{GFRP}} = 6500$ ksi (ASTM D7957)

Modulus of Elasticity of CFRP, $E_{\text{CFRP}} = 22400$ ksi (FDOT specifications 932-3)

$$\text{Area of FRP required, } A_{\text{FRP}} = \frac{F_{\text{steel}}}{\varepsilon E_{\text{FRP}}} \quad (3.10)$$

where

A_{FRP} , ε , and E_{FRP} are the required area, effective strain, and modulus of elasticity of the FRP reinforcement, respectively.

Therefore,

$$\text{Area of GFRP required, } A_{\text{GFRP}} = \frac{2.38}{(0.006)(6500)} = 0.061 \text{ in.}^2$$

$$\text{Area of CFRP required, } A_{\text{CFRP}} = \frac{2.38}{(0.006)(22400)} = 0.018 \text{ in.}^2$$

Table 3.5 provides a comparison of the required area for GFRP and CFRP transverse reinforcement based on the calculations, along with the area of CFRP transverse reinforcement recommended by Roddenberry et al. (2014) and the newly prescribed area for GFRP transverse reinforcement. The #3 GFRP rebar was prescribed, which has a nominal diameter of 0.375 in. and cross-sectional area of 0.11 in.².

Table 3.5: Required area of transverse reinforcements and the prescribed area

Spiral type	Required area in. ²	Prescribed area in. ²	Spiral size for prescribed area
Steel	—	0.034	W3.4
CFRP	0.018	0.024	0.2 Ø
GFRP	0.061	0.11	#3

3.6.2 Size of CFRP and GFRP Spiral Based on Equivalent Steel Spiral Shear Capacity

This approach involves calculating the shear capacity of conventional steel spirals and identifying an FRP bar size that can provide a similar level of performance. The total nominal shear capacity, V_n , is typically the sum of the concrete shear capacity, V_c , and the shear capacity contributed by the transverse reinforcement, V_s . This relationship can be expressed using Equation (3.11).

$$V_n = V_c + V_s \quad (3.11)$$

This section focuses on the shear contribution from the spirals, including steel, CFRP, and GFRP spirals. According to ACI 440.1R-15, the shear capacity mechanisms for steel and FRP reinforcements are similar. As a result, the shear contributions from all three spiral types are summarized in Table 3.6. However, it is important to note that the shear contributions for CFRP and GFRP spirals were calculated using two different methods, resulting in different results. The first method is based on tensile strength estimates when the strain limit is 0.004, as described in Section 3.6.1. The second method is based on the tensile strength of the FRP spiral's bent portion. ACI 440.1R-15 recommends selecting the lesser value of the tensile strength calculated by these methods when determining the tensile strength of the FRP for shear design. As shown in Table 3.6, the values obtained for #3 GFRP spirals are adequate because they exceed those of the standard steel and CFRP spirals. For detailed calculations of V_c and V_s , refer to Appendix B.

For PSG1/PSG2, V_s is determined as the least of the values shown in Table 3.6 for GFRP, resulting in V_c and V_n values of 85.19 kips and 101.66 kips, respectively. However, if the contribution of the transverse reinforcement to the nominal shear capacity is ignored (i.e., $V_s = 0$), then V_n for PSG1/PSG2 is taken as 85.19 kips.

Table 3.6: Comparison of the shear capacity of transverse reinforcement

Spiral type	Shear contribution from spirals (V_s)	
	Shear contribution (kips)	Spiral size
Steel	13.71	W3.4
CFRP	9.13*	0.2 Ø
	18.45†	
GFRP	16.47*	#3
	26.61†	

*Spiral shear contribution based on tensile strength estimates when the strain limit is 0.004
 †Spiral shear contribution based on the tensile strength of the bent portion of the FRP spiral.

3.7 Other Design-Related Parameters

Using a design concrete strength of 8500 psi, parameters calculated include those described in the following sections.

3.7.1 Prestress Loss

The PCI Design Handbook (2010) provides recommended straightforward equations for approximating the decrease in tensile stress within prestressing strands. This stress reduction, also known as prestress loss, arises from factors such as concrete contraction around the strands, relaxation of stress in the strands, and external elements that decrease the overall initial force within the strands before it is applied to the concrete. In the case of each strand within the pile specimens initially stressed at 34 kips, the cumulative prestress losses were determined to be 13.8%. The total prestress loss (TL) encompasses the summation of losses attributed to elastic shortening (ES), concrete creep (CR), concrete shrinkage (SH), and strand relaxation (RE), as illustrated in Equation (3.12).

$$TL = ES + CR + SH + RE \quad (3.12)$$

For a detailed calculation of prestress losses, please refer to Appendix B.

3.7.2 Moment Capacity

The moment capacity of a pile specimen was calculated (see Appendix B) based on equilibrium equations using the rectangular stress block. This calculation involved making strain compatibility assumptions, estimating the depth of the neutral axis, calculating strains in the strands, and

determining the depth of the stress block. Furthermore, the forces in the concrete and strands were assessed, and the sum of compression and tension forces was computed. To ensure equilibrium, the location of the neutral axis was adjusted until the sum of compressive and tensile forces equaled zero. The moments generated by these forces were then combined to determine the nominal flexural strength of the pile specimen. According to the calculations in Appendix B, the designed nominal moment capacity at the pile section is 8245 kip-in.

3.7.3 Driving Stress Limits and Axial Capacity

Driving stress limits in compression were calculated using AASHTO (2017) and FDOT (2019) recommended equations discussed in Section 2.9.

In addition, the nominal axial load capacity P_o according to PCI (1999) was calculated as 3,801 kips while the service-load based allowable axial capacity, N , for prestressed concrete piles fully supported laterally by soil and primarily subjected to axial according to PCI (1999, 2010) was calculated as 1,455 kips. Also, see Appendix B for calculations.

CHAPTER 4. PHASE 1 EXPERIMENTS

4.1 Introduction

This chapter provides a detailed description of the specimens used in the first phase of this research, the materials utilized, the instrumentation, the construction process, the testing procedures, and the results of the tests conducted on the phase 1 specimens. The data obtained from these tests on the phase 1 test piles served as the foundation for the design and recommendations for the phase 2 test piles.

4.2 Specimen Description

To assess the effectiveness of GFRP spiral reinforcement in prestressed concrete piles, this study was conducted in two phases. The first phase involved testing four prestressed concrete piles, each measuring 28 feet in length and having a cross-sectional dimension of 24 inches by 24 inches. The first pile (PSS), which is the control specimen was constructed using steel strands and steel spirals, adhering to the FDOT's standard specifications for a 24-inch square prestressed concrete pile. The subsequent two piles (PSG1 and PSG2) were reinforced with steel strands and GFRP spirals. Additionally, one pile (PCC) with CFRP strands and spirals, sourced from a prior project (Roddenberry et al., 2014) was also be tested. The nomenclature used to distinguish phase 1 test piles is detailed in Table 4.1 and will be consistently referenced in this report.

Table 4.1: Pile nomenclature and test matrix for phase 1 test piles

Pile label	Strand type	Spiral type	Note
PSS	Steel	Steel	Control specimen for impact test
PSG1 PSG2	Steel	GFRP	One for impact test; the other for axial & bending tests
PCC	CFRP	CFRP	Pile donated from a previous project for impact test

The naming convention for the piles is as follows: The first letter 'P' denotes 'pile'. The second letter signifies the type of longitudinal reinforcement utilized, where 'S' represents steel, 'G' designates GFRP bars, and 'C' denotes CFRP bars. The final letter indicates the type of spiral

reinforcement used. For instance, 'PSG' corresponds to a pile featuring steel longitudinal reinforcement and GFRP spirals.

The prestressing strand pattern in all three piles constructed for the first phase followed the FDOT standard plans for 24 in. square piles with twenty 0.5 in. diameter (special) steel strands. Also, the pile with steel spirals had the same configuration as the FDOT standard plans for 24 in. square piles in terms of spiral pitch, number of turns, and spiral size (Figure 4.1 and Appendix C.1). However, the spiral pitch and number of turns at the ends of the piles with GFRP spirals were adjusted due to spacing, symmetry, and spiral size considerations (Figure 4.2 and Appendix C.1). The steel spiral diameter was 0.207 in. compared to the GFRP spiral with a diameter of 0.375 in.

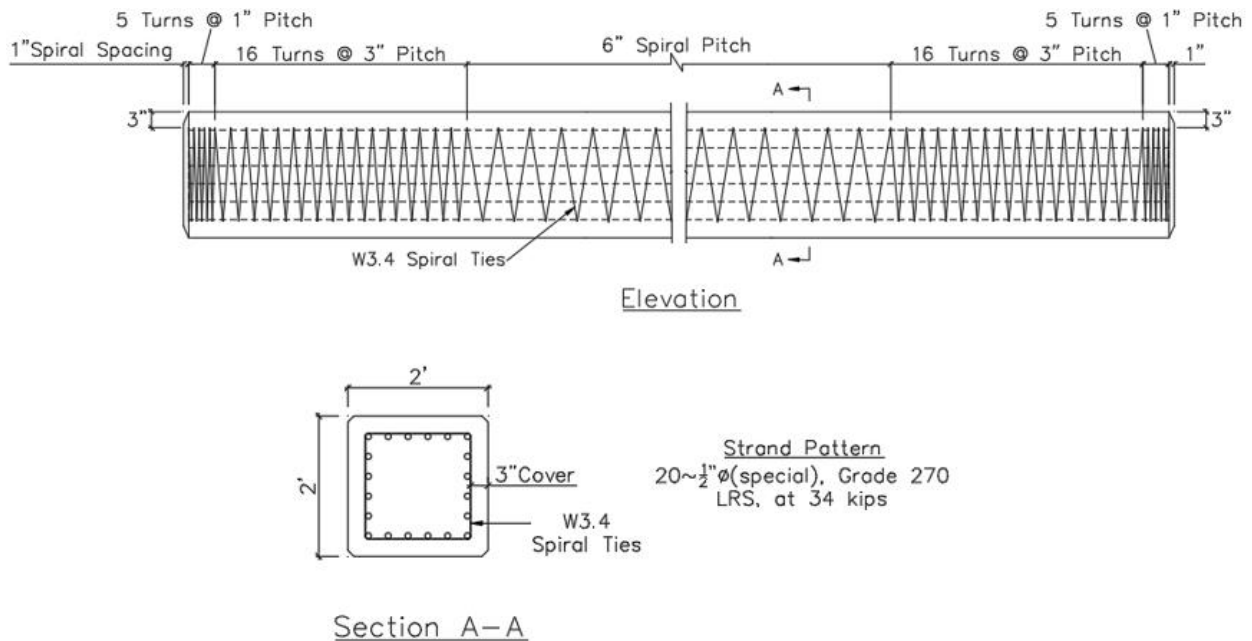


Figure 4.1: Pile with steel strand and steel spirals (PSS)

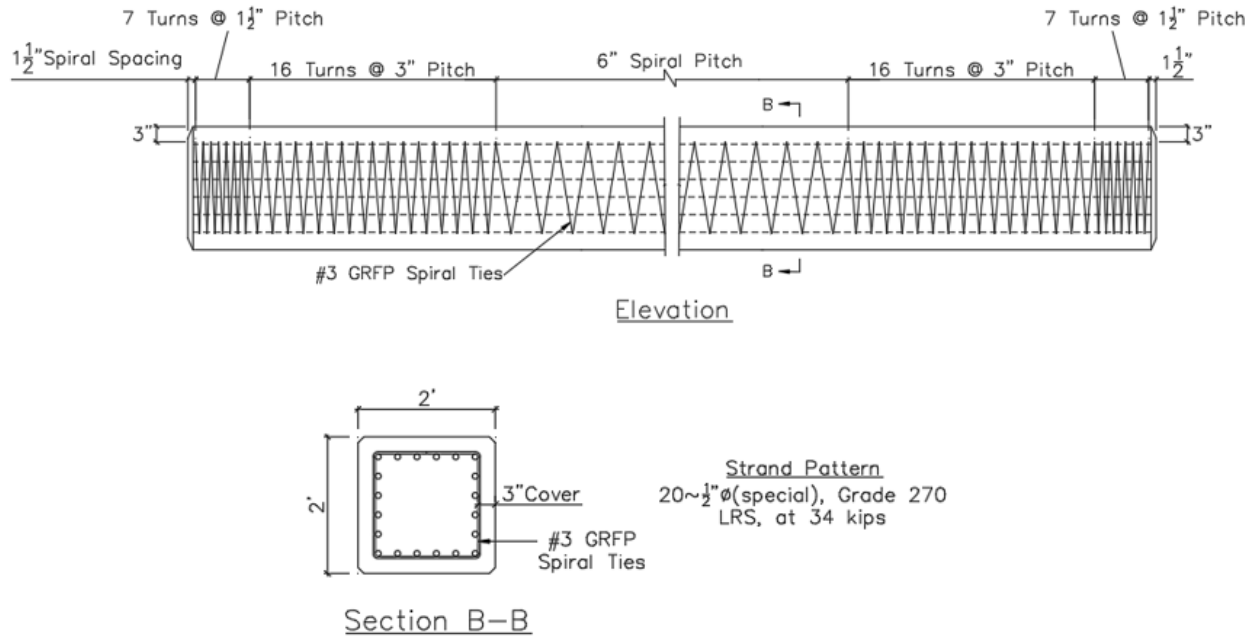


Figure 4.2: Pile with steel strand and GFRP spirals (PSG1 and PSG2)

4.3 Materials for Phase 1 Test Piles

4.3.1 Prestressing Strands and Spirals

For the manufactured phase 1 specimens, a W3.4 steel wire with diameter 0.21 in. and 0.375 in. diameter GFRP were used as transverse reinforcement, and twenty 0.5 in. (special) seven-wire 270 ksi low-relaxation steel strands were used for longitudinal prestressing. The strands have a nominal cross-sectional area of 0.167 in². and modulus of elasticity of 28,500 ksi. The GFRP transverse reinforcement were manufactured by V-Rod and the minimum tensile strength of the straight portion and bent portion of the bar as reported by the manufacturer are 148 ksi and 67 ksi, respectively. Also, the steel wire had a nominal are of 0.034 in.², an elastic modulus of 29,000 ksi and a tensile strength of 70 ksi.

4.3.2 Concrete

The FDOT Standard Plans for the prestressed concrete piles recommend class V concrete as the minimum requirement. In this project, class VI concrete with minimum compressive strength of 8500 psi was used in casting phase 1 piles. The concrete was self-consolidating; hence it was highly workable and flowed under its own weight. The 28-day compressive strength of the concrete was 10,980 psi after testing by Durastress at their precasting yard in Leesburg, Florida.

4.3.3 Plywood Cushion

During the impact experiments, pine plywood pile cushions were employed. Each plywood cushion had a cross-section of 2 ft × 2 ft and a nominal thickness of 3/4 in. The cushions used at the pile top and pile tip were created by bonding multiple plywood pieces together to achieve the desired thicknesses.

4.4 Instrumentation (Phase 1 Test Piles)

4.4.1 Strain Gauges

Phase 1 specimens were subject to measurements of external concrete strain and internal spiral strain using strain gauges from KYOWA Electronic Instruments. Three distinct models of strain gauges were employed for this purpose. For the external concrete strain measurements, the KC-60-120-A1-11 wire strain gauge model was used. These electrical resistance strain gauges (ERSGs) were used to measure concrete strains. Meanwhile, for internal spiral strain measurements, two different models were utilized, namely, KFGS-5-120-C1-11 for the steel spiral and KFRPB-5-120-C1-9 for the GFRP spiral. The choice of strain gauge model for spiral strain measurements was made to ensure compatibility with the specific materials under evaluation, namely steel and GFRP spirals. According to the manufacturer, the KFRPB model series features a unique gauge pattern designed to minimize the impact of self-heating caused by gauge current and the effects of low elasticity reinforcement. Although all three gauge models share a resistance rating of 120 ohms, they possess distinct characteristics, which are summarized in Table 4.2.

The layout and placement of the external gauges (KC-60-120-A1-11) and internal gauges (KFGS-5-120-C1-11 and KFRPB-5-120-C1-9) can be found in Appendix C.

Table 4.2: Distinguishing characteristics of strain gauges used

Strain Gauge Model	Gauge Length/width mm	Backing Length/width mm	Linear Expansion Coefficients $\times 10^{-6}/^{\circ}\text{C}$
KC-60-120-A1-11	60/0.6	74/8	11
KFGS-5-120-C1-11	5/1.4	9.4/2.8	11
KFRPB-5-120-C1-9	5/1.4	15/5	9

4.4.2 Deflection Gauges

For the flexural test of PSG2, deflection was measured using non-contact laser deflection gauges, which were supplied by the FDOT Structures Research Center. These specialized deflection gauges are capable of projecting lasers to measure deflection in areas that are inaccessible to traditional contact deflection gauges. Furthermore, in instances where the spreader beam was positioned above the top surface of the specimen, lasers from these deflection gauges were directed onto 2-inch angles affixed to the top side of the specimen to prevent any interference with the spreader beam, as described by Roddenberry et al. (2014). Non-contact laser deflection gauges offer the advantage of easy installation, and you can find detailed information on the placement and arrangement of these deflection gauges in Appendix C.

4.4.3 Accelerometers

To measure acceleration and indirectly estimate the impact force during the impact event, accelerometers were affixed externally to both the impactor and the pile under investigation in the direction of the impact. Specifically, an accelerometer was attached to the center of the top face of the impactor, and another accelerometer was mounted on the side of the pile at 3 ft from the pile top, as detailed in Appendix C8. The placement of these transducers adheres to the guidelines outlined in ASTM D4945-17, which recommends locating transducers at a distance of at least 1.5 times the width of the pile from the pile tip and/or the pile top. This strategic positioning minimizes irregular stress concentrations at the ends of the pile during data collection. The accelerometers used on both the impactor and the pile (at 3 ft from the pile top) were model EGCS-D5 accelerometers, manufactured by TE Connectivity. These accelerometers boast a measurement range of $\pm 5,000$ g and a shock limit of 20,000 g. To ensure precision and reliability in the accelerometer measurements, they underwent calibration by TE Connectivity, accounting for their respective cable lengths. Data sheets containing detailed specifications for these accelerometers are provided in Appendix D.

4.4.4 Pile Driving Analyzer® (PDA)

Piles PSS, PSG1, and PCC were subjected to monitoring during impact events using the PDA system. This system was equipped with strain transducers and accelerometers positioned in proximity to the pile's top and tip to gauge the axial stress induced by the impactor. For this

research, the placement of PDA sensors adhered to the guidelines specified in ASTM D4945-17, with the sensors located at a distance of 4 ft from both ends of the pile. This arrangement, as illustrated in Appendix C.8, was selected to prevent the occurrence of localized contact stresses at the pile ends, and it was in accordance with recommendations from the PDA contractor, Terracon Consultants, Inc.

4.4.5 Infrared Optical Break Beam Sensors

To measure the pendulum speed near the point of impact, infrared optical break beam sensors were installed, and this setup is illustrated in Figure 4.3. Two pairs of sensors were used, each consisting of a transmitter and a receiver, which were mounted on aluminum stands. One pair of sensors was placed near the impact point, while the other pair was positioned 1 ft away from the first pair. By measuring the distance between the sensors and the duration between interruptions in the infrared beams, it became possible to calculate the speed of the impactor just before it struck the cushion at the top of the pile. All of these sensors were positioned at a level corresponding to the mid-height of the impactor at the bottom of its swinging motion.

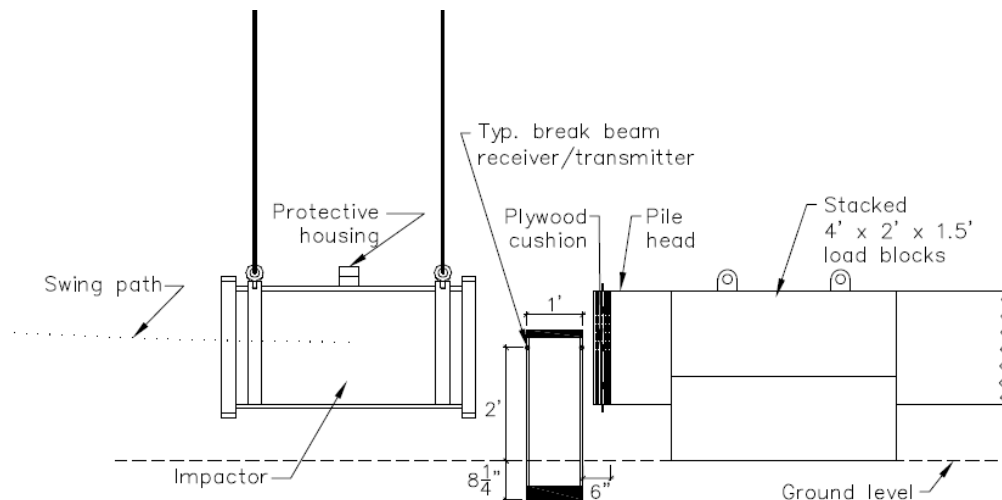


Figure 4.3: Location of break beams (elevation).

4.4.6 High-Speed Cameras

Two high-speed video cameras were employed to capture the impact event. These high-speed cameras were triggered to start recording when the impactor passed by the break beams. The video footage from these cameras offered an additional method for estimating the speed of the impactor just before impact. One of the cameras provided a close-up side view of the impact event, while

the second camera captured a wide-angle perspective of the entire impact experiment. Both cameras recorded at a rate of 2,000 frames per second.

4.5 Construction of Test Piles

4.5.1 Preparation and Instrumentation of Spirals

The surfaces of the GFRP spirals intended for strain gauge installation underwent meticulous grinding, smoothing, and cleaning procedures to ensure a secure and effective bond for the strain gauges. After the surface preparation was completed, the strain gauges were affixed in place and then shielded with moisture-resistant protective covering. A functional check was carried out to verify the proper operation of the installed gauges. In contrast, the steel spiral surfaces for strain gauge installation did not require grinding, and the gauges were applied using the same procedure as described for the GFRP spirals. Figure 4.4 displays the placement of these gauges on the spirals.

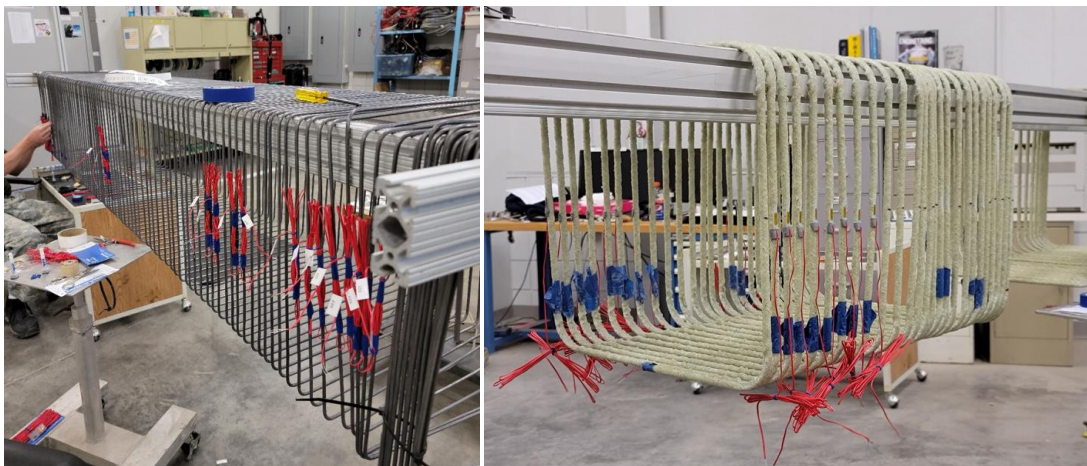


Figure 4.4: Strain gauge installation

4.5.2 Casting Bed Layout

The prestressing bed at Dura-Stress had a length of approximately 500 feet. Therefore, for economic reasons piles were cast with other piles from other projects. Figure 4.5 illustrates the positioning of the piles on the casting bed in relation to the live end. As shown, PSG1 was located closest to the live end, followed by PSG2, and finally PSS.

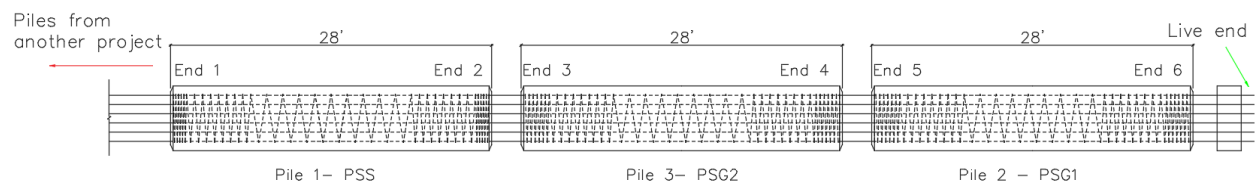


Figure 4.5: Casting bed layout

4.5.3 Spiral/Strand Installation and Stressing of Strands

The spirals for each pile were positioned within the forms at their respective pile locations. Subsequently, strands were threaded through the headers from the dead end of the prestressing bed and mechanically drawn along the entire length of the piles, extending to the live end. Following the placement of the strands, an initial pre-tensioning process was carried out, where all strands were tensioned to a force of 5 kips using a hydraulic jack. Subsequently, all strands underwent full stressing to a force of approximately 34 kips, following the sequence depicted in Figure 4.6. To maintain the force within the strands after jacking, grips were used to secure the strands at the live end.

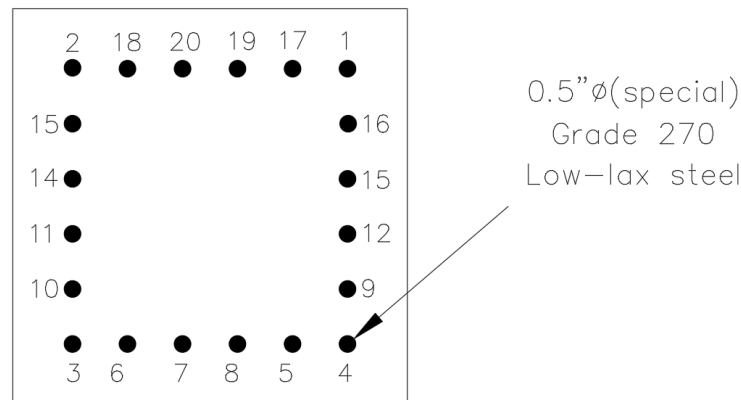


Figure 4.6: Strand stressing sequence

However, during and after the strand tensioning process, it was observed that the GFRP spirals became taut at the four corner strands of PSG1 and PSG2. This tightness led to the displacement of the steel headers, resulting in skewing. Furthermore, it became challenging to adjust the position of the GFRP spirals near the skewed steel headers. To address these issues, modifications were made by shortening the lengths of the pile specimens from 30 feet to 28 feet. This was achieved by placing wooden headers close to the spirals ends.

4.5.4 Spiral Splicing

Unlike PSS where the steel spiral is continuous along the entire length of the pile, GFRP spirals in PSG1 and PSG2 were spliced at similar locations from one end of the piles. Spirals of PSG1 were spliced at 5.5 ft from End 5 and spirals of PSG2 were spliced at 5.5 ft from End 4.



Figure 4.7: Spiral splicing: (a) PSG2, (b) PSG1

4.5.5 Concrete Pouring

A class VI 8500 self-consolidating concrete mix was used (Figure 4.8). The self-consolidation nature of the concrete avoids the need for mechanical vibration. After pouring the concrete surface was leveled and smoothed. After casting, the surface of the concrete was sprayed with an anti-cracking agent. Also, plastic coverings were placed over the cast piles to prevent rapid loss of moisture and to facilitate uniform curing temperature.



Figure 4.8: Pile casting

4.5.6 Strand Stress Release

One day after the piles were cast, the strands were cut in a symmetrical sequence using the flame cutting technique. The cutting of the strands was carried out simultaneously at both the live end and the dead end, as shown in Figure 4.9. Subsequently, following the detensioning procedure, the piles were removed from the casting bed.

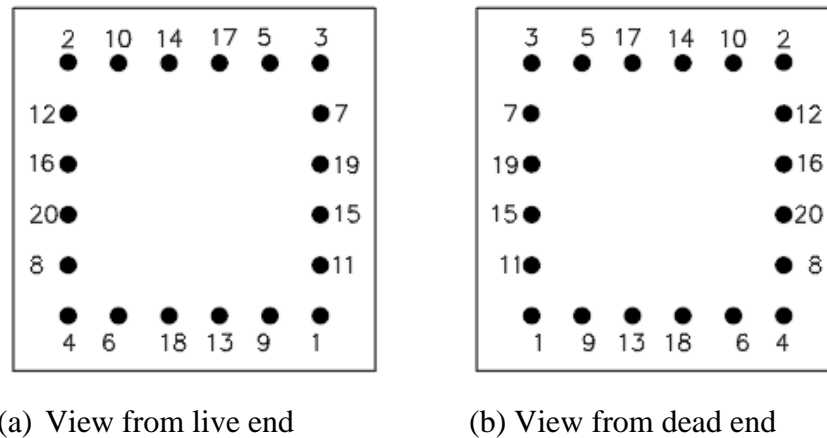


Figure 4.9: Strand cutting sequence

4.6 Testing Procedure

4.6.1 Impact Test Procedure

Prior to conducting the impact tests, the impactor was suspended using cables to create a pendulum mechanism when released from a specific drop height. Before any swing was initiated, the pile, restraining blocks, and supports were set up as depicted in Figure 4.10. Plywood cushions were then placed at both the pile top and the pile tip to provide protection for the concrete as shown in Figure 4.11. For PSS, 0.75 in. thick plywood cushions were placed at the pile top and tip, while for PSG, 1.5 in. thick plywood cushion was used at the top and 0.75 in. thick cushion at the tip. Following this, the installation of sensors on the impactor and the pile took place. An EGCS-D5 accelerometer was mounted at the center of the top face of the suspended impactor, while external sensors utilized include an EGCS-D5 accelerometer, electrical resistance strain gauges (ERSGs), infrared optical break beam sensors, and PDA accelerometers and transducers. These sensors were connected to data acquisition systems to facilitate the collection of data during the testing process.

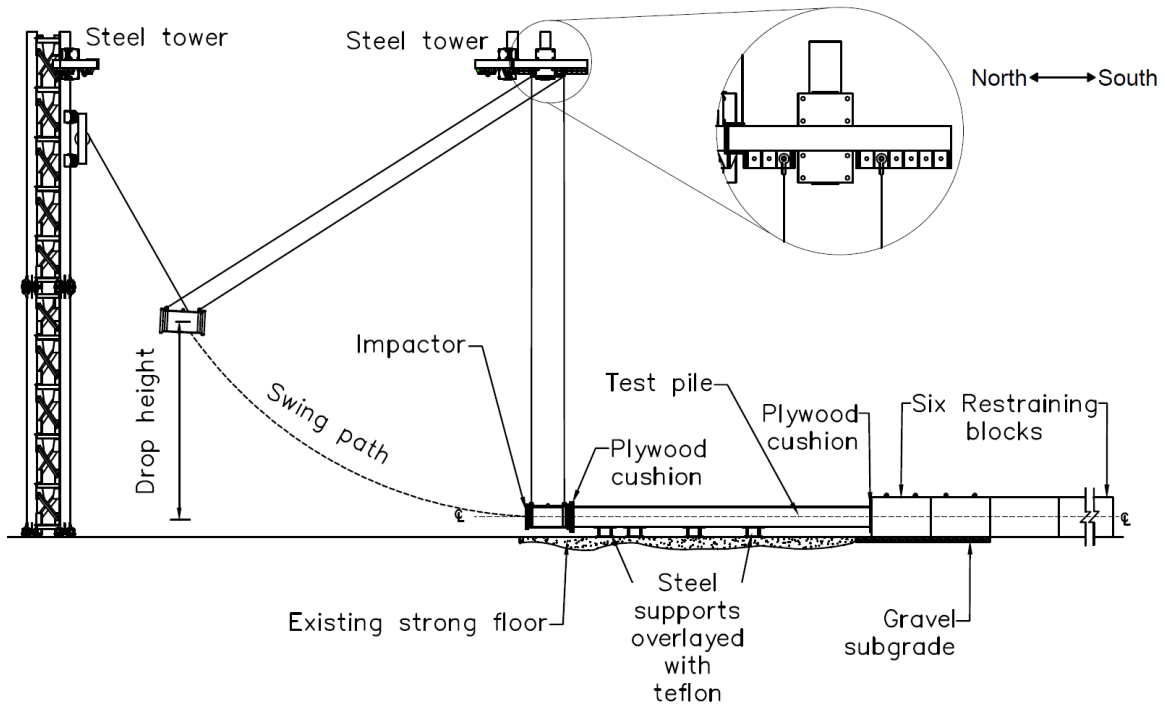


Figure 4.10: Pile impact test setup drawing

During testing, piles for impact tests were subjected to dynamic forces from the impactor for the following drop heights; 4 ft, 7 ft, 10 ft, 15 ft, and 20 ft. For each swing test, the data acquisition system was activated just before the release of the impactor. All sensor responses were recorded at a high sampling rate of 10,000 samples/sec (10 kHz) for a duration of 10 seconds, starting from the moment the impactor was released. This sampling rate and duration ensured that sufficient data was captured during each swing test. If necessary, the setup was realigned at the end of each swing.

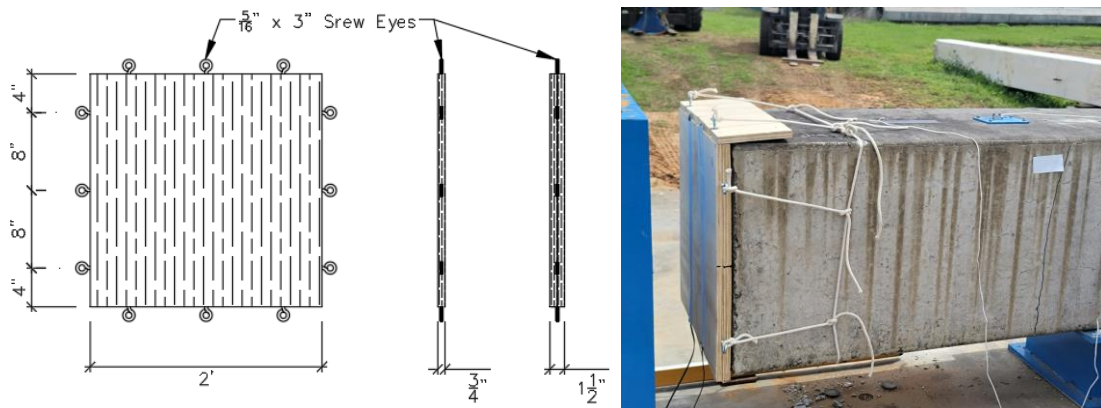


Figure 4.11: Pile cushion with screw eyes and its placement

4.6.2 Procedure for Flexural Test

The four-point bending experiment was setup as described in Appendix C.6 for PSG2. The gauges were checked to ensure they were in good condition, and malfunctioning gauges were replaced. Load was using a 1000-kip actuator which applied load at a rate of 250 pounds per second until the first flexural cracks were noticed. Afterward, the load rate was changed to 200 pounds per second. Crack patterns were intermittently marked and sketched. Measured data were recorded at a rate of 10 samples per second (10 Hz) through the data acquisition system. The test was continued until failure occurred, and then the pile was unloaded. The predicted flexural displacement at failure was 3.88 inches.

4.7 Test Results for Phase 1 Test Piles

Three piles; PSS, PSG1 and PCC, were tested under impact loads. For each pile, impact load was delivered by a 6000 lbm impactor at various drop heights. Impact test results reported in this section include the impactor velocity and acceleration, pile driving analyzer (PDA) strain gauges and accelerometers measurements, spiral strain measurements, and a comparison of external electrical resistance strain gauges (ERSGs) attached to the concrete surface readings to the PDA measurements. To describe these results, the orientation of the impact test setup is shown in Figure 4.12.

Furthermore, because piles are usually cut after driving them to the desired elevation on the field, PSS and PSG1 were cut at locations close to ends of the piles and spiral responses were examined and reported. Additionally, the results of the flexural test conducted on PSG2 are also included in this report.

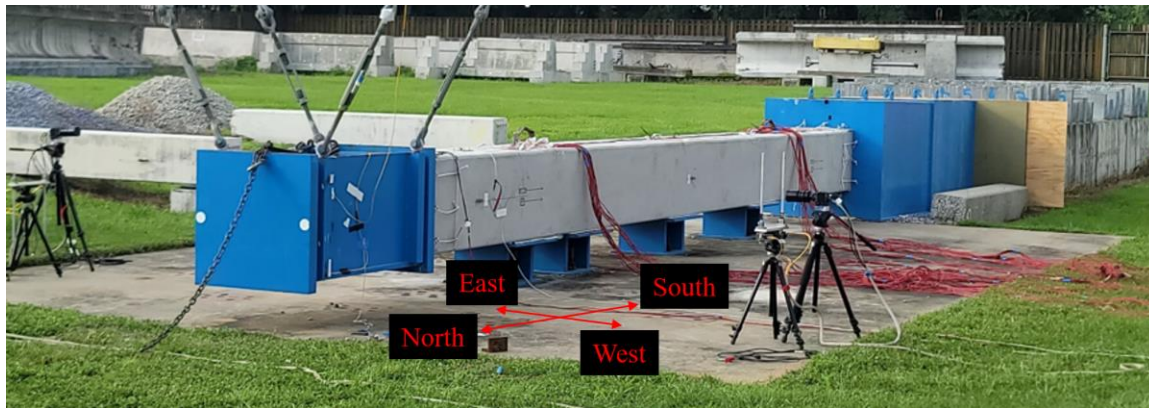


Figure 4.12: Pile orientation

4.7.1 Impactor Velocity and Acceleration

Using the impactor velocity, as outlined in Equation (2.2), it is possible to estimate the energy generated by the impactor. This estimated energy corresponds to the kinetic energy of the impactor, as described in Equation (2.3). In Figure 4.13, the velocity of the impactor during the experiment is compared to the theoretical calculation. As depicted, it becomes evident that the energy dissipated in the pendulum's swing prior to the contact between the impactor and the pile cushion is minimal and negligible.

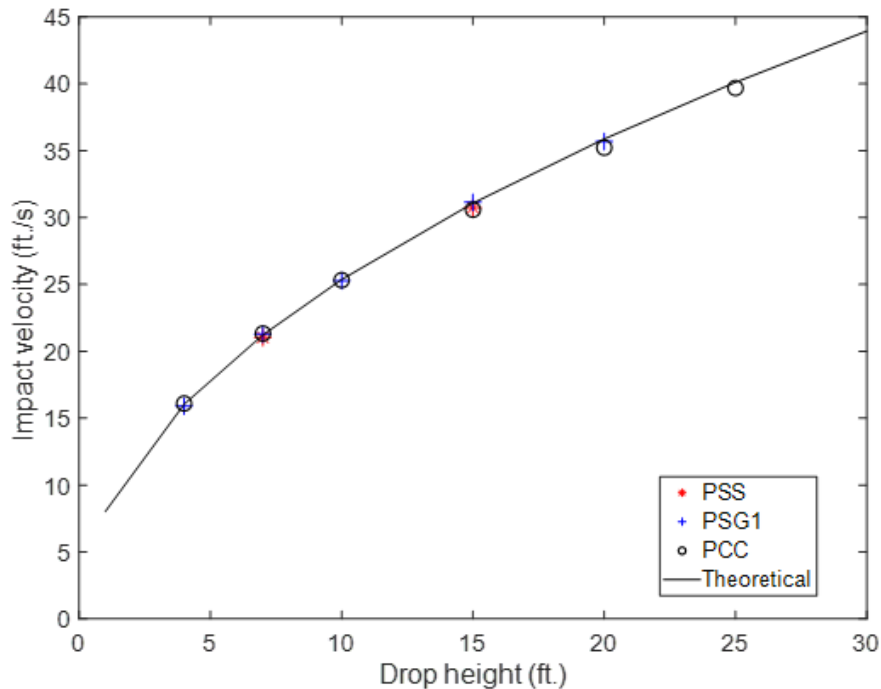


Figure 4.13: Impactor velocity

Additionally, the impact velocity and the peak impactor acceleration was compiled and summarized in Table 4.3. It's important to note that the peak acceleration of the impactor was determined after the point of contact between the impactor and the pile top cushion.

Table 4.3: Summary of impactor velocity and acceleration readings

Drop height (ft)	Impact velocity (ft/s)			Impactor acceleration ($\times 10^4$ ft/s ²)		
	PSS	PSG1	PCC	PSS	PSG1	PCC
4	—	15.90	16.10	—	0.522	0.467
7	21.03	21.29	21.33	0.764	0.735	0.692
10	—	25.28	25.32	—	0.976	0.949
15	30.74	31.13	30.58	1.421	1.286	1.324
20	—	35.68	35.22	—	1.781	1.754
25	—	—	39.68	—	—	1.941

4.7.2 Pile Driving Analyzer (PDA) Measurements

Monitoring pile responses during dynamic testing is frequently accomplished using the Pile Driving Analyzer (PDA). Utilizing the PDA for monitoring not only saves time but is also a cost-effective approach, as indicated by Herrera, Jones, and Lai (2009). In the impact tests described in this report, PDA instrumentation was installed on both sides of the piles, positioned 4 ft from both the top and the tip of each pile. The following sections will discuss the PDA measurements obtained from PDA strain gauges and PDA accelerometers for each of the piles.

4.7.2.1 PSS PDA Measurements

In the impact test conducted on pile PSS, a pile cushion thickness of 0.75 in. was used at the top and tip of the pile. The drop heights for which PSS was tested were 7 ft and 15 ft, ultimately leading to pile failure. As shown in Figure 4.14, the magnitudes of strains recorded on the east and the west side were different for the 15-ft drop. This indicated that the contact between the impactor and the pile at the time of impact was eccentric, which in turn led to uneven stress distribution across the cross-section of the pile. The maximum top strain from an individual sensor (MEI) resulting from dropping the impactor from 15 ft was $-1151 \mu\epsilon$.

Generally, axial impact on piles with a fixed boundary condition at the pile tip can lead to an amplification of the compressive stress wave at the pile tip. However, since the setup for the impact test in this research did not provide complete fixity at the pile tip, acceleration amplification was

observed at the pile tip compared to the pile top. This acceleration amplification indicated relatively small tip resistance. Figure 4.15 shows that the first peak acceleration at the top was $1.8 \times 10^4 \text{ ft/s}^2$, whereas at the tip of the pile, the first peak acceleration was $2.3 \times 10^4 \text{ ft/s}^2$. However, no amplification was observed for the strain (force) measurements shown in Figure 4.14, partially associated with the failure of the pile which is discussed later in this report. The failure also seemed to influence the strain symmetry more than the acceleration symmetry between the east and west sides. The first peak of acceleration measured on the east side of the pile closely matched those on the west side, both at the top and the tip. However, as previously discussed, significant differences in strains were observed between the two sides.

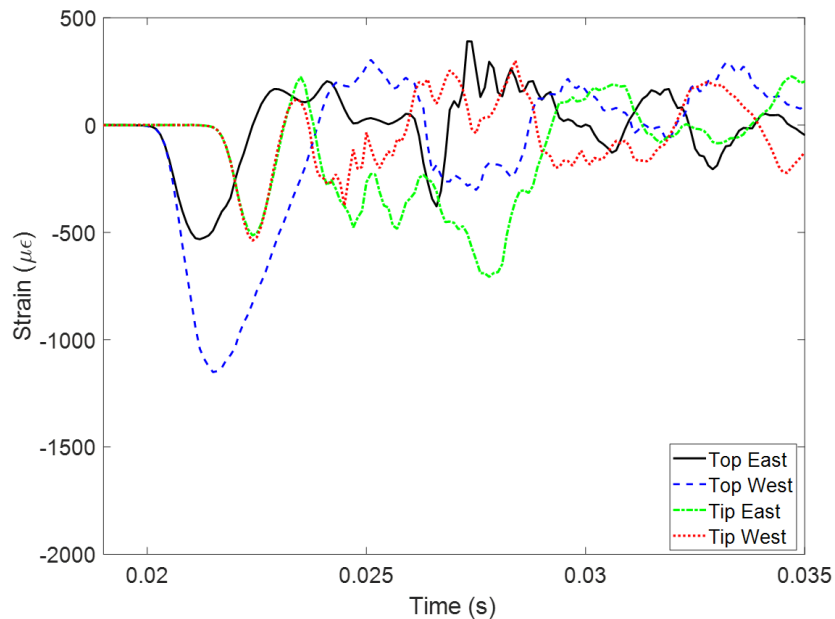


Figure 4.14: Top and tip strains from PDA strain gauges at impact drop height of 15 ft (PSS)

To obtain peak stresses, maximum axial strains from the gauges were multiplied by the pile's elastic modulus, E . The elastic modulus, derived from PDA measurements was estimated to be 5727 ksi, using the wave speed, c and density of the pile, ρ through Equation (2.7). For PSS the recorded wave speed was 13300 ft/s. Multiplying the axial strain, ϵ , by the pile's elastic modulus and cross-sectional area, A , provided the axial force, F , in the pile according to Equation (2.5).

Additionally, the force, F_d in the traveling waves along the pile can be obtained as the product of the particle velocity, V and pile impedance, Z , according to Equation (2.8). As shown in Equation (2.9), Z is a function of the elastic modulus, E , the wave speed, c , and the cross-sectional area, A , of the pile. The pile force traces for the highest drop height for which PSS was tested are displayed

in Figure 4.16, where F and $V \times Z$ are based on the average strains of the top two gauges and the top accelerometer, respectively. When the bounce-back occurred in the test setup, the strain gauge and the accelerometer responded differently on the reflective wave, which caused the discrepancy in the second peak.

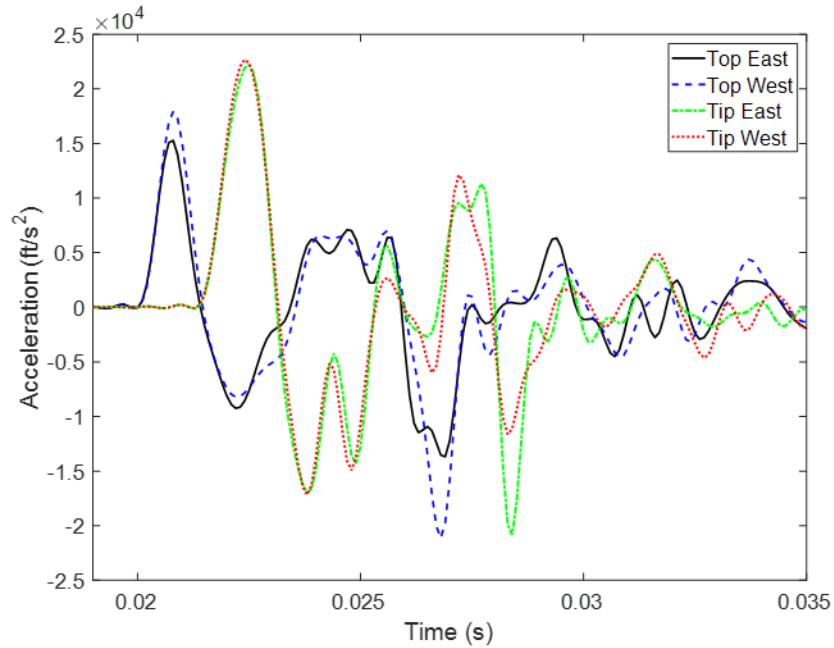


Figure 4.15: PDA measured acceleration at pile top and tip at a drop height of 15 ft (PSS)

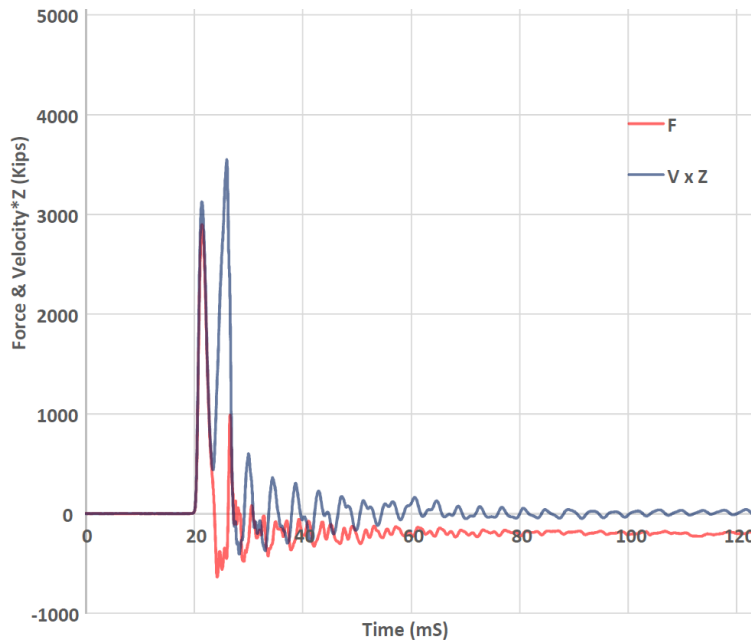


Figure 4.16: Pile force traces from PDA resulting from impact drop height of 15 ft (PSS). (Compressive force is positive in this figure which was produced by Terracon)

Peak strain, acceleration, stress, and maximum axial force, FMX, values for each drop height are summarized in Table 4.4. In this table, CSI represents the peak compressive stress from individual gauges, CSX is the peak compressive stress, and TSX is the peak tensile stress. The magnitude of TSX and its location along the pile are illustrated in Figure 4.17.

Strain, acceleration, pile force and stress results from the PDA for other drop heights at which PSS was tested can be found in Appendix E.

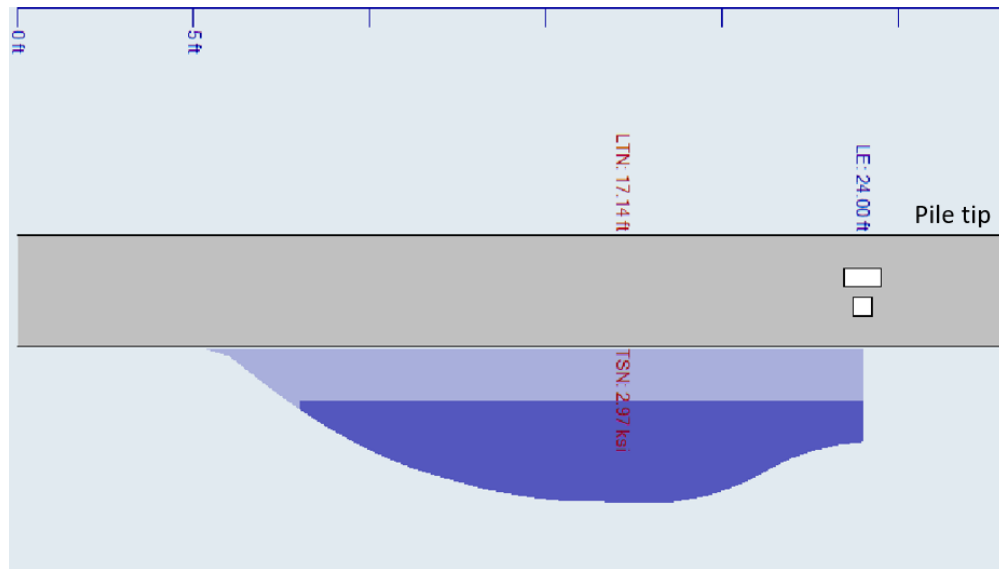


Figure 4.17: Peak tensile stress (TSX) resulting from impact drop height of 15 ft (PSS) and its location along the pile. (This figure was produced by Terracon)

Table 4.4: Peak strain, acceleration, and stresses (PSS)

Drop height (ft)	Peak top comp. strain (MEI) ($\mu\epsilon$)	Particle acceleration ($\times 10^4$ ft/s ²)		CSI (ksi)	CSX (ksi)	TSX (ksi)	FMX (kips)	
		Top	Tip				Top	Tip
7	-647	0.31	0.59	-3.70	-2.31	1.68	1328	720
15	-1151	1.79	2.26	-7.04	-5.03	2.97	2898	1691

4.7.2.2 PSG1 PDA Measurements

The PSS impact test used 0.75 in. top cushion, which could not continue beyond the 15-ft drop height. A decision was made to increase the top cushion thickness to gather more data before the

pile failed. In the impact test conducted on PSG1, the pile cushion thickness at the top was 1.5 in., and at the tip, it was 0.75 in. PSG1 was tested at drop heights of 4 ft, 7 ft, 10 ft, 15 ft, and 20 ft. The pile ultimately failed after the 20-ft drop. As demonstrated in Figure 4.18, the magnitude of strain recorded on both sides of the pile during the 20-ft drop was similar. However, for impact tests on PSG1 at other drop heights, the strain varied due to the eccentricity of impact. Despite efforts to align the pile as accurately as possible with the impactor for all drop heights, some slight eccentricity was still evident in the results.

Figure 4.19 illustrates that the acceleration at the tip of the pile was greater than the acceleration at the top. This was in contrast to the trend observed in the strains, where the top strains were greater than the strains measured at the tip of the pile. Moreover, unlike the strain measurements, where variations between the sides of the pile were common, except for the 20-ft drop test, the magnitudes of acceleration on both sides of the pile were similar. The first peak of the acceleration recorded at the pile top and tip is summarized in Table 4.5. The unamplified and unsymmetrical strain response was possibly due to the influence of local details, such as nearby reinforcements.

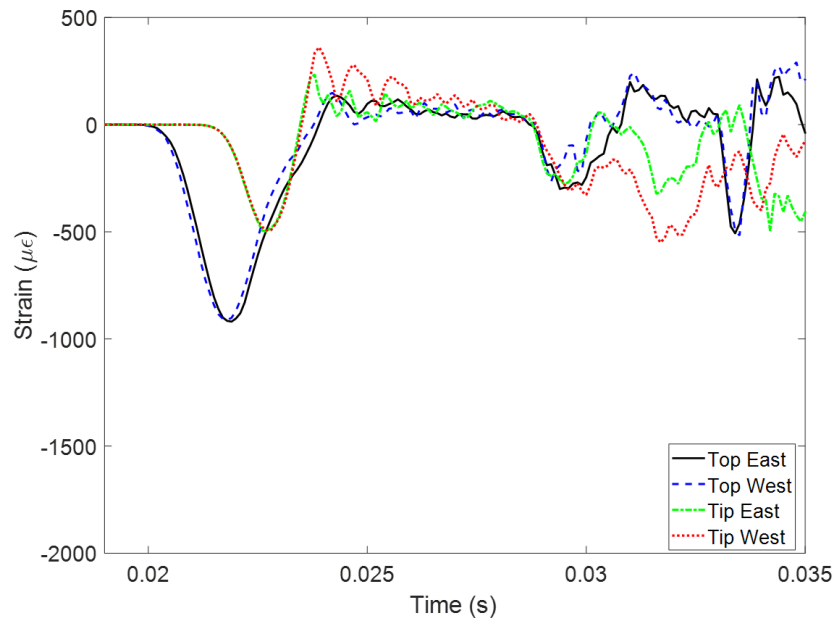


Figure 4.18: Top and tip strains from PDA strain gauges at impact drop height of 20 ft (PSG1)

Similar to PSS, the recorded wave speed, c , for PSG1 was 13,300 ft/s, and the elastic modulus was 5,727 ksi. The pile stresses and forces, which are summarized in Table 4.5, were calculated as previously described in Section 4.7.2.1. The pile force traces and the magnitude of TSX, along

with its location along the pile, for the highest drop height at which PSG1 was tested, are depicted in Figure 4.20 and Figure 4.21, respectively.

Strain, acceleration, pile force and stress results from the PDA for other drop heights at which PSG1 was tested can be found in Appendix E.

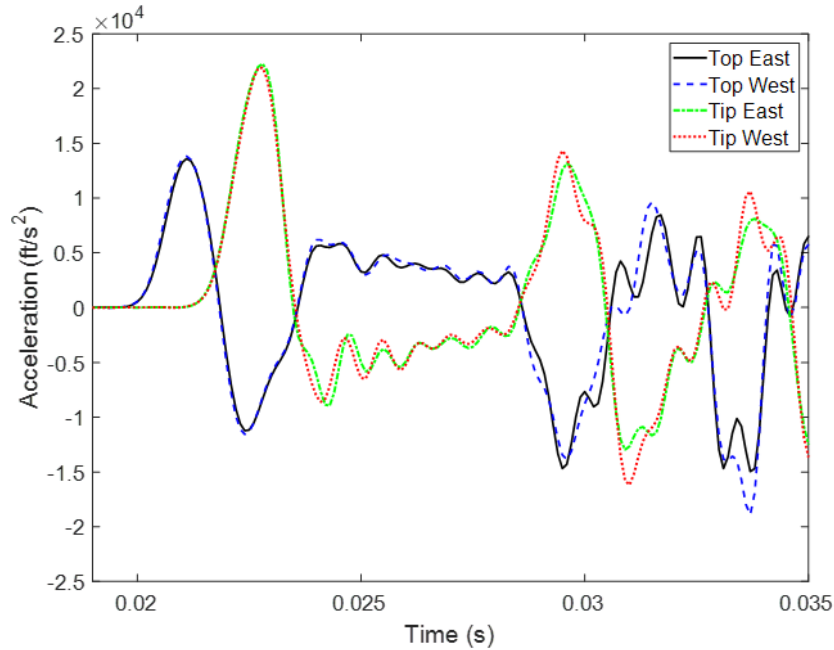


Figure 4.19: PDA measured acceleration at pile top and tip at a drop height of 20 ft (PSG1)

Table 4.5: Peak top strain, acceleration, and stress (PSG1)

Drop height (ft)	Peak top comp. strain (MEI) ($\mu\epsilon$)	Particle acceleration ($\times 10^4$ ft/s ²)		CSI (ksi)	CSX (ksi)	TSX (ksi)	FMX (kips)
		Top	Tip				
4	-291	0.26	0.42	-1.68	-1.39	0.87	803
7	-472	0.43	0.69	-2.70	-1.98	0.99	1141
10	-755	0.65	0.99	-4.33	-2.78	2.28	1600
15	-776	0.70	1.25	-4.44	-3.86	2.88	2221
20	-919	1.38	2.22	-5.67	-5.63	3.50	3245

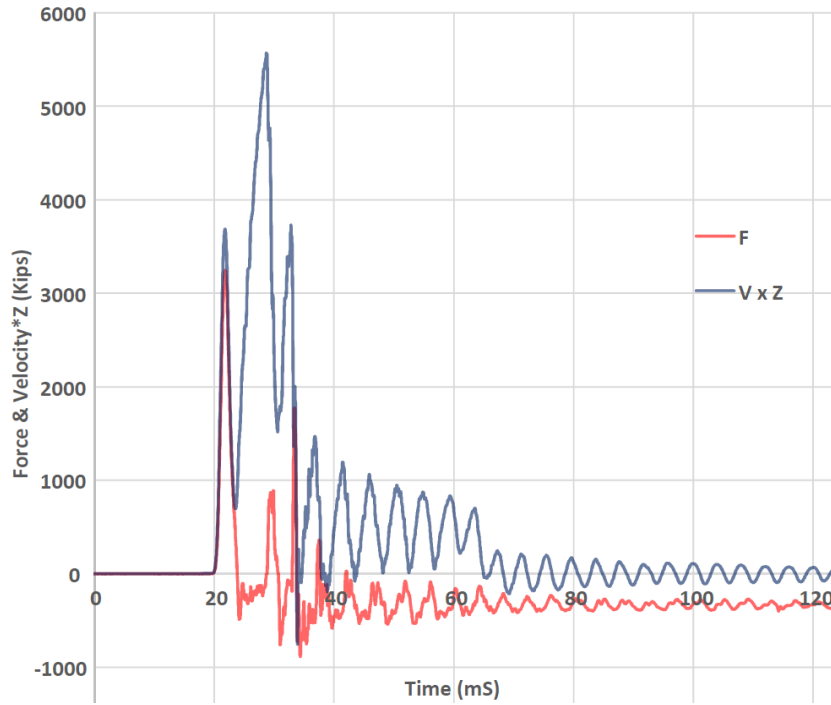


Figure 4.20: Pile force traces from PDA resulting from impact drop height of 20 ft (PSG1) (Compressive force is positive in this figure which was produced by Terracon)

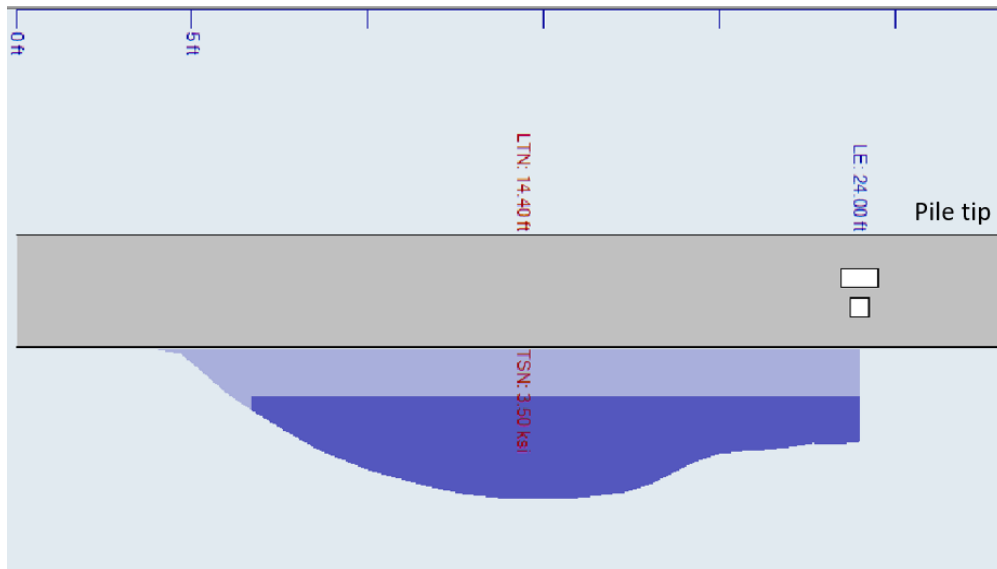


Figure 4.21: Peak tensile stress (TSX) resulting from impact drop height of 20 ft (PSG1) and its location along the pile. (This figure was produced by Terracon)

4.7.2.3 PCC PDA Measurements

In the impact test conducted on PCC, the pile cushion thickness was 1.5 in. at the top and 0.75 in. at the tip. PCC was subjected to drop heights of 4 ft, 7 ft, 10 ft, 15 ft, 20 ft, and 25 ft. The pile exhibited multiple transverse cracks resulting from the impact during the 20-ft drop, so the measurements presented in this section are from the 20-ft drop.

As observed in Figure 4.22, and consistent with the impact tests on the other piles (PSS and PSG1), imperfect (eccentric) contact between the impactor and the pile led to differences in strain measurements across the pile's cross-section. For PCC, the recorded wave speed, c , was 13,800 ft/s, and the elastic modulus was 6,166 ksi, indicating that PCC had a higher compressive strength than PSS and PSG1 at the time of testing.

Figure 4.23 illustrates that the magnitude of acceleration on both sides of the pile was similar. Additionally, the acceleration at the tip was greater than the acceleration at the top due to the reflection of the compressive wave at the tip of the pile.

Table 4.6 summarizes the maximum top strain (MEI), the first peak of acceleration recorded at the pile top and tip, pile tensile and compressive stress, and force. Furthermore, the pile force traces and the magnitude of TSX, along with its location along the pile for the highest drop height at which PCC was tested, are displayed in Figure 4.24 and Figure 4.25, respectively.

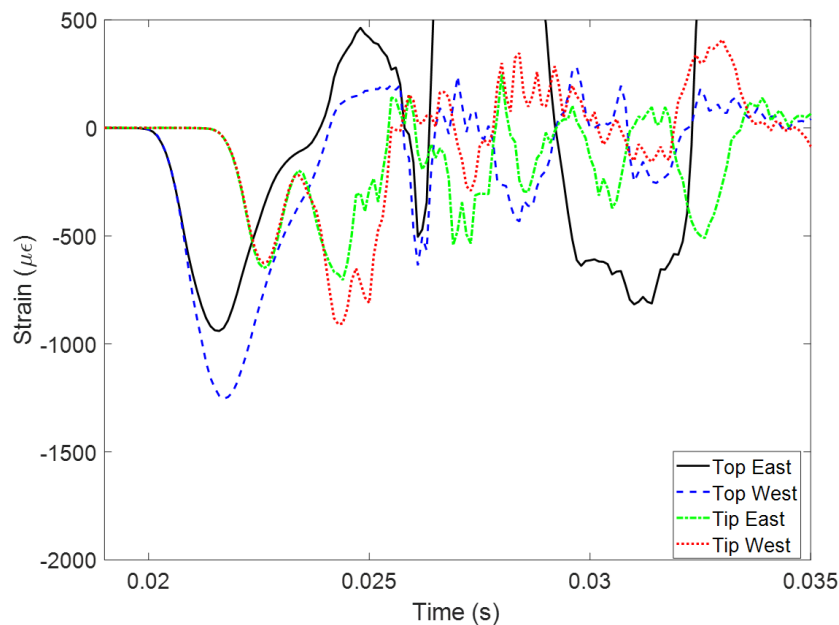


Figure 4.22: Top and tip strains from PDA strain gauges at impact drop height of 20 ft (PCC)

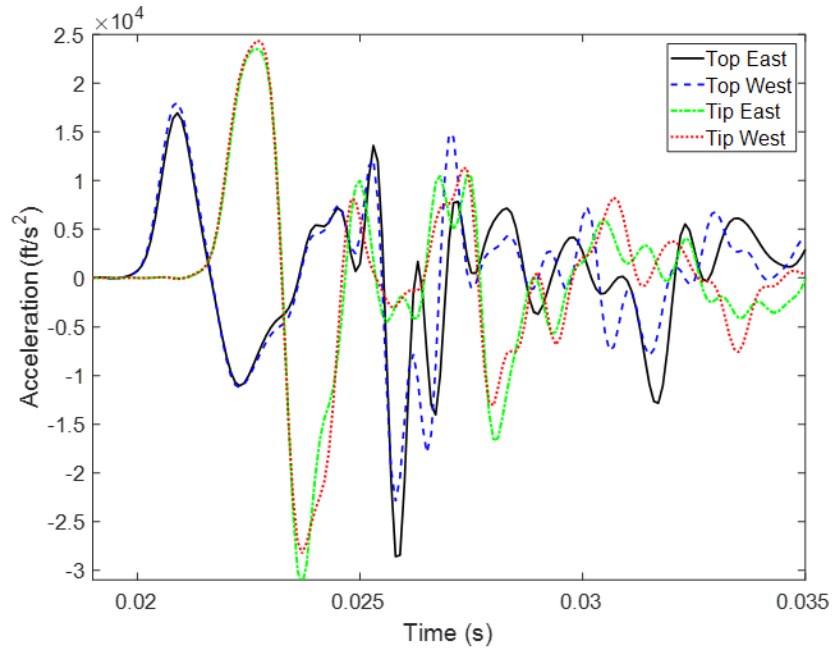


Figure 4.23: PDA measured acceleration at pile top and tip at a drop height of 20 ft (PCC)

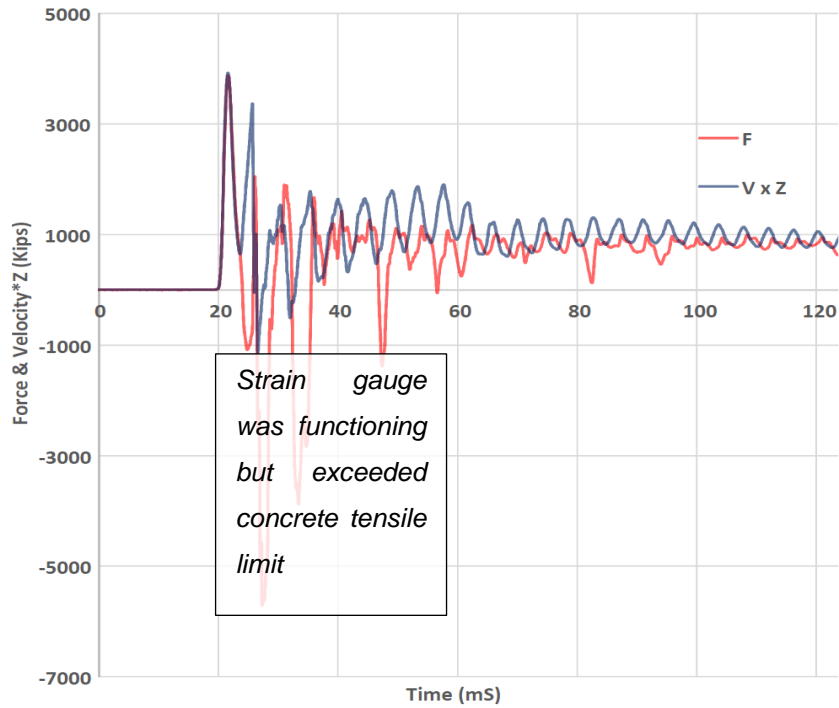


Figure 4.24: Pile force traces from PDA resulting from impact drop height of 20 ft (PCC) (Compressive force is positive in this figure which was produced by Terracon)

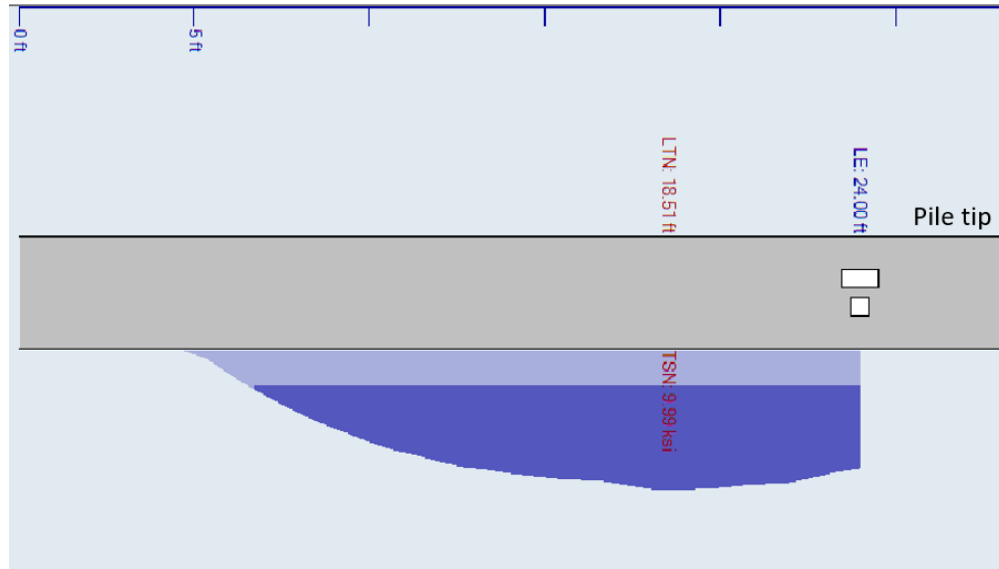


Figure 4.25: Peak tensile stress (TSX) resulting from impact drop height of 20 ft (PCC) and its location along the pile. (This figure was produced by Terracon)

Table 4.6: Peak top strain, acceleration, and stress (PCC)

Drop height (ft)	Peak top comp. strain (MEI) ($\mu\epsilon$)	Particle acceleration ($\times 10^4$ ft/s ²)		CSI (ksi)	CSX (ksi)	TSX (ksi)	FMX (ksi)
		Top	Tip				
4	-324	0.29	0.45	-2.00	-1.55	0.51	893
7	-449	0.64	0.75	-2.77	-2.30	0.43	1325
10	-638	0.80	1.08	-3.93	-3.38	1.64	1889
15	-871	1.21	1.58	-5.37	-4.69	2.45	2699
20	-1254	1.80	2.24	-7.73	-6.72	–	3873
25	-1496	2.56	3.34	-9.23	-8.80	–	5070

4.7.3 Spiral Strain

Spiral strain gauges were strategically placed on the spirals to record their responses during the impact tests. The layouts of the spiral strain gauges installed in PSS and PSG1 can be seen in Appendix C. The spiral strains presented in Figure 4.26 and Figure 4.27 were obtained from the highest drop heights at which the piles failed.

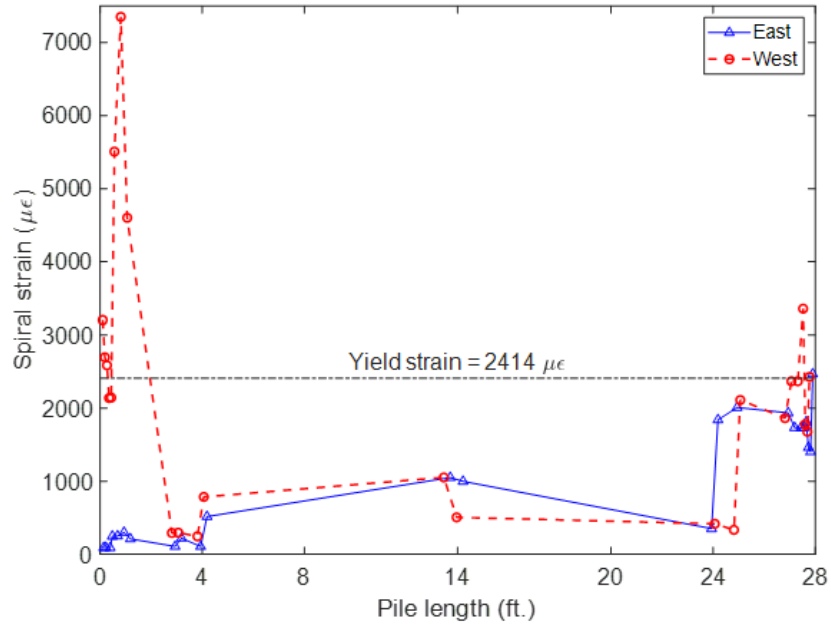


Figure 4.26: Steel spiral strain PSS (15-ft drop height)

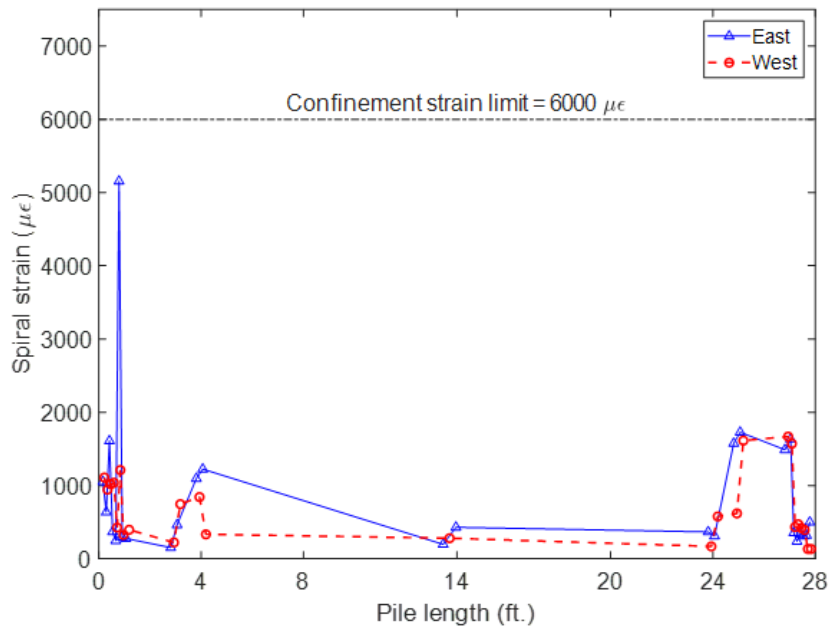


Figure 4.27: GFRP spiral strain PSG1 (20-ft drop height)

These figures clearly illustrate that the spiral strains are more pronounced at the ends of the pile when compared to the center of the pile. This variation in strain distribution is a result of the higher stresses experienced by the core of the pile under impact at the top and tip. This observation underscores the significant role of confinement at the ends of the pile in preserving the integrity of the pile. As shown in Figure 4.26, the steel spirals at the ends of the pile exceeded their yield strain

limit, indicating that the tensile capacity of the steel spiral was reached as the pile failed. In contrast, as depicted in Figure 4.27, the GFRP spiral did not reach the confinement strain limit recommended by CSA-806, which was utilized in the design of the spiral.

Furthermore, the graphs depicting the maximum spiral tensile strains recorded anywhere along the piles versus the drop heights for which PSS and PSG1 were tested are presented in Figure 4.28 and Figure 4.29, respectively. It's important to note that PSS was tested at only two drop heights before failure, while PSG1 underwent testing at five different drop heights before reaching failure. Consequently, Figure 4.29 can be regarded as statistically significant, and it demonstrates a linear relationship between the maximum spiral tensile strain and the drop height. Maximum tensile spiral strains were consistently observed within the region between the pile top and 1 ft from the pile top or the region between the pile tip and 3 ft from the pile tip.

Figure 4.30 and Figure 4.31 also illustrate the increase in tensile strain both at the center and towards the pile tip (in the region between the pile tip and 3 ft from the pile tip) as the drop height increased. This clearly indicates that the spiral strains measured at the center were considerably lower than those measured towards the ends of the piles.

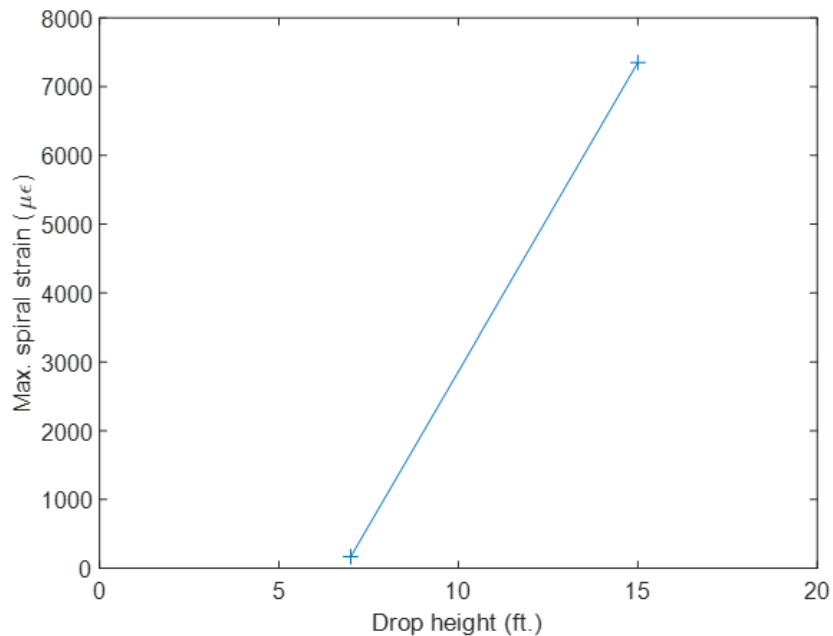


Figure 4.28: Maximum spiral tensile strain vs. drop height (PSS)

A simplified representation of the spiral behavior relative to spiral spacing is depicted in Figure 4.32 and Figure 4.33 for PSS and PSG, respectively. Please refer to Section 4.2 for a detailed

discussion on spiral spacing. In Figure 4.32 and Figure 4.33, the spiral tensile strains on both sides of the pile were averaged for specific regions along the pile length, such as 0 to 2 ft, 2 ft to 3 ft, and the pile center. These figures reveal the pattern of spiral responses under impact. It's important to note that the constant strain region between 4 ft and 25 ft along the length of the piles, as shown in Figure 4.32 and Figure 4.33, represents the average strain recorded at the center of the piles.

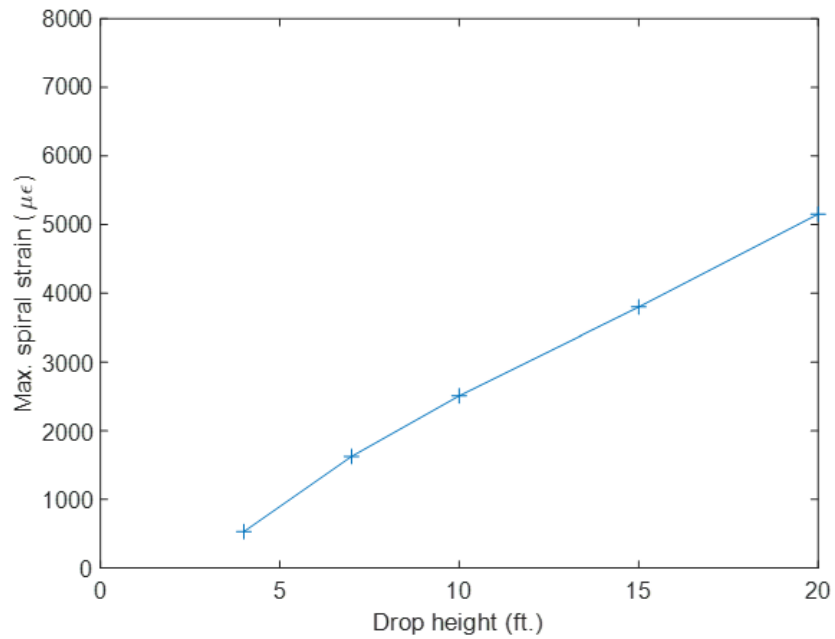


Figure 4.29: Maximum spiral tensile strain vs. drop height (PSG1)

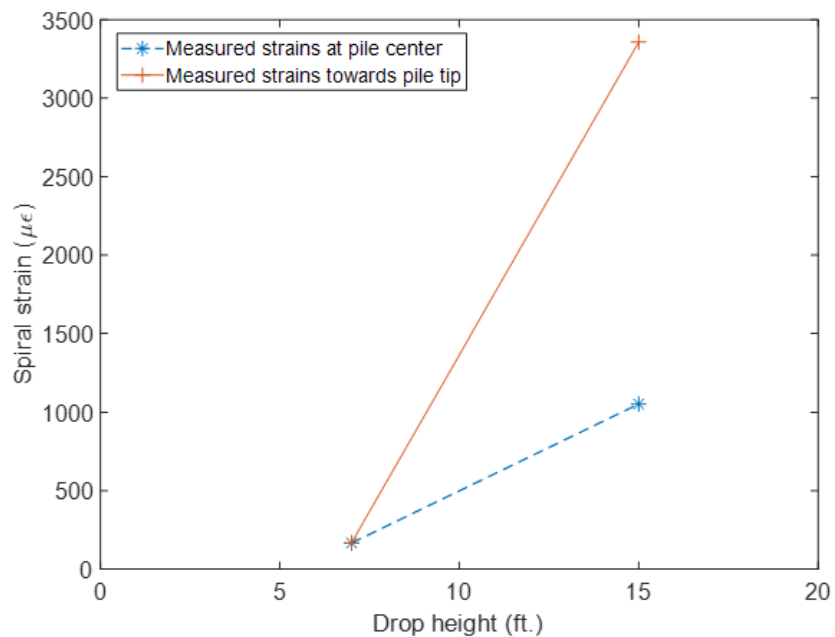


Figure 4.30: Spiral tensile strain at pile center and pile tip region vs. drop height (PSS)

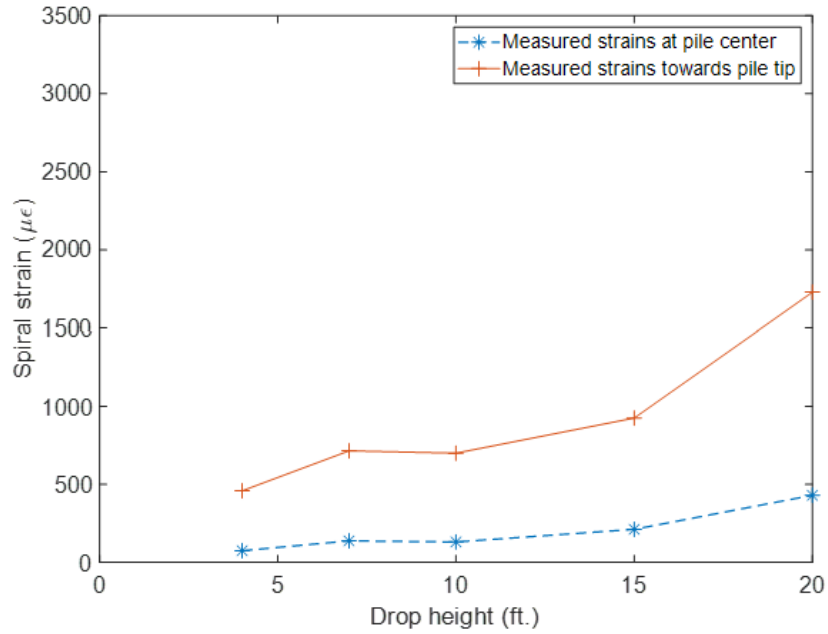


Figure 4.31: Spiral tensile strain at pile center and pile tip region vs. drop height (PSG1)

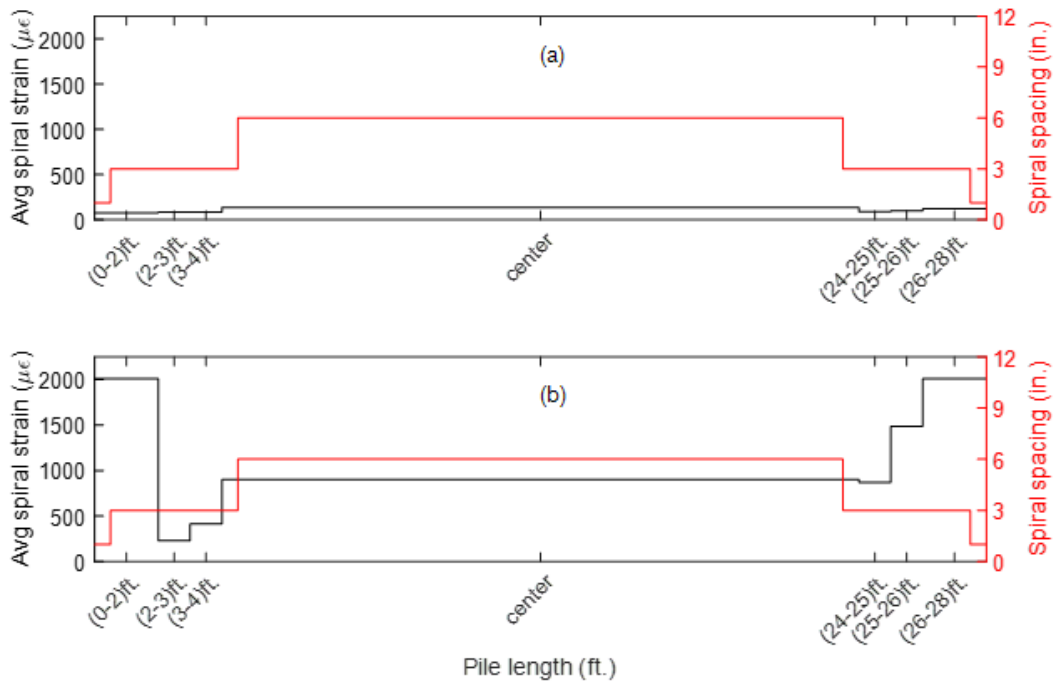


Figure 4.32: Average strains along pile (PSS) length resulting from impact from (a) 7-ft drop height, and (b) 15-ft drop height

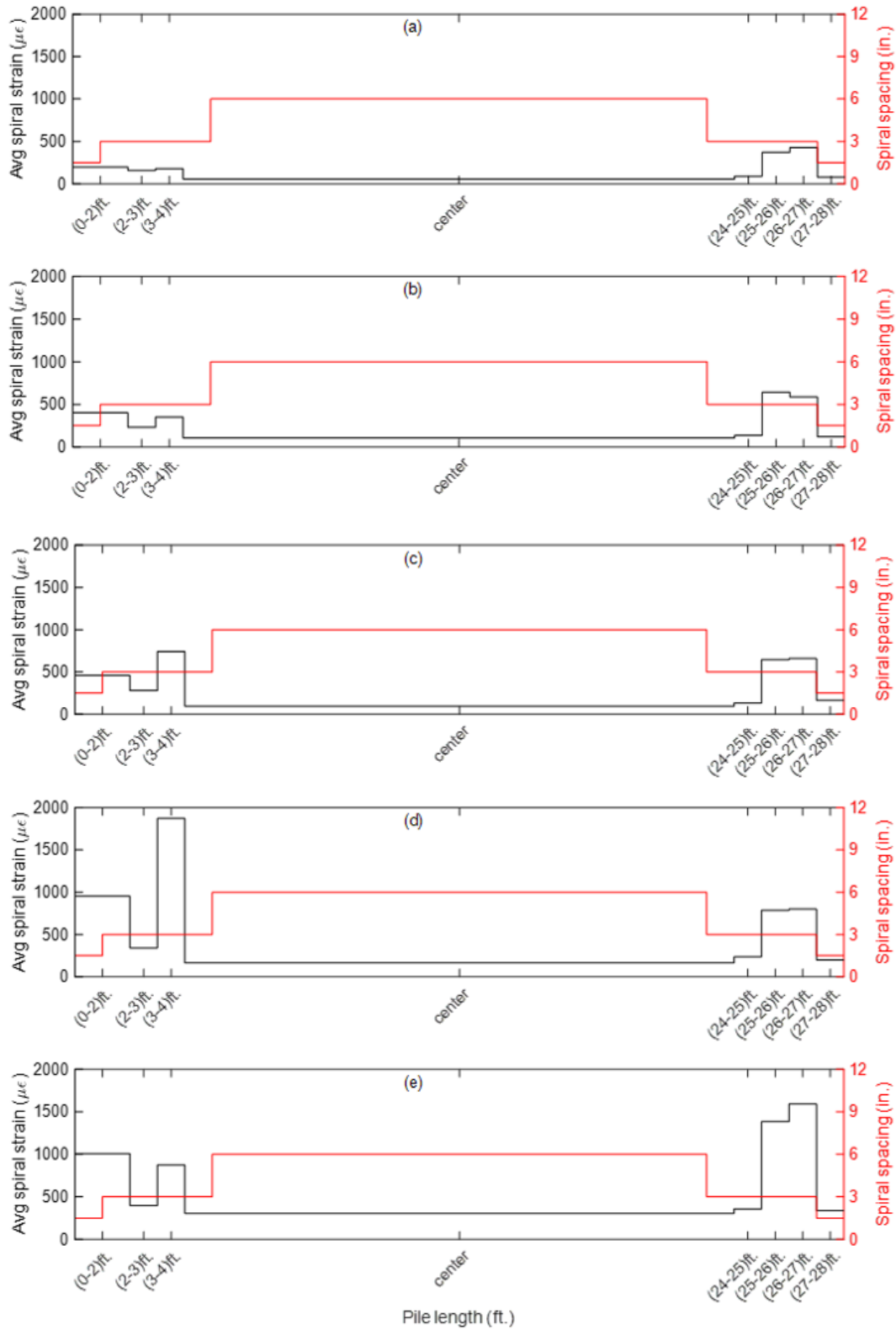


Figure 4.33: Average strains along pile (PSG1) length resulting from impact from (a) 4-ft, (b) 7-ft, (c) 10-ft, (d) 15-ft, and (e) 20-ft drop heights

4.7.4 Failure of Pile under Impact

After failure was achieved in the impact tests, crack propagations on the concrete surface were marked. Three major types of failure were observed for all piles tested under impact, as shown in Figure 4.34 to Figure 4.38:

1. **Concrete Spalling:** This type of failure was characterized by local damage and the loss of concrete cover at the pile tops or tips. It led to the exposure of spirals and strands.
2. **Tensile Cracks:** Tensile failure was evident through the presence of multiple transverse cracks along the length of the piles. This occurred due to high tensile stress waves traveling along the piles, resulting from the rebound of the pile after impact, i.e., the pile boundary condition changed from fixed to free after the pile bounced backwards after the first stress wave.
3. **Horizontal Cracks:** Horizontal cracks appeared on the east side of PSS and the west side of PCC. These cracks corresponded to the PDA strain measurements, which showed higher compressive strains on the west side for PSS (Figure 4.14). This indicated that the impact was eccentric to the west, leading to horizontal cracks on the east side of PSS, as shown in Figure 4.34. Similarly, for PCC, the impact was eccentric to the east, resulting in horizontal cracks on the west side, as depicted in Figure 4.38. However, no horizontal crack was observed for PSG1, as shown in Figure 4.36. This observation aligned with the strain measurements in Figure 4.18, indicating good alignment between the impactor and the pile.



Figure 4.34: Crack pattern after final impact for PSS



Figure 4.35: Failure at top and tip after final impact for PSS and PSG1



Figure 4.36: Crack pattern after final impact for PSG1



Figure 4.37: Failure at top and tip after final impact for PCC



Figure 4.38: Crack pattern after final impact for PCC

4.7.5 Pile Cutting Test

With strain gauges S21 to S24 for PSS (or S73 to S76 for PSG1) still connected to the data acquisition system, piles PSS and PSG1 were cut according to standard field practice. In the field, piles are typically cut after driving them to the desired elevation. The cutting process was carried out by Great Southern Demolition Inc, as depicted in Figure 4.39. Both piles were cut 2.5 ft from

the top, and spiral strain measurements were taken approximately 1.5 ft from the cut-off location. Spiral strain measurements near the cut-off location are presented in Figure 4.40 and Figure 4.41, showing that no significant strain was induced in the spirals as a result of the cutting process or vibrations caused by the cut.



Figure 4.39: Pile cutting process

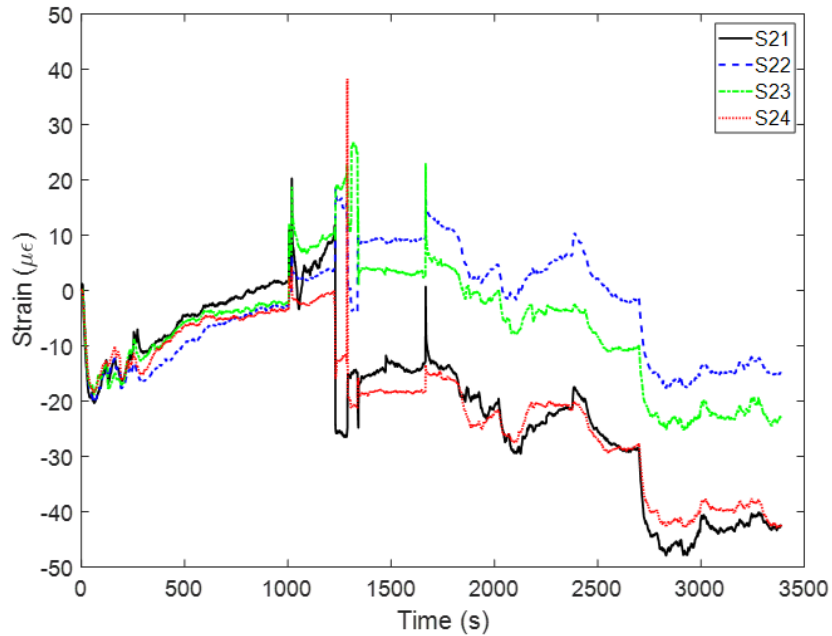


Figure 4.40: PSS pile cut

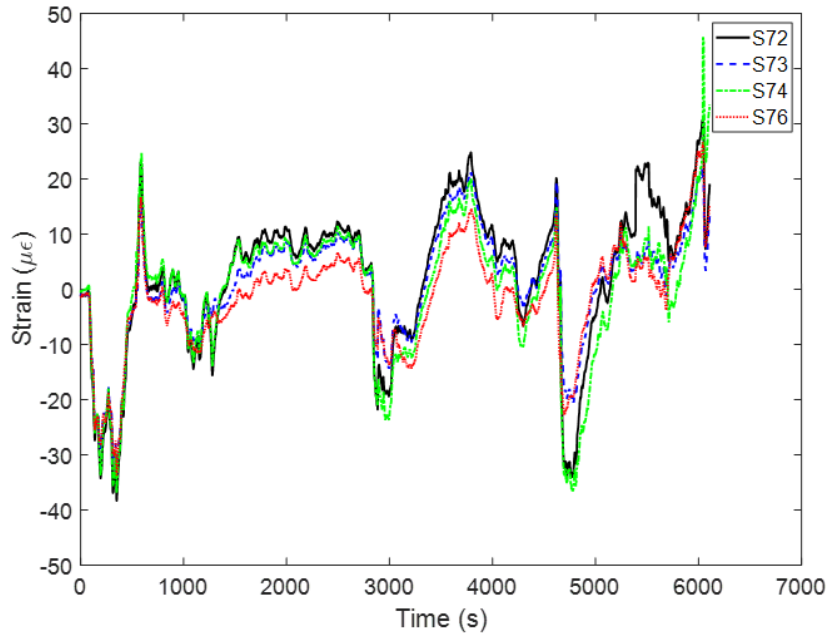


Figure 4.41: PSG1 pile cut

4.7.6 Flexural Test (PSG2)

The results from the flexural test of PSG2 have been reported in this section. The flexural test was performed using four-point loading, wherein load was generated by an actuator and transferred to the simply supported pile through a spreader beam. Durastress reported the pile's average 28-day compressive strength as 10,980 psi. However, after conducting tests on core samples from the pile, the average compressive strength at the time of testing was 14,651 psi.

The load-deflection curve for the pile at midspan is presented in Figure 4.42. The behavior of the pile was linear until the occurrence of the first flexural crack, which happened at a load of 45 kips, in the tensile region of the pile under flexure. At the cracking load, the pile deflection was 0.19 inches. After cracking, the load-deflection curve became non-linear as multiple flexural cracks propagated from the tension region of the pile. Eventually, the pile failed at a load of 153 kips, excluding the self-weight of the pile or the spreader beam. Moreover, at the point of failure, the mid-span deflection reached a value of 5.46 inches, as shown in Figure 4.43. The pile's deflection serves as a measure of its ductility, signifying its ability to endure inelastic deformation before failing.

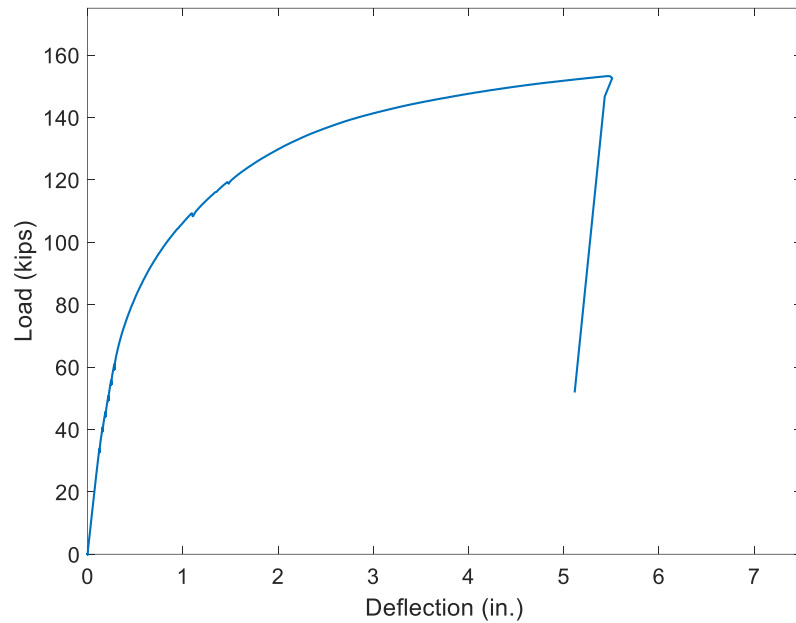


Figure 4.42: Load-deflection curve from flexural test

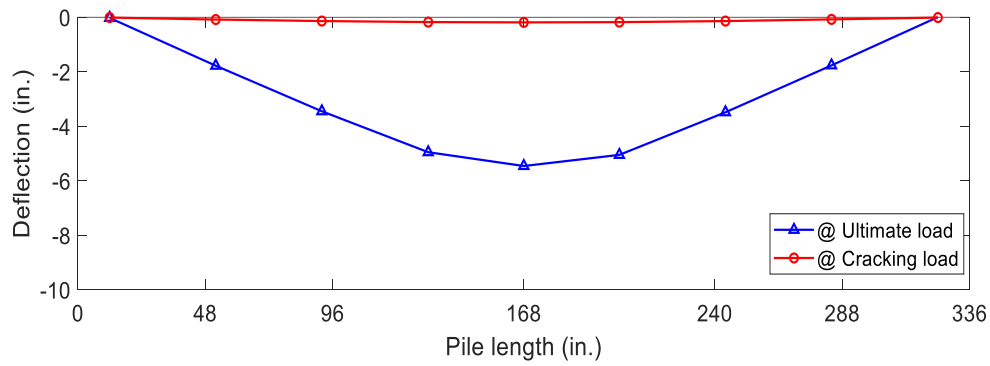


Figure 4.43: Deflection along the length of the pile

The load-strain curve (Figure 4.44) illustrates that the maximum strain in the top fiber of the pile in the constant moment region at the point of failure was $-2985 \mu\epsilon$ (microstrain). Figure 4.45 displays the crushed concrete between the load points in the compression region after the pile's failure. Additionally, flexural cracks extended beyond the constant moment region up to 1.5 ft from the load points. Upon further examination of the failed member, rupture of GFRP spirals was observed in the compression region (Figure 4.46).

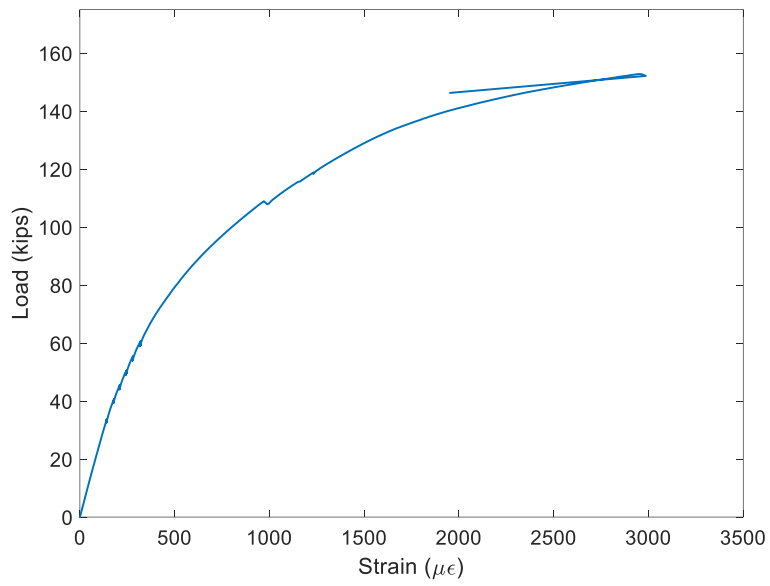


Figure 4.44: Load-strain curve from flexural test



Figure 4.45: Concrete crushed in the compression zone

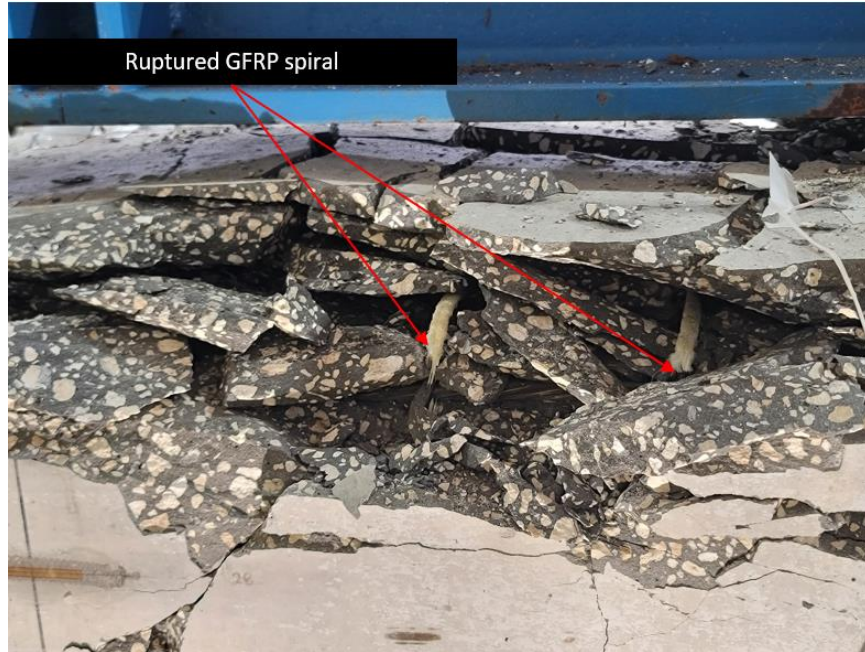


Figure 4.46: Spiral rupture in the compression zone

The pile specimen failed at an applied actuator load of 153 kips, which corresponds to a calculated moment of 765 kip-ft. When combined with the moment due to the self-weight of the pile and the spreader beam, the total calculated experimental moment capacity was 821 kip-ft. However, the theoretical moment capacity of the pile, calculated using a compressive strength of 14651 psi, was 801 kip-ft. This results in an experimental-to-theoretical moment ratio of 1.03 (Table 4.7).

Table 4.7: Experimental vs. Theoretical moment capacity

Results	Moment capacity (kip-ft)
Experimental	821
Theoretical	801
Ratio (Experimental/Theoretical)	1.03

CHAPTER 5. DISCUSSION AND FE ANALYSIS BASED ON PHASE 1 EXPERIMENTS

5.1 Comparison of Spiral Design Strength to Test Results

5.1.1 Introduction

The design for steel spirals in prestressed concrete piles by FDOT relies on established and proven methods. In this project, the size of GFRP spiral was selected by combining the FDOT-design-based force capacity, which has shown its adequacy, with the principle of force equilibrium. More details on this model and a comparison with experimental results are presented in Sections 5.1.2 and 5.1.3.

Furthermore, the spiral force was predicted using the concrete core behavior. However, this method resulted in an overestimation of the spiral force due to its assumption of complete failure or spalling of the outer concrete. Despite its widespread usage, this model's shortcomings are also addressed and discussed 5.1.4.

5.1.2 GFRP Spiral Design Summary and Prediction of Spiral Stress

Recall that details of the GFRP spiral design were discussed in Section 3.6. Also discussed were the assumptions in the force equilibrium model used in the design:

- Quasi-static loading condition
- For the same axial loading, the force in the GFRP spiral should not exceed the force of the steel spiral
- At the design requirement of 5-ksi concrete stress, the upper limit of the force was obtained by using the steel yield stress of 70 ksi. The corresponding spiral force was 2.38 kips.

A summary of the design approach given in Section 3.6 is as follows. From the force equilibrium, the stress in the GFRP spiral is:

$$\sigma = F_{spiral}/A_{GFRP} \quad (5.1)$$

where

A_{GFRP} is the cross-sectional area of the GFRP spiral and F_{spiral} is the tensile force in the spiral. By substituting the upper bound of the spiral force and the design requirement of 5-ksi concrete stress, i.e., 5×24^2 kips = 2880 kips axial force:

$$\sigma = \frac{2.38}{2880} F_{axial} / A_{GFRP} \quad (5.2)$$

This equilibrium-based model can be used to predict the stress (and force) in the GFRP spiral.

5.1.3 Observed Spiral Force from Impact Tests vs. Predicted Force and Design Tensile Capacity

Recall that PSG1 pile spiral was designed to match the tensile capacity of the PSS pile spiral, calculated to be 2.38 kips. This design capacity was then compared to the actual observed force in the spirals after impact forces were applied to the pile from varying drop heights. For ease of comparison between the steel and GFRP spirals, force was chosen over stress as the parameter. The observed force was determined using the measured strain, elastic modulus, and cross-sectional area of the spiral. For instance, a measured strain of 169 $\mu\epsilon$ for a steel spiral with a cross-sectional area of 0.034 in.² and an elastic modulus of 29000 ksi resulted in a calculated spiral force of 0.17 kips. Table 5.1 provides a summary of the axial force and the corresponding maximum spiral force in PSS for the various drop heights at which the pile was subjected to impact testing, utilizing a 0.75 in. top plywood cushion. In contrast, the axial force and the corresponding maximum spiral force in PSG1 for the drop heights at which PSG1 underwent impact testing, employing a 1.5 in. top plywood cushion, are compiled in Table 5.2. Furthermore, both tables present the percentage of the spiral design capacity achieved (with respect to the yield stress of 70 ksi for PSS and a strain limit of 0.006 for PSG1). Table 6.2 introduces an additional column, showcasing the predicted force using Equation 1.2. Predicted maximum spiral forces resulting from impacts at drop heights of 4 ft, 7 ft, and 10 ft were found to be lower than the observed (measured) maximum spiral forces. However, at the 20 ft impactor drop height, which led to the pile's failure, the predicted maximum spiral force exhibited an overestimation of approximately 6% compared to the measured maximum force.

Table 5.1: Axial pile force and corresponding maximum spiral stress (PSS)

Drop heights (ft)	Axial force (kips)	Observed max spiral force (kips)	Observed stress / yield stress (70 ksi) (%)
7	1328	0.17	7.1
15	2692	2.38	100

Table 5.2: Axial pile force and corresponding maximum spiral stress (PSG1)

Drop heights (ft)	Axial force (kips)	Predicted max spiral force [Equation (5.2)× A] (kips)	Observed max spiral force (kips)	Observed strain / strain limit (0.006) (%)
4	803	0.66	0.70	16.3
7	1141	0.94	1.11	25.9
10	1600	1.32	1.77	41.3
15	2221	1.84	1.81	42.2
20	3014	2.49	2.34	54.5

The overestimation was unsurprising, given that the upper limit of the force (i.e., the force corresponding to the yielded steel) was employed during the design phase. Furthermore, considering that the maximum observed force in the spiral approached the design capacity, a deliberate choice was made to incorporate a more conservative design alternative.

5.1.4 Prediction Using the Concrete Core Behavior

When a pile is subjected to an axial load, the concrete expands laterally due to the Poisson's effect. The lateral expansion of the concrete core is restrained by the spirals, which then causes a tensile stress on the spirals. Therefore, the concrete core is under triaxial compression due to the axial load and the restraint. Equations from this behavior is commonly used by researchers to relate the axial load and stresses in the concrete and the spiral, particularly to compute the maximum axial load.

However, the equations from the concrete core behavior provided very large spiral force, because the approach assumes complete failure/spalling of the outer concrete while maintaining the load carrying capacity of the pile using the core of the concrete alone. Specifically, the spiral area, concrete stress, and the spiral stress were related using ACI recommended equations (Equations (2.30) and (2.31)).

By using 5 ksi design requirement instead of f'_c and corresponding spiral stress σ instead of f_{yh} , the spiral stress and the force can be computed using Equations (2.30) and (2.31). The force in the spiral becomes about 6 kips, which is about 2.5 times greater than the approach explained in the

previous section. The result is consistent with observations from the design stage, i.e., spiral designed with this approach results in excessively large bar diameter because the outer concrete cover was ignored.

5.1.5 Limitations of the Analytical Model

The equilibrium-based model presented in Section 5.1.2 was constructed in alignment with the design approach adopted for this project. However, the outcomes of this model revealed an average absolute difference of approximately 11% in the force exerted on the spiral when compared to the experimental findings. This model, while straightforward and practical but, lacked the depth of rigor as it relied on empirical knowledge and adhered to the prescriptive guidelines of the FDOT design guide.

The commonly used core behavior model fully explains the stress development in the axially loaded member, but it led to very large overestimation of the spiral force, because the approach assumed complete failure/spalling of the outer concrete. The approach will be useful at the ultimate loading condition but was not suitable for the purpose of this project.

The next section, finite element prediction, will fully account for all structural elements of the pile as well as dynamic loading effect.

5.2 Finite Element Model Prediction

5.2.1 Background

Due to the highly complicated stress distribution during the pile impact, relying solely on the analytical model would prove insufficient for accurately predicting the pile's response. While the analytical model played a crucial role during the design phase, the prediction of impact test outcomes necessitates the incorporation of dynamic loading effects. This section delves into the finite element model and its capacity to forecast the testing results by accounting for the dynamic loading effects.

5.2.2 General Model Details

In this section, we will describe the modeling and analysis of the impact loading on two prestressed concrete piles using the finite element software ABAQUS. These prestressed concrete piles had a cross-section of 24 in. \times 24 in. and a length of 28 ft. The finite element model included the materials

for concrete, steel strands, steel spirals, GFRP spirals and plywood cushion. Further information on the properties and behavior of these materials is discussed in upcoming sections of this report. Moreover, the dimensions and reinforcement details of the pile subjected to impact loading, as simulated, were outlined in Section 4.2.

The experimental test setup for the actual impact experiments was extensively discussed in Chapter 3. In summary, it involved an impactor attached to a pendulum mechanism, with the pile placed longitudinally on steel supports covered with a layer of Teflon material. The use of Teflon helped reduce friction between the pile and supports and elevated the pile above the ground. Plywood cushions were positioned at both the top and tip of the pile, and restraining blocks were placed at the pile tip to limit post-impact pile displacement.

For the finite element analyses, two modeling decisions were made to ensure the efficiency of dynamic analysis. First, the pile models were fixed at the tip, as shown in Figure 5.1. This simplified approach was chosen to minimize potential uncertainties related to the interactions between the pile, support blocks, and the ground soil.

Another modeling decision involved directly applying the impact load at the pile top, instead of using a pendulum mechanism to drop the load from a specified height. These modeling choices resulted in increased impact energy applied to the pile. This increase was due to the lack of pile sliding and the absence of centripetal force dynamics. It is important to note that the finite element modeling did not consider additional energy losses such as tower (steel pylon) and cable vibrations, compression of the gap between plywood cushions and the pile, or other miscellaneous forms of energy dissipation like heat and sound. Incorporating these unaccounted energy losses into the FE analysis necessitated the introduction of an energy-equivalent velocity, denoted as $V_{FE} < V$, for the impactor. This adjustment was prompted by the insights garnered from high-speed camera image analyses conducted across all impact experiments. The data revealed that the percentage of initial potential energy dissipated solely due to centripetal force exerted by the pendulum mechanism post-impact ranged between 23% and 26%. To accommodate these and other potential energy dissipation factors, the energy-equivalent velocity V_{FE} was derived for specific drop heights. This estimation was achieved by multiplying the original impact velocity V with a reduction factor α , as depicted in Equation (5.4). This reduction factor α was designed to

encapsulate the non-linear relationship between energy loss and the drop height encountered during testing.

$$V = \sqrt{2gh} \quad (5.3)$$

$$V_{FE} = \alpha V \quad (5.4)$$

where

h is the impactor drop height, and g is gravitational constant.

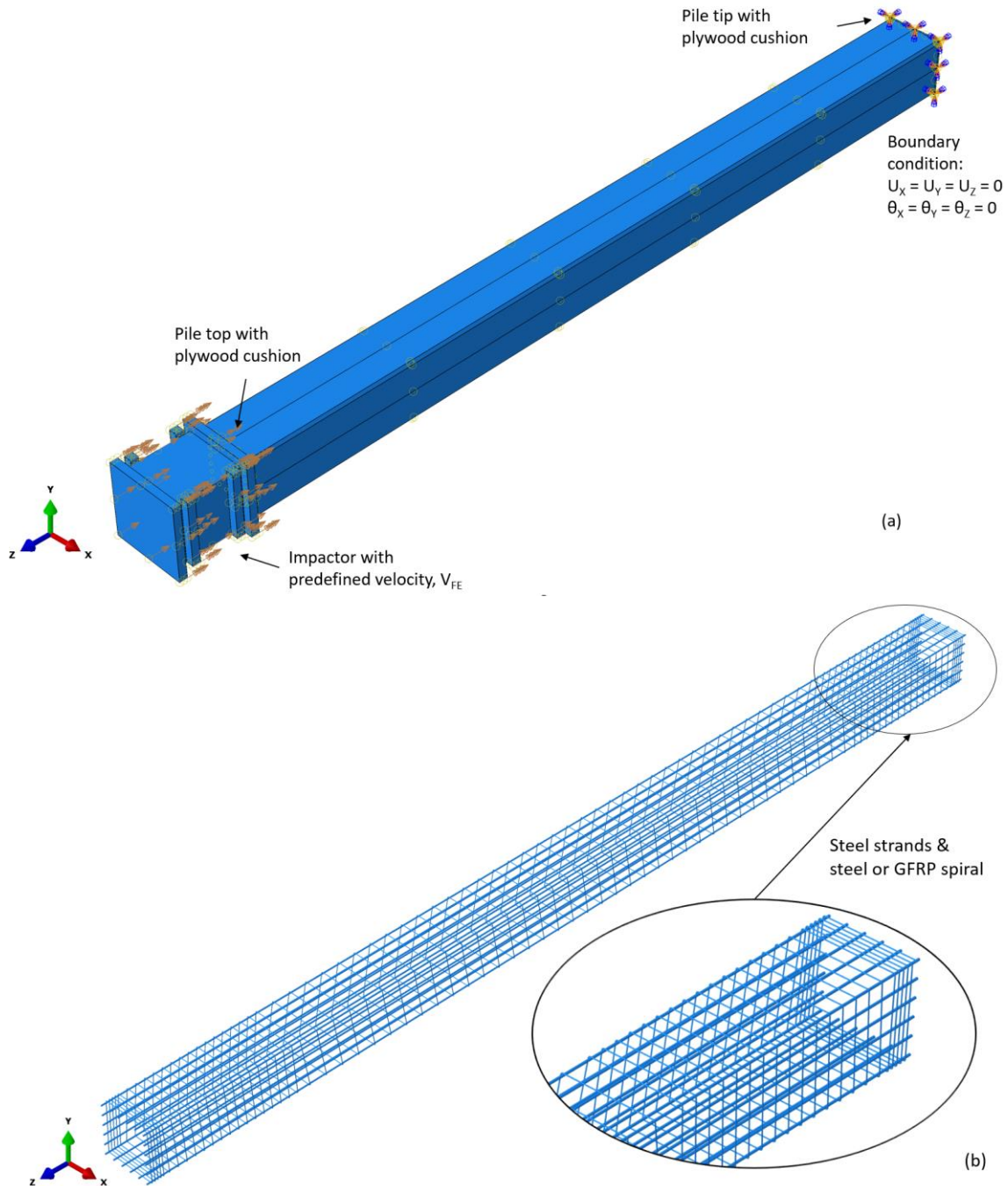


Figure 5.1: (a) Test setup assembly in ABAQUS; (b) Reinforcement embedded in pile model

The reduction in energy was more significant for lower drop heights due to a larger portion of the total impact energy being absorbed by energy losses at these lower heights. One example is the closing of the gap between the plywood cushion and the pile, which is more pronounced at lower heights compared to higher ones, as shown in Table 5.3.

Table 5.3: Reduction factor for estimating energy-equivalent velocity in FE

Drop height (ft)	Reduction factor (α)	Energy-equivalent velocity (V_{FE}) (ft/s)
4	0.476	7.64
7	0.480	10.19
10	0.528	13.40
15	0.652	20.27
20	0.809	29.01

The model used in the pile impact experiment comprised various components: pile concrete, steel strands, steel or GFRP spirals, a steel impactor, and plywood cushions. These components were represented in the model using specific element types. C3D8R elements were employed for the concrete, impactor, and plywood cushions. C3D8R elements are 8-node linear brick elements with reduced integration, and each node had three degrees of freedom. The concrete part of the model consisted of 15,680 elements and 18,193 nodes, while the impactor had 2,876 elements and 4,238 nodes. Each pile cushion was represented by 144 elements and 338 nodes.

The prestressing strands, steel wire spiral, and GFRP spiral were represented using three-dimensional 2-node truss elements (T3D2). The model included 3,360 elements with 3,380 nodes to accurately depict the 20 prestressing strands. The steel wire spiral consisted of 2,965 elements and 2,966 nodes, while the GFRP spiral had 2,959 elements and 2,960 nodes.

For the finite element impact analysis of PSS, which had one plywood cushion at both the top and tip of the pile, the total number of elements was 21,809. Similarly, for PSG1, which had two plywood cushions at the top and one at the tip, the total elements in the analysis amounted to 21,947.

The interaction between the reinforcement assembly (strands and spiral) and the concrete was implemented using embedded region constraints. This constraint assumed a perfect bond between the reinforcements and the concrete interface, which was considered appropriate based on minimal observed movement between the concrete and reinforcements during physical experiments.

The finite element analyses for the test piles involved a combined approach using both the ABAQUS implicit and explicit solvers. The implicit solver was used for applying prestressing to establish the piles' prestressed condition. Subsequently, the stressed state was transferred to the explicit solver for dynamic analysis. ABAQUS explicit is typically used for solving dynamic problems with high speed and short durations, such as drop tests, automotive crash analysis, and impact tests. The time step for the explicit analyses was set to 0.1 milliseconds. The concrete mesh size was 3 inches, while other components of the model had a 2-inch mesh size.

5.2.3 Concrete Material Model

In ABAQUS, a variety of constitutive models are available to simulate concrete behavior. For this study, the concrete damaged plasticity (CDP) model was selected. This plasticity-based model has demonstrated its suitability for both static and dynamic analyses of prestressed concrete, as evidenced by previous researches (Chung et al., 2014; Mercan et al., 2010, 2016).

The CDP model was initially developed by Lubliner et al. in 1989, with subsequent improvements by Lee & Fenves in 1998. Figure 5.2 illustrates the tensile and compressive responses of concrete as represented by the CDP model. This model takes into account stress-strain relationships, damage parameters, and strain rates in both compression and tension.

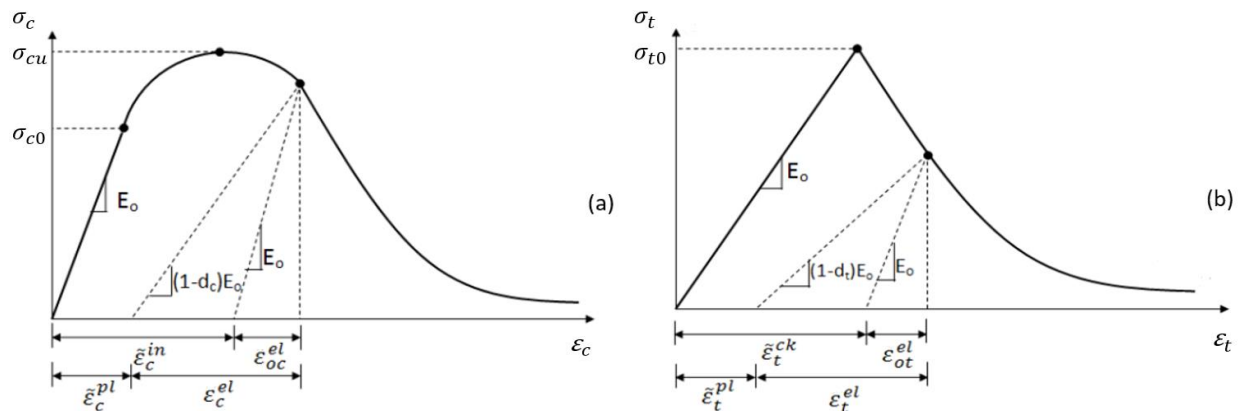


Figure 5.2: Stress-strain curve of concrete in (a) compression and (b) tension for the CDP model

As shown in Figure 5.2, the CDP model incorporates the compressive crushing and tensile cracking modes of concrete failure through damage parameters denoted as d_c and d_t for compression and tension, respectively. These damage parameters range from zero, indicating an absence of damage, to a value of one, signifying complete damage and a loss of material strength.

The post-failure behavior of concrete in compression and tension, characterized by the post-failure stress, is determined by the crushing strain $\tilde{\varepsilon}_c^{in}$ and cracking strain $\tilde{\varepsilon}_t^{ck}$, respectively. The crushing strain is computed as the total strain minus the elastic strain associated with the undamaged material, as indicated in Equation (5.5).

$$\tilde{\varepsilon}_c^{in} = \varepsilon_c - \varepsilon_{oc}^{el} = \varepsilon_c - \frac{\sigma_c}{E_0} \quad (5.5)$$

where

ε_c is the total compressive strain, ε_{oc}^{el} is the elastic compressive strain, σ_c is the concrete compressive strength at any point and E_0 is the undamaged elastic modulus.

The cracking strain on the other hand is calculated as shown in Equation(5.6).

$$\tilde{\varepsilon}_t^{ck} = \varepsilon_t - \varepsilon_{ot}^{el} = \varepsilon_t - \frac{\sigma_t}{E_0} \quad (5.6)$$

where

ε_t is the total tensile strain, ε_{ot}^{el} is the elastic tensile strain, σ_t is the concrete tensile strength at any point.

The crushing and cracking strains calculated as described above is automatically converted to corresponding plastic strain values by the ABAQUS program as according to Equation (5.7) and Equation (5.8) below. Plastic strain values calculated using Equation (5.7) and Equation (5.8) should neither be negative or of a decreasing value with increasing inelastic (crushing) strain or cracking strain values, otherwise, ABAQUS indicates an error.

$$\tilde{\varepsilon}_c^{pl} = \tilde{\varepsilon}_c^{in} - \left(\frac{d_c}{1 - d_c} \right) \left(\frac{\sigma_c}{E_0} \right) \quad (5.7)$$

$$\tilde{\varepsilon}_t^{pl} = \tilde{\varepsilon}_t^{ck} - \left(\frac{d_t}{1 - d_t} \right) \left(\frac{\sigma_t}{E_0} \right) \quad (5.8)$$

The input values of d_c and d_t under uniaxial compression and tension, respectively, can be approximated using Equation (5.9) and Equation (5.10) (Othman & Marzouk, 2018; Ren et al., 2015; Tao & Chen, 2015).

$$d_c = 1 - \frac{\sigma_c}{\sigma_{cu}} \quad (5.9)$$

$$d_t = 1 - \frac{\sigma_t}{\sigma_{t0}} \quad (5.10)$$

The CDP model involves the definition of several parameters, including the dilation angle (ψ), flow potential eccentricity (e), the ratio of initial biaxial compressive yield stress to initial uniaxial compressive yield stress (σ_{b0}/σ_{c0}), the shape factor (or the ratio of the second stress invariant on the tensile meridian to compressive meridian at initial yield) denoted as K , and the viscosity parameter (μ). The specific values of these CDP parameters utilized for the pile model are presented in Table 6.4. It is worth noting that the values for e , σ_{b0}/σ_{c0} , and K are default values.

Table 5.4: Concrete damaged plasticity (CDP) model parameters

Dilation angle ψ	Eccentricity e	σ_{b0}/σ_{c0}	K	viscosity parameter μ
30	0.1	1.16	0.667	0.0001

5.2.4 Concrete Stress-Strain Curve

The numerical model adopted the stress-strain curve for concrete in compression as suggested by Collins & Mitchell (1991). The equations representing this stress-strain curve are provided in Equations (5.11) to (5.18).

$$f_c = \left(\frac{n \left(\varepsilon_{cf} / \varepsilon'_c \right)}{n - 1 \left(\varepsilon_{cf} / \varepsilon'_c \right)^{nk}} \right) f'_c \quad (5.11)$$

$$\varepsilon'_c = \frac{f'_c}{E_c} \frac{n}{n - 1} \quad (5.12)$$

$$k = \begin{cases} 1 & \text{if } \varepsilon_{cf} < \varepsilon'_c \\ 0.67 + \frac{f'_c}{9000} & \text{if } \varepsilon_{cf} \geq \varepsilon'_c \end{cases} \quad (5.13)$$

$$n = 0.8 + \frac{f'_c}{2500} \quad (5.14)$$

$$E_c = 40,000\sqrt{f'_c} + 1,000,000 \quad (5.15)$$

where

ε_{cf} is the concrete compressive strain; f_c is the concrete compressive strength at ε_{cf} (psi); f'_c is the concrete compressive strength (psi); ε'_c is the strain corresponding to compressive strength; k and n are factors given in Equation (5.13) and (5.14); and E_c is the elastic modulus of concrete (psi).

The modulus of elasticity of concrete (E_c) was correlated to its compressive strength using Equation (5.15), and the Poisson's ratio was defined as 0.2. Figure 5.3 illustrates the stress-strain curve for concrete behavior in compression.

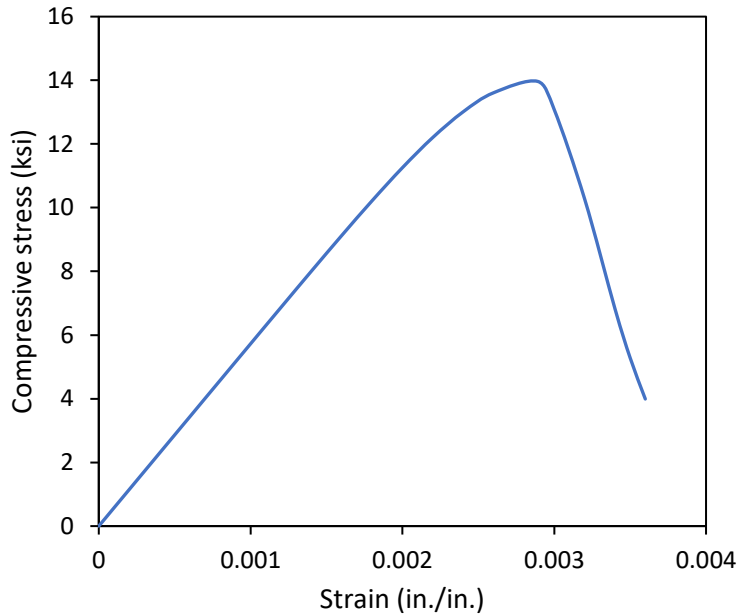


Figure 5.3: Concrete stress-strain curve in compression utilized in FE

Also, the behavior of concrete in tension was modeled using Equations (5.16) to (5.18) as recommended by Belarbi & Hsu, (1994).

$$f_t = \begin{cases} E_c \varepsilon_t & \text{if } \varepsilon_{cf} \leq \varepsilon'_c \\ f_{cr} \left(\frac{\varepsilon_{cr}}{\varepsilon_t}\right)^{0.4} & \text{if } \varepsilon_{cf} > \varepsilon'_c \end{cases} \quad (5.16)$$

$$\varepsilon_{cr} = \frac{f_{cr}}{E_c} \quad (5.17)$$

$$f_{cr} = 4\sqrt{f'_c} \quad (5.18)$$

where

ε_t is the concrete tensile strain; f_t is the concrete tensile stress at ε_t (psi); ε_{cr} is the cracking strain of concrete in tension; and f_{cr} is cracking stress of concrete in tension (psi).

The stress-strain curve used to define the tensile behavior of concrete is depicted in Figure 5.4. Also, the mechanical properties of the concrete incorporated into the finite element model are provided in Table 5.5.

Table 5.5: Mechanical properties of concrete

Density	f'_c	f_{cr}	E_c	ν
lbf s ² /in ⁴	ksi	ksi	ksi	
2.24e-04	13.9	0.47	5727	0.2

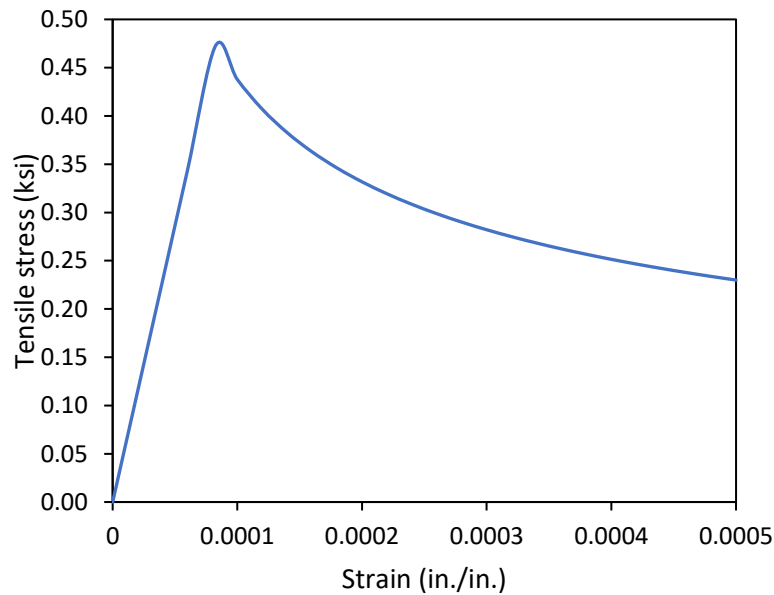


Figure 5.4: Concrete stress-strain curve in tension utilized in FE

5.2.5 Prestressing Strand, Steel Wire, and GFRP Material Model

This investigation utilized two different forms of steel reinforcements: Grade 270 low relaxation prestressing strands and a steel wire spiral. For the analysis, the stress-strain relationship for the prestressing steel, as originally presented by Devalapura et al. (1992), was incorporated, and its representation can be observed in Figure 5.5. The equation that describes this curve is as follows:

$$f_{ps} = \varepsilon_{ps} \left[A + \frac{B}{\{1 + (C\varepsilon_{ps})^D\}^{1/D}} \right] \leq f_{pu} \quad (5.19)$$

where

f_{ps} is the stress in the prestressing strand corresponding to a given strain ε_{ps} ; f_{pu} is the maximum strand stress and A, B, C, and D are constants obtained by curve fitting.

The constants A, B, C, and D for a 270 ksi low-relaxation steel strand are as follows: 887, 27613, 112.4, and 7.360, respectively. It's crucial not to round these constants, as they significantly impact the calculated value of f_{ps} .

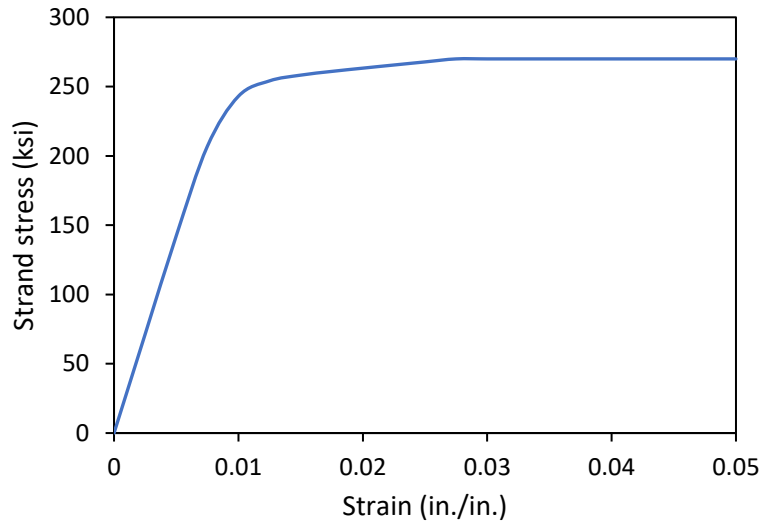


Figure 5.5: Stress-strain curve for prestressing steel strands

The behavior of the steel wire spiral was modeled using a bilinear stress-strain curve that incorporates both an elastic and strain hardening portion, as depicted in Figure 5.6. Within this model, E_s represents the elastic modulus, while f_y and f_u denote the yield strength and ultimate strength of the steel wire.

On the other hand, the GFRP spiral, which exhibits elastic-brittle behavior, was represented as a linear elastic material in the model until it reaches failure. In the ABAQUS analysis, a small value of $1.00e-05$ was assigned to the plastic strain at failure, as per the approach outlined by Almusallam et al. (2013). The properties of the prestressing strand, steel wire spiral, and GFRP spirals can be found in Table 5.6 for reference.

Table 5.6: Mechanical properties of reinforcement

Reinforcement type	Area in. ²	ρ lbf s ² /in ⁴	$E_{ps}/E_s/E_f$ ksi	f_{py}/f_y ksi	$f_{pu}/f_u/f_{fu}$ ksi	ν
Prestressing strand	0.167	7.3×10^{-4}	28,500	243	270	0.3
Steel wire spiral	0.034	7.3×10^{-4}	29,000	70	80	0.3
#3 GFRP spiral	0.11	1.97×10^{-4}	6,500	—	120	0.25

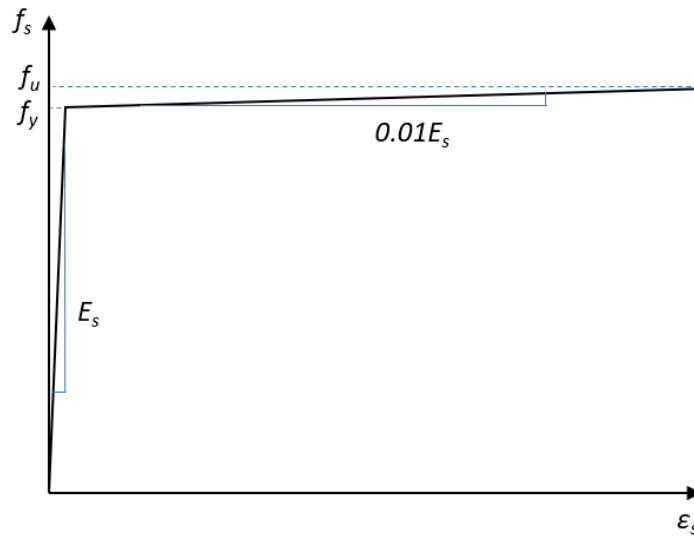


Figure 5.6: Stress-strain curve for steel wire spiral

To establish the initial stress state in the prestressed concrete pile within the ABAQUS/explicit model, it was necessary to apply prestressing force. This force could be introduced directly, involving the prescription of a constant initial stress along the s'trands' length. Alternatively, an indirect method involves creating an artificial temperature drop in the strands to achieve the desired prestress. In this study, the direct method of applying prestress was employed using the ABAQUS implicit solver. The initial stress state established through this method was subsequently transferred to the ABAQUS explicit solver for further analysis.

Another approach, though not used in this study, entails applying the prestressing force through a predefined temperature reduction, which can be calculated using Equation (5.20).

$$\Delta T = -\frac{f_{pe}}{\alpha_{ps} E_{ps}} \quad (5.20)$$

Where

ΔT represents the required temperature reduction, f_{pe} is the effective prestress in the strands after loss, α_{ps} denotes the coefficient of thermal expansion in the strands (taken as $1.15 \times 10^{-5} / ^\circ C$), and E_{ps} stands for the elastic modulus of the prestressing strands.

5.2.6 Plywood Material Model

To replicate the properties of plywood in the finite element model, linear properties were assumed. Each plywood cushion had a uniform thickness of 0.75 in., therefore, where a thickness of 1.5 in. was required, two plywood sheets were virtually joined together using a tie constraint within the ABAQUS software. For reference, you can find the mechanical properties of the plywood employed in the finite element model summarized in Table 5.7.

Table 5.7: Mechanical properties of plywood

Density	E_{ply}	ν	Yield stress
lbf s ² /in ⁴	ksi		ksi
5.8×10^{-10}	7300	0.45	5

5.3 Comparison of Test Results to FE Model Results

First, sample plots from the FE analysis are discussed before they are compared to the test results. In Figure 5.7, axial stress plots at four different time steps for the PSS pile are presented. Upon impact, the stress wave originates from the pile top (Figure 5.7a) and propagates towards the pile tip (Figure 5.7b, c). At the tip, the stress wave is reflected and propagates backward (Figure 5.7d).

In Figure 5.8, stress at the pile head is depicted at the time steps $t = 0.003$ and 0.004 seconds for the PSS pile. As anticipated, there was a localized high stress of approximately 9 ksi at the pile head surface, while slightly away from the pile head, the peak stress was around 5 ksi. A similar behavior was observed in the PSG1 pile, as illustrated in Figure 5.9.

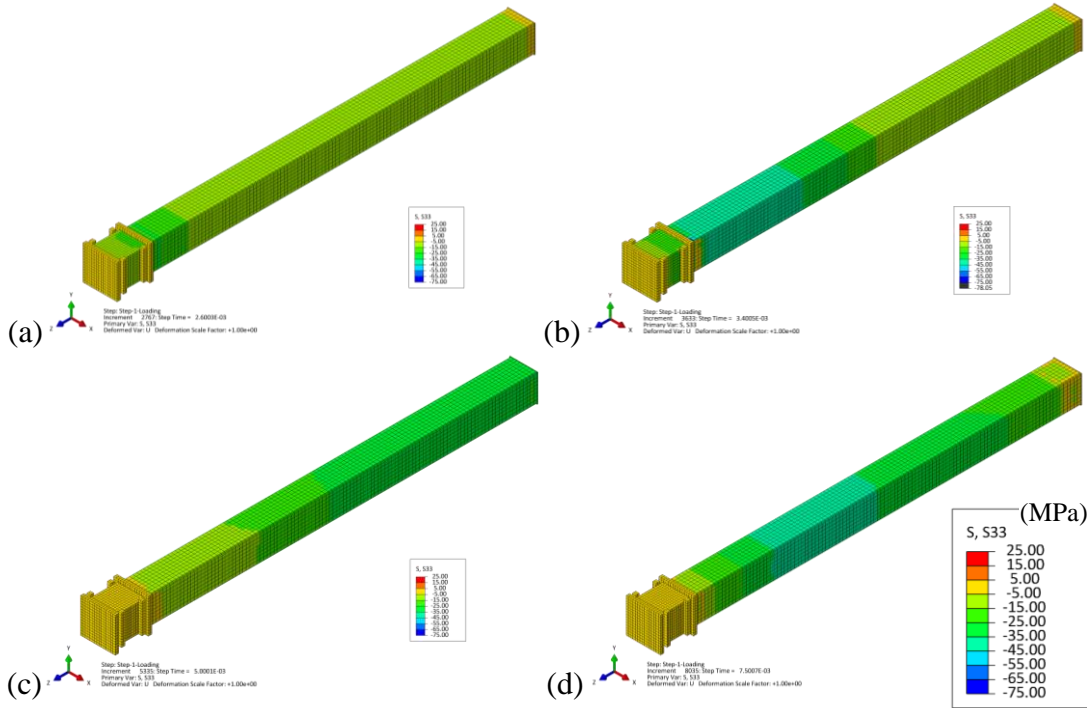


Figure 5.7: Stress propagation after impact, the PSS pile, 15-ft drop height. (a), (b), (c) forward propagation ($t = 0.0026, 0.0034,$ and 0.0050 sec), and (d) reflection and backward propagation ($t = 0.0075$ sec)

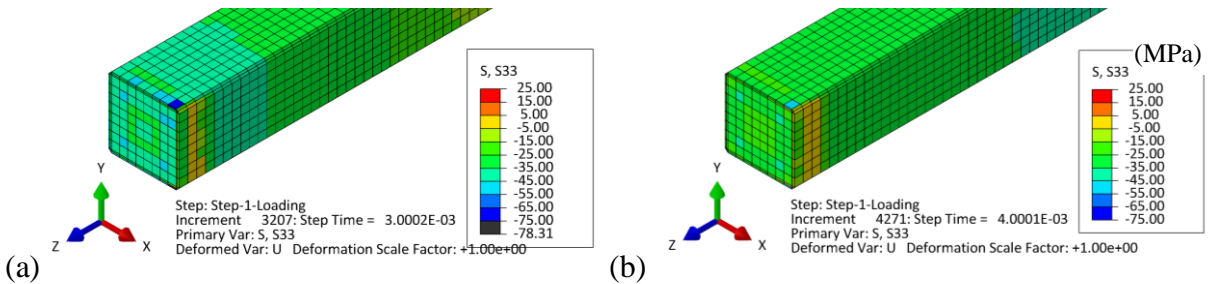


Figure 5.8: Stress at the pile top, the PSS pile, 15 ft drop height. (a) $t = 0.003$ sec, (b) $t = 0.004$ sec

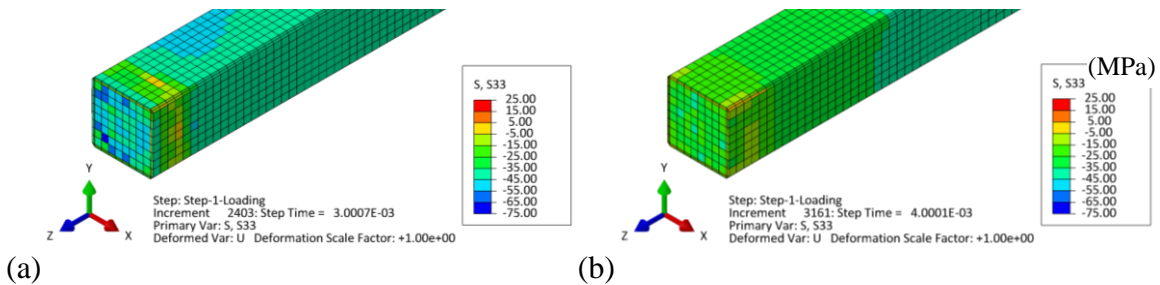


Figure 5.9: Stress at the pile top, the PSG1 pile, 20-ft drop height. (a) $t = 0.003$ sec, (b) $t = 0.004$ sec

Subsequently, the FE analyses are juxtaposed with the test results. To facilitate a comparison of concrete stress on the surface, the value measured at a distance of 4 ft from the pile head was utilized. As illustrated in Figure 5.10 and Figure 5.11, the time history of stress for both the PSS pile and the PSG1 pile is presented. In each case, the maximum stress was documented and subsequently compared to the testing results, as depicted in Figure 5.12 and Figure 5.13. The FE analysis exhibited a close match with the testing results, with a difference of less than 4% observed for concrete axial stress. The FE stress data was extracted from the result file, whereas the experimental stress was acquired from the PDA measurements, averaging the stress values from both the east and west sides to obtain the maximum stress.

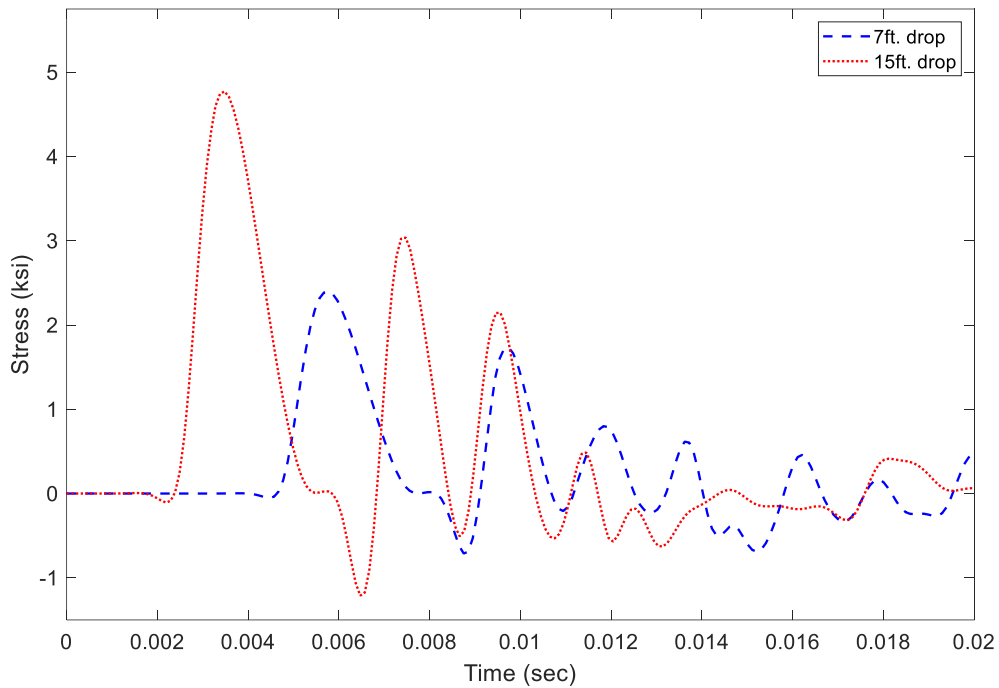


Figure 5.10: PSS FE stress plot (concrete stress on the surface, 4 ft from the top)

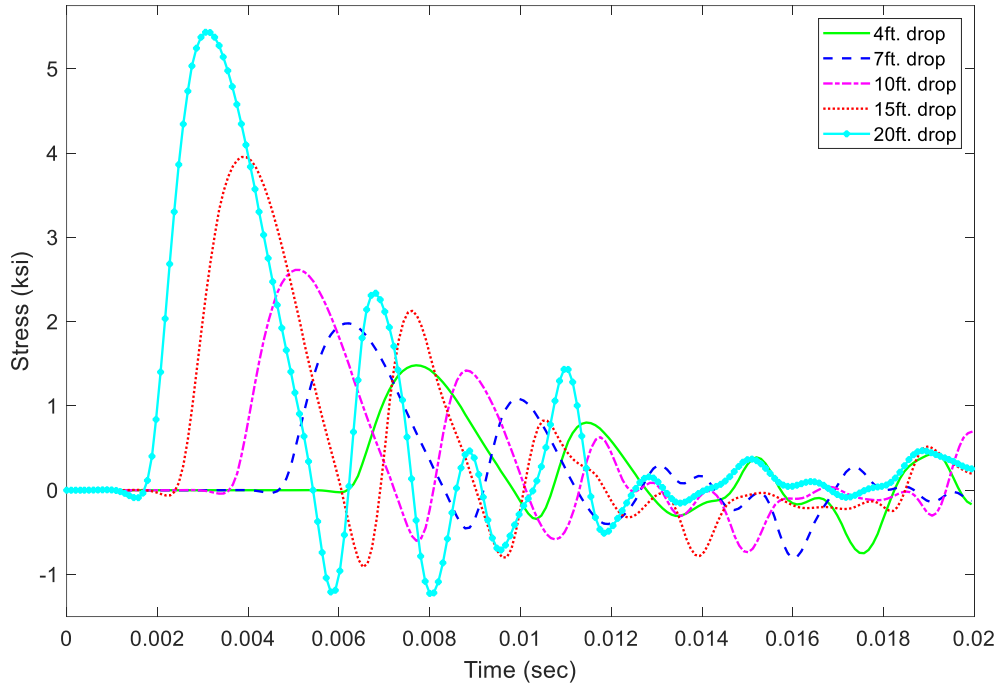


Figure 5.11: PSG1 FE stress plot (concrete stress on the surface, 4 ft from the top)

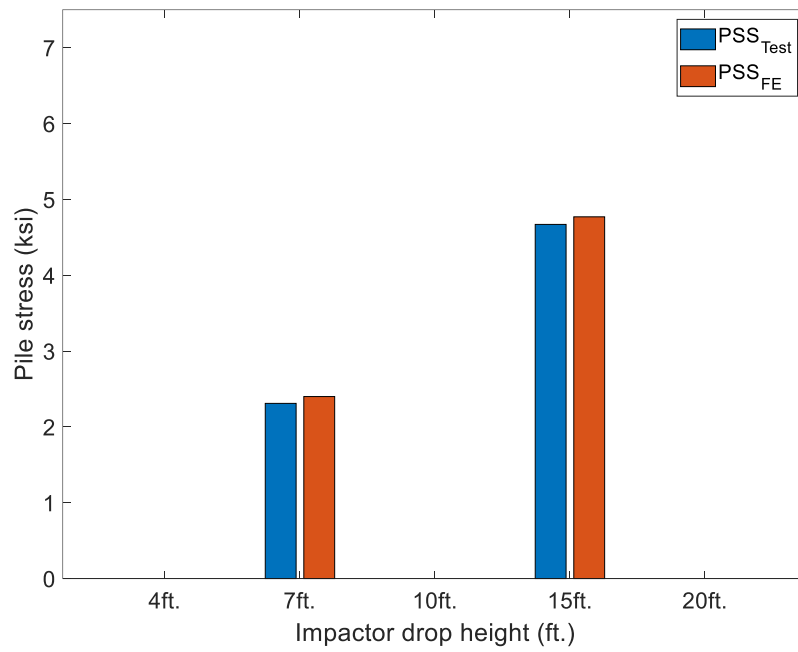


Figure 5.12: Comparison of experimental pile stress results to FE stress results (PSS)

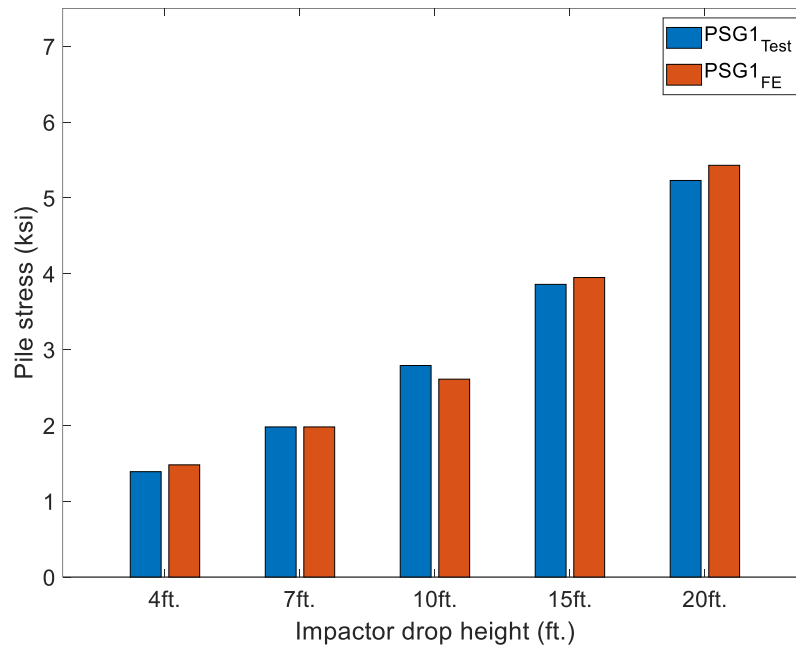


Figure 5.13: Comparison of test pile stress results to FE stress results (PSG1)

Figure 5.14 and Figure 5.15 provide a comparative analysis of the spiral strain between the test results and the FE analyses. In contrast to the test results, the FE analyses displayed nearly symmetrical behavior between the east and west sides, thus only one side is represented in the plot. The legend "FE" denotes the strain at the same location as the testing, while the legend "FE corner strain" signifies the strain derived from the round corner, which exhibited higher values at certain locations. The following observations can be made from the figures:

- Overall, the FE strain was significantly lower than the strains observed in the PSS testing. This contrast can be attributed to the PSS specimen experiencing eccentric impact, resulting in pile whipping. The substantial strains observed in the PSS testing were a consequence of this issue. Conversely, the FE model was subjected to axial impact loading only, resulting in smaller strains.
- For the PSS specimen, the pile head strain closely matched the results from the east side of the testing and the FE analysis.
- In the case of the PSG1 pile, the FE strain closely aligned with the testing results overall. The peak strain at the pile head closely matched the results from the west side testing. However, the FE results were notably lower than the two localized peaks observed on the east side of the testing specimen.

- Owing to the completely fixed boundary conditions in the FE analysis, the strain amplification at the pile tip was approximately 2.5 times that of the pile head strain, as opposed to the roughly 1.5 times amplification observed in the testing. Nonetheless, the amplified strain remained below the established limit, as illustrated in the figure.

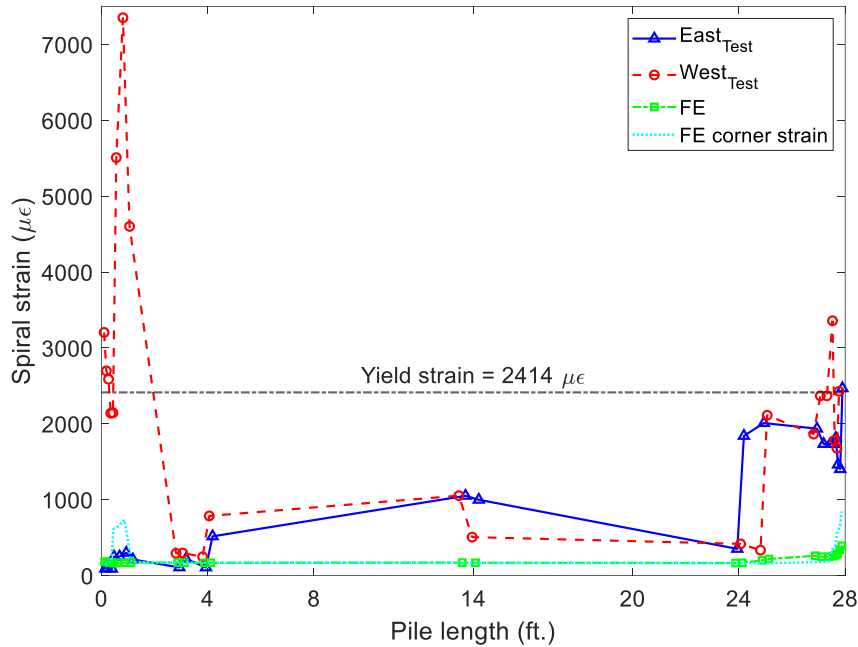


Figure 5.14: Test vs. FE steel spiral strain for PSS (15-ft drop height)

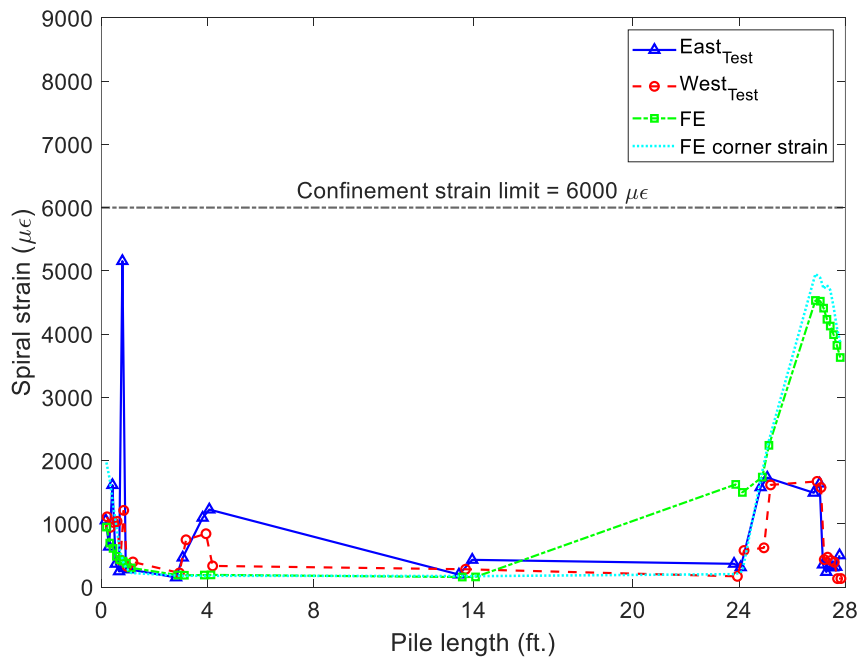


Figure 5.15: Test vs. FE steel spiral strain for PSG1 (20-ft drop height)

CHAPTER 6. PHASE 2 EXPERIMENTS

6.1 Updated Spiral Design (Utilized in Phase 2 Piles)

In the pursuit of the overarching project goal, which is the integration of GFRP spiral design into prestressed concrete piles to enhance their corrosion resistance, test piles were constructed for the second phase of impact testing. These test piles adhered to the FDOT standard plan for 24" square CFRP prestressed concrete piles, which prescribes the use of 16 CFRP strands, each with a diameter of 0.6 in., and a single-strand configuration. This section primarily centers on the exploration of GFRP spiral sizes for the test piles, with reference to Table 6.1 for the pile nomenclature.

Table 6.1: Pile nomenclature (updated design)

Pile label	Strand type	Spiral type	Number of spiral turns at pile ends
PCG1	CFRP	#3 GFRP	7
PCG2	CFRP	#3 GFRP	11
PCG3	CFRP	#4 GFRP	7

6.2 Design Calculations, Specifications, and Construction Plans

6.2.1 Analytical Calculation

Phase 1 design, PSG1, has undergone experimental validation, as detailed in Chapter 4. Also, The FE analysis and model validation were covered in Chapter 5. The primary distinction between PSG1 and PCG1 lies in the prestressing strand, which does not affect the spiral design process when utilizing the analytical calculation.

The PCG2 design closely resembles PCG1, with the exception of having more spiral turns at the pile top and tip, driven by the observation that these regions encountered the highest stresses. Consequently, the analytical calculation mirrors the PCG1 design mentioned earlier.

In comparison, PCG3 mirrors PCG1 design with one key variation: it employs a #4 GFRP spiral instead of a #3 GFRP spiral. The rationale behind this design adjustment is to reduce strain in the spiral. As outlined in Section 5.1.3, the PSG1 spiral reached 54.5% of the design strain limit, a satisfactory result. However, it's worth noting that this figure was an average of measurements

from both the east and west sides of the sensors, with the east side reaching 86.3% of the limit. By switching to a #4 spiral, the strain was further reduced by 0.11/0.20, equating to a 55% reduction based on the quasi-static analytical equation.

In summary, the quasi-static analytical calculations indicate the adequacy of all designs, with PSG3 demonstrating lower strain (and stress) levels compared to PSG1 and PSG2. However, it is essential to subject all designs to further scrutiny through FE analysis due to the impact of dynamic loading and the intricate stress distribution that occurs during impact.

6.2.2 Finite Element Analysis

For FE aided design, only the highest drop height of 20 ft was needed. Nonetheless, in order to demonstrate the response of the three different designs, three drop heights were initially examined for each pile being simulated. Energy-equivalent velocities (V_{FE}) of 13.40 ft/s, 20.27 ft/s, and 29.01 ft/s were assigned to the impactor for the 10-ft, 15-ft, and 20-ft drop tests, respectively.

Moreover, since the FE analysis of the PSS phase 1 test results exhibited a close match to the experimental findings in terms of concrete stress (measured at 4 ft from pile top), as indicated in Figure 6.1 and Figure 6.2, PSS' (PSS with a 1.5 in. top cushion) was included in the simulation to enable a direct comparison with the PSG1 (phase 1) pile. The summary of the piles compared in the FE analysis is presented in Table 6.2.

The material models employed for concrete, GFRP spiral, and plywood cushion in the FE simulation of phase 1 test piles served as the basis for the design of phase 2 piles. The properties of the CFRP strands, a new addition, are summarized in Table 6.3. The prestressing force in the CFRP strands was established by directly specifying an initial stress assumed to be constant along the length of the strands. Subsequently, the stress in the strands, after prestress losses, was applied, inducing a compressive stress of 1.2 ksi in the pile.

Table 6.2: FE specimens for stress comparison

Pile specimen	Strand type	Spiral type	Top cushion thickness (in.)
PSS'	Steel	Steel	1.5
PSG1	Steel	GFRP	1.5
PCG1	CFRP	GFRP	1.5
PCG2	CFRP	GFRP	1.5

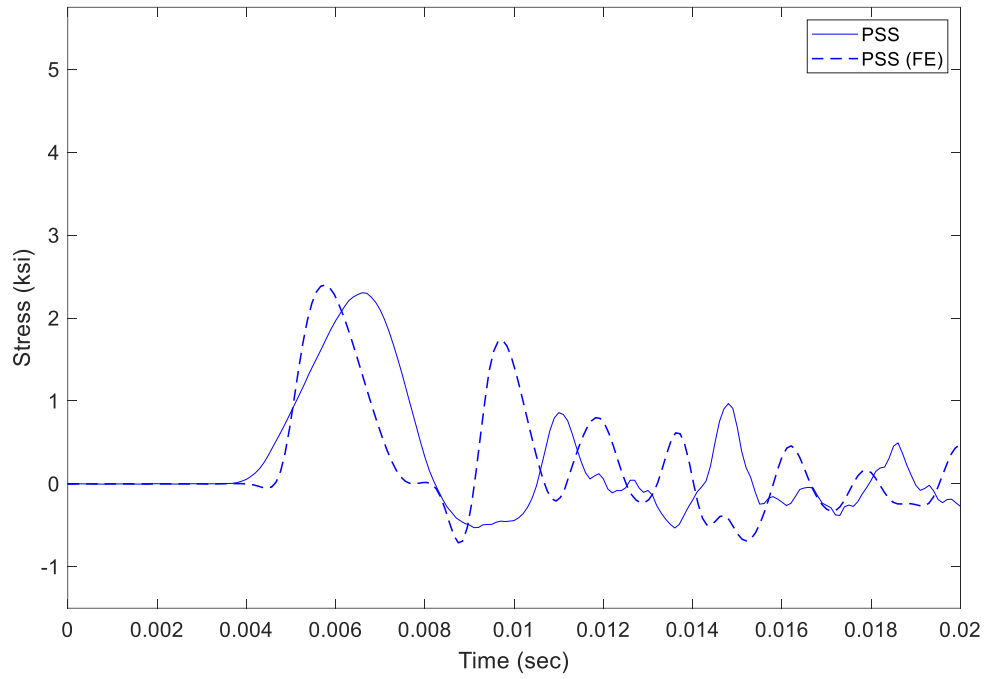


Figure 6.1: PSS-test vs. PSS -FE stress plot using 0.75 in. top plywood cushion (7-ft drop)

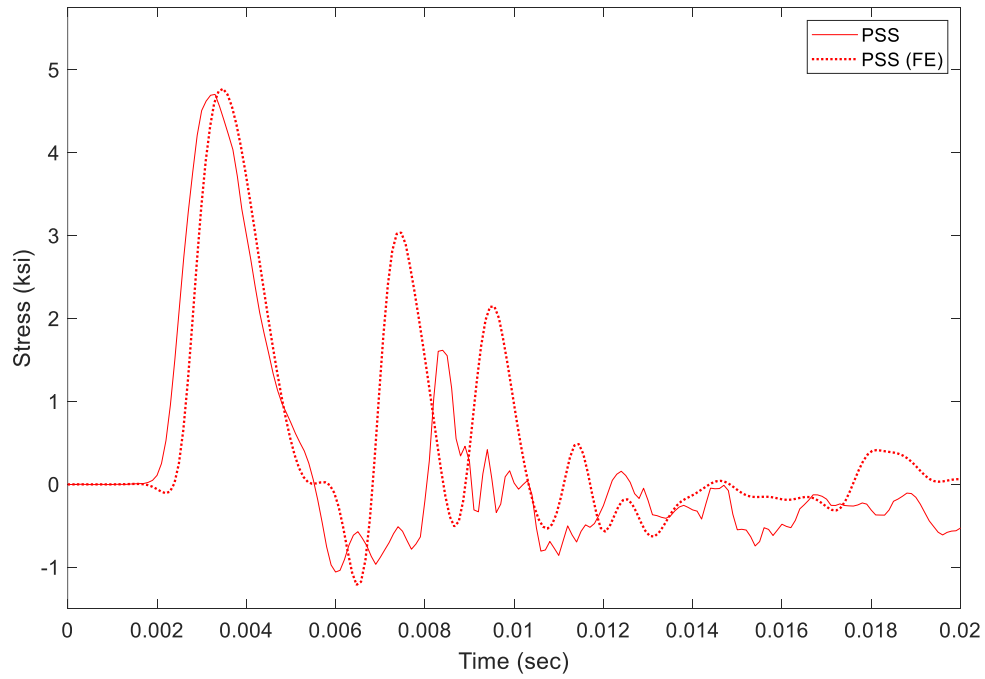


Figure 6.2: PSS-test vs. PSS -FE stress plot using 0.75 in. top plywood cushion (15-ft drop)

Table 6.3: Mechanical properties of CFRP strand

Reinforcement type	Area in. ²	ρ lbf s ² /in ⁴	$E_{CFRP-ps}$ ksi	$f_{u_{CFRP-ps}}$ ksi	ν
CFRP strands	0.179	1.87e-04	22,480	369	0.28

Figure 6.3 to Figure 6.7 depict the time history of stress for PSS', PSG1, PCG1, PCG2, and PCG3 subjected to 10-ft, 15-ft, and 20-ft drops, with measurements taken at 4 ft from the pile head. Maximum stress values were obtained by averaging the stress from both sides of the piles (east and west). The results, as shown in Figure 6.3 to Figure 6.7, revealed that the measured concrete stresses were within 99% of each other for the initial peak response. However, there were some variations in the stress propagation characteristics among these different designs.

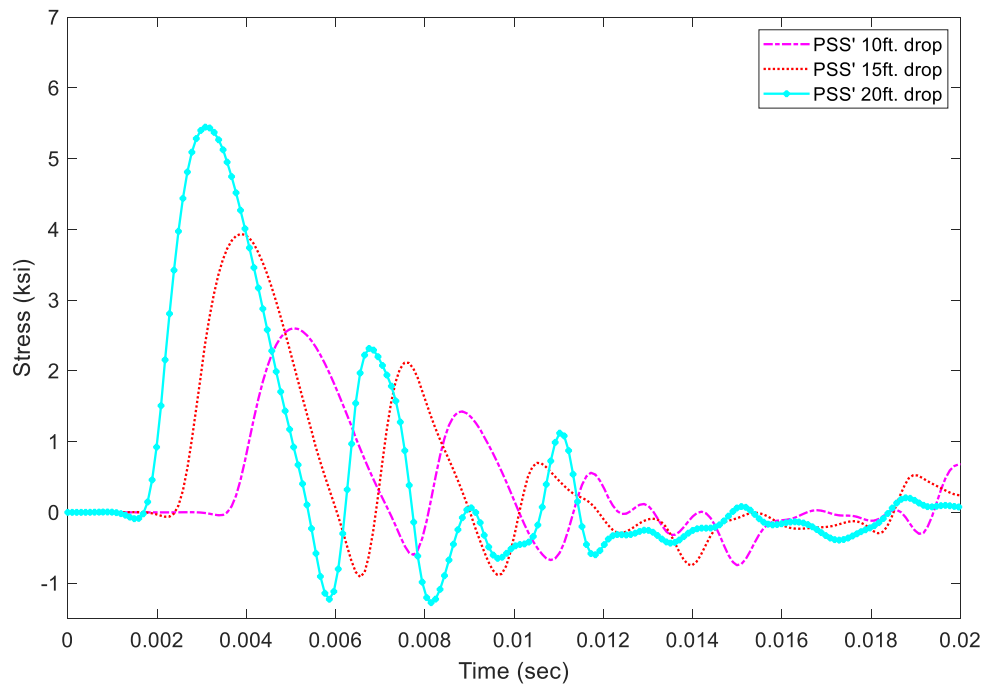


Figure 6.3: PSS' FE stress plot corrected for 1.5 in. top plywood cushion (concrete stress on the surface, 4 ft from the top)

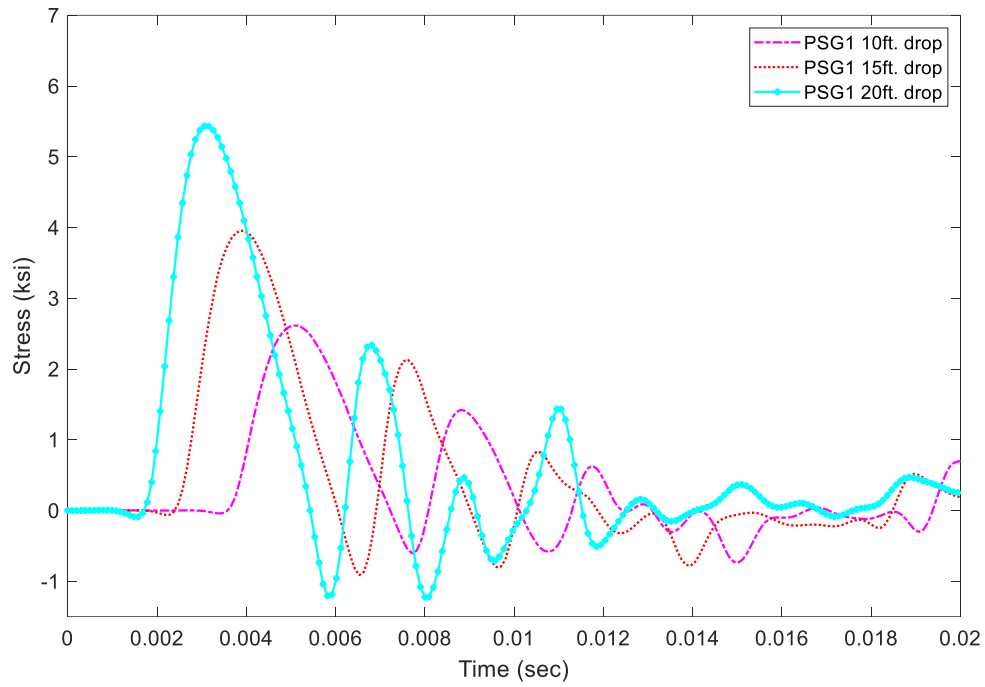


Figure 6.4: PSG1 FE stress plot (concrete stress on the surface, 4 ft from the top)

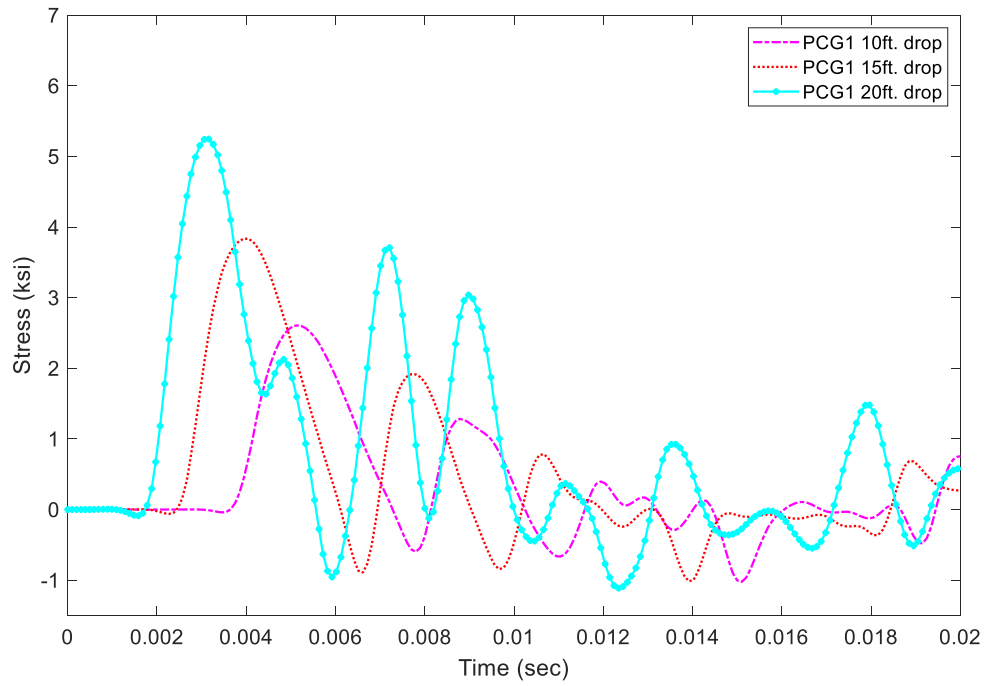


Figure 6.5: PCG1 FE stress plot (concrete stress on the surface, 4 ft from the top)

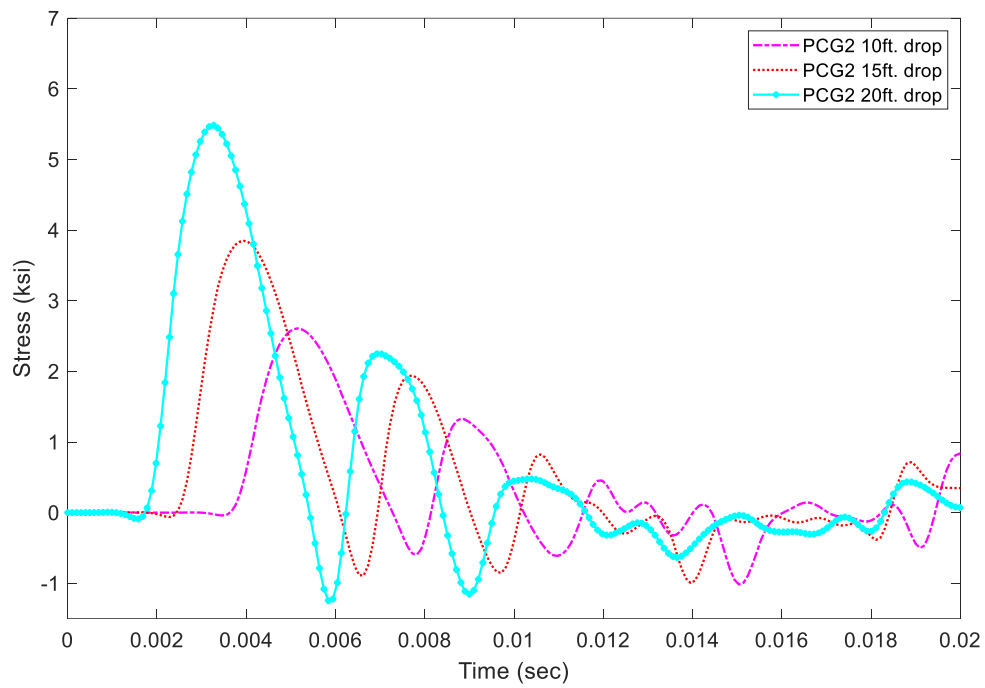


Figure 6.6: PCG2 FE stress plot (concrete stress on the surface, 4 ft from the top)

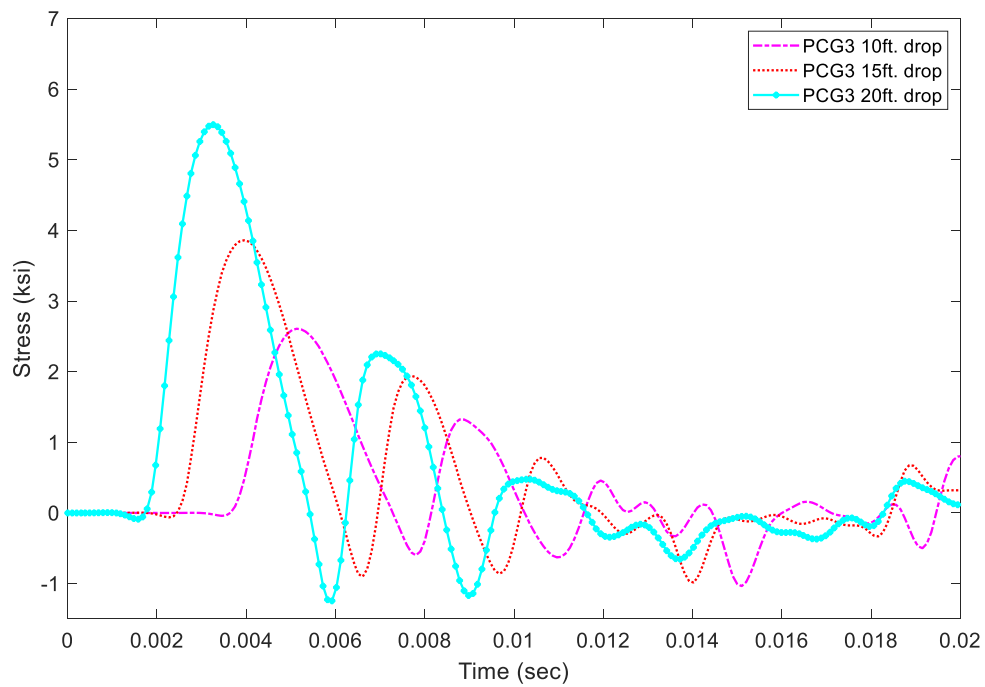


Figure 6.7: PCG3 FE stress plot (concrete stress on the surface, 4 ft from the top)

The stress immediately after the impact was greater at the pile head as shown in Figure 6.8. Compared to approximately 5.5 ksi measured 4 ft from the top, the pile top stress was approximately 9.5 ksi. The concrete surface stress for PCG2 and PCG3 was similar to that of PCG1, as observed from the contour plots. Although the stress response of PCG3 may provide benefits, a decision was made to choose PCG2, over PCG3, as one of the final candidates as the benefit of increasing the spiral area was limited.

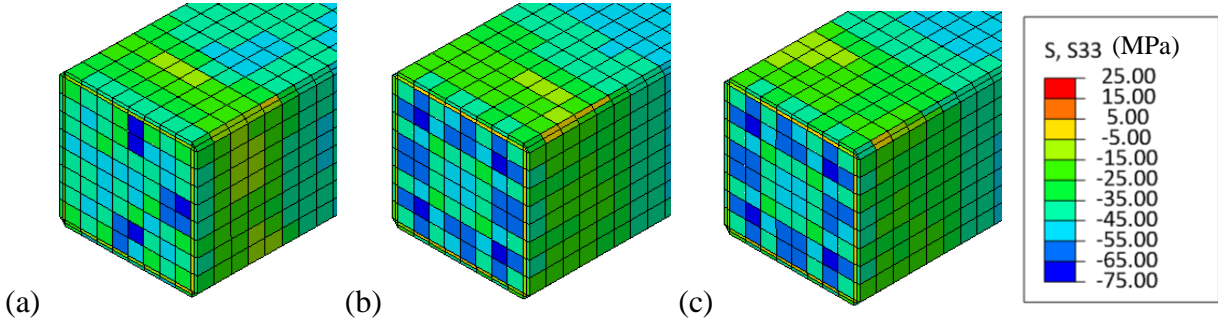


Figure 6.8: Pile head stress, 20-ft drop, $t = 0.003$ sec, (a) PCG1, (b) PCG2, (c) PCG3

Figure 6.9 shows the spiral strain for the final two designs (PCG1, PCG2), along with the design tested in phase 1 (PSG). The CFRP prestressing strand according to the FE model increased the strain magnitude, but still lower than the design limit of 0.006. Note that the strain amplification at the pile tip is with a completely fixed boundary condition that does not allow any movement — the real-world response even with hard surface have at least some movements, and therefore the spiral strain at the tip is expected to be lower than what is shown in the figure.

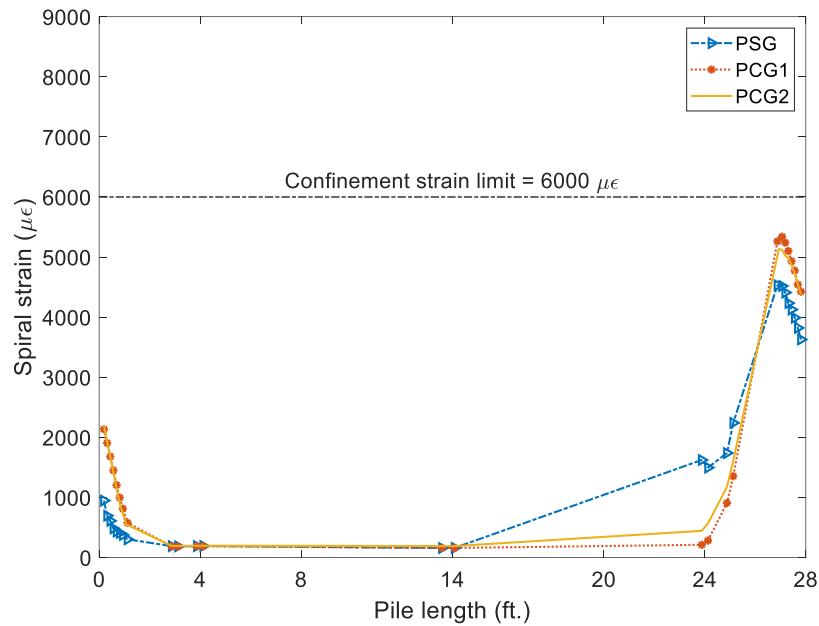


Figure 6.9: FE GFRP spiral strain comparison for PSG, PCG1 and PCG2 (20-ft drop height)

6.3 Construction of Test Piles (Phase 2)

To test how the GFRP spirals perform when utilized with CFRP strands as pile reinforcements, the second phase of this research (Phase 2) involved the fabrication of two 28-foot-long prestressed concrete piles with a cross-section of 24 in. × 24 in. at CDS Manufacturing Inc. in Gretna, Florida (See casting bed layout in Appendix G. These piles were reinforced with CFRP (or CFCC) cables running longitudinally and #3 GFRP spirals transversely. The construction of the Phase 2 piles commenced on May 15, 2023, with the preparation and instrumentation of the spirals and concluded on May 23, 2023, when the CFRP cables were cut, and the piles were demolded. Subsequently, the piles were transported to the FDOT H. Ansley Structures Research Center on May 24, 2023, in readiness for testing. This section provides details of the construction phase which began with internal instrumentation of the piles.

6.3.1 Specimen Description and Design Configuration (Phase2)

The prestressing strand pattern in the piles followed the FDOT standard plans for 24 in. CFRP square piles with sixteen 0.6 in. diameter CFRP 7-strand cables. However, the #3 GFRP spirals used followed the pitch and spacing shown in Figure 6.10 and Figure 6.11. These figures show

that spiral turns at the ends of PCG1 and PCG2 were 7 and 11, respectively. The cross-section of the piles and spiral bending details are shown in Figure 6.12.

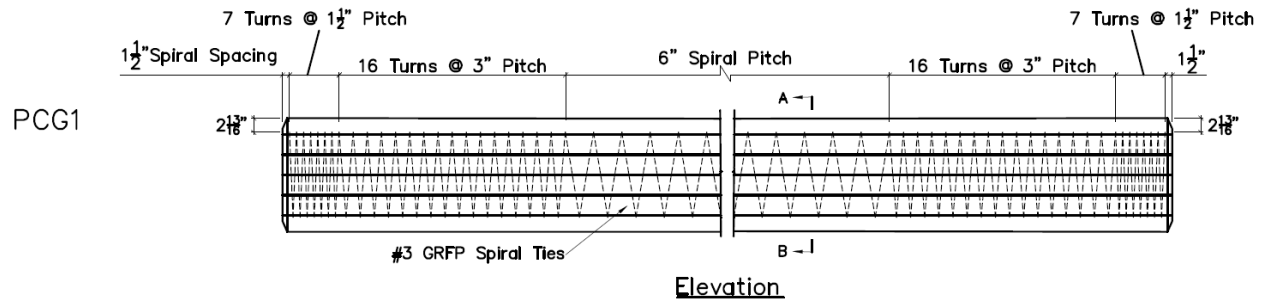


Figure 6.10: PCG1

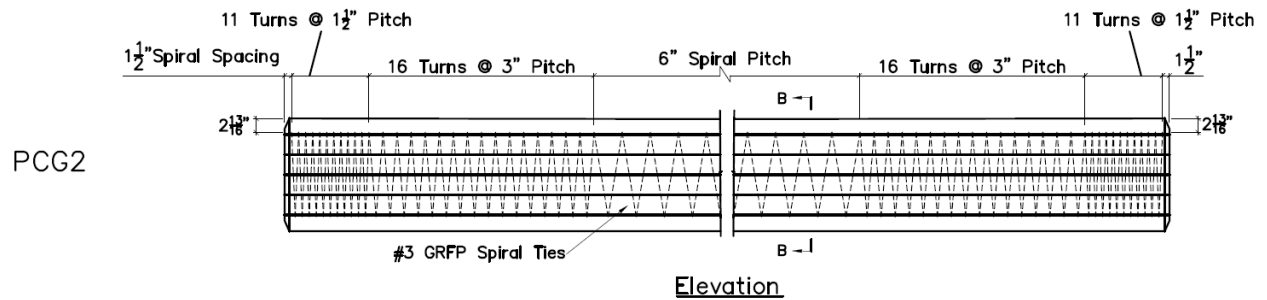


Figure 6.11: PCG2

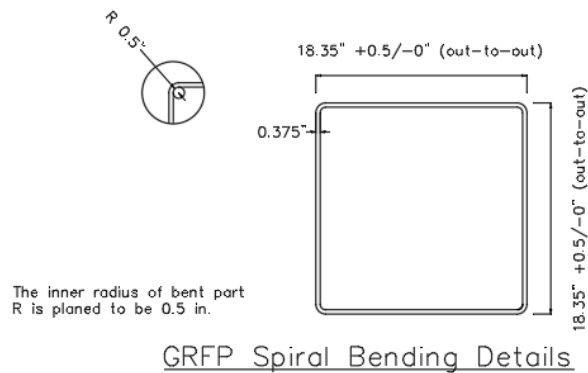
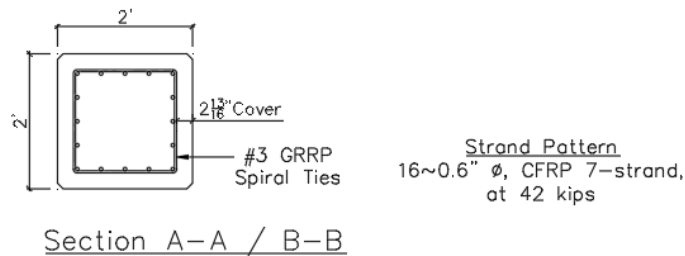


Figure 6.12: Pile cross-section and GFRP spiral bending details

The properties of the #3 GFRP rebar used as transverse reinforcement have been previously described. However, the 0.6-in. diameter CFRP 7-strand cables used for longitudinal prestressing have a nominal cross-sectional area of 0.179 in.², modulus of elasticity of 22,480 ksi, and an ultimate strength of 369 ksi. Class VI concrete with minimum compressive strength of 8500 psi was used in casting phase 2 piles.

6.3.2 Preparation and Instrumentation of Spirals (Phase 2)

GFRP spiral surfaces for strain gauge installation were prepared following the same procedure for phase 1 test piles as described in Section 4.5.1. Internal instrumentation of piles involved strain gauges installed on the spirals only, at specific locations. The strain gauges used were model KC-60-120-A1-11 L1M2R and model KFH-6-120-C1-11 L3M3R by KYOWA Electronic Instruments and Omega Engineering, Inc, for PCG1 and PCG2, respectively.

6.3.3 Strand and Spiral Installation

After tensioning all but one strand (strand 5B as described in Appendix F), it was observed that the GFRP spiral was tight along the last 1 ft of End 4 of PCG2 because the out-to-out spacing of the spiral was 18 in. at this location. This was below the 18.35 in. recommended in Figure 6.12. However, the issue was resolved by the application of some force in moving the spiral to the required location without pinching the CFRP cables. This shows that GFRP spiral manufacturers must follow the minimum spacing requirement along the entire length of the spiral.

6.3.4 Concrete Pouring

A class VI 8500 self-consolidating concrete mix was used. The self-consolidation nature of the concrete avoids the need for mechanical vibration. After pouring, the concrete surface was leveled and smoothed. Details of the concrete mix can be found in Appendix F.

6.4 Phase 2 Impact Testing Procedure

The testing procedure employed is similar to those described for phase 1 impact tests. However, impact load on phase 2 test piles was delivered by a 6000-lbm impactor at the following drop heights; 5 ft, 10 ft, 15 ft, 20 ft, and 25 ft. Also, pile cushion at the pile top had a thickness of 1.5 in. compared to 0.75-in.-thick cushion at the pile tip.

6.5 Impact Test Results for Phase 2 Test Piles

Impact test results reported in this section include the impactor velocity and acceleration, Pile Driving Analyzer (PDA) strain gauges and accelerometers measurements, spiral strain measurements, and a comparison between PDA measurements and electrical resistance strain gauges (ERSGs) installed on pile's concrete surface. To describe these results, the same orientation of the impact test setup described for phase 1 impact tests (Figure 4.12) was utilized for phase 2 impact tests.

6.5.1 Impactor Velocity and Acceleration (Phase 2)

Figure 6.13 shows the velocity of the impactor from the experiment compared to the theoretical calculation. As shown, the energy lost in the pendulum swing prior to contact between the impactor and the pile cushion was negligible.

Also, the impact velocity and peak impactor acceleration are summarized in Table 6.4. While impactor velocity was measured prior to impact, the peak acceleration of the impactor was obtained after contact between the impactor and the cushion/pile. Impactor acceleration on contact is influenced by pile cushion thickness and flushness of the concrete pile surface at the impact location. As shown in Table 6.4, impactor velocity and acceleration values for tests on PCG1 and PCG2 were comparable.

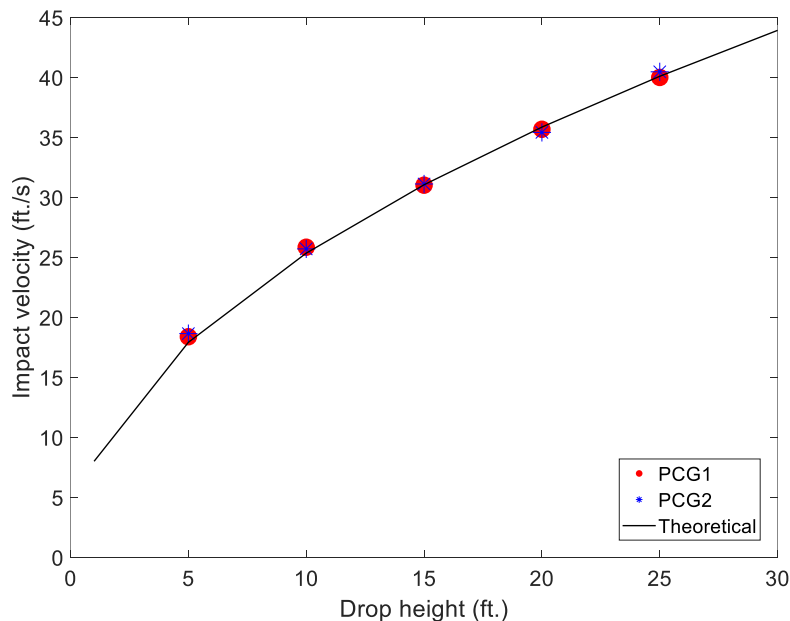


Figure 6.13: Impactor velocity

Table 6.4: Summary of impactor velocity and acceleration readings

Drop height (ft)	Impact velocity (ft/s)		Impactor acceleration ($\times 10^4$ ft/s ²)	
	PCG1	PCG2	PCG1	PCG2
5	18.42	18.66	-0.490	-0.496
10	25.86	25.72	-0.826	-0.844
15	31.03	31.13	-1.316	-1.351
20	35.69	35.43	-1.820	-1.830
25	40.01	40.48	-1.928	-1.927

6.5.2 Pile Driving Analyzer (PDA) measurements (Phase 2)

For the phase 2 impact tests, PDA instrumentation was installed on both sides of the tested piles, 4 ft from the top and tip of the piles. The observed responses from PDA strain gauges and PDA accelerometer for each pile are discussed in subsequent sections.

At each drop height during pile testing, concrete strain and particle acceleration measurements were recorded for PCG1 and PCG2. Figure 6.14 and Figure 6.15 illustrate the concrete strains resulting from pile impact at a 20-ft drop height for PCG1 and PCG2, while Figure 6.16 and Figure 6.17 show the responses due to pile impact from a 25-ft drop height for both piles. The impact response appeared predominantly symmetric, with similar strain measurements on both the east and west sides. However, in some cases, eccentricity led to differing strain responses across the pile's cross-section. To account for these eccentric cases, measurements from both sides of the test piles were averaged and reported. As a result, it can be observed that the maximum averaged strain (MEX) increased from $-1186 \mu\epsilon$ to $-1456 \mu\epsilon$ for PCG1 and from $-1116 \mu\epsilon$ to $-1403 \mu\epsilon$ for PCG2 between the 20-ft and 25-ft drop heights.

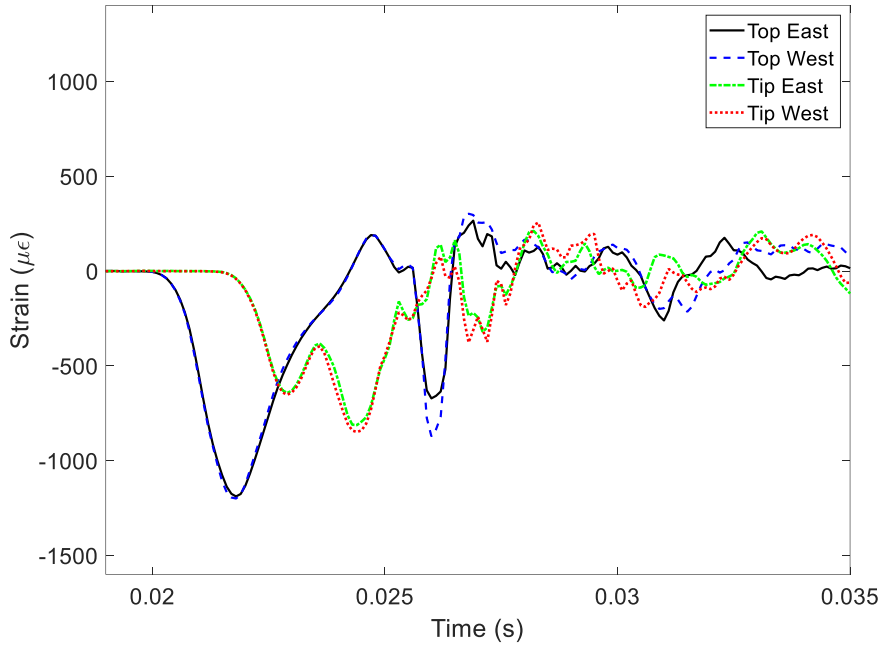


Figure 6.14: Top and tip concrete strains from PDA strain gauges at impact drop height of 20 ft (PCG1)

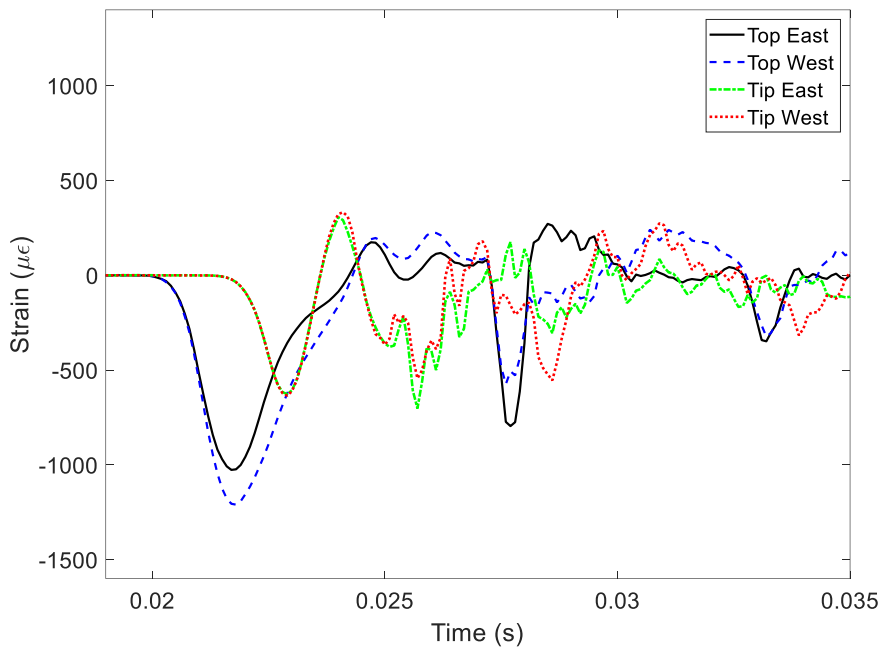


Figure 6.15: Top and tip concrete strains from PDA strain gauges at impact drop height of 20 ft (PCG2)

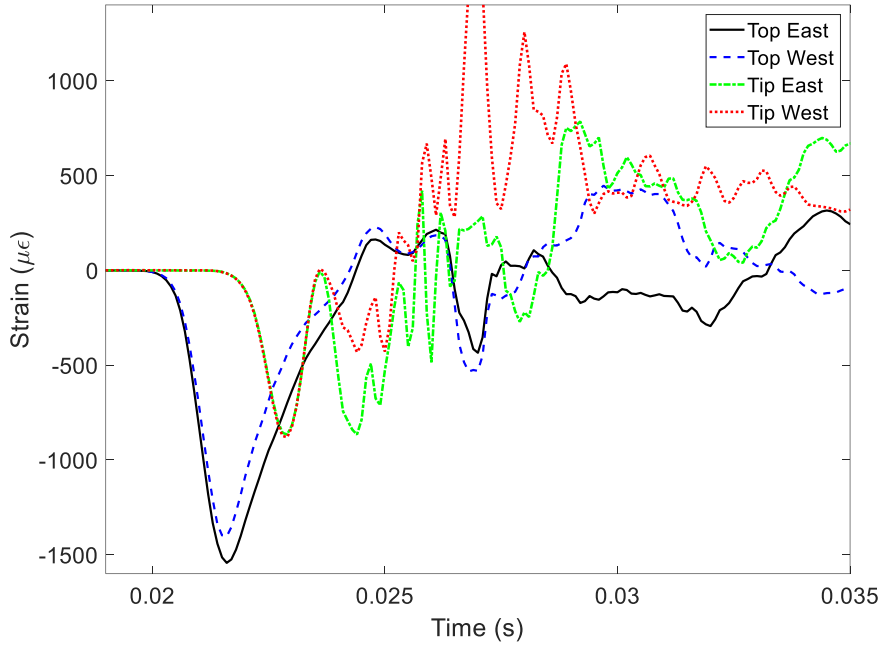


Figure 6.16: Top and tip concrete strains from PDA strain gauges at impact drop height of 25 ft (PCG1)

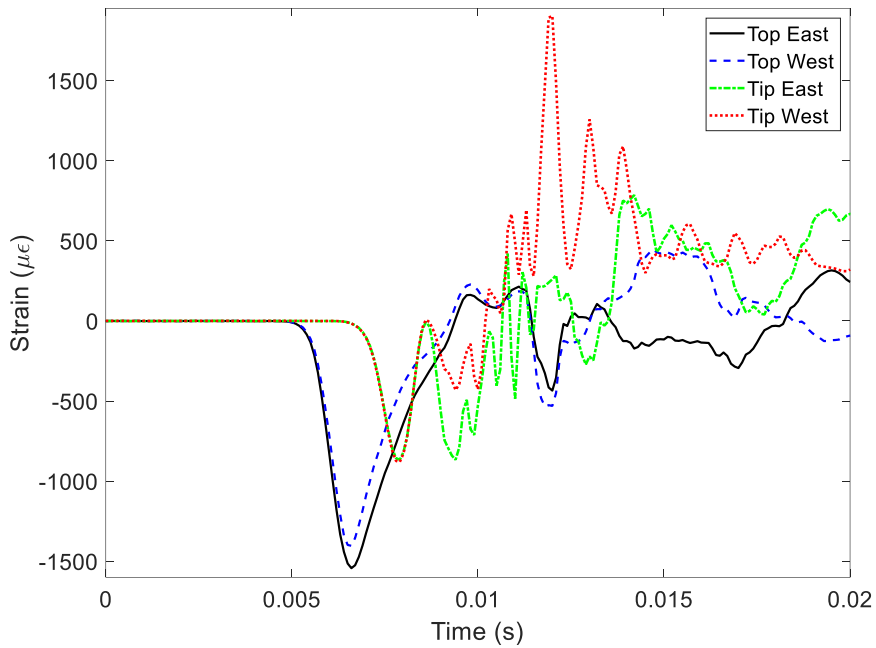


Figure 6.17: Top and tip concrete strains from PDA strain gauges at impact drop height of 25 ft (PCG2)

Similarly, Figure 6.18 and Figure 6.19 show particle acceleration due to pile impact from 20-ft drop height for PCG1 and PCG2, while Figure 6.20 and Figure 6.21 show the acceleration responses due to pile impact from 25-ft drop height for the piles. As shown, particle acceleration

was amplified at the tip compared to the pile top. Strain and acceleration results from the PDA for other drop heights at which PCG1 and PCG2 were tested can be found in Appendix H.

Measurements of strains and particle acceleration are useful in interpreting pile behavior due to impact loads from the impactor. Observed stresses or forces in the pile can be estimated from PDA acceleration and strain measurements. Based on the acceleration response, force (F_d) in the wave traveling down the pile was calculated as the product of the particle velocity (V) of the pile and pile impedance (Z) as shown in Equation (6.1).

$$F_d = ZV = \frac{EA}{c} V \tag{6.1}$$

where E is the pile’s elastic modulus, A is the pile’s cross-sectional area, and c is the wave speed along the pile.

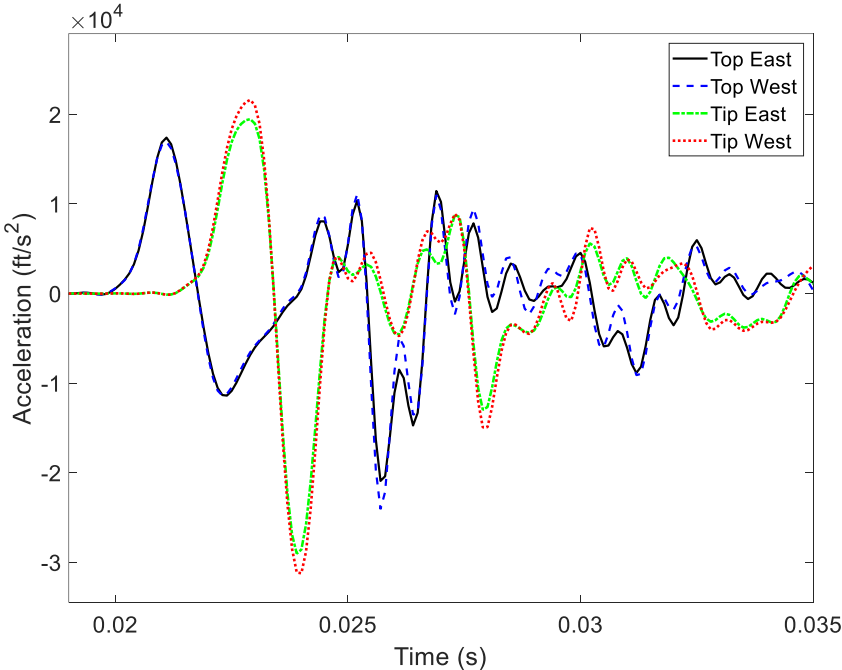


Figure 6.18: PDA measured acceleration at pile top and tip at a drop height of 20 ft (PCG1)

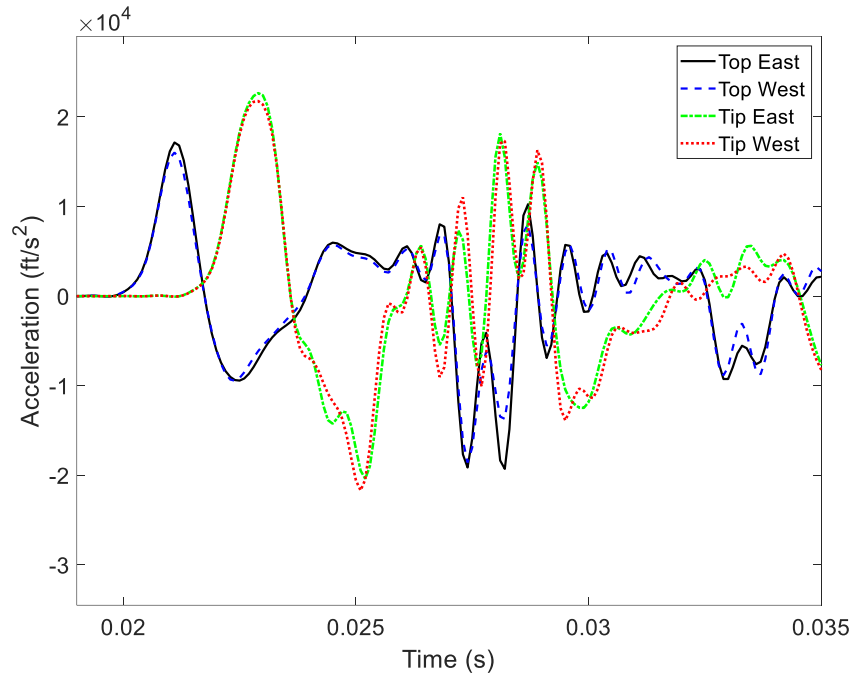


Figure 6.19: PDA measured acceleration at pile top and tip at a drop height of 20 ft (PCG2)

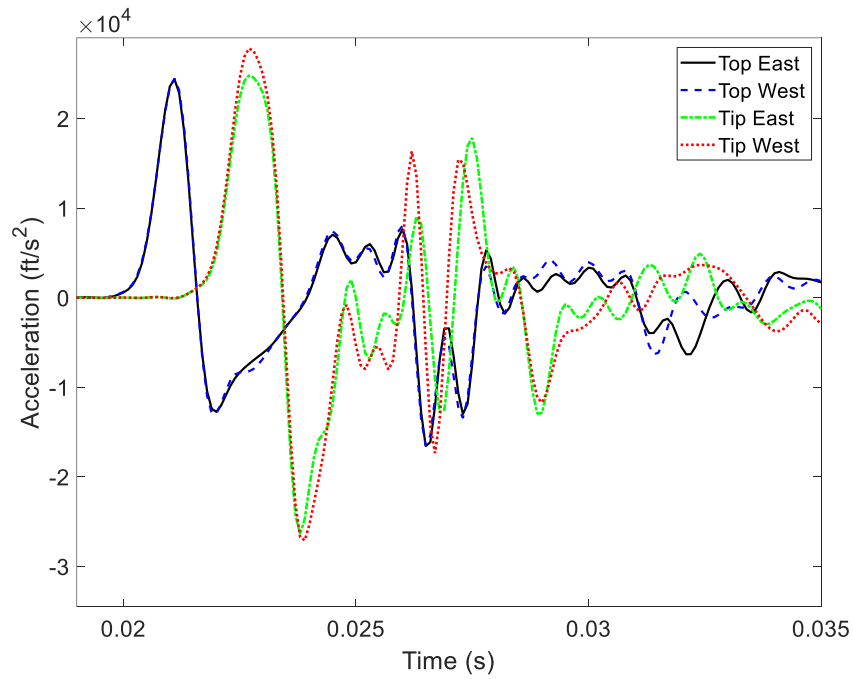


Figure 6.20: PDA measured acceleration at pile top and tip at a drop height of 25 ft (PCG1)

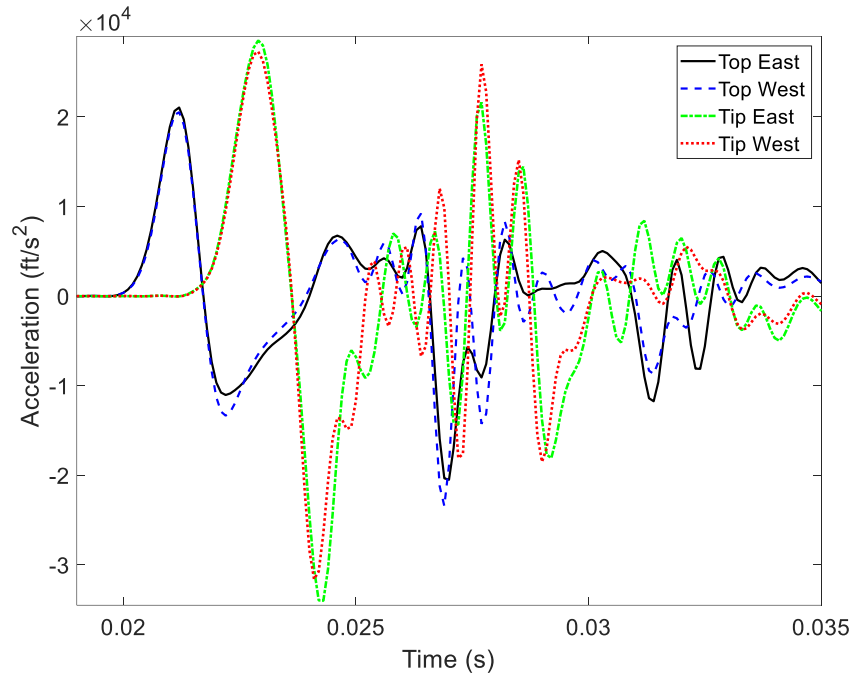


Figure 6.21: PDA measured acceleration at pile top and tip at a drop height of 25 ft (PCG2)

Furthermore, to calculate axial force, F , at a section along the pile length, axial strains, ϵ , and the pile's cross-sectional area, A , were multiplied by the pile's elastic modulus as shown in Equation (6.2). The elastic modulus of the pile was obtained from the concrete density (ρ) and the wave speed along the pile through Equation (6.3). For PCG1 and PCG2 the wave speed and resulting elastic modulus were 13700 ft/s and 6077 ksi, respectively.

$$F = \epsilon EA \quad (6.2)$$

$$E = c^2 \rho \quad (6.3)$$

Figure 6.22 and Figure 6.23 compares pile force graphs of PCG1 and PCG2 for 20-ft drop height impact, while Figure 6.24 and Figure 6.25 compares pile force graphs of PCG1 and PCG2 for 25-ft drop height impact. As shown, $Z * V$ plots capture wave reflection. See Appendix H for pile forces resulting from impacts from other test drop heights.

Another parameter estimated from PDA responses was the energy (E_t) transferred to the pile, calculated as shown in Equation (6.4). The energy transmitted through the pile is a function of the impedance (Z) of the pile. The greater the impedance of the pile the greater the energy transmitted through the pile (Guades et al., 2012). For the impact test conducted, the minimum value of

transferred energy recorded at the pile top ranged from 11 kip-ft at 5-ft drop height, to 112 kip-ft at 25-ft drop height, which corresponds to 37 % and 75 % of the initial impact energy from the impactor at the respective drop heights.

$$E_t(t) = \int_0^t F(t)V(t)dt \quad (6.4)$$

Peak strain, acceleration, stress, and maximum axial force (FMX) values from each drop height are summarized in Table 6.5 and Table 6.6 for PCG1 and PCG2. In Table 6.5 and Table 6.6, MEI is maximum compressive strain from individual gauges, CSI is the peak compressive stress from individual gauges, CSX is the peak averaged compressive stress based on the top two strain gauges, and TSX is the peak averaged tensile stress. MEI, CSI, CSX, TSX and FMX shown in Table 6.5 and Table 6.6 were values recorded at the top gauges. Also, the magnitude of TSX and its location along the pile length for PCG1 and PCG2 is as shown in Figure 6.26 and Figure 6.27 for impact from the 20-ft drop height, while Figure 6.28 and Figure 6.29 shows the magnitude of TSX and its location along the pile length for PCG1 and PCG2 for impact from the 25-ft drop height. For details of TSX resulting from other test drop heights at which PCG1 and PCG2 were tested see Appendix H. EMX shows the maximum energy recorded at the pile top. Using the impactor potential energy (equation 3.1), the percent energy transfer can easily be computed.

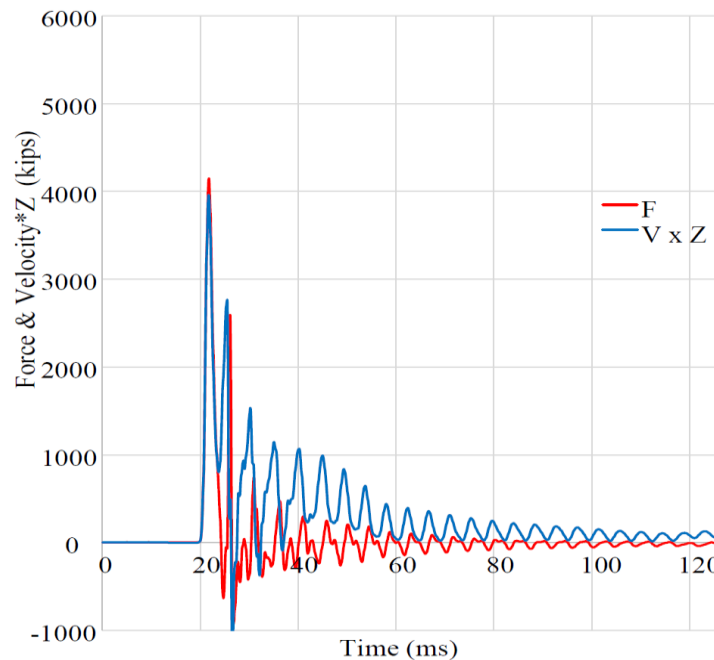


Figure 6.22: Pile force traces from PDA resulting from impact drop height of 20 ft (PCG1). (Compressive force is positive in this figure which was produced by Terracon)

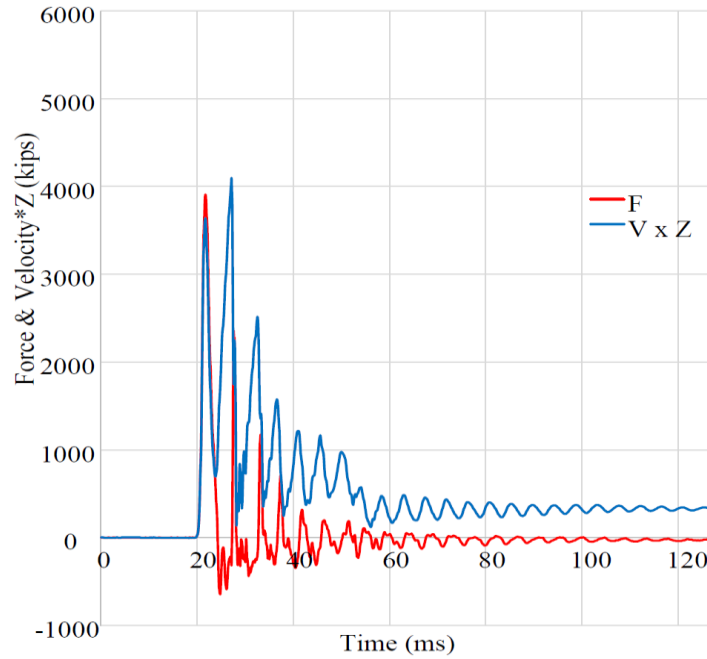


Figure 6.23: Pile force traces from PDA resulting from impact drop height of 20 ft (PCG2). (Compressive force is positive in this figure which was produced by Terracon)

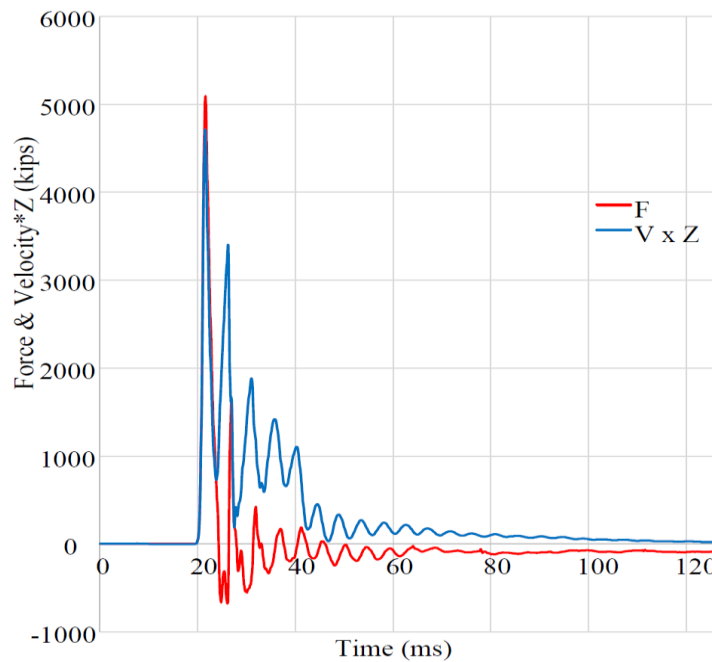


Figure 6.24: Pile force traces from PDA resulting from impact drop height of 25 ft (PCG1). (Compressive force is positive in this figure which was produced by Terracon)

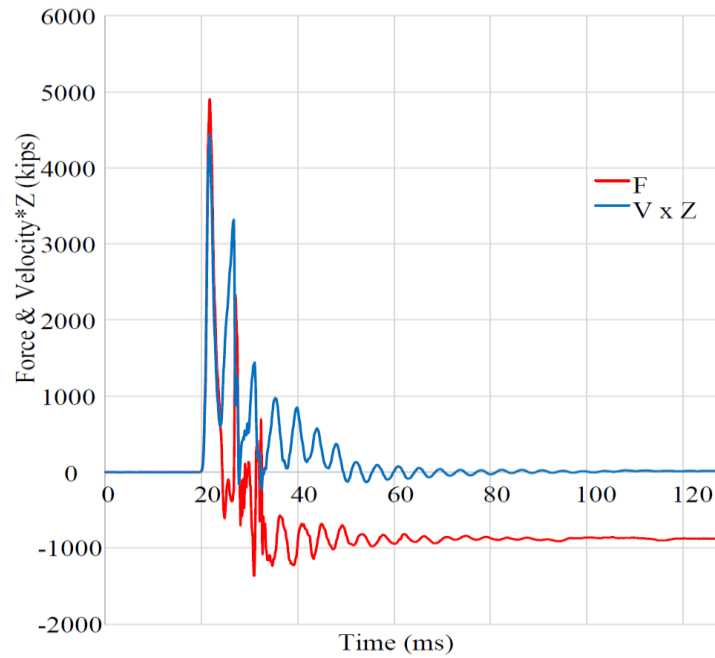


Figure 6.25: Pile force traces from PDA resulting from impact drop height of 25 ft (PCG2). (Compressive force is positive in this figure which was produced by Terracon)

Table 6.5: Acceleration, peak concrete strain and stress (PCG1)

Drop height (ft)	Peak top comp. strain ($\mu\epsilon$)	Particle acceleration ($\times 10^4$ ft/s ²)		CSI (ksi)	CSX (ksi)	TSX (ksi)	FMX (kips)	EMX (kip-ft)
		Top	Tip					
		5	-269					
10	-471	0.57	0.72	2.86	2.85	0.55	1641	26.44
15	-817	0.95	1.25	4.95	4.77	1.65	2745	48.47
20	-1200	1.74	2.16	7.24	7.20	3.21	4150	83.12
25	-1543	2.45	2.78	9.28	8.85	2.67	5096	111.47

Table 6.6: Acceleration, peak concrete strain and stress (PCG2)

Drop height (ft)	Peak top comp. strain ($\mu\epsilon$)	Particle acceleration ($\times 10^4$ ft/s ²)		CSI (ksi)	CSX (ksi)	TSX (ksi)	FMX (kips)	EMX (kip-ft)
		Top	Tip					
		5	-299					
10	-490	0.57	0.70	2.98	2.83	0.62	1629	24.02
15	-802	0.92	1.31	4.87	4.77	1.99	2750	44.66
20	-1210	1.72	2.27	7.35	6.78	3.06	3907	73.24
25	-1553	2.11	2.85	9.44	8.52	2.77	4909	101.20

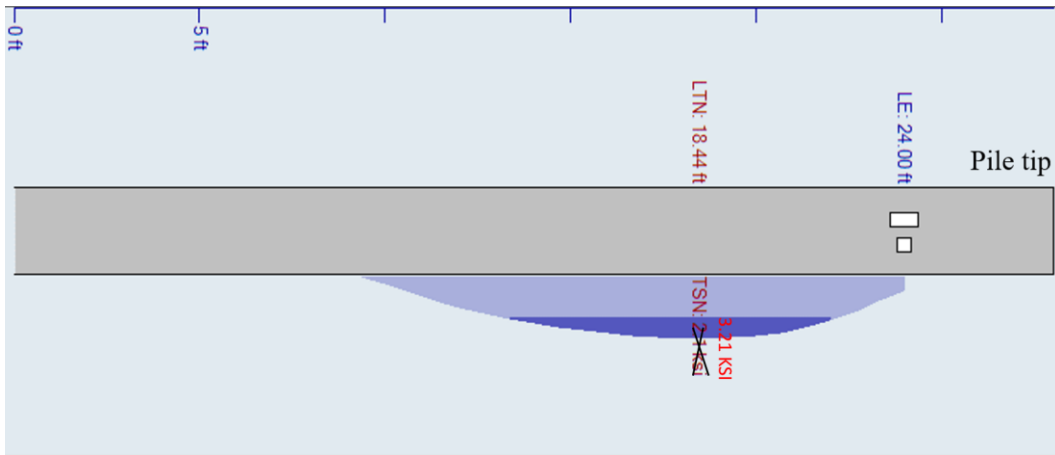


Figure 6.26: Peak tensile stress (TSX) resulting from impact drop height of 20 ft (PCG1) and its location along the pile. (This figure was produced by Terracon)

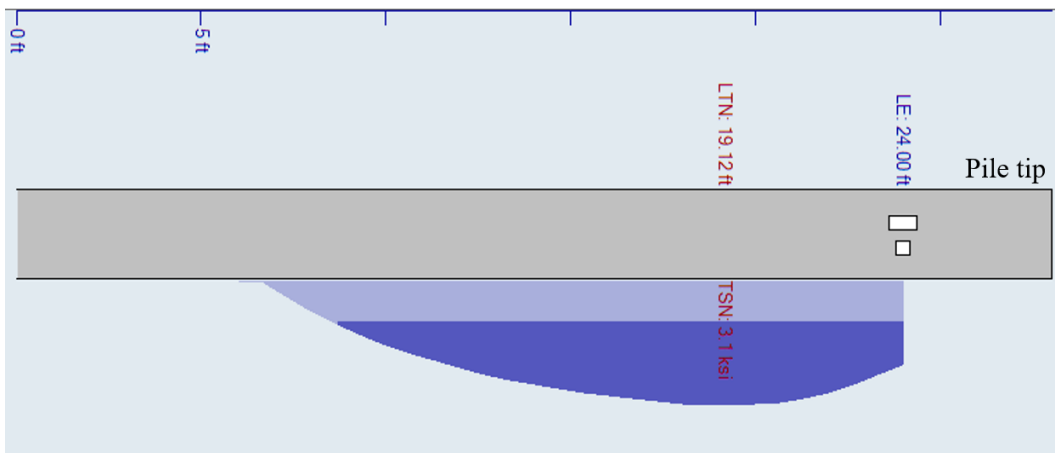


Figure 6.27: Peak tensile stress (TSX) resulting from impact drop height of 20 ft (PCG2) and its location along the pile. (This figure was produced by Terracon)

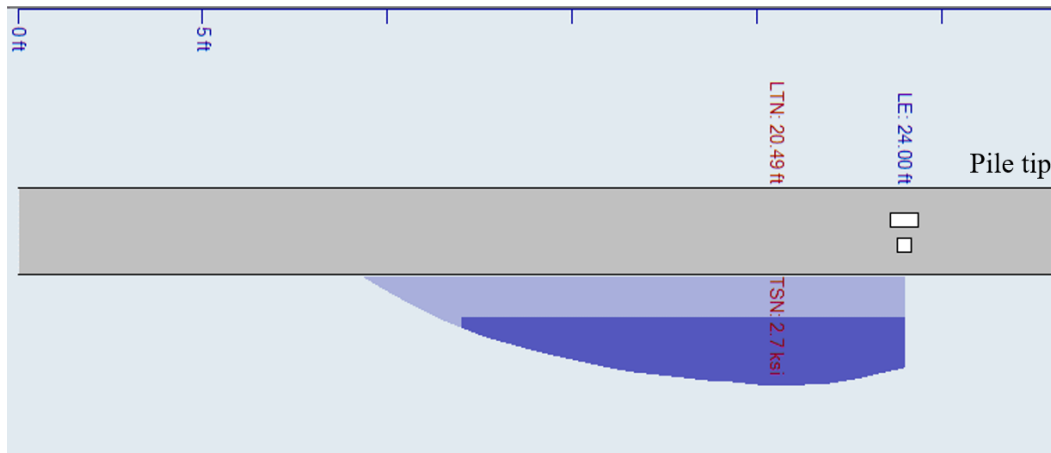


Figure 6.28: Peak tensile stress (TSX) resulting from impact drop height of 25 ft (PCG1) and its location along the pile. (This figure was produced by Terracon)

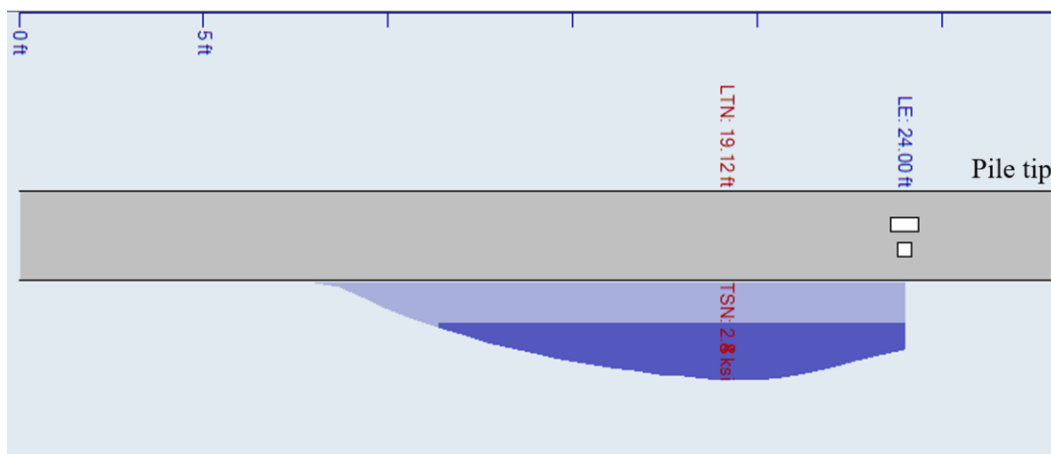


Figure 6.29: Peak tensile stress (TSX) resulting from impact drop height of 25 ft (PCG2) and its location along the pile. (This figure was produced by Terracon)

6.6 Spiral Strain Measurements

6.6.1 Spiral Strain Profile along Pile Length

Strain gauges were installed on the spirals to capture spiral responses during impact. The layouts of the spiral strain gauges installed inside test piles can be found in Appendix C. Spiral strains shown in Figure 6.30 and Figure 6.31 are from 15-ft drop height, Figure 6.32 and Figure 6.33 are from 20-ft drop height, while strains in Figure 6.34 and Figure 6.35 are those recorded due to the maximum drop height (25 ft). Spiral strains recorded from impact from other drop heights can be found in Appendix H. From these figures, it can be observed that the spiral strains are greater at the ends of the pile than towards the center of the pile due to higher stresses of the core of the pile

under impact at the top and tip. This implies that confinement at the ends of the pile play a significant role in preserving the integrity of the pile.

At the drop height of 15 ft, the peak averaged compressive stress (CSX) was at 4.77 ksi, about 5% below the design limit of 5.0 ksi. The spiral strains were all within the design strain limit, except one localized exceedance at the pile tip in the PCG2 pile. Except this one outlier, the spiral strains all met the design limit. At the drop height of 20 ft, the CSX exceeding 6 ksi, and at the drop height of 25 ft, peak compressive stress from individual gauges reach up to 9.44 ksi, the GFRP spirals in PCG1 and PCG2 began to exceed the confinement strain limit recommended by CSA-806 utilized in design. Phase 2 piles showed greater forces than specimens from phase 1 impact tests, which appeared to be due to the CFRP strands in phase 2. This invariably led to high stress transfer to spirals in PCG1 and PCG2. However, no spiral failure was observed after concrete failure in the piles.

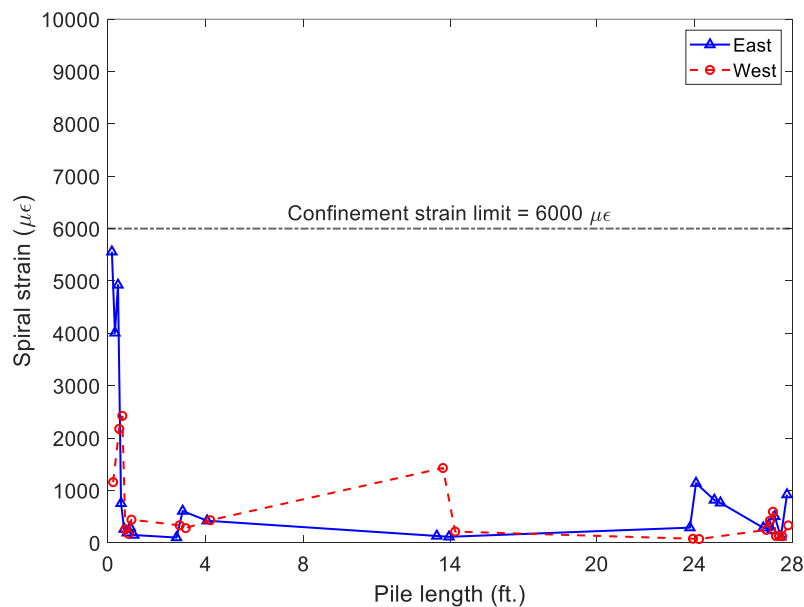


Figure 6.30: PCG1 spiral strain (15-ft drop height)

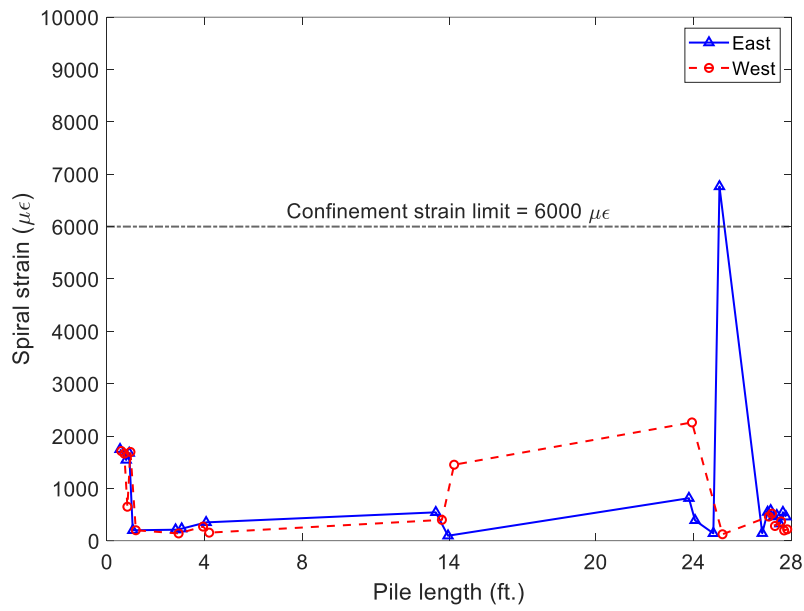


Figure 6.31: PCG2 spiral strain (15-ft drop height)

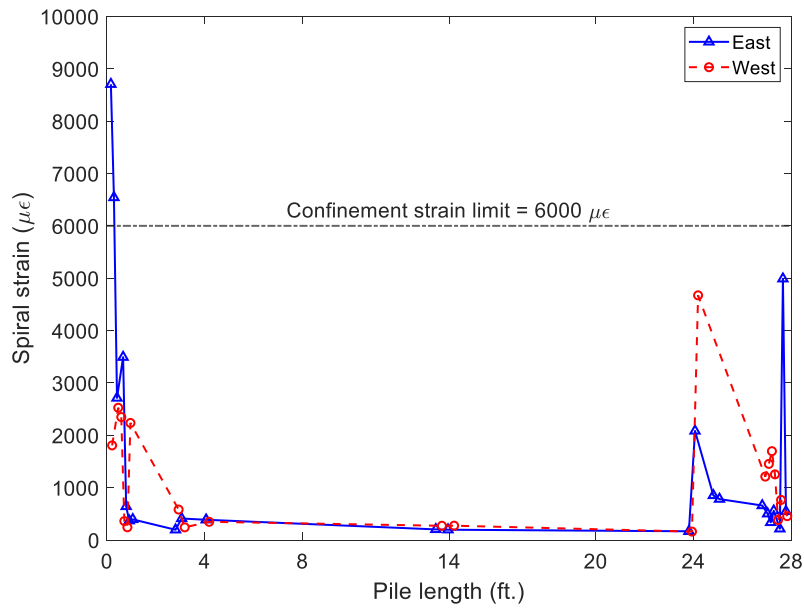


Figure 6.32: PCG1 spiral strain (20-ft drop height)

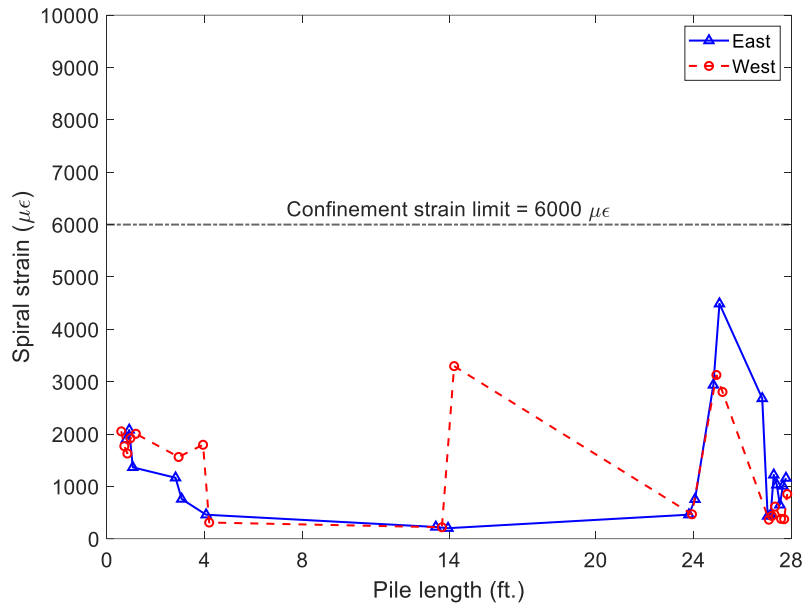


Figure 6.33: PCG2 spiral strain (20-ft drop height)

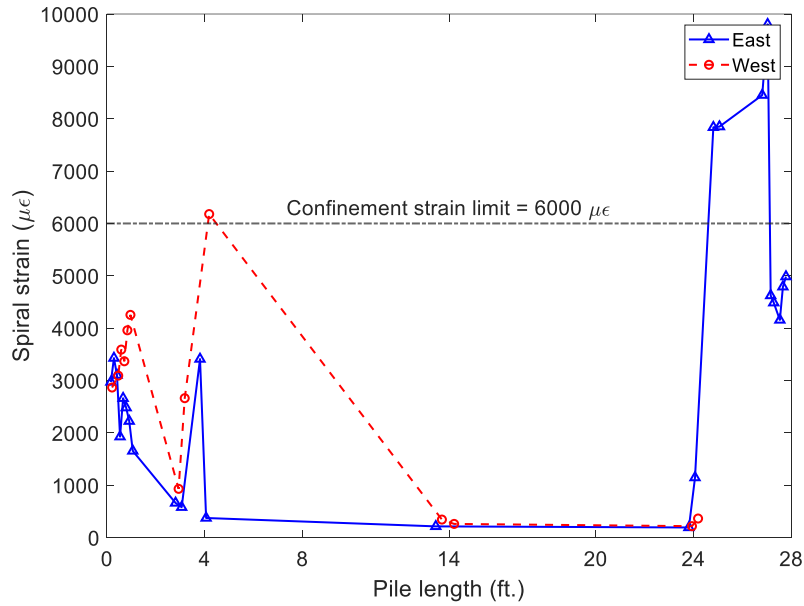


Figure 6.34: PCG1 spiral strain (25-ft drop height)

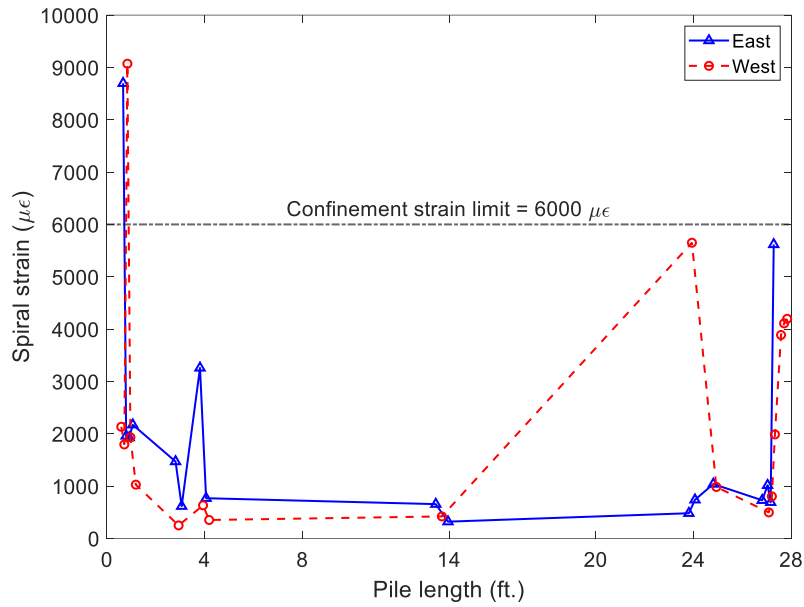


Figure 6.35: PCG2 spiral strain (25-ft drop height)

6.6.2 Maximum Spiral Strain vs. Drop Height

A plot of the maximum spiral tensile strains recorded anywhere along PCG1 and PCG2 as the test drop height increased is shown in Figure 6.36, showing a linear trend. Maximum tensile spiral strains were typically observed along either the region between the pile top and 1 ft from the pile top or the region between the pile tip and 3ft from the pile tip.

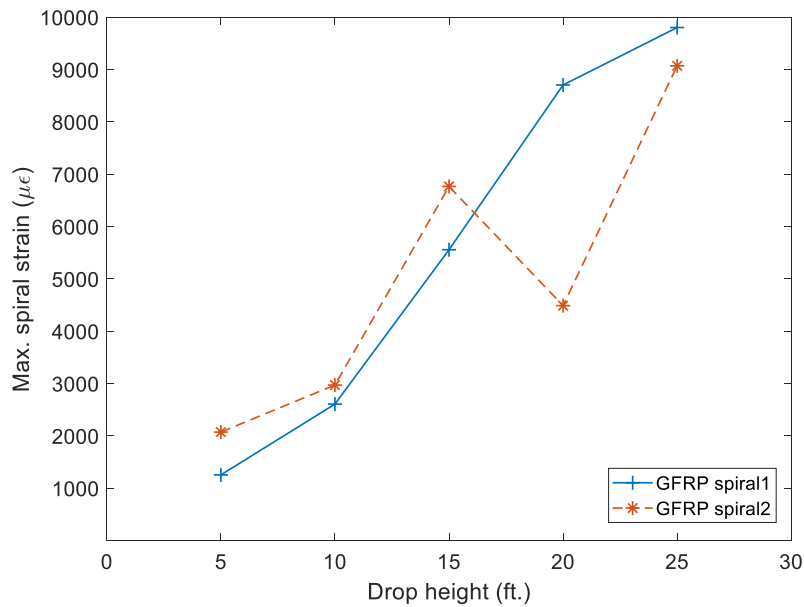


Figure 6.36: Maximum spiral tensile strain vs. drop height (PCG1 and PCG2)

6.6.3 A Stepped Simplification of Spiral Behavior Relative to the Spiral Spacing

A stepped simplification of spiral behavior relative to the spiral spacing is shown in Figure 6.37 and Figure 6.38 for PCG1 and PCG2, respectively. Refer to Section 6.3.1 for spiral spacing. In Figure 6.37 and Figure 6.38, spiral tensile strains on both sides of the pile were averaged for specific regions along the pile length e. g. 0 to 2 ft, 2 ft to 3 ft, pile center etc. The figures show the trend of spiral responses under impact. It should be noted that the constant strain region between 4 ft and 24 ft along the length of the piles as shown in Figure 6.37 and Figure 6.38 is only representative of the average strain recorded at the center of the piles. From the figures, higher strains were recorded close to the top and tip of the piles as impact drop height went up. Also, gauges near the tip PCG2 notably failed due to high impact force from the 25-ft drop height and were therefore excluded from the results.

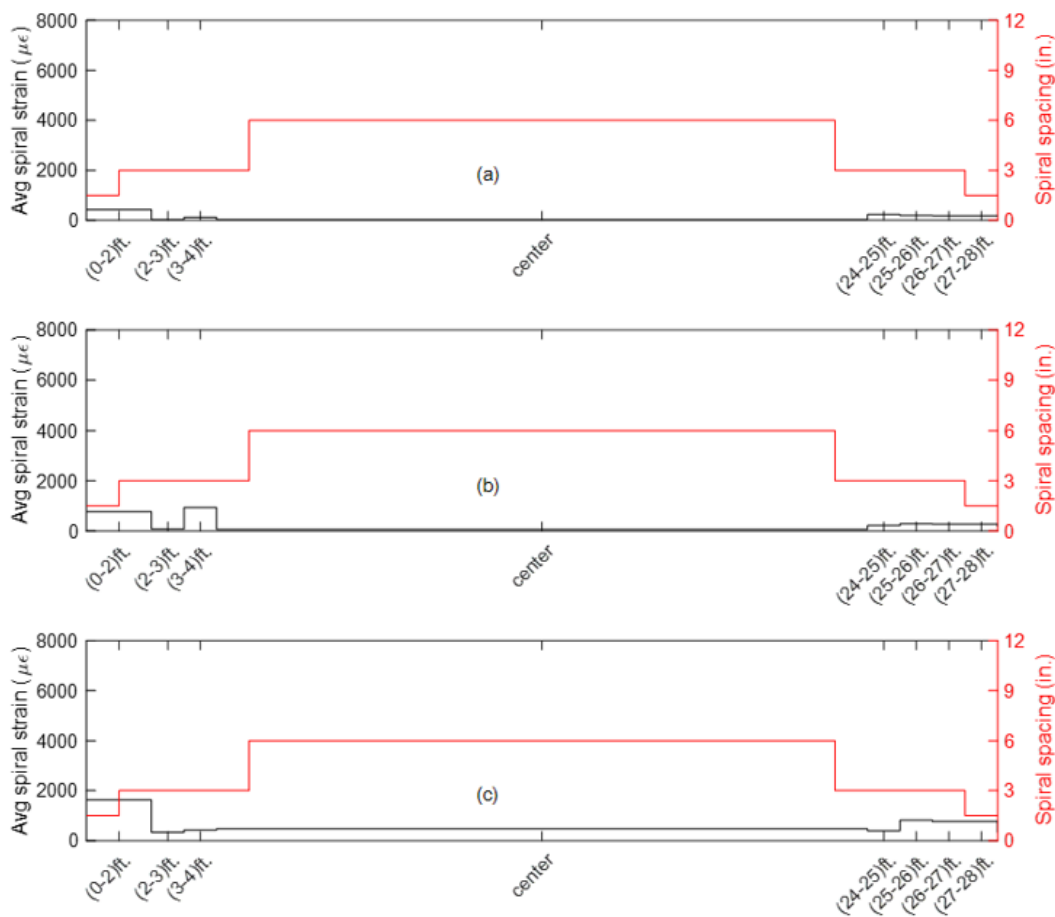


Figure 6.37: Average strains along pile (PCG1) length resulting from impact from (a) 5-ft (b) 10-ft (c) 15-ft (d) 20-ft, and (e) 25-ft drop heights

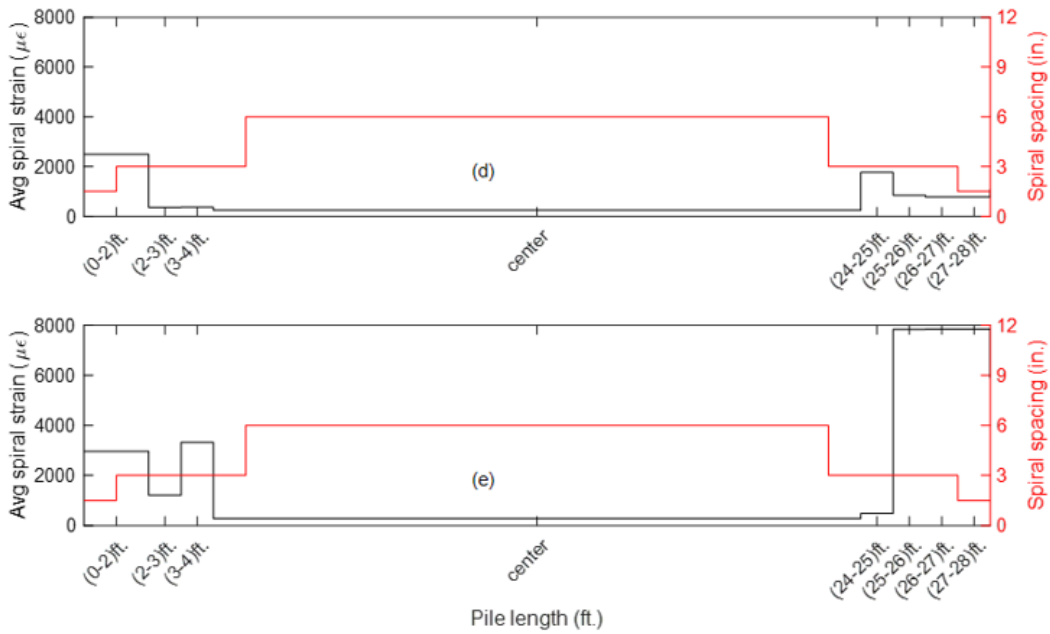


Figure 6.37: Average strains along pile (PCG1) length resulting from impact from (a) 5-ft (b) 10-ft (c) 15-ft (d) 20-ft, and (e) 25-ft drop heights – continued

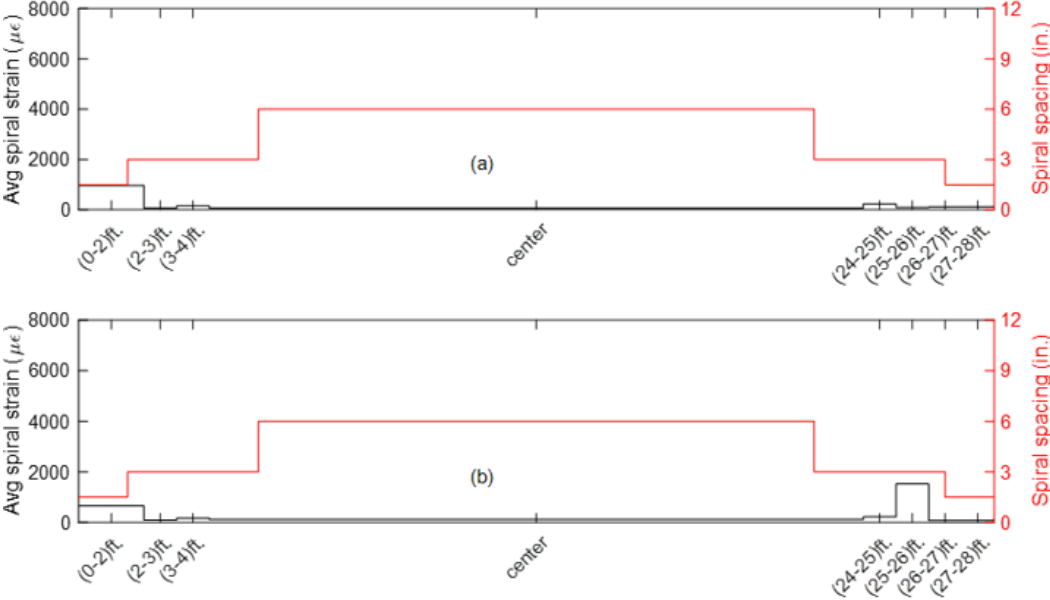


Figure 6.38: Average strains along pile (PCG2) length resulting from impact from (a) 5-ft (b) 10-ft (c) 15-ft (d) 20-ft, and (e) 25-ft drop heights

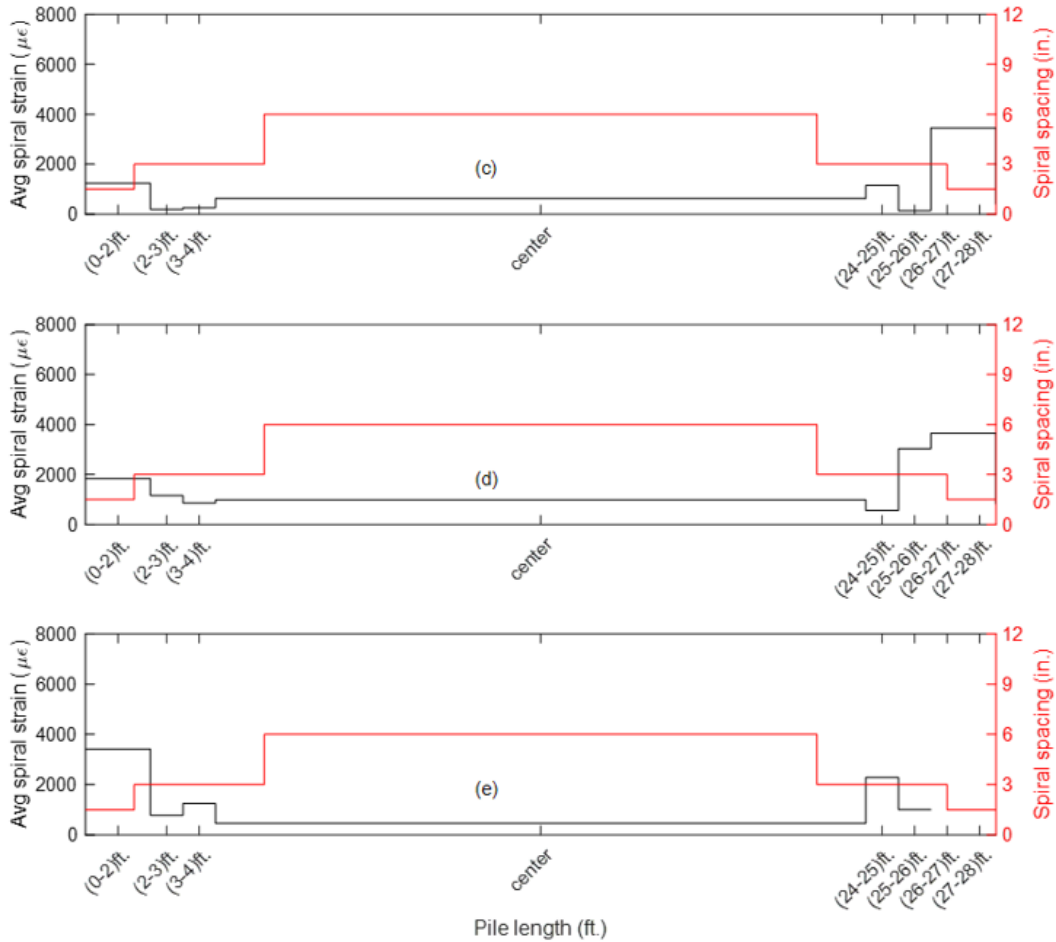


Figure 6.38: Average strains along pile (PCG2) length resulting from impact from (a) 5-ft (b) 10-ft (c) 15-ft (d) 20-ft, and (e) 25-ft drop heights – continued

6.7 Failure of Pile under Impact

After failure was achieved for both piles (PCG1 and PCG2), crack propagations on the concrete surface were marked. The types of failure observed (Figure 6.39 to Figure 6.43) are discussed as follows:

- **Concrete spalling**, evidenced by local damage and loss of concrete cover at the pile top or tip. This led to spiral and strand exposure as shown Figure 6.39 and Figure 6.40.
- **Tensile crack**, evidenced by multiple transverse cracks along the length of the piles (see Figure 6.41 and Figure 6.42). This was due to high tensile stress wave traveling along the piles because of pile rebound after impact. Initial tensile cracks were observed after 20 ft drop test for PCG1, while PCG2, initial tensile crack propagation was observed after the 15-ft drop test.

- **Horizontal cracks** were also observed indicative of eccentric impact, especially from the 20-ft and 25-ft drop tests on PCG2 as shown in Figure 6.42.
- **Bond slippage of CFRP strands** were observed and measured at both ends of the piles tested. The maximum bond slippage for PCG1 was 0.82 in., while for PCG2 bond slippage summed up from both ends of the pile was 0.88 in.

In prestressed concrete members, the bond between pretensioned strands and the surrounding concrete is a result of factors such as adhesion, mechanical interlock, and the friction and 'wedge-action' caused by the radial expansion of the strand following release (commonly referred to as the Hoyer effect). As depicted in Figure 6.43, when significant cracks form along the prestressing strand, the surrounding concrete expands. Consequently, the prestressing strands lose a portion of their initial radial expansion, which leads to bond slippage.

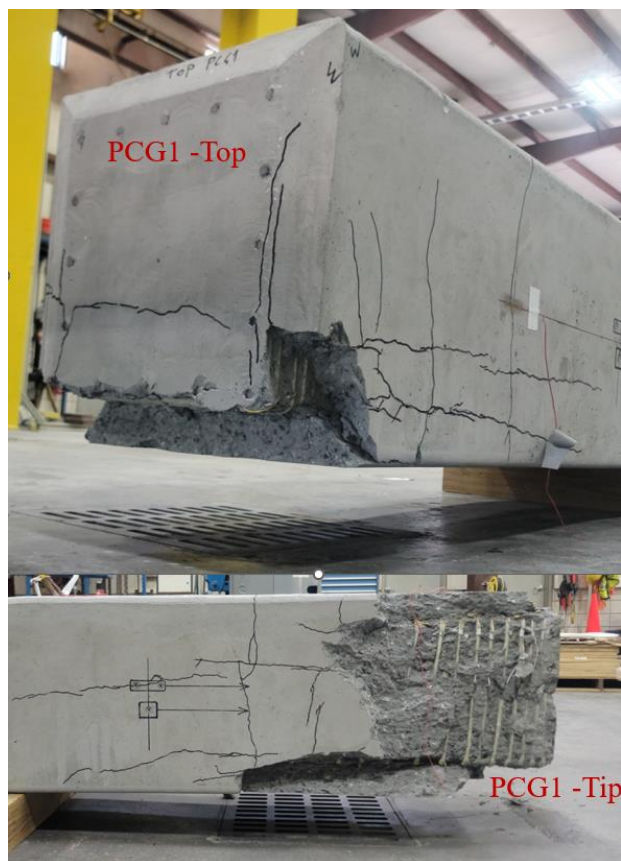


Figure 6.39: Failure at top and tip after final impact for PCG1

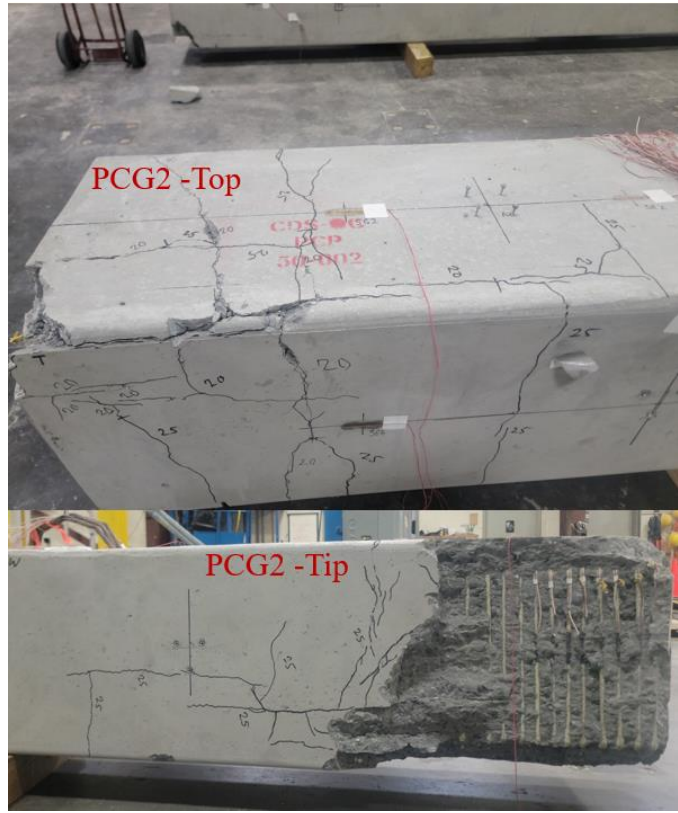


Figure 6.40: Failure at top and tip after final impact for PCG2



Figure 6.41: Crack pattern after final impact for PCG1



Figure 6.42: Crack pattern after final impact for PCG2

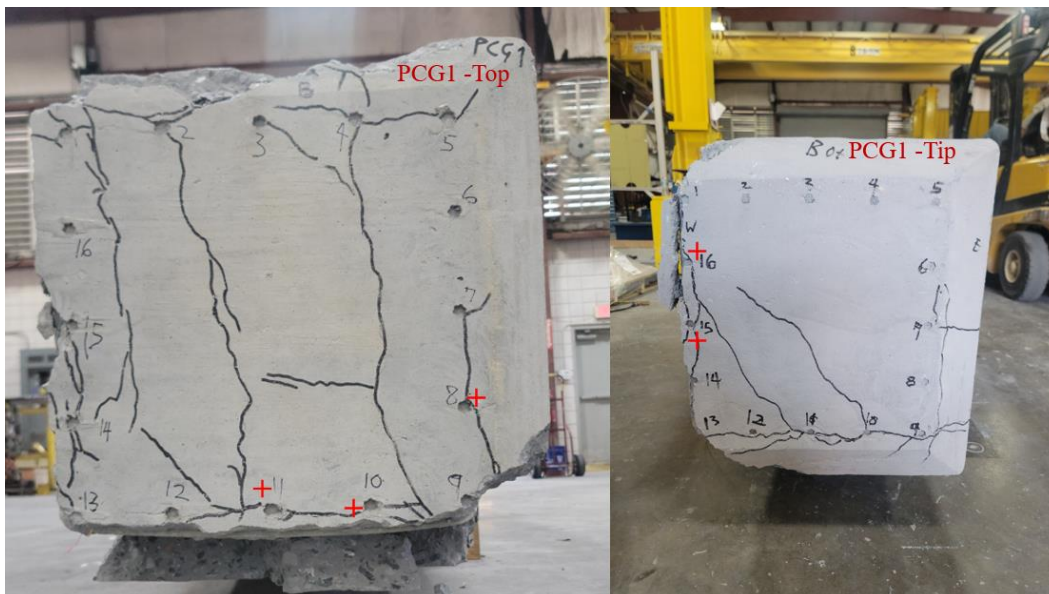


Figure 6.43: Bond slippage (PCG1)

CHAPTER 7. SUMMARY, DISCUSSION, and RECOMENDATIONS

7.1 Summary

This study investigated the response of piles with GFRP spirals to impact and flexural loading conditions. To meet research objectives, firstly, an impactor and test setup that simulate pile driving impact load was developed. Then the behavior of piles with glass fiber reinforced polymer (GFRP) spirals was investigated through two distinct phases.

Phase 1 involved a series of impact, flexural tests, and pile cutting tests, wherein GFRP spirals were utilized in conjunction with steel strands to reinforce two of the test piles. Also, a control specimen was also constructed using steel strands and steel spirals, adhering to the FDOT's standard specifications for a 24-inch square prestressed concrete pile. Additionally, one pile with CFRP strands and spirals, sourced from a prior project (Roddenberry et al., 2014) was also to be tested.

In contrast, Phase 2 focused exclusively on impact tests, evaluating the performance of two corrosion-resistant piles reinforced with GFRP spirals in combination with CFRP or CFCC prestressing strands.

All test piles for both phases of this project were 28 feet in length and had a cross-sectional dimension of 24 inches by 24 inches.

7.2 Discussion from Impact Test

The impact tests described utilized a pile top cushion of 0.75 in. for PSS and a 1.5 in. top cushion for the other test piles discussed in this research. The thinner cushion for PSS evidently restricted compression stress development compared to other test piles. Specifically, for PSS, the maximum compression at failure was 4.67 ksi, while the maximum compression at failure for other test piles exceeded 5 ksi, with over 8 ksi recorded for PCG1 and PCG2. Therefore, based on the measured concrete compressive strength, the stresses in the piles did reach or exceed the limit recommended by FDOT equations (which is 5.2 ksi, assuming a nominal 8500-psi concrete strength and 1000 psi for initial prestress). Additionally, the theoretical tension stress limit of 1.65 ksi was exceeded based on measured concrete tension stress from the PDA gauges.

Regarding the observed failure pattern under impact, phase 1 and phase 2 test piles exhibited similarities, with the exception of bond slippage observed in the phase 2 piles with CFRP strands. The summation of this slippage at both ends of the piles was less than 1 in. This slippage resulted from major cracks along the strands of phase 2 piles, a phenomenon not observed in phase 1 piles after failure.

Based on the impact test on phase two piles, PCG1 and PCG2 showed very similar compression stress and tension stress measurements. Therefore, the extra end-spiral turns for PCG2 provided no significant advantage under the reported test conditions. Consequently, the spiral pattern for PCG1 proved to be sufficient.

7.3 Recommendations for Different Pile Sizes

7.3.1 Introduction

The method employed to ascertain the size of GFRP spirals for 14", 18", 24", and 30" square concrete piles involved selecting a GFRP spiral size that offers equivalent tensile performance to the conventional steel spirals that have been successfully utilized in piles throughout the years.

Furthermore, to facilitate discussion and ensure the consistency of the aforementioned method, it was also utilized to determine the spiral sizes for stainless steel (SS) and CFRP spirals. Subsequently, the obtained sizes were compared to the specifications outlined in FDOT Index 455-114 through 455-130.

7.3.2 Selection of GFRP Spiral Size

The initial step involved calculating the tensile capacity of the conventional steel spirals by multiplying their yield stress with the cross-sectional area. The properties of the steel spiral specified for a 14", 18", and 24" square prestressed concrete pile are as follows: the area of the steel spiral (A_s) is 0.034 in.², the tensile stress (f_u) is 80 ksi, and the yield stress (f_y) is 70 ksi (as per ASTM A1064-18a). Hence, the tensile capacity of the steel spiral is determined as:

$$F_{\text{steel,w3.4}} = A_s f_{yh}$$

$$F_{\text{steel,w3.4}} = 70 \text{ ksi} (0.034 \text{ in.}^2) = 2.38 \text{ kips}$$

Similarly, for a 30" square prestressed concrete pile with $A_s = 0.04 \text{ in.}^2$, the tensile capacity is calculated as:

$$F_{\text{steel,w4.0}} = 2.8 \text{ ksi}$$

Subsequently, the necessary GFRP spiral size was determined based on the previously obtained tensile capacity for steel. Unlike steel, GFRP exhibits linear elasticity until failure. Therefore, the stress limit of GFRP for design was calculated using the elastic modulus of 6500 ksi (ASTM D7957-17) and a strain limit of 0.6% for confinement, as recommended by CSA-806. The GFRP stress limit calculation is as follows:

$$f_{\text{GFRP}} = 0.006(6500) = 39 \text{ ksi}$$

Hence, the cross-sectional area of GFRP rebar that provides an equivalent tensile capacity to $F_{\text{steel,w3.4}}$ and $F_{\text{steel,w4.0}}$ is 0.061 in.^2 and 0.072 in.^2 , respectively.

Based on the calculations in this section, the recommendations for 14", 18", and 24" square prestressed concrete piles reinforced with GFRP spirals is summarized in Table 7.1.

Table 7.1: Required area and recommended area of GFRP spirals compared to steel spirals

Spiral material	Pile cross-section (in. ²)	Required area (in. ²)	Recommended area (in. ²)	Spiral size designation
Steel	14	–	0.034	W3.4
	18	–	0.034	W3.4
	24	–	0.034	W3.4
	30	–	0.040	W4.0
GFRP	14	0.061	0.110	#3
	18	0.061	0.110	#3
	24	0.061	0.110	#3
	30	0.071	0.110	#3

7.3.3 Spiral Size Check for Stainless Steel and CFRP Spirals

The objective of this check is to assess the feasibility of applying the methodology outlined in Section 7.3.2, for GFRP spirals, to determine appropriate sizes for stainless steel spirals and CFRP spirals across various pile dimensions.

For stainless steel spiral type 304, grade 75 used in SS prestressed concrete piles, the minimum yield stress (f_{yss}) is 75 ksi (ASTM A276). Therefore, the necessary SS spiral size was determined

based on the previously obtained tensile capacity for steel as $A_{SS} = \frac{F_{\text{steel}}}{f_{yss}}$.

Hence, the cross-sectional area of SS that provides an equivalent tensile capacity to $F_{\text{steel,w3.4}}$ and $F_{\text{steel,w4.0}}$ is 0.032 in.^2 and 0.037 in.^2 , respectively.

For CFRP spirals utilized in CFRP prestressed concrete piles, the elastic modulus is 22480 ksi. Applying a strain limit of 0.6% for confinement, as recommended by CSA-806, the calculation for the CFRP stress limit is as follows:

$$f_{\text{CFRP}} = 0.006(22480) = 134.9 \text{ ksi}$$

Consequently, the cross-sectional area of CFRP rebar that provides an equivalent tensile capacity to $F_{\text{steel,w3.4}}$ and $F_{\text{steel,w4.0}}$ is 0.018 in.^2 and 0.021 in.^2 , respectively.

According to Table 7.2, the application of the tensile equivalency method to determine the GFRP spiral size is consistent for the standardized SS and CFRP spirals.

Table 7.2: SS and CFRP spiral size check

Spiral material	Pile cross-section (in. ²)	Required area (in. ²)	Recommended area (in. ²)	Spiral size designation
Stainless Steel	14	0.032	0.040	W4.0
	18	0.032	0.040	W4.0
	24	0.032	0.040	W4.0
	30	0.037	0.040	W4.0
CFRP	14	0.018	0.024	0.2 Ø
	18	0.018	0.024	0.2 Ø
	24	0.018	0.024	0.2 Ø
	30	0.021	0.024	0.2 Ø

7.3.4 #3 GFRP Bent Portion Strength Check

Given the importance of correctly manufacturing the bent portion of the recommended GFRP spiral, especially given that incorrect radius of bent portion can result in construction challenges. This section shows the adequacy of the bent details of the GFRP spiral recommended.

Material properties:

Bar diameter, $d_b = 0.375 \text{ in.}$

Area of FRP bar, $A_{\text{GFRP}} = 0.11 \text{ in.}^2$

The guaranteed ultimate tensile load, $F_{fu}^* = 13.20$ kips (FDOT (2019))

The guaranteed ultimate tensile strength, $f_{fu}^* = 120$ ksi

Modulus of elasticity, $E_{GFRP} = 6500$ ksi (ASTM D7957-17)

Environmental reduction factor, $C_E = 0.7$ (Table 6.2, ACI 440.1R-15)

Design tensile strength, $f_{fu} = C_E \times f_{fu}^* = 84$ ksi

Curvature of bent spiral bars, $\frac{r_b}{d_b} = \frac{0.5}{0.375}$

r_b = bend radius of the bar = 0.5 in.

Tensile stress in transverse reinforcement based on tensile strength of bent bar, $f_{fb} = \left(0.05 \frac{r_b}{d_b} + 0.3\right) f_{fu} \leq f_{fu}$ (ACI 440.1R-15)

$f_{fb} = 30.8$ ksi

Design tensile capacity of transverse reinforcement along the bent portion of the bar,

$F_{\#3GFRP} = f_{fb} \times A_{GFRP} = 3.39$ kips $>$ 2.38 kips and 2.8 kips for $F_{steel,w3.4}$ and $F_{steel,w4.0}$, respectively.

#3 GFRP spiral is satisfactory.

7.3.5 Corrosion Resistant Pile Details and GFRP Spiral Patterns

In this section, the specifications for 14", 18", 24", and 30" square concrete piles with CFRP strands and GFRP spirals are provided. During the development of these drawings, the designs, and drawings for steel, CFRP, and stainless steel (SS) spirals were examined as references to determine the orientation, pitch, and spacing considerations for the GFRP spirals. Subsequently, the concrete cover, spiral spacing, and pitch requirements were revised accordingly to accommodate the use of GFRP spirals. See drawings in Appendix I. Unlike steel spirals, GFRP spirals could not be adjusted during the construction stage. GFRP spirals should be manufactured with the quality control limit given in the drawings.

7.4 Recommendations for Pile Driving and Testing

When the developed GFRP spiral piles are installed, the driving stress limit is recommended as up to 5 ksi in concrete. Although the testing showed that the pile could be loaded at greater stress up to 7 ksi (see Table 6.5), the design stress was 5 ksi.

The testing apparatus developed in this project can be used in the future to test other piles. As summarized in Table 2.1, the impact velocity of real-world pile driving hammers typically ranged from about 5 ft/s to 33 ft/s. In contrast, the rated energy of these hammers had a wide range, varying from about 5 kip-ft to over 2000 kip-ft. As shown in Figure 3.2 and Figure 4.13, the impact velocity of the developed apparatus was about 40 ft/s at the 25-ft drop height, greater than the driving hammers summarized in Table 2.1. Therefore, as far as the impact velocity is concerned, the developed impactor will be able to reproduce real-world impactor velocity. The impact energy was about 140 kip-ft at the 25-ft drop height.

There are two major differences between the developed testing setup and real-world pile driving. The first is the energy absorption by the soil. Since the testing setup does not have the soil, more energy will be transferred to the pile. The second is the boundary condition at the pile tip. Since the testing setup is designed to allow sliding, this condition leads to loss of energy potentially greater than the boundary condition of the real-world driving. If greater energy should be transferred to the pile in a future experiment, the support condition could be modified to minimize the sliding.

REFERENCES

- AASHTO. (2012). *AASHTO LRFD Bridge Design Specification, 6th Ed.* American Association of State Highway and Transportation Officials, Washington, D.C.
- AASHTO. (2017). *AASHTO LRFD Bridge Design Specification, 8th Ed.* American Association of State Highway and Transportation Officials, Washington, D.C.
- AASHTO. (2018). *AASHTO Guide Specifications for the Design of Concrete Bridge Beams Prestressed with Carbon Fiber-Reinforced Polymer (CFRP) Systems, 1st Ed.* American Association of State Highway and Transportation Officials, Washington, D.C.
- ACI. (2012). *ACI 543-12 Guide To Design, Manufacture, and Installation of Concrete Piles.* American Concrete Institute Farmington Hills, MI.
- ACI. (2014). *ACI 318-14 Building Code Requirements for Structural Concrete.* American Concrete Institute Farmington Hills, MI.
- ACI. (2015). *ACI 440.1 R-15 Guide for the Design and Construction of structural concrete reinforced with Fiber Reinforced Polymer (FRP) bars.* American Concrete Institute Farmington Hills, MI.
- Afifi, M. Z., Mohamed, H. M., & Benmokrane, B. (2015). Theoretical stress-strain model for circular concrete columns confined by GFRP spirals and hoops. *Engineering Structures*, 102, 202-213. <https://doi.org/10.1016/j.engstruct.2015.08.020>
- Ahmed, E. A., El-Salakawy, E. F., & Benmokrane, B. (2010). Performance evaluation of glass fiber-reinforced polymer shear reinforcement for concrete beams. *ACI Structural Journal*, 107, 53-62. <https://doi.org/10.14359/51663388>
- Ali, A. H., Mohamed, H. M., & Benmokrane, B. (2016). Shear Behavior of Circular Concrete Members Reinforced with GFRP Bars and Spirals at Shear Span-to-Depth Ratios between 1.5 and 3.0. *Journal of Composites for Construction*, 20, 04016055. [https://doi.org/10.1061/\(ASCE\)CC.1943-5614.0000707](https://doi.org/10.1061/(ASCE)CC.1943-5614.0000707)
- Almusallam, T. H., Elsanadedy, H. M., Al-Salloum, Y. A., & Alsayed, S. H. (2013). Experimental and numerical investigation for the flexural strengthening of RC beams using near-surface mounted steel or GFRP bars. *Construction and Building Materials*, 40, 145–161.
- Ashford, S. A., & Jakrapiyanun, W. (2001). Drivability of glass FRP composite piling. *Journal of Composites for Construction*. [https://doi.org/10.1061/\(ASCE\)1090-0268\(2001\)5:1\(58\)](https://doi.org/10.1061/(ASCE)1090-0268(2001)5:1(58))
- ASTM A1064-18a. (2018). *Standard Specification for Carbon-Steel Wire and Welded Wire Reinforcement, Plain and Deformed, for Concrete.* American Society for Testing and Materials, West Conshohocken, PA.
- ASTM A276. (2013). *Standard Specification for Stainless Steel Bars and Shapes.* ASTM International. West Conshohocken, PA.
- ASTM D4945-17. (2017). *Standard Test Method for High-Strain Dynamic Testing of Deep Foundations.* In *American Society for Testing and Materials*. American Society for Testing and Materials, West Conshohocken, PA.

- ASTM D7957-17. (2017). Solid Round Glass Fiber Reinforced Polymer Bars for Concrete Reinforcement. In *American Society for Testing and Materials*. American Society for Testing and Materials, West Conshohocken, PA.
- Belarbi, A., & Hsu, T. T. (1994). Constitutive laws of concrete in tension and reinforcing bars stiffened by concrete. *ACI Structural Journal*, 91(4), 465–474.
- Benmokrane, B., Mohamed, H. M., ElSafty, A., & Nolan, S. (2018). *Field Driving Tests of Precast Concrete Piles Reinforced with GFRP Bars and Spirals*. International Federation for Structural Concrete, Melbourne.
- Bullock, P. J. (2012). Advantages of dynamic pile testing. In *Full-Scale Testing and Foundation Design: Honoring Bengt H. Fellenius*. 694–709.
- Bullock, P. J., Schmertmann, J. H., McVay, M. C., & Townsend, F. C. (2005). Side shear setup. I: Test piles driven in Florida. *Journal of Geotechnical and Geoenvironmental Engineering*. 131, 292-300.
- Canadian Standards Association. (2012). Design and Construction of Building Structures with Fibre-Reinforced Polymers,(CAN/CSA S806-12). *Canadian Standards Association Mississauga, Ont*.
- Cantwell, W. J., & Morton, J. (1991). The impact resistance of composite materials - a review. *Composites*. 22, 347-362. [https://doi.org/10.1016/0010-4361\(91\)90549-V](https://doi.org/10.1016/0010-4361(91)90549-V)
- Chung, C. H., Lee, J., & Gil, J. H. (2014). Structural performance evaluation of a precast prefabricated bridge column under vehicle impact loading. *Structure and Infrastructure Engineering*, 10(6), 777–791.
- Clough, R., & Penzien, J. (1993). Dynamics of Structures, 2nd ed. *New York: McGraw-Hill*.
- Collins, M. P., & Mitchell, D. (1991). *PreStressed Concrete Structures*. Prentice Hall, Englewood Cliffs, NJ.
- Comm Rep. (1974). Recommendations for Design, Manufacture, and Installation of Concrete Piles. *J Am Concr Inst*, 71(10), 477–492.
- Consolazio, G. R., Bui, L. H., & Walters, R. A. (2012). *Pendulum impact testing of an impact-breakaway, windresistant base connection for multi-post ground signs*. University of Florida. Dept. of Civil and Coastal Engineering.
- Correia, J. R., Branco, F. A., & Ferreira, J. G. (2007). Flexural behaviour of GFRP-concrete hybrid beams with interconnection slip. *Composite Structures*. 77, 66-78. <https://doi.org/10.1016/j.compstruct.2005.06.003>
- Crapps, D. K. (2004). The role of RAM momentum in pile driving. *Geotechnical Special Publication*. 276-309. [https://doi.org/10.1061/40743\(142\)16](https://doi.org/10.1061/40743(142)16)
- CSA-806. (2012). Design and construction of building components with fibre-reinforced polymers. In *CSA S806-12*.
- De Luca, A., Matta, F., & Nanni, A. (2010). Behavior of full-scale glass fiber-reinforced polymer reinforced concrete columns under axial load. *ACI Structural Journal*. 107, 589-596.

<https://doi.org/10.14359/51663912>

- Devalapura, R. K., Tadros, M. K., & Prewett, C. W. (1992). Stress-Strain Modeling of 270 ksi Low-Relaxation Prestressing Strands. *PCI Journal*, 37(2), 100–106.
- Ding, X., Liu, H., Liu, J., & Chen, Y. (2011). Wave propagation in a pipe pile for low-strain integrity testing. *Journal of Engineering Mechanics*. 137, 598-609. [https://doi.org/10.1061/\(ASCE\)EM.1943-7889.0000263](https://doi.org/10.1061/(ASCE)EM.1943-7889.0000263)
- El-Garhy, B., Galil, A. A., Youssef, A. F., & Raia, M. A. (2013). Behavior of raft on settlement reducing piles: Experimental model study. *Journal of Rock Mechanics and Geotechnical Engineering*. 5, 389-399. <https://doi.org/10.1016/j.jrmge.2013.07.005>
- El-Mogy, M., El-Ragaby, A., & El-Salakawy, E. (2011). Effect of transverse reinforcement on the flexural behavior of continuous concrete beams reinforced with FRP. *Journal of Composites for Construction*. 15, 672-81. [https://doi.org/10.1061/\(ASCE\)CC.1943-5614.0000215](https://doi.org/10.1061/(ASCE)CC.1943-5614.0000215)
- Fam, A., Pando, M., Filz, G., & Rizkalla, S. (2003). Precast piles for route 40 bridge in Virginia using concrete filled FRP tubes. *PCI Journal*. 48, 32-45. <https://doi.org/10.15554/pcij.05012003.32.45>
- FDOT. (2015). Pile Driving Inspectors Qualification Course. Florida Department of Transportation, Tallahassee, FL.
- FDOT. (2019). *FDOT Standard Specifications for Road and Bridge Construction*. Florida Department of Transportation, Tallahassee, FL.
- FDOT. (2023). *FDOT Standard Specification for Road and Bridge Construction*. Florida Department of Transportation, Tallahassee, FL.
- FDOT SDG. (2018). *FDOT Structures Design Guidelines*. Florida Department of Transportation, Tallahassee, FL.
- Graybeal, B., & Pessiki, S. P. (1998). *Confinement Effectiveness of High Strength Spiral Reinforcement in Prestressed Concrete Piles*. Lehigh University.
- Guades, E., Aravinthan, T., Islam, M., & Manalo, A. (2012). A review on the driving performance of FRP composite piles. In *Composite Structures*. 94, 1932-1942. <https://doi.org/10.1016/j.compstruct.2012.02.004>
- Hannigan, P. J., Rausche, F., Likins, G. E., Robinson, B. R., & Becker, M. L. (2016a). Design and construction of driven pile foundations. In *Federal Highway Administration* (Vol. 1).
- Hannigan, P. J., Rausche, F., Likins, G. E., Robinson, B. R., & Becker, M. L. (2016b). Design and construction of driven pile foundations. In *Federal Highway Administration* (Vol. 2).
- Hartt, W. H., Powers, R. G., Lysogorski, D. K., Liroux, V., & Virmani, Y. P. (2007). *Corrosion Resistant Alloys for Reinforced Concrete*. Turner-Fairbank Highway Research Center,
- Hawkins, N. M., Kuchma, D. A., Mast, R. F., Marsh, M. L., & Reineck, K. (2005). *NCHRP Report 549: Simplified Shear Design of Structural Concrete Members*. Transportation Research Board, Washington, DC.

- Herrera, R., Jones, L. E., & Lai, P. (2009). Driven concrete pile foundation monitoring with embedded data collector system. *Geotechnical Special Publication*. [https://doi.org/10.1061/41021\(335\)78](https://doi.org/10.1061/41021(335)78)
- Holeyman, A. E. (1992). Keynote lecture: Technology of pile dynamic testing. *Proc. 4th Application of Stress Wave Theory to Piles*, 195–215.
- Hussein, M. H., & Goble, G. G. (2004). A brief history of the application of stress-wave theory to piles. *Geotechnical Special Publication*. 621-628. [https://doi.org/10.1061/40743\(142\)11](https://doi.org/10.1061/40743(142)11)
- Hussein, M. H., Woerner, W. A., Sharp, M., & Hwang, C. (2006). Pile driveability and bearing capacity in high-rebound soils. *GeoCongress 2006: Geotechnical Engineering in the Information Technology Age*. 1-4. [https://doi.org/10.1061/40803\(187\)63](https://doi.org/10.1061/40803(187)63)
- Kantrales, G. C., Consolazio, G. R., Wagner, D., & Fallaha, S. (2016). Experimental and Analytical Study of High-Level Barge Deformation for Barge-Bridge Collision Design. *Journal of Bridge Engineering*. 21, 04015039. [https://doi.org/10.1061/\(ASCE\)BE.1943-5592.0000801](https://doi.org/10.1061/(ASCE)BE.1943-5592.0000801)
- Lee, J., & Fenves, G. L. (1998). Plastic-Damage Model for Cyclic Loading of Concrete Structures. *Journal of Engineering Mechanics*, 124(8), 892–900.
- Lee, S. L., Chow, Y. K., Karunaratne, G. P., & Wong, K. Y. (1988). Rational wave equation model for pile-driving analysis. *Journal of Geotechnical Engineering*. 114, 306-325. [https://doi.org/10.1061/\(ASCE\)0733-9410\(1988\)114:3\(306\)](https://doi.org/10.1061/(ASCE)0733-9410(1988)114:3(306))
- Likins, G. E. (1984). Field measurements and the pile driving analyzer “. *Proceedings Of the Second International Conference on the Application of Stress-Wave Theory on Piles, Stockholm*, 298–305.
- Likins, Garland E, Rausche, F., & Goble, G. G. (2000). High strain dynamic pile testing, equipment and practice. *Proceedings of the Sixth International Conference on the Application of Stress-Wave Theory to Piles*, 327–333.
- Lotfy, E. M. (2010). Behavior of reinforced concrete short columns with Fiber Reinforced polymers bars. *International Journal of Civil and Structural Engineering*, 1(3), 545.
- Lublinter, J., Oliver, J., Oller, S., & Oñate, E. (1989). A plastic-damage model for concrete. *International Journal of Solids and Structures*, 25(3), 299–326.
- Mander, J. B., Priestley, M. J., & Park, R. (1988). Theoretical stress-strain model for confined concrete. *Journal of Structural Engineering (United States)*. 114, 1804-1826. [https://doi.org/10.1061/\(ASCE\)0733-9445\(1988\)114:8\(1804\)](https://doi.org/10.1061/(ASCE)0733-9445(1988)114:8(1804))
- Martinez, S., Nilson, A. H., & O., S. F. (1984). Spirally Reinforced High-Strength Concrete Columns. *ACI Journal Proceedings*, 81(5). 431-442. <https://doi.org/10.14359/10693>
- McVay, M., Bloomquist, D., Vanderlinde, D., & Clausen, J. (1994). Centrifuge modeling of laterally loaded pile groups in sands. *Geotechnical Testing Journal*. 17, 129-137. <https://doi.org/10.1520/gtj10085j>
- McVay, M. C., Zhang, L., Han, S., & Lai, P. (2000). Experimental and numerical study of laterally

- loaded pile groups with pile caps at variable elevations. *Transportation Research Record*. 1736, 12-18. <https://doi.org/10.3141/1736-02>
- McVay, Michael, Bloomquist, D., Xie, Y., Johnson, J., Ko, J., Wasman, S., & Faraone, Z. (2009). Analyses of Embedded Data Collector (EDC). *Final Report, Department of Civil and Coastal Engineering University of Florida*.
- McVay, Michael C, Alvarez, V., Zhang, L., Perez, A., & Gibsen, A. (2002). *Estimating driven pile capacities during construction*. University of Florida.
- McVay, Michael, Zhang, L., Molnit, T., & Peterlai, P. (1998). Centrifuge testing of large laterally loaded pile groups in sands. *Journal of Geotechnical and Geoenvironmental Engineering*. 124, 1016-1026. [https://doi.org/10.1061/\(ASCE\)1090-0241\(1998\)124:10\(1016\)](https://doi.org/10.1061/(ASCE)1090-0241(1998)124:10(1016))
- Mercan, B., Schultz, A. E., & Stolarski, H. K. (2010). Finite element modeling of prestressed concrete spandrel beams. *Engineering Structures*, 32(9), 2804–2813.
- Mercan, B., Stolarski, H. K., & Schultz, A. E. (2016). Arc-length and explicit methods for static analysis of prestressed concrete members. *Computers and Concrete*, 18(1), 17–37.
- Mohamed, H. M., Afifi, M. Z., & Benmokrane, B. (2014). Performance Evaluation of Concrete Columns Reinforced Longitudinally with FRP Bars and Confined with FRP Hoops and Spirals under Axial Load. *Journal of Bridge Engineering*. 19, 04014020. [https://doi.org/10.1061/\(asce\)be.1943-5592.0000590](https://doi.org/10.1061/(asce)be.1943-5592.0000590)
- Mousa, S., Mohamed, H. M., & Benmokrane, B. (2018). Flexural strength and design analysis of circular reinforced concrete members with glass fiber-reinforced polymer bars and spirals. *ACI Structural Journal*. 115, 1353-1364. <https://doi.org/10.14359/51702282>
- Murray, Y. (2007a). Manual for LS-DYNA Wood Material Model 143. In *U.S. Department of Transportation*.
- Murray, Y. (2007b). Users Manual for LS-DYNA Concrete Material Model 159. *Federal Highway Administration*.
- Othman, H., & Marzouk, H. (2018). Applicability of damage plasticity constitutive model for ultra-high performance fibre-reinforced concrete under impact loads. *International Journal of Impact Engineering*, 114, 20–31.
- Pantelides, C. P., Gibbons, M. E., & Reaveley, L. D. (2013). Axial Load Behavior of Concrete Columns Confined with GFRP Spirals. *Journal of Composites for Construction*. 17, 305-313. [https://doi.org/10.1061/\(asce\)cc.1943-5614.0000357](https://doi.org/10.1061/(asce)cc.1943-5614.0000357)
- PCI. (1999). *PCI Design Handbook: Precast and prestressed concrete, 6th Ed.* Precast/Prestressed Concrete Institute, Chicago, IL.
- PCI. (2010). *PCI Design Handbook: Precast and Prestressed Concrete, 7th Ed.* Precast/Prestressed Concrete Institute, Chicago, IL.
- Precast/Prestressed Concrete Institute (PCI). (2003). *PCI bridge design manual*.
- Rajakapse, R. (2008). Pile Design and Construction Rules of Thumb. In *Pile Design and Construction Rules of Thumb*. Butterworth-Heinemann. <https://doi.org/10.1016/B978-0->

- Rausche, F. (2000). Pile driving equipment: Capabilities and properties. *Keynote Lecture, Proceedings of the 6th International Conference on the Application of Stress-Wave Theory to Piles, Rotterdam*. 11-13.
- Rausche, F, Likins, G., Miyasaka, T., & Bullock, P. J. (2008). The effect of ram mass on pile stresses and pile penetration. *Proceedings of the Eighth International Conference on the Application of Stress-Wave Theory to Piles*, 389–394.
- Rausche, Frank, Hussein, M. H., Likins, G., & Thendean, G. (1994). Static pile load-movement from dynamic measurements. *Vertical and Horizontal Deformations of Foundations and Embankments*, 291–302.
- Rausche, Frank, Likins, G., Liang, L., & Hussein, M. (2010). Static and dynamic models for CAPWAP signal matching. *Geotechnical Special Publication*. 534-553. [https://doi.org/10.1061/41093\(372\)27](https://doi.org/10.1061/41093(372)27)
- Ren, W., Sneed, L. H., Yang, Y., & He, R. (2015). Numerical Simulation of Prestressed Precast Concrete Bridge Deck Panels Using Damage Plasticity Model. *International Journal of Concrete Structures and Materials*, 9(1), 45–54.
- Robert, M., & Benmokrane, B. (2013). Combined effects of saline solution and moist concrete on long-term durability of GFRP reinforcing bars. *Construction and Building Materials*. 38, 274-284. <https://doi.org/10.1016/j.conbuildmat.2012.08.021>
- Roddenberry, M., Mtenga, P., & Joshi, K. (2014). Investigation of carbon fiber composite cables (CFCC) in prestressed concrete piles. In *Final Rep., Florida Dept. of Transportation, Tallahassee, FL*. (Issues BDK83-977–17).
- Škrlec, A., & Klemenc, J. (2016). Estimating the strain-rate-dependent parameters of the Cowper-Symonds and Johnson-Cook material models using taguchi arrays. *Strojniski Vestnik/Journal of Mechanical Engineering*. 62, 220-230. <https://doi.org/10.5545/sv-jme.2015.3266>
- Smith, E. A. (1960). Pile-driving analysis by the wave equation. *American Society of Civil Engineers Transactions*. 86, 35-61.
- So, A. K. O., & Ng, C. W. W. (2010). Impact compression behaviors of high-capacity long piles. *Canadian Geotechnical Journal*. 47, 1335-1350. <https://doi.org/10.1139/T10-031>
- Tao, Y., & Chen, J. F. (2015). Concrete Damage Plasticity Model for Modeling FRP-to-Concrete Bond Behavior. *Journal of Composites for Construction*, 19(1). 04014026.
- Tobbi, H., Farghaly, A. S., & Benmokrane, B. (2012). Concrete columns reinforced longitudinally and transversally with glass fiber-reinforced polymer bars. *ACI Structural Journal*. 109, 551-558. <https://doi.org/10.14359/51683874>
- Vicaria, J. J. D., Diaz, F. D., Arroyo, M. E., & Paulotto, C. (2014). Analysis of the technical viability of GFRP reinforced precast concrete piles. *16th European Conference on Composite Materials, ECCM 2014*.

APPENDICES

Appendix A. Impact Test Setup (Impactor, Restraining Blocks, and Support) Drawing

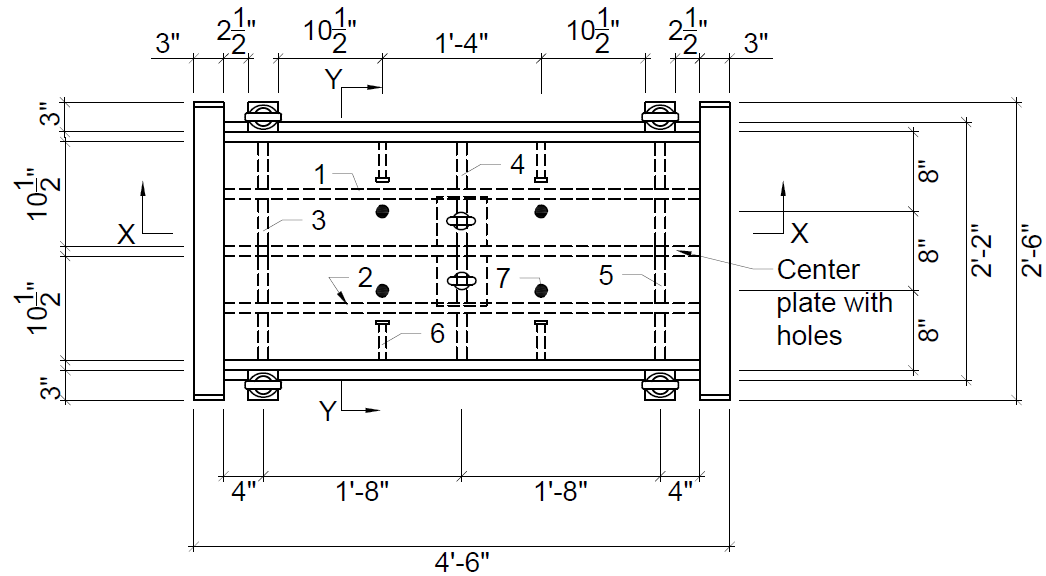
PILE IMPACTOR

General Notes:

- Impactor consists of the following elements:
 1. Three (3) 26" x 48" x 1" 1018 carbon steel plates (impactor side and bottom plates).
 2. One (1) 22" x 48" x 1" 1018 carbon steel plate (impactor top plate).
 3. One (1) 24" x 48" x 1" 1018 carbon steel plate with nine (9) holes for #8 rebar to run through (impactor center plate).
 4. Four (4) 3" square 1018 carbon steel solid eyelet attachment blocks of length 26", with $\frac{7}{8}$ " threaded holes for VRS - 1"- 8 UNC lifting eyebolts.
 5. Two (2) 30" x 30" x 3" carbon steel plate A572.
 6. Two (2) 5" x 5" x $\frac{1}{2}$ " carbon steel plate A572.
 7. Four (4) RUD lifting eyebolts (VRS - 1"- 8 UNC).
 8. Two (2) eye nuts ($\frac{3}{4}$ "-10).
 9. Two (2) $7\frac{1}{2}$ " threaded rod $\frac{3}{4}$ "-10 UNC grade 7B.
 10. Four (4) $\frac{3}{4}$ "-10 Hex Nuts Grade 5.
 11. Nine (9) 22" long #8 rebar.
 12. Six (6) 48" long #8 rebar.
 13. Twelve (12) $3/4"$ \varnothing $4 \frac{3}{16}"$ LG shear studs.

- All steel plates used in constructing the impactor shall be grade 50 steel
- The rebars shall be ASTM A706 grade 60 steel.
- Provide weld connection between steel plates using a filler metal of at least 70 ksi tensile strength
- Weld rebar to steel plates as shown in the diagrams
- Concrete with a 28 day minimum compressive strength of 4500 psi shall be used to fill the compartments of the impactor
- See Sheet 28 for impactor pull back attachment

Pile Impactor				Revisions:	2020-08-26	2021-12-15
General Notes for Pile Impactor	2019-05-24	FAMU-FSU College of Engineering	Sheet 1 of 31		2021-03-10	
					2021-03-15	

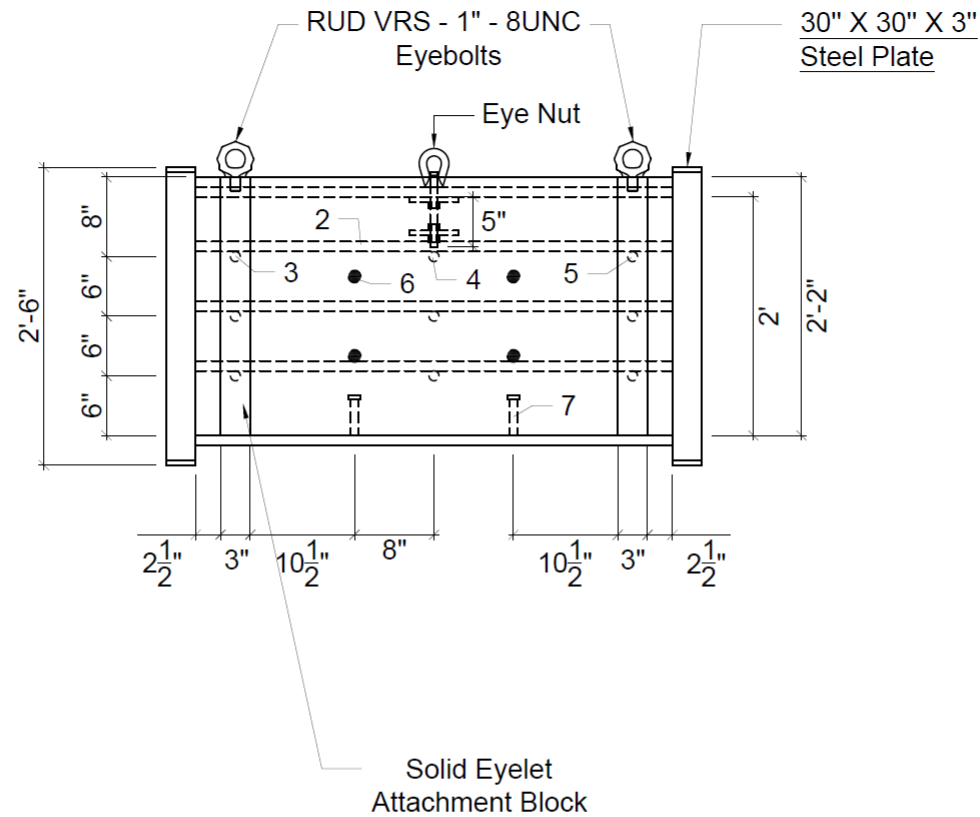


Plan View

NOTE:

- 3, 4, and 5 are rebars in the transverse direction, running through and welded to the center plate
- 1 and 2 are rebars in the longitudinal direction, and are tied to the transverse rebars
- Weld the opposite ends rebars 1, 2, 3, 4 and 5 to the respective plates as shown in the diagram
- 6 is a $3/4" \text{ } \varnothing \text{ } 4 \frac{3}{16}"$ LG shear stud on the side plate of the impactor. There are four studs on each side plate
- 7 is a $3/4" \text{ } \varnothing \text{ } 4 \frac{3}{16}"$ LG shear stud on the bottom plate of the impactor. There are four studs on the bottom plate

Pile Impactor				Revisions:	2020-08-26	2021-12-15
Pile Impactor Plan View	2019-05-24	FAMU-FSU College of Engineering	Sheet 2 of 31		2021-03-10	
					2021-03-15	

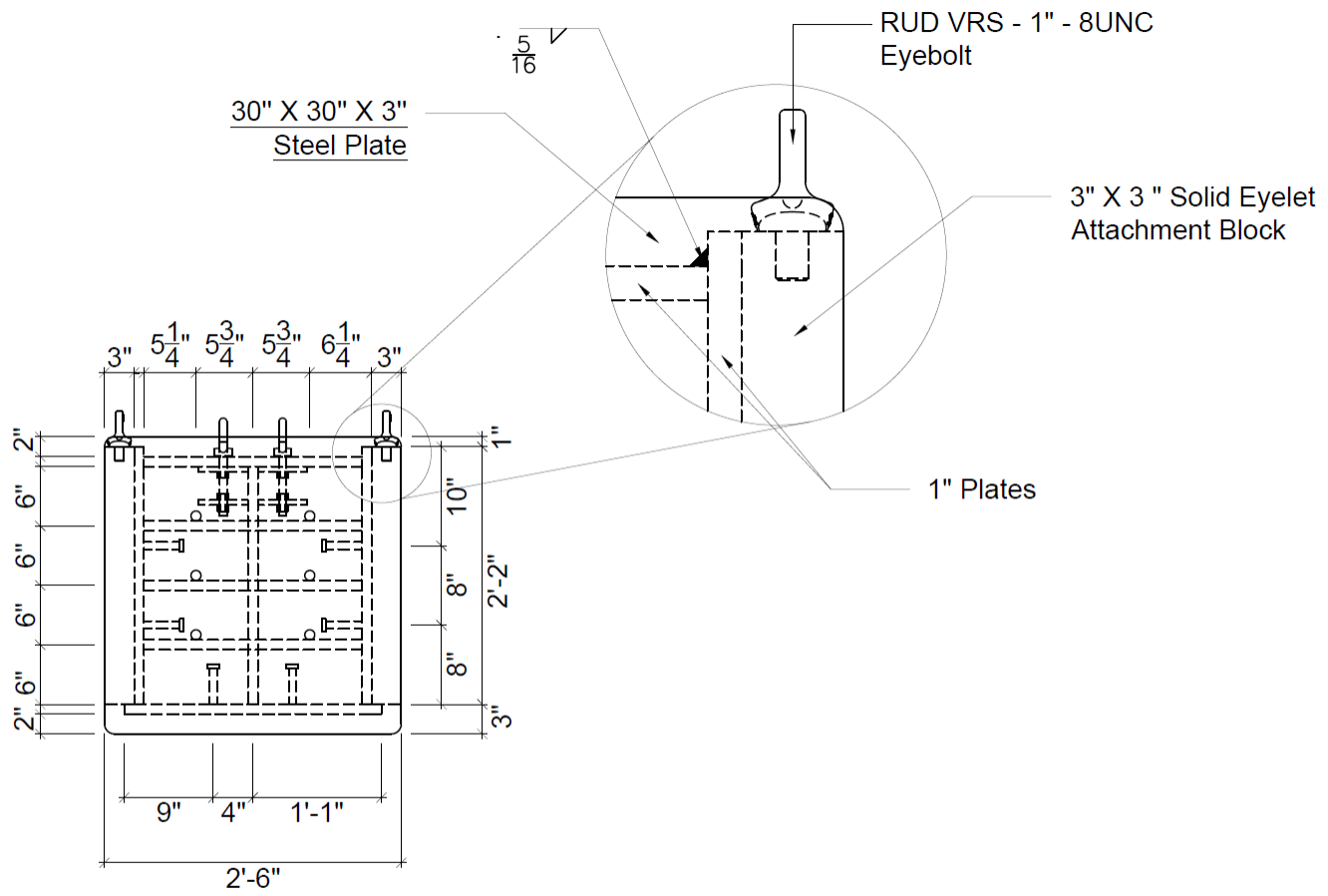


NOTE:

- Check what each number represents from the previous page

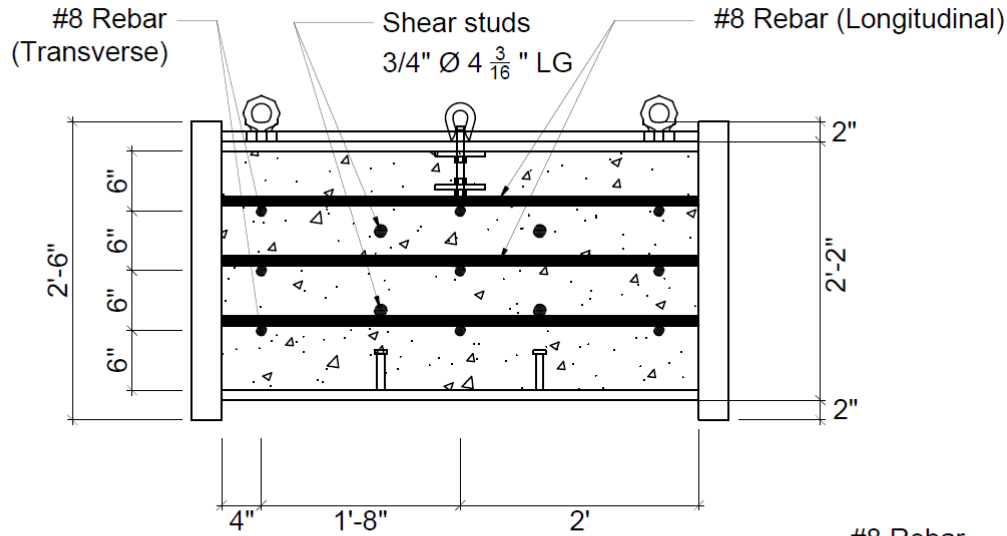
Elevation

Pile Impactor				Revisions:	2020-08-26	2021-12-15
Pile Impactor Elevation	2019-05-24	FAMU-FSU College of Engineering	Sheet 3 of 31		2021-03-10	
					2021-03-15	

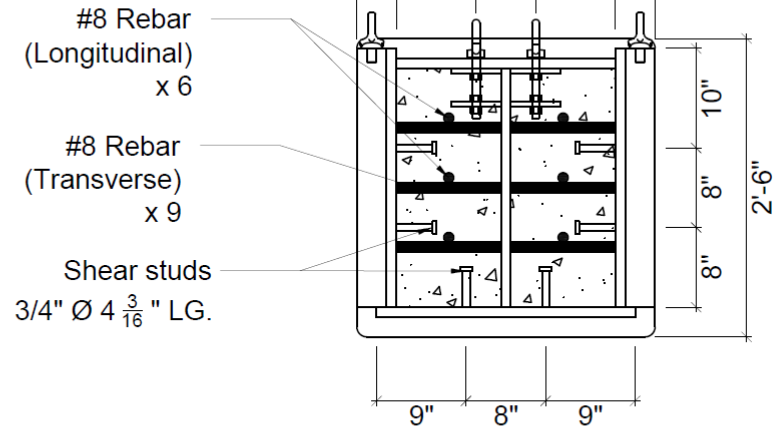


Front View

Pile Impactor				Revisions:	2020-08-26	2021-12-15
Pile Impactor Front View	2019-05-24	FAMU-FSU College of Engineering	Sheet 4 of 31		2021-03-10	
					2021-03-15	

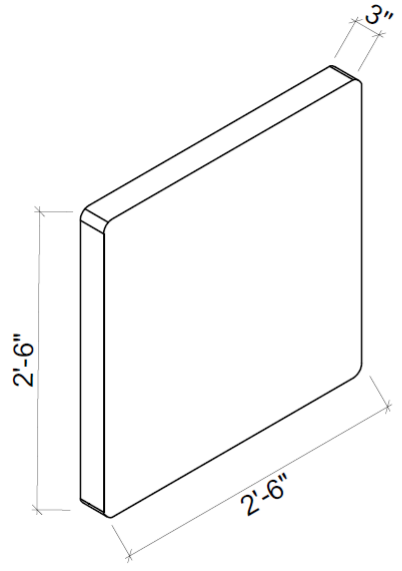


Section X-X

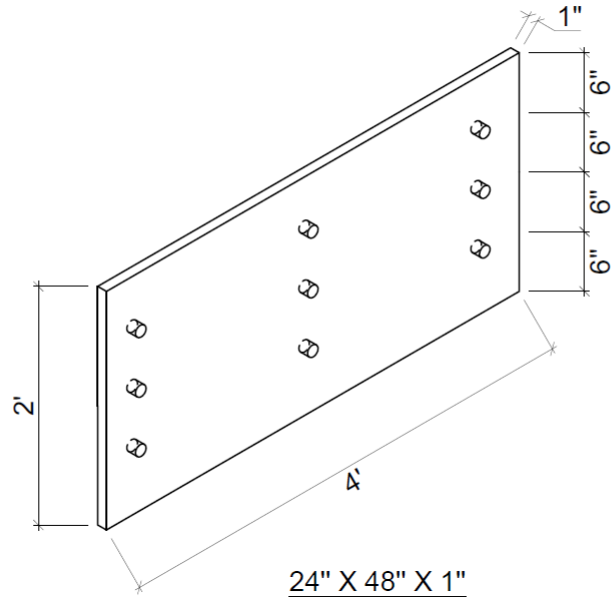


Section Y-Y

Pile Impactor				Revisions:	2020-08-26	2021-12-15
Pile Impactor Sections	2019-05-24	FAMU-FSU College of Engineering	Sheet 5 of 31		2021-03-10	
					2021-03-15	

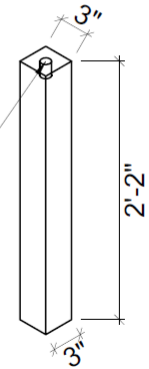


30" X 30" X 3"
Carbon Steel Plate
A572 GR50 x 2



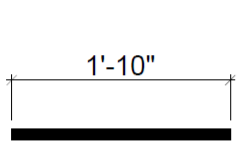
24" X 48" X 1"
1018 Carbon Steel Plate with
Holes for 1" Diameter Rebar

Shear stud
3/4" Ø 4 3/16" LG. x 12

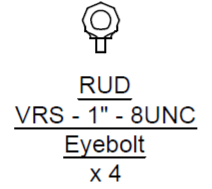


1018 Carbon Steel
Solid Eyelet Attachment Block x 4

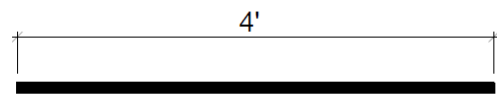
Threaded Hole
for Rud Eye-bolt
(Drill Size - $\frac{7}{8}$ "
Tap Size - 1" - 8)



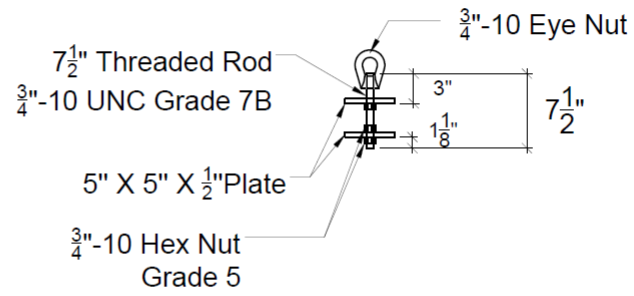
#8 Rebar x 9



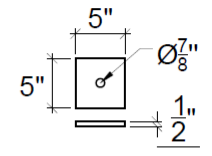
RUD
VRS - 1" - 8UNC
Eyebolt
x 4



#8 Rebar x 6

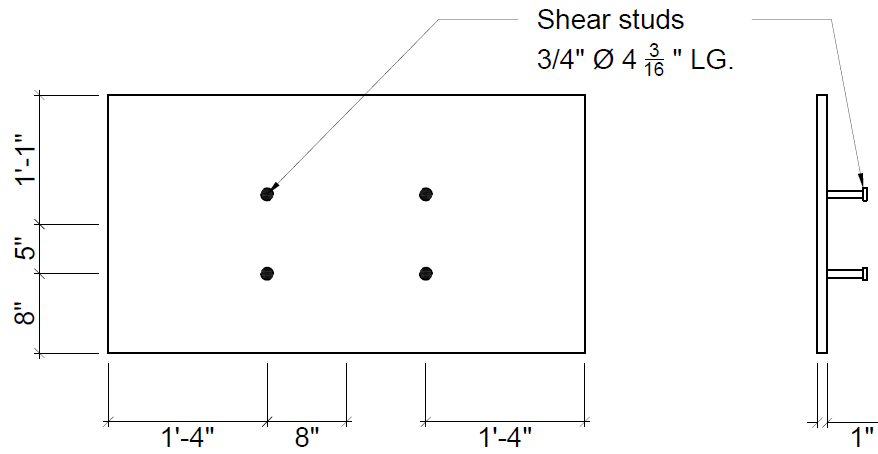


Anchor and Plate Connection x 2

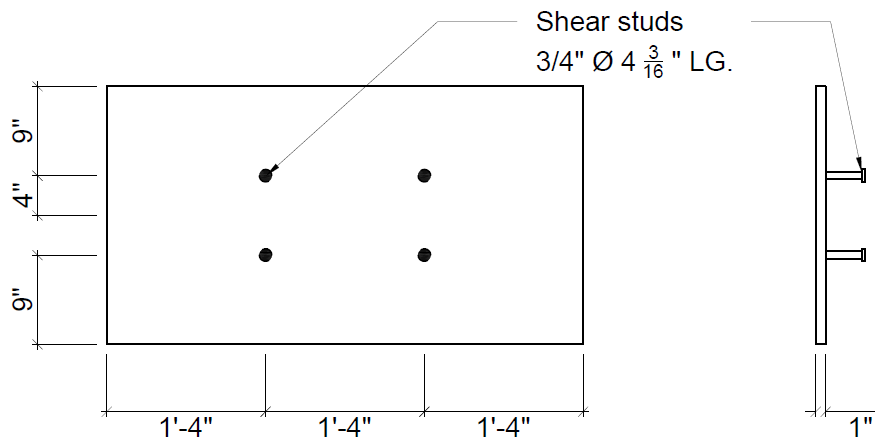


5" X 5" X 1/2"
GR. 50 Plate x 4

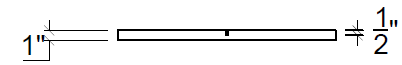
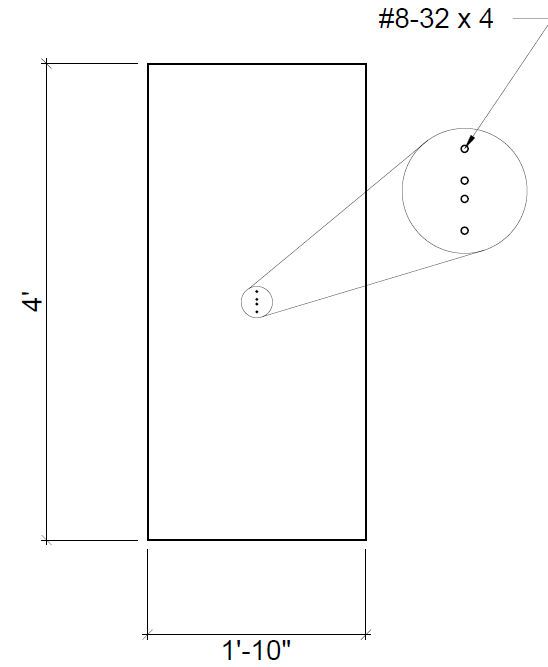
Pile Impactor				Revisions:	2020-08-26	2021-12-15
Pile Impactor Elements	2019-05-24	FAMU-FSU College of Engineering	Sheet 6 of 31		2021-03-10	
					2021-03-15	



26" X 48" X 1" 1018 Carbon Steel Plate (Side Plate) x 2



26" X 48" X 1" 1018 Carbon Steel Plate (Bottom Plate) x 1



20" X 48" X 1"
1018 Carbon Steel Plate
(Top Plate) x 1

Shear studs
3/4" Ø 4 3/16" LG.

#8-32 x 4

Shear studs
3/4" Ø 4 3/16" LG.

Pile Impactor				Revisions:	2020-08-26	2021-12-15
Pile Impactor Elements	2019-05-24	FAMU-FSU College of Engineering	Sheet 7 of 31		2021-03-10	
					2021-03-15	

PILE RESTRAINT

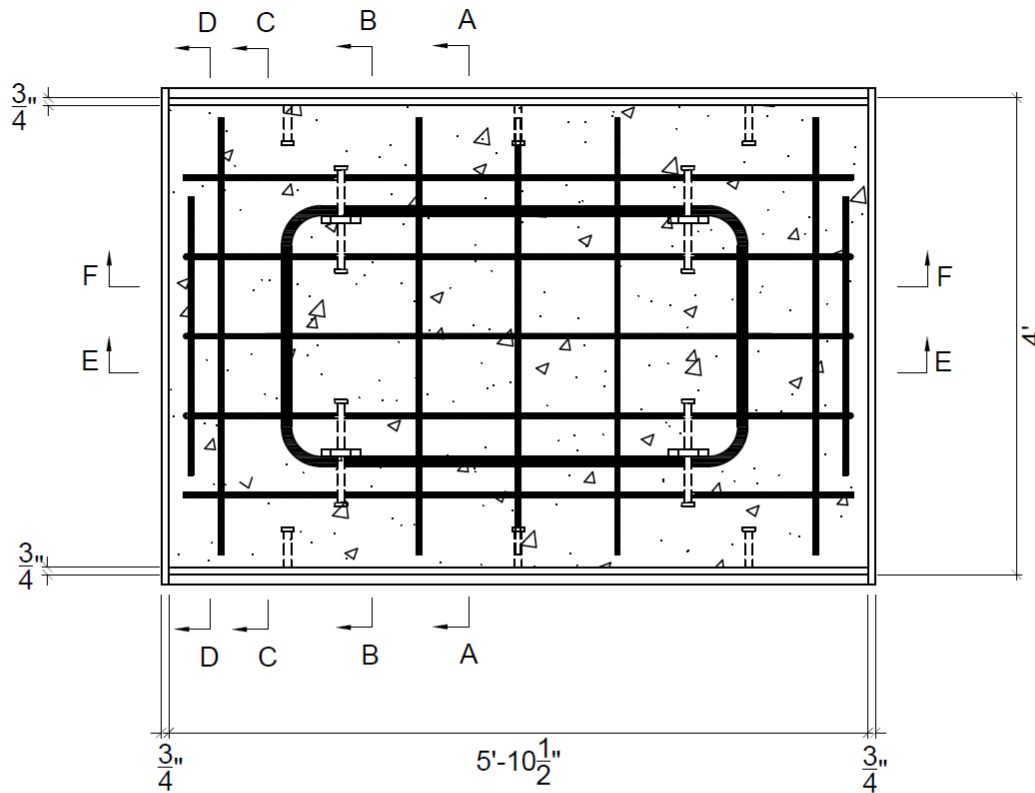
General Notes:

- Grade 50 steel shall be used in the construction of the pile restraint
- For the anchor plates use grade 50 steel
- The rebars shall be ASTM A706 grade 60 steel
- Use concrete with a 28 day minimum compressive strength of 4500 psi
- Proper welding procedure shall be followed using a filler metal of at least 70 ksi tensile strength

Procedures:

1. Weld the front plate (Part 2) to the base plate (Part 1).
2. Weld anchor plates to the base plate (Part 1).
3. Follow the steps stated in sheet 17.
4. Connect side plates (Part 3) to the base plate (Part 1) and to the front and back plates (Part 2) by welds.
5. Weld the back plate (Part 2) to the base plate (Part 1).
6. Pour concrete and allow to gain the required strength.

Pile Restraint				Revisions:	2020-08-26	2021-12-15
					2021-03-10	
Notes and Procedures	2019-05-24	FAMU-FSU College of Engineering	Sheet 8 of 31		2021-03-15	

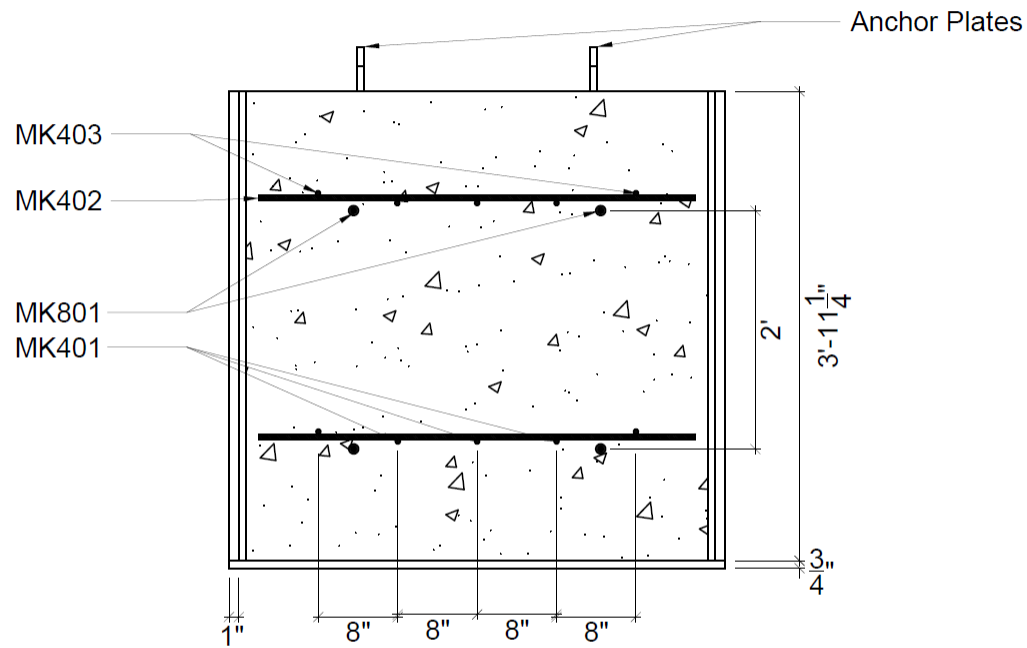


Plan View

NOTE:

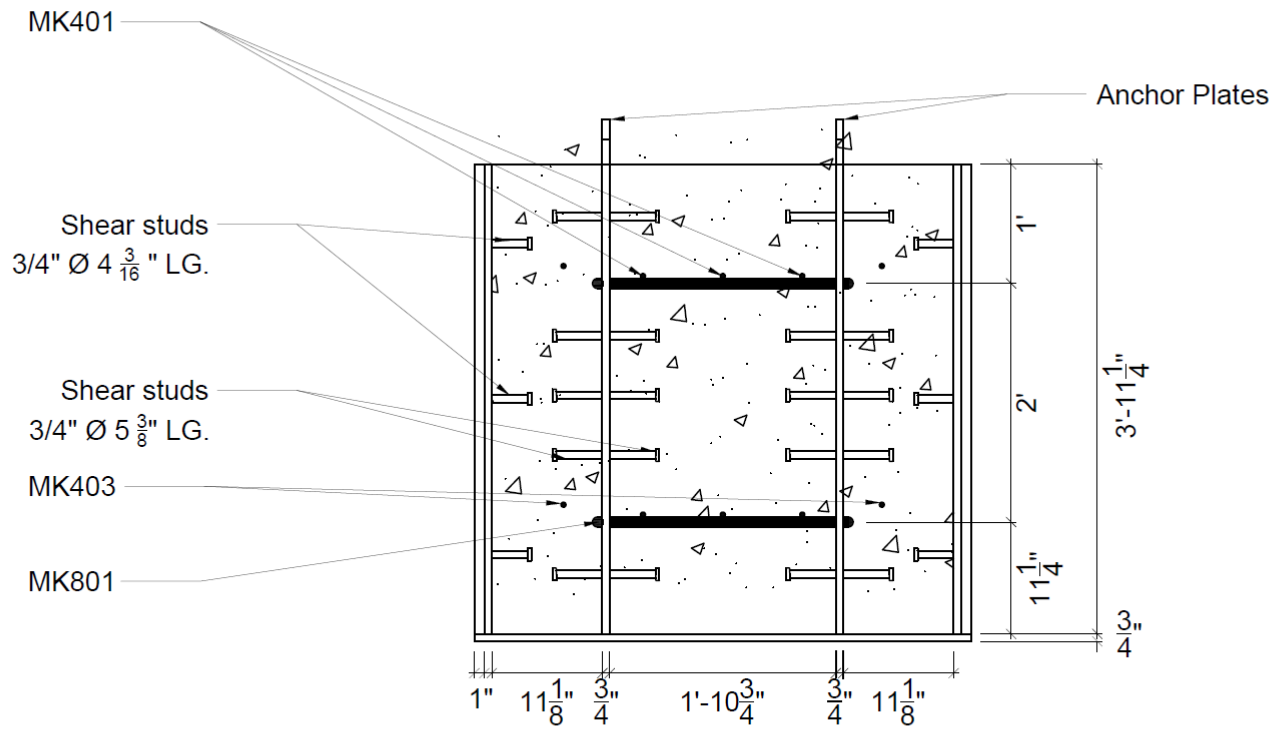
Refer to rebar layout for instructions on the placement of reinforcing bars

Pile Restraint				Revisions:	2020-08-26	2021-12-15
Plan View of Pile Restraint	2019-05-24	FAMU-FSU College of Engineering	Sheet 9 of 31		2021-03-10	
					2021-03-15	



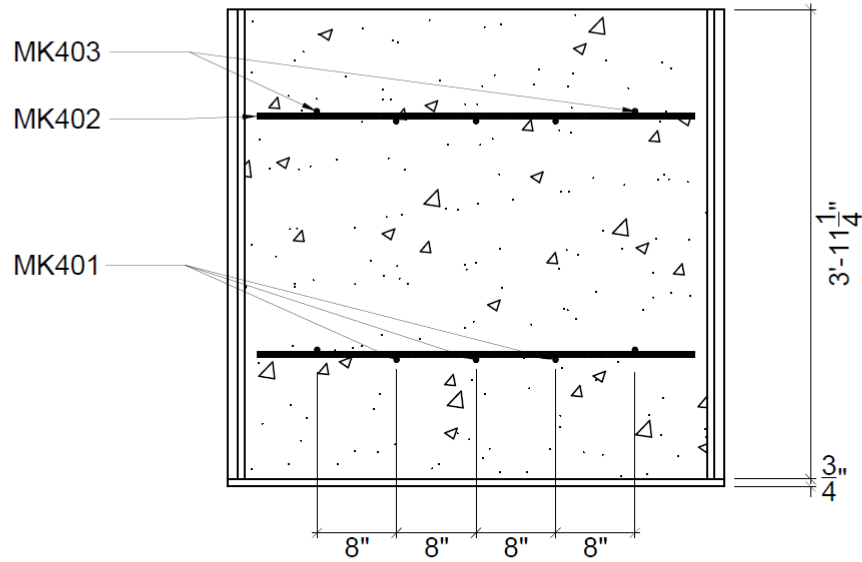
Section A-A

Pile Restraint				Revisions:	2020-08-26	2021-12-15	
Pile Restraint - Section A-A					2019-05-24	FAMU-FSU College of Engineering	Sheet 10 of 31
					2021-03-10		
					2021-03-15		



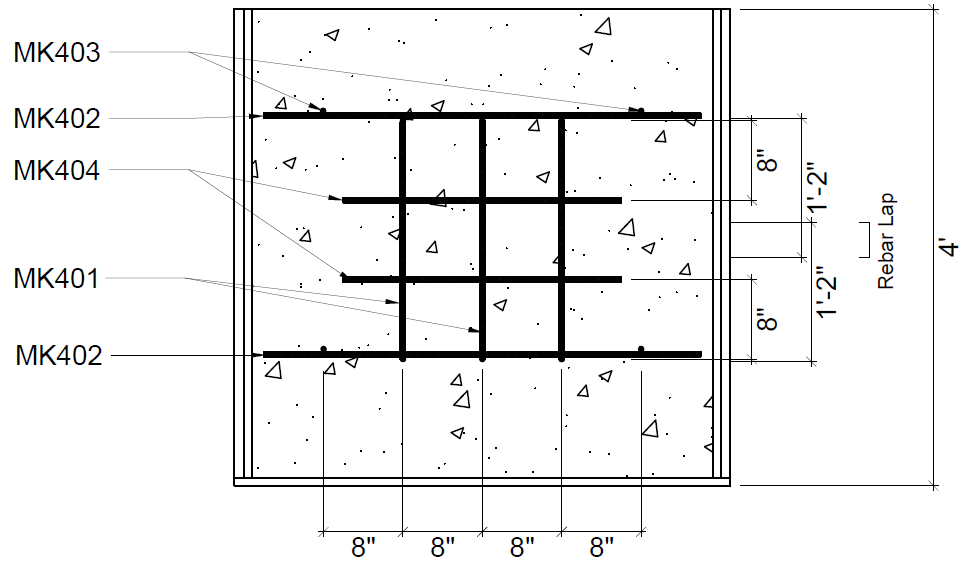
Section B-B

Pile Restraint				Revisions:	2020-08-26	2021-12-15
Pile Restraint - Section B-B	2019-05-24	FAMU-FSU College of Engineering	Sheet 11 of 31		2021-03-10	
					2021-03-15	



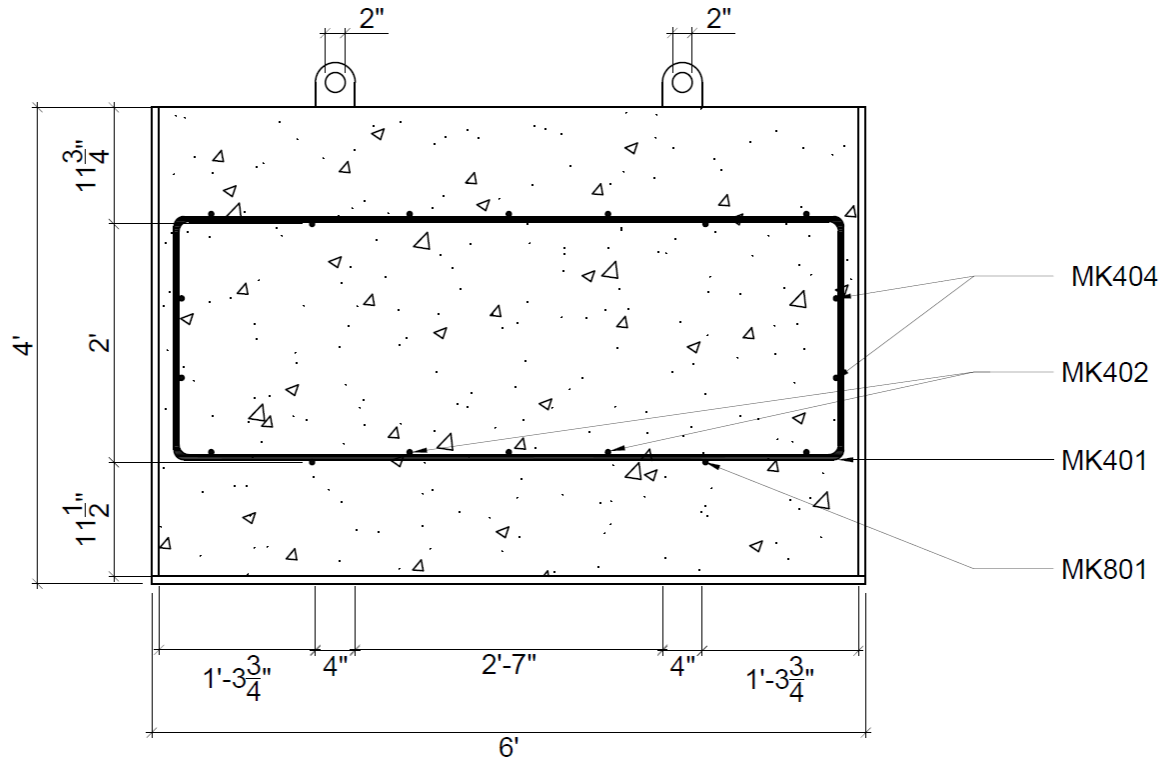
Section C-C

Pile Restraint				Revisions:	2020-08-26	2021-12-15
Pile Restraint - Section C-C	2019-05-24	FAMU-FSU College of Engineering	Sheet 12 of 31		2021-03-10	
					2021-03-15	



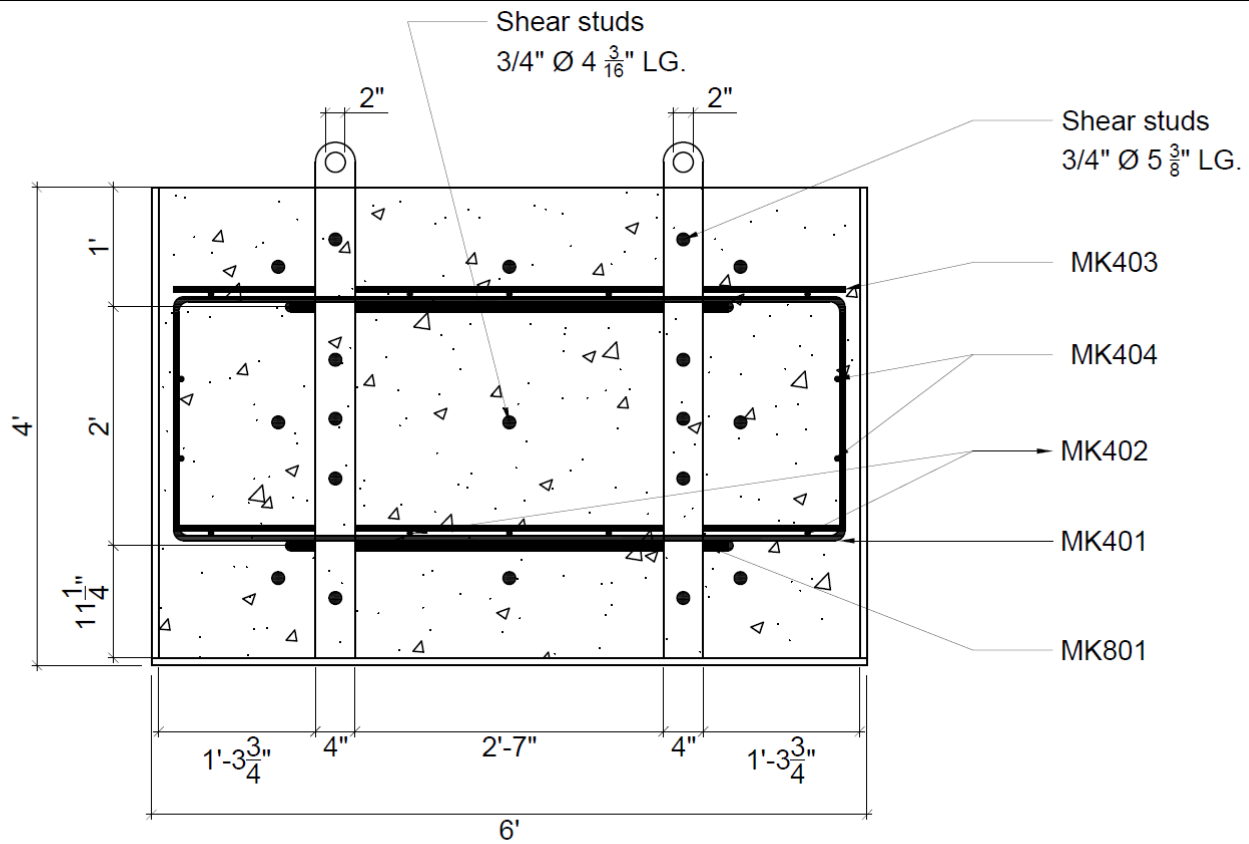
Section D-D

Pile Restraint				Revisions:	2020-08-26	2021-12-15
Pile Restraint - Section D-D					2021-03-10	
2019-05-24	FAMU-FSU College of Engineering	Sheet 13 of 31	2021-03-15			



Section E-E

Pile Restraint				Revisions:	2020-08-26	2021-12-15
Pile Restraint - Section E-E	2019-05-24	FAMU-FSU College of Engineering	Sheet 14 of 31		2021-03-10	
					2021-03-15	

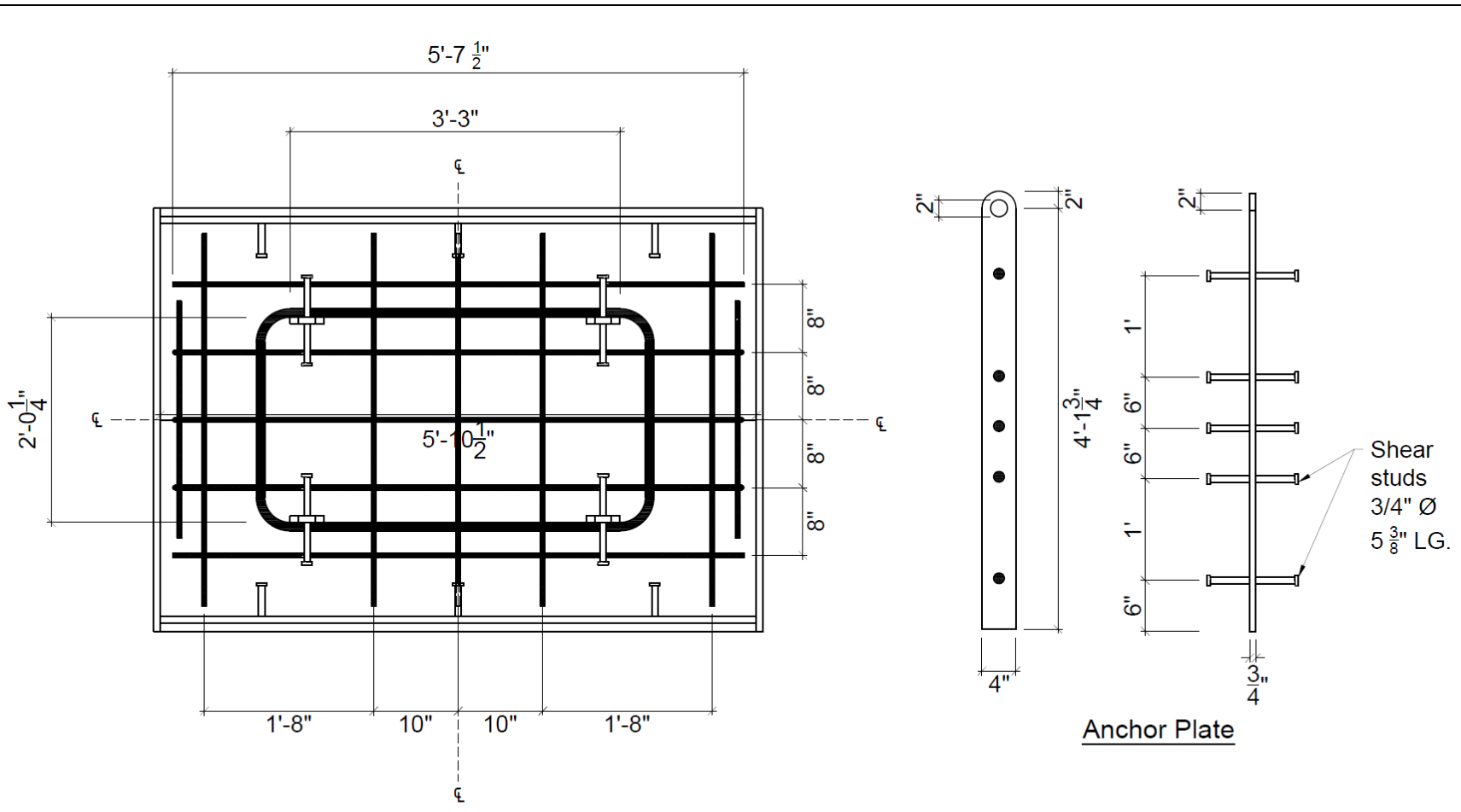


NOTE:

Anchor plate should be welded to the bottom plate of the pile restraint

Section F-F

Pile Restraint				Revisions:	2020-08-26	2021-12-15
Pile Restraint - Section F-F	2019-05-24	FAMU-FSU College of Engineering	Sheet 15 of 31		2021-03-10	
					2021-03-15	



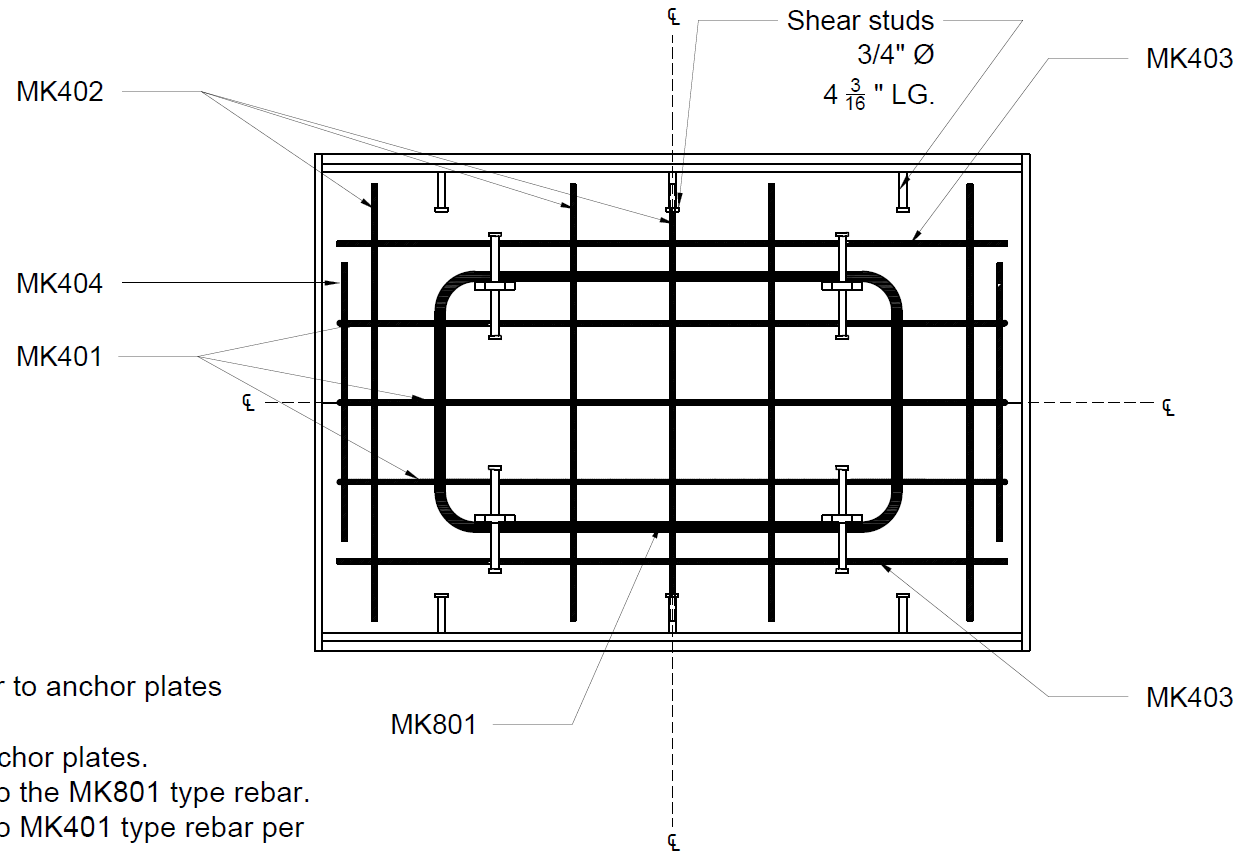
Rebar Layout

Anchor Plate

NOTE:

Four anchor plates required

Pile Restraint				Revisions:	2020-08-26	2021-12-15
Rebar layout and Anchor plate details	2019-05-24	FAMU-FSU College of Engineering	Sheet 16 of 31		2021-03-10	
					2021-03-15	

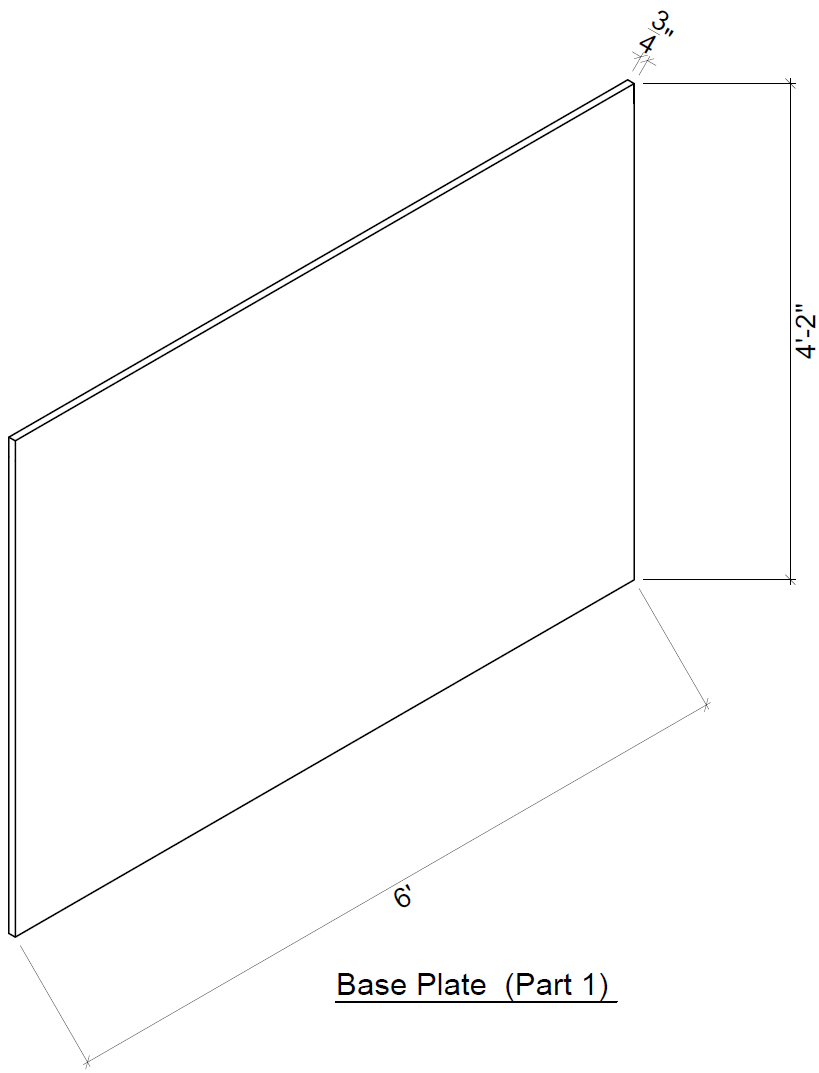


NOTE:

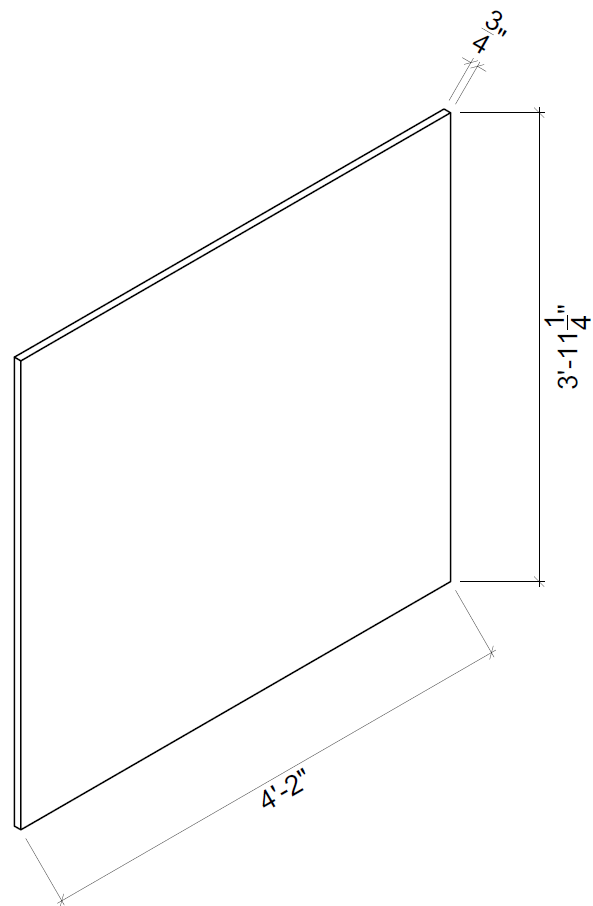
1. Weld MK801 type rebar to anchor plates (without shear studs).
2. Weld shear studs to anchor plates.
3. Tie MK401 type rebar to the MK801 type rebar.
4. Tie MK404 type rebar to MK401 type rebar per sheet 13.
5. Tie MK402 to the setup in 3 above in the transverse direction.
6. On the setup in 4 above tie MK403 type rebar in the longitudinal direction.

Rebar Layout

Pile Restraint				Revisions:	2020-08-26	2021-12-15
					2021-03-10	
Rebar Layout	2019-05-24	FAMU-FSU College of Engineering	Sheet 17 of 31		2021-03-15	

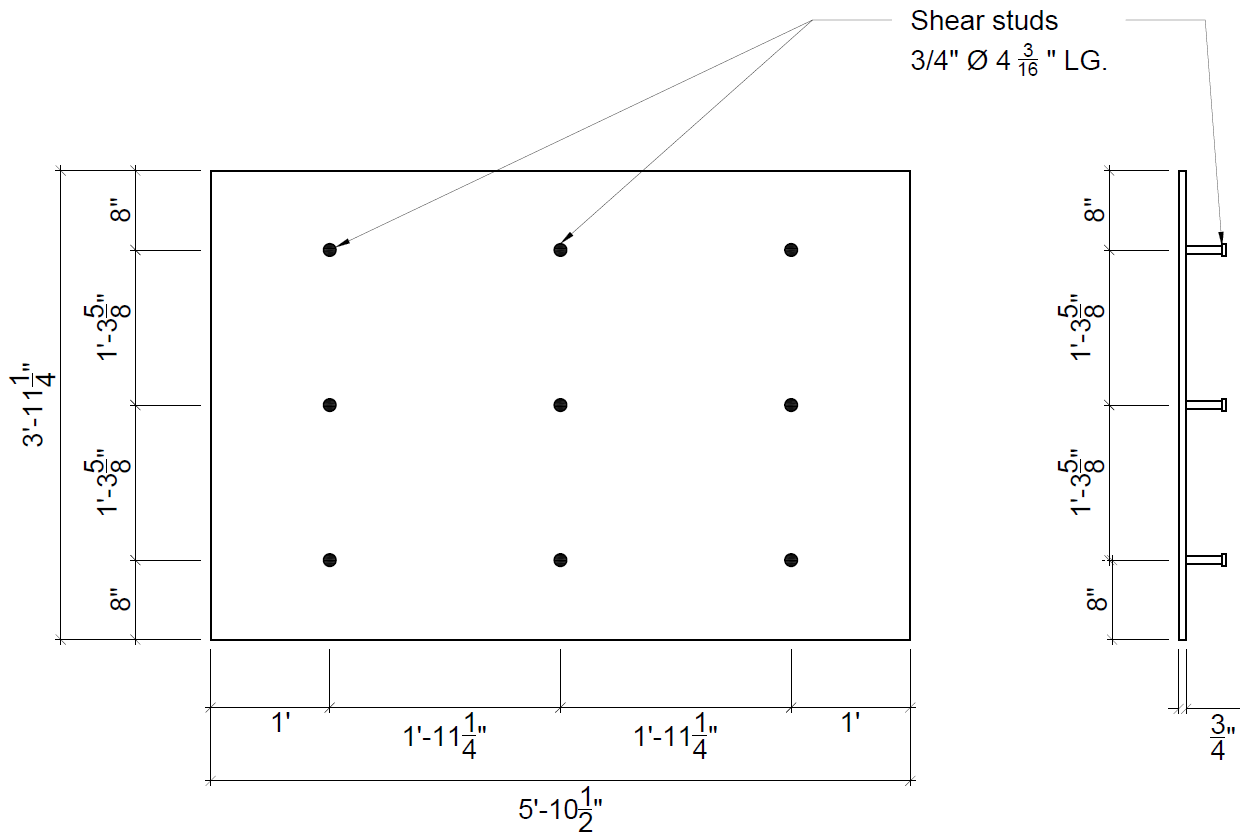


Base Plate (Part 1)



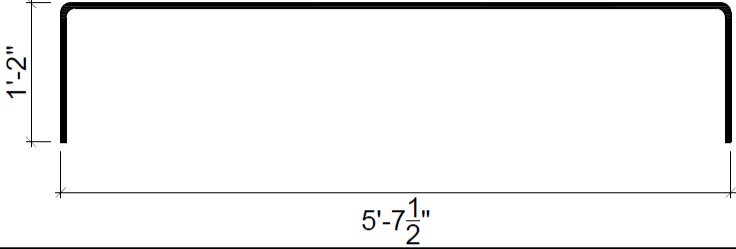
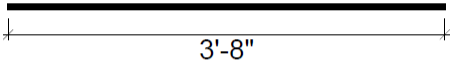
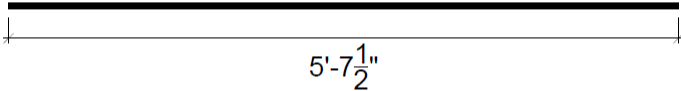
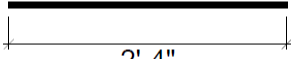
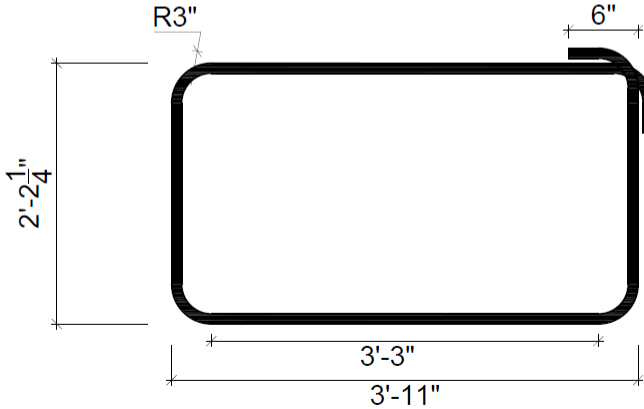
Part 2 x 2

Pile Restraint				Revisions:	2020-08-26	2021-12-15
Plate Details	2019-05-24	FAMU-FSU College of Engineering	Sheet 18 of 31		2021-03-10	
					2021-03-15	



Part 3 x 2

Pile Restraint				Revisions:	2020-08-26	2021-12-15
					2021-03-10	
					2021-03-15	
Plate Details	2019-05-24	FAMU-FSU College of Engineering	Sheet 19 of 31			

Bar Size	Details	Mark No.	Quantity		
No. 4		MK401	6		
No. 4		MK402	10		
No. 4		MK403	4		
No. 4		MK404	4		
No. 8		MK801	2		
Pile Restraint		Revisions:	2020-08-26	2021-12-15	
Rebar details	2019-05-24		FAMU-FSU College of Engineering	Sheet 20 of 31	2021-03-10
					2021-03-15

PILE SUPPORT

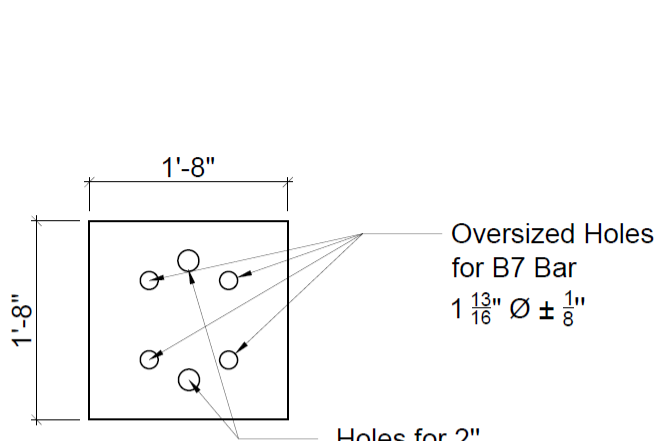
General Notes:

- Grade 50 steel shall be used in the construction of the pile support
- Proper welding procedure shall be followed using a filler metal of at least 70 ksi tensile strength
- Bolt hole pattern on bottom plate (plate A) shall follow the existing bolt holes on the FDOT strong floor

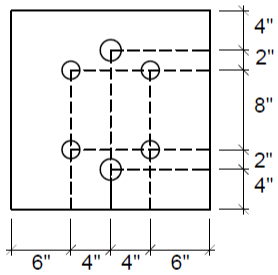
Procedures:

1. Weld Plates A and B on either side of the W-Section per sheet 23.
2. Bolt the support assembly to the strong floor following at points 1, 2, 3 and 4 per sheet 24.
3. Place teflon sheets on the supports to reduce the transfer of shear force into the foundation.
4. Place pile restraint blocks as shown on sheet 27
5. Place FDOT load blocks next to the support assemblies to provide lateral support for the pile.

Pile Support				Revisions:	2020-08-26	2021-12-15
					2021-03-10	
General Notes and Procedures	2019-05-24	FAMU-FSU College of Engineering	Sheet 21 of 31		2021-03-15	

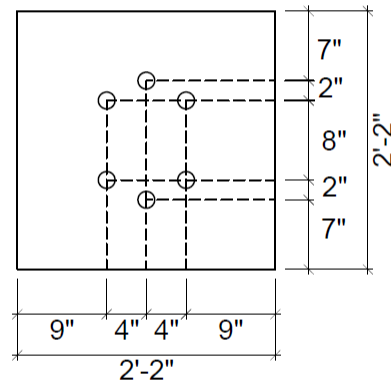
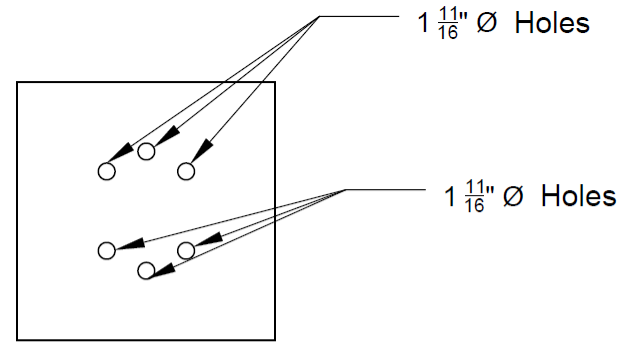


Holes for 2" Shear Pin
 $2 \frac{1}{8} \text{ } \varnothing \pm \frac{1}{16}$



Elevation

Plate A Details



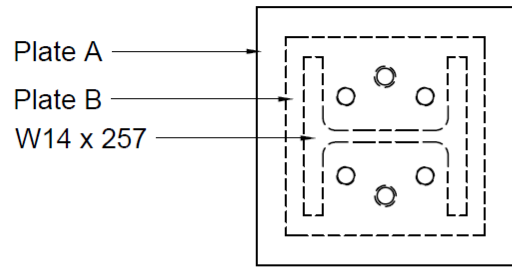
Plan



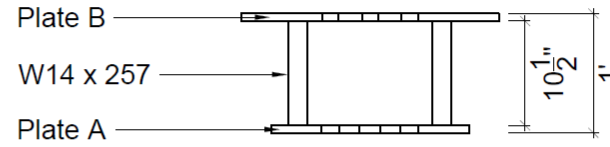
Elevation

Plate B Details

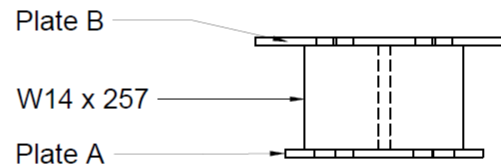
Pile Support				Revisions:	2020-08-26	2021-12-15
Support Member Details	2019-05-24	FAMU-FSU College of Engineering	Sheet 22 of 31		2021-03-10	
					2021-03-15	



Plan



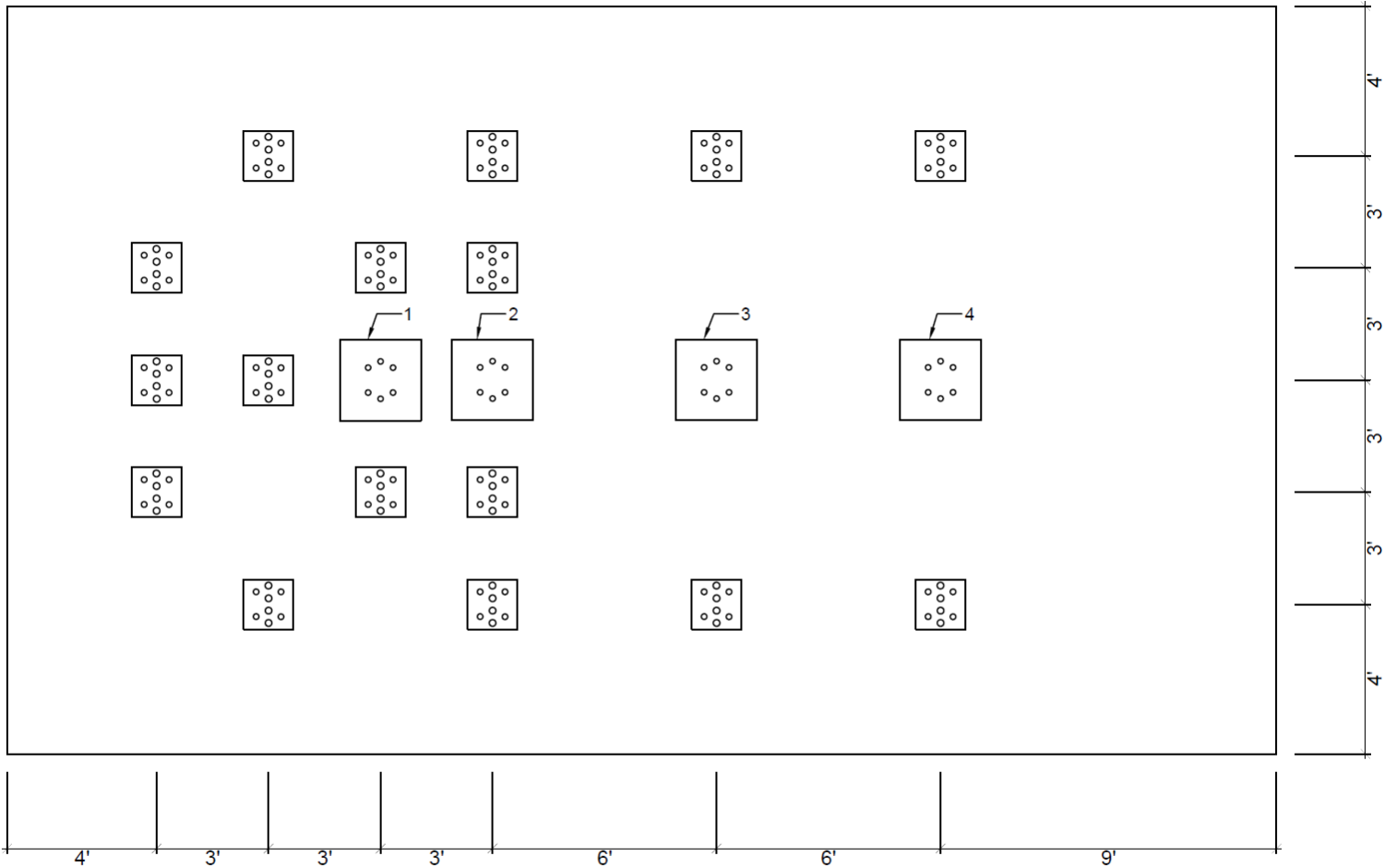
Elevation



Front View

Support Assembly x 4

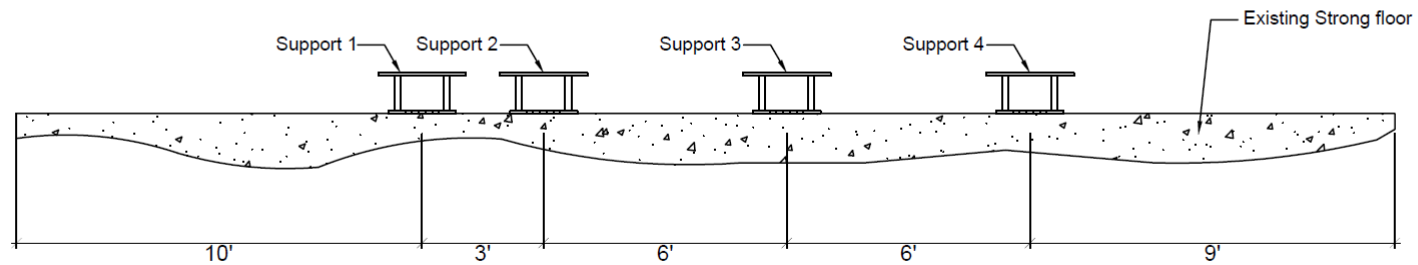
Pile Support				Revisions:	2020-08-26	2021-12-15
Support Member Details	2019-05-24	FAMU-FSU College of Engineering	Sheet 23 of 31		2021-03-10	
					2021-03-15	



NOTE:

Pile supports provided on the existing strong floor are at points 1, 2, 3 and 4.

Pile Support				Revisions:	2020-08-26	2021-12-15
					2021-03-10	
Plan view	2019-05-24	FAMU-FSU College of Engineering	Sheet 24 of 31		2021-03-15	

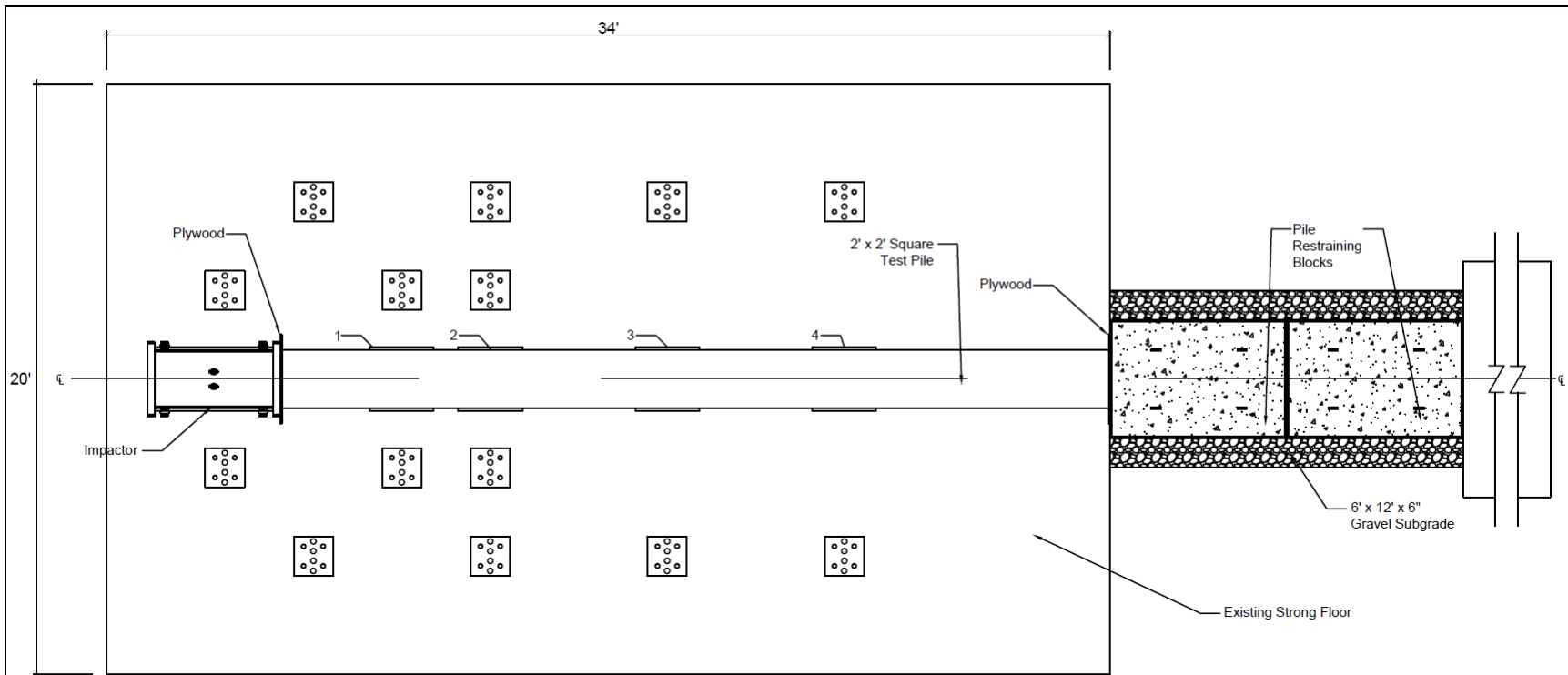


SECTION

NOTE:

Supports are bolted to the strong floor following existing bolt layout on the floor.

Pile Support				Revisions:	2020-08-26	2021-12-15
Section A-A					2021-03-10	
2019-05-24	FAMU-FSU College of Engineering	Sheet 25 of 31	2021-03-15			



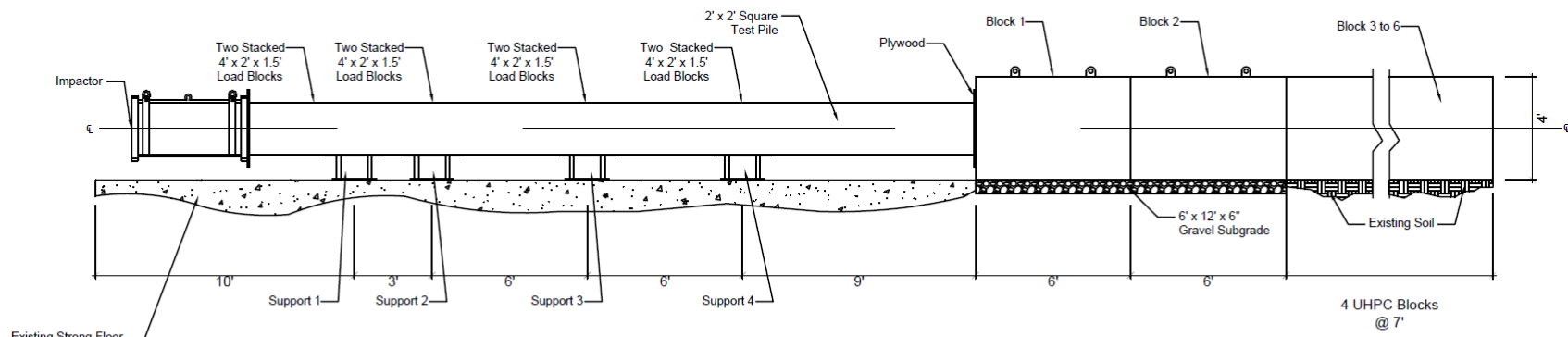
Impact Test Set-up Plan View

NOTE:

Pile supports provided on the existing strong floor are at points 1, 2, 3 and 4.

LB 1 & 2, LB 3 & 4 to LB 15 & 16 represent stacked load blocks providing lateral support on either side of the pile supports.

Impact Test Set-up				Revisions:	2020-08-26	2021-12-15
Impact Test Set-up Plan View					2021-03-10	
2019-05-24	FAMU-FSU College of Engineering	Sheet 26 of 31	2021-03-15			



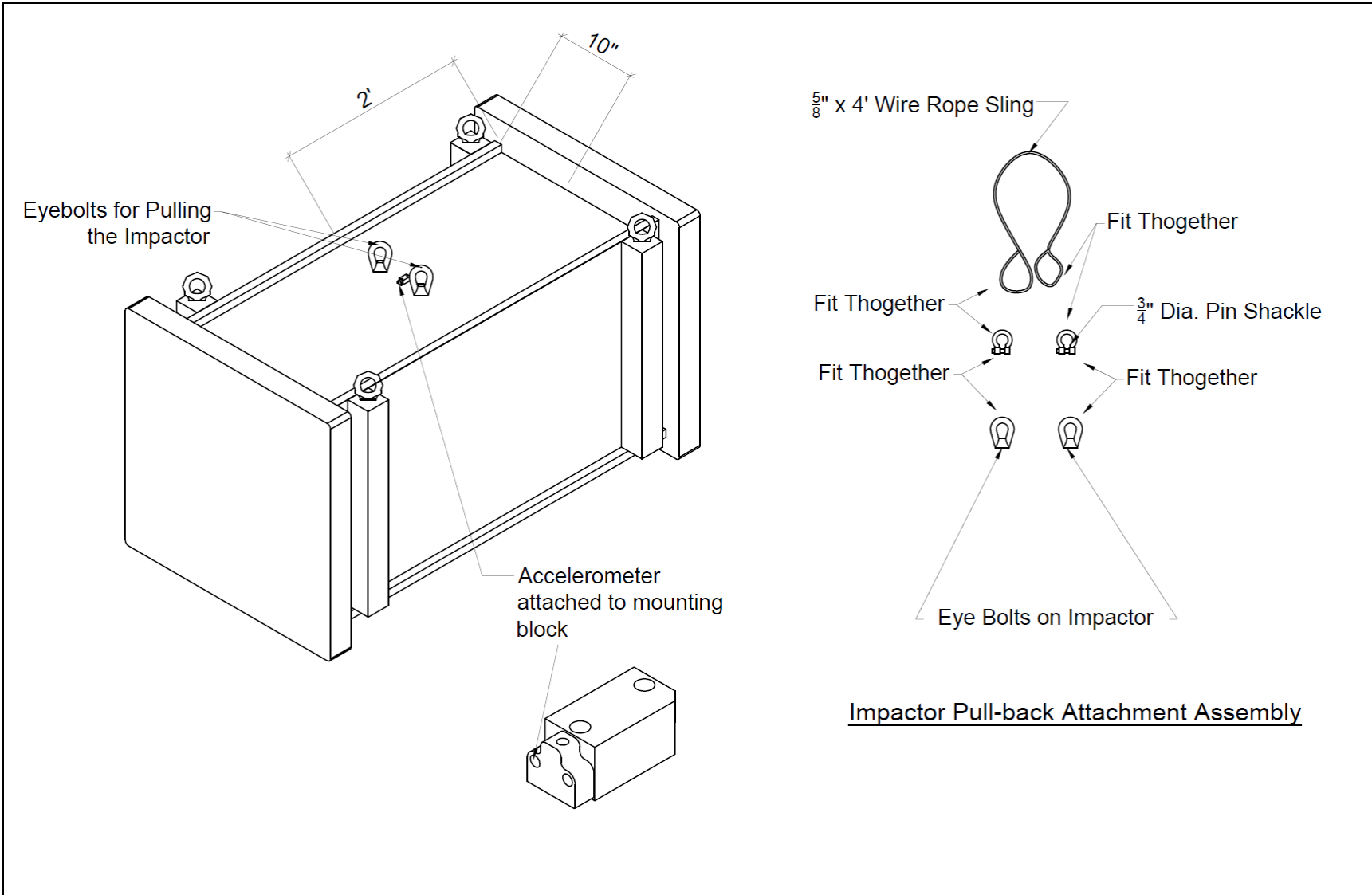
Impact Test Set-up Elevation

NOTE:

Extra restraint blocks placed behind blocks 1 and 2 as shown above.

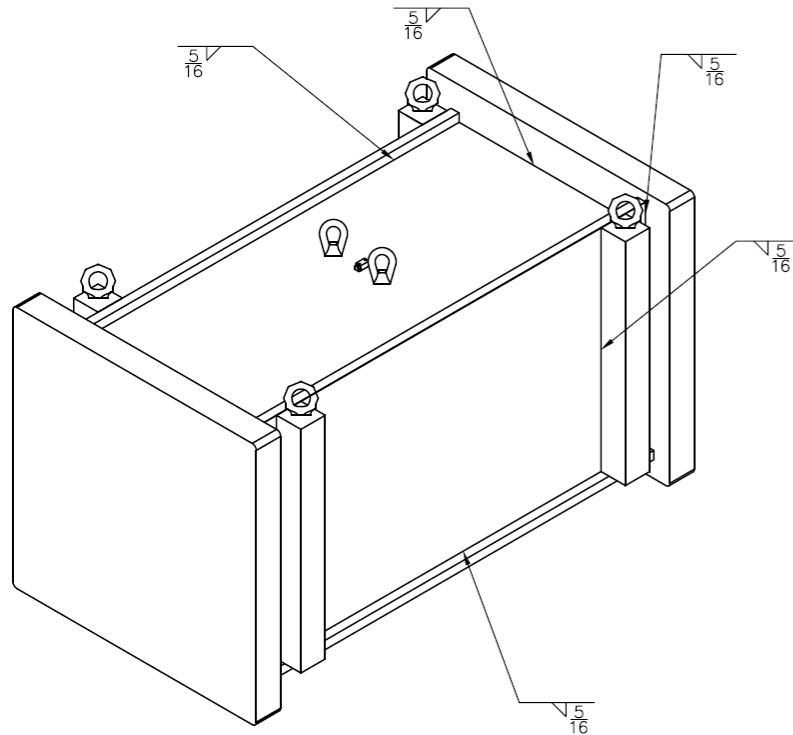
FDOT load blocks placed for lateral support on either side of the pile supports.

Impact Test Set-up				Revisions:	2020-08-26	2021-12-15
Impact Test Set-up Elevation					2021-03-10	
2019-05-24	FAMU-FSU College of Engineering	Sheet 27 of 31	2021-03-15			

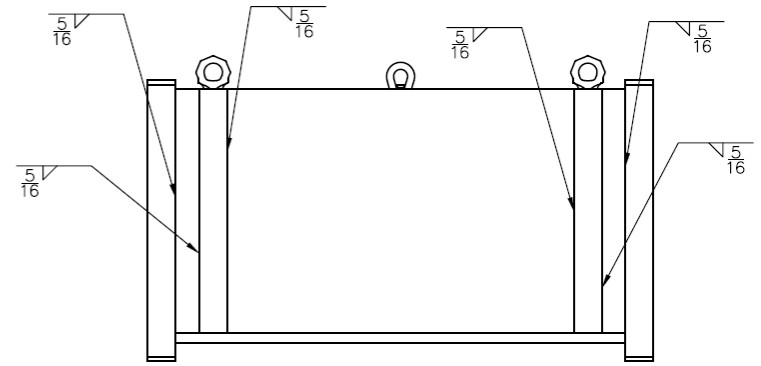


Impactor Pull-back Attachment Assembly

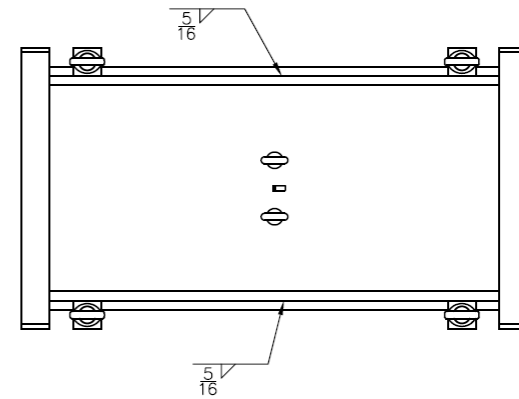
Impactor Pull-back Attachment				Revisions:	2020-08-26	2021-12-15
					2021-03-10	
Impactor Pull-back Attachment	2019-05-24	FAMU-FSU College of Engineering	Sheet 28 of 31		2021-03-15	



Isometric view

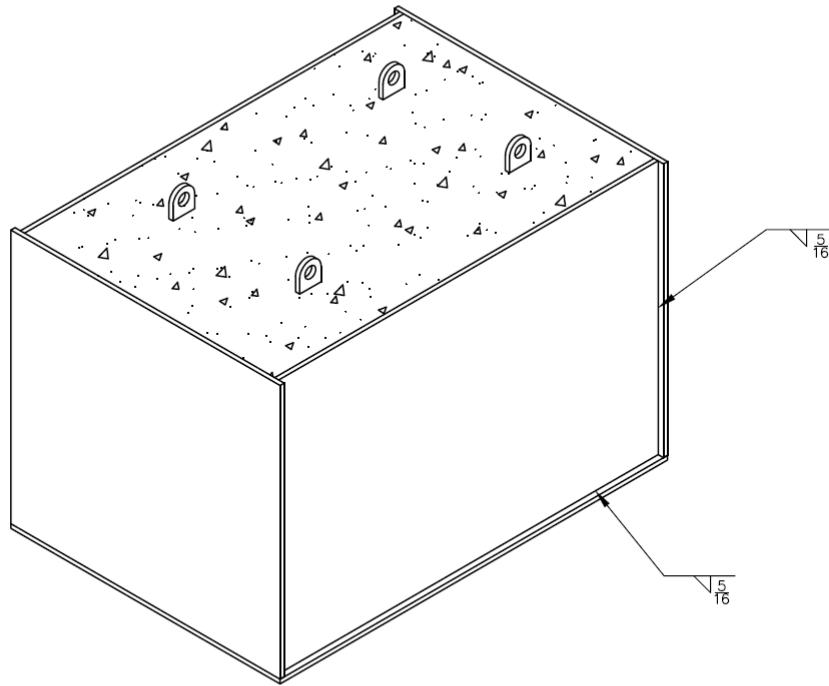


Elevation

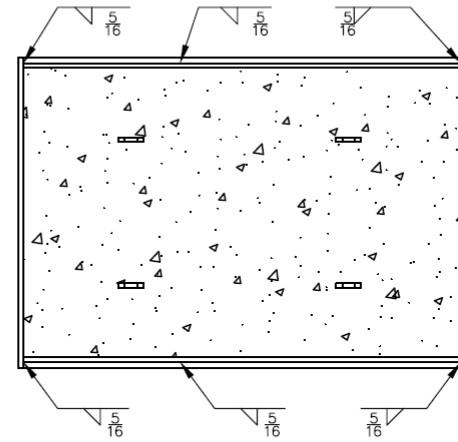


Plan View

Location of Welds				Revisions:	2020-08-26	2021-12-15
Location of Welds on Impactor	2019-05-24	FAMU-FSU College of Engineering	Sheet 29 of 31		2021-03-10	
					2021-03-15	

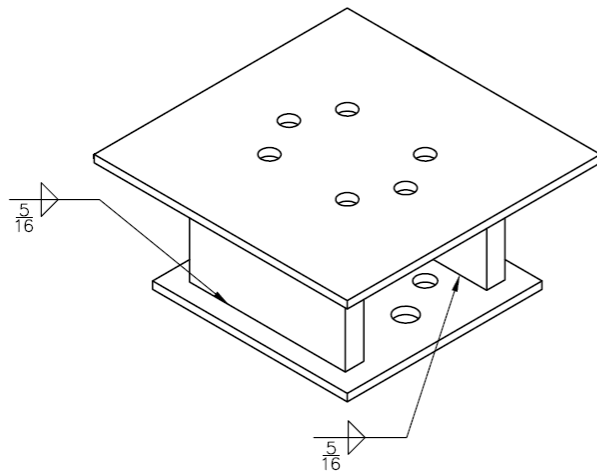


Isometric View

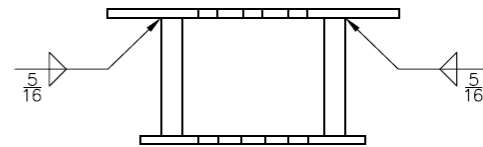


Plan View

Location of Welds				Revisions:	2020-08-26	2021-12-15
Location of Welds on Restraint	2019-05-24	FAMU-FSU College of Engineering	Sheet 30 of 31		2021-03-10	
					2021-03-15	



Isometric View



Elevation

Location of Welds				Revisions:	2020-08-26	2021-12-15
Location of Welds on Support	2019-05-24	FAMU-FSU College of Engineering	Sheet 31 of 31		2021-03-10	
					2021-03-15	

Appendix B. Spiral Size, Shear Capacity, Prestress Loss, Moment Capacity, and Driving Stress Limit Calculations.

B.1. Size of CFRP and GFRP Spiral Based on Force Equilibrium

The approach in this section assumes that the strength reduction because of spalling should be equal to the strength gain of the concrete core resulting from confinement. The following information was used for the calculations:

Compressive strength of concrete, $f'_c = 8.5$ ksi

Gross area, $A_g = 574$ in²

Concrete cover = 3 in

Core area, $A_{core} = 324$ in.²

Spiral spacing, $s = 1$ in. (for steel and CFRP spirals) or 1.5 in (for GFRP spiral), in the confinement provided at the pile top and the pile tip.

Core width, $b_c = 18$ in.

Yield strength of steel transverse reinforcement, $f_{yh} = 70$ ksi (ASTM A1064-18a)

Tensile strength of bent FRP bars, $f_{fb} = \left(0.05 \frac{r_b}{d_b} + 0.3\right) f_{fu} \leq f_{fu}$ (ACI 440.1R-15)

Assumed curvature of bent stirrup bars, $\frac{r_b}{d_b} = 4$

Environmental reduction factor, $C_E = 1.0$ for internal CFRP spiral (AASHTO, 2018) or 0.7 for GFRP spiral assuming concrete exposure to earth and weather (ACI 440.1R-15).

Design tensile strength, $f_{fu} = C_E \times f_{fu}^*$

The guaranteed ultimate tensile strength, $f_{fu}^* = 361.9$ ksi (for 0.2Ø CFRP spiral) or 120 ksi (for #3 GFRP spiral), according to FDOT (2019)

According to Section 5.11.4.1.4 of AASHTO (2017), force equilibrium requires that the minimum total cross-sectional area in a direction for a square section be no less than Equation (B.1) and Equation (B.2). The results for the minimum areas are summarized in Table B.1.

$$A_{sh} = 0.3sb_c \frac{f'_c}{f_{yh}} \left(\frac{A_g}{A_c} - 1 \right) \quad (B.1)$$

$$A_{sh} = 0.12sb_c \frac{f'_c}{f_{yh}} \quad (B.2)$$

Table B.1: AASHTO requirement for the required total cross-sectional area A_{sh} of transverse reinforcement in the direction considered.

Spiral Type	A_{sh} in. ²
Steel	0.357
CFRP	0.138
GFRP	0.893

f_{yh} in Equation (B.1) and Equation (B.2). were replaced by the bent strength, f_{fb} , of CRFP or GFRP transverse reinforcement.

For a square transverse reinforcement $A_{sh} = 2A_{sp}$. Table B.2 shows the resulting required reinforcement area (A_{sp}) and diameter (d_{sp}). The bar diameters in Table suggest that Equation (B.1) and Equation (B.2) are applicable to piles in seismic regions only, and therefore cannot be used to predict or verify the requires spiral sizes in this project.

Table B.2: Required area of transverse reinforcements based on AASHTO equations

Spiral Type	A_{sp} in. ²	d_{sp} in.
Steel	0.178	0.48
CFRP	0.069	0.30
GFRP	0.447	0.75

B.2. Prestress Loss Calculations

Strand properties

Elastic modulus of strand, $E_{ps} = 28500000$ psi

Area of one strand, $A_{strand} = 0.167$ in.² (0.5" ϕ (special) Grade 270 Low-lax strand)

Guaranteed ultimate strength of strand, GUTS = 270000 psi

Number of strands = 20

Initial prestress in each of the 20 strands, $f_{pi} = 202500$ psi (75% of GUTS)

Initial force in each of the 20 strands, $P_i = 33.82$ kips

Concrete properties

$f'_{ci} = 4000$ psi (at 24 hours)

$E_{ci} = 57000\sqrt{f'_{ci}} = 3604996$ psi

$f'_c = 6000$ psi (at 28 days)

$E_c = 57000\sqrt{f'_c} = 5255140$ psi

Length of pile, $L = 336$ in.

Losses due to elastic shortening of concrete (ES):

$$ES = \frac{K_{es}E_{ps}f_{cir}}{E_{ci}} \quad (B.3)$$

where:

$K_{es} = 1.0$ for pretensioned components

E_{ps} = modulus of elasticity of prestressing strands (28.5×10^6 psi)

E_{ci} = modulus of elasticity of concrete at time prestress is applied, psi

f_{cir} = net compressive stress in concrete at center of gravity of prestressing force immediately after the prestress has been applied to the concrete, psi:

$$f_{cir} = k_{cir} \left(\frac{P_i}{A_g} + \frac{P_i e^2}{I_g} \right) - \frac{M_g e}{I_g} \quad (B.4)$$

where:

$k_{cir} = 0.9$ for pretensioned components

$P_i =$ initial prestress force, lb.

$e =$ eccentricity of center of gravity of tendons with respect to center of gravity of concrete at the cross section considered, in.

$A_g =$ area of gross concrete section at the cross section considered, in.²

$I_g =$ moment of inertia of gross concrete section at the cross section considered, in.⁴

$M_g =$ bending moment due to dead weight of prestressed component and any other permanent loads in place at time of prestressing, lb.-in.

Therefore,

$K_{es} = 1.0$

$k_{cir} = 0.9$

$P_i = 33.82$ kips

$e = 0$

$A_g = 574$ in.²

$I_g = 27647.7$ in.⁴

$M_g = 0$

$f_{cir} = 1060.48$ psi

ES = 8383 psi (for each of the 20 strands)

Losses due to creep of concrete (CR):

$$CR = k_{cr} \left(\frac{E_{ps}}{E_c} \right) (f_{cir} - f_{cds}) \quad (B.5)$$

where:

$k_{cr} = 2.0$ for normal weight concrete and 1.6 for sand-lightweight concrete

E_c = modulus of elasticity of concrete at 28 days, psi

f_{cds} = stress in concrete at center of gravity of prestressing force due to all superimposed, permanent dead loads that are applied to the member after it has been prestressed, psi

$$f_{cds} = \frac{M_{sd}(e)}{I_g} \quad (B.6)$$

where:

M_{sd} = moment due to all superimposed, permanent dead load and sustained load applied after prestressing, lb.-in.

Therefore,

$$k_{cr} = 2$$

$$f_{cds} = 0 \text{ (no eccentricity)}$$

$$\mathbf{CR = 11503 \text{ psi}}$$

Losses due to shrinkage of concrete (SH):

$$SH = (8.2 \times 10^{-6})K_{sh}E_{ps} \left(1 - 0.06 \frac{V}{S}\right) (100 - RH) \quad (B.7)$$

where:

$K_{sh} = 1.0$ for pretensioned components

$\frac{V}{S}$ = volume-to-surface ratio

RH = average ambient relative humidity (given in Design Aid 4.11.12 of PCI (2010)).

Therefore,

$$K_{sh} = 1.0$$

$$V = A_g \times L = 192864 \text{ in.}^3$$

$$S = 34479 \text{ in.}^2$$

$$\frac{V}{S} = 5.59 \text{ in}$$

$$RH = 75 \%$$

$$\mathbf{SH = 3882 \text{ psi}}$$

Losses due to relaxation of strands (RE):

$$RE = [K_{re} - J](SH + CR + ES)]C \quad (B.8)$$

where:

Values for K_{re} and J are obtained from Table 5.7.1 of PCI (2010), and for values of coefficient C see Table 5.7.2 of PCI (2010).

$$C = \left[\left(\frac{f_{pi}}{f_{pu}} \right) / 0.21 \right] \left[\left(\left(\frac{f_{pi}}{f_{pu}} \right) / 0.9 \right) - 0.55 \right] \quad \text{for } \left(\frac{f_{pi}}{f_{pu}} \right) > 0.54$$

$$C = \left(\frac{f_{pi}}{f_{pu}} \right) / 4.25 \quad \text{for } \left(\frac{f_{pi}}{f_{pu}} \right) < 0.54$$

$$K_{re} = 5000 \text{ (taken from Table 5.7.1 of PCI (2010))}$$

$$J = 0.04 \text{ (taken from Table 5.7.1 of PCI (2010))}$$

$$SH + CR + ES = 23768 \text{ psi}$$

$$\text{ultimate strength of prestressing, } f_{pu} = 270000 \text{ psi}$$

$$f_{pi} = 202500 \text{ psi}$$

$$\frac{f_{pi}}{f_{pu}} = 0.750$$

$$C = 1.012$$

$$\mathbf{RE = 4098 \text{ psi}}$$

Total prestress losses, (TL):

$$TL = ES + CR + SH + RE \quad (B.9)$$

TL = 27866 psi

$$\text{Percentage prestress loss, TL \%} = \frac{TL}{f_{pi}} \times 100 = 13.76 \%$$

Stress in each strand after losses (f_{ps}):

$$f_{ps} = f_{pi} - TL \quad (B.10)$$

$$f_{ps} = 174635 \text{ psi}$$

$$\text{Force in each strand after losses, } P_{ps} = f_{ps} \times A_{strand} = 29.16 \text{ kips}$$

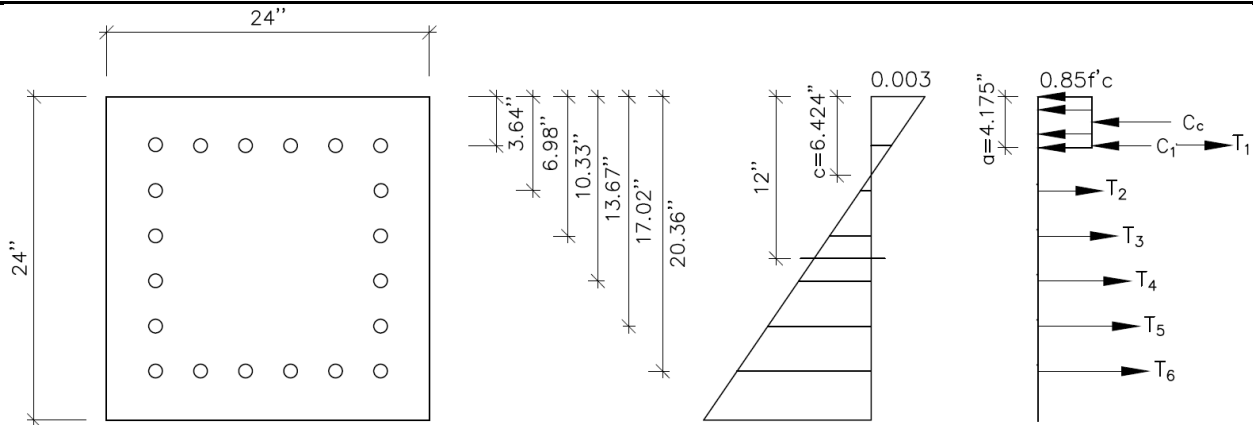
$$\text{Force equivalent to effective prestress, } P_e = 20 \times P_{ps}$$

$$\text{Compressive stress in pile due to effective prestress, } f_{pe} = [P_e/A_g]$$

Compressive stress in pile due to effective prestress, $f_{pe} = 1.016 \text{ ksi}$

B.3. Moment Capacity Calculations

24 in. \times 24 in. pile with 20 0.5" ϕ (special) strands



Parameters

$$A_{strand} = 0.167 \text{ in.}^2$$

GUTS = 270 ksi

$f_{pi} = 202.5$ ksi (75% of GUTS)

$P_i = 33.82$ kips

Initial strain in strands, $\epsilon_{psi} = 0.007105$ in./in.

$f'_{ci} = 8.5$ ksi

$\beta_1 = 0.65$

Neutral axis, $c = 6.424$ in. (based on iterations)

Stress block depth, $a = 4.175$ in.

Concrete strain limit, $\epsilon_c = 0.003$ in./in.

$E_{ps} = 28500$ ksi

Pile width, $b = 24$ in.

Pile height, $h = 24$ in.

Force in concrete, C_c :

$$C_c = 0.85f'_c ab \quad (B.11)$$

$C_c = -716.78$ kips (negative sign represents compression).

Concrete moment (taken about $\frac{h}{2}$), $M_c = 7104.96$ kip – in

Force and moment due to prestressing strands:

f_{ps} = Effective stress in prestressing after losses

ϵ_{ps} = Effective strain in prestressing after losses = $\frac{f_{ps}}{E_{ps}}$

ϵ_p = Strain in prestressing due to applied moment = $\epsilon_c \left[\frac{d}{c} - 1 \right]$

ϵ_{final} = Strain in prestressing due at ultimate moment = $\epsilon_{ps} + \epsilon_p$

$$f_{\text{final}} = \text{Stress in the prestressing at ultimate moment} = E_{\text{ps}} \times \epsilon_{\text{final}} \text{ or } 270 - \left[\frac{0.004}{\epsilon_{\text{final}} - 0.007} \right] \text{ for}$$

$$\epsilon_{\text{final}} > 0.0085 \text{ (Design Aid 15.3.3 of PCI (2010))}$$

$$F_{\text{strands}} = \text{Force in prestressing at ultimate moment} = \text{Number of strands per layer} \times A_{\text{strand}} \times f_{\text{final}}$$

Table B.3: Strand moment calculation

Nominal initial force (kips)	No of strands per layer	A_{strand} (in. ²)	d_p (in)	f_{ps} (ksi)	ϵ_{ps} (in./in.)	ϵ_p (in./in.)	ϵ_{final} (in./in.)	f_{final} (ksi)	F_{strands} (kips)	subtract		
										force if strand is in comp (kips)	F_{strands} minus holes (kip)	M_{ps} about h/2 (kip-in)
33.82	6	1.002	3.64	174.63	0.00613	-0.00130	0.00483	137.58	137.73	-7.24	145.10	-1213.01
33.82	2	0.334	6.98	174.63	0.00613	0.00026	0.00639	182.04	60.80	0.00	60.80	-3105.22
33.82	2	0.334	10.33	174.63	0.00613	0.00182	0.00795	226.63	75.69	0.00	75.69	-126.41
33.82	2	0.334	13.67	174.63	0.00613	0.00338	0.00951	254.07	84.86	0.00	84.86	141.72
33.82	2	0.334	17.02	174.63	0.00613	0.00495	0.01108	260.19	86.90	0.00	86.90	436.25
33.82	6	1.002	20.36	174.63	0.00613	0.00651	0.01264	262.90	263.43	0.00	263.43	2202.26
											716.78	1135.59

$$\text{Sum of forces} = C_c + F_{\text{strands}} = 0.00 \text{ kips}$$

$$\text{Nominal moment, } M_n = M_c + M_{\text{ps}} = 8240.55 \text{ kip-in}$$

B.4. Calculations for Axial Capacities and Compression Driving Stress Limits

Parameters

$$f'_c = 8500 \text{ psi}$$

$$A_g = 574 \text{ in.}^2$$

$$f_{pe} = 1.004 \text{ ksi}$$

Allowable service axial capacity, N:

$$N = (0.33f'_c - 0.27f_{pe})A_g \text{ (according to PCI (1999, 2010))} \quad (\text{B.12})$$

$$N = 1455 \text{ kips}$$

Nominal axial load capacity, P_o:

$$P_o = (0.85f'_c - 0.6f_{pe})A_g \text{ (according to PCI (1999))} \quad (\text{B.13})$$

$$P_o = 3801 \text{ kips}$$

The maximum allowable driving stresses (compression stress limits):

$$S_{apc-AASHTO} = (0.85f'_c - f_{pe}) \text{ (AASHTO (2017) compression driving stress limit)} \quad (\text{B.14})$$

$$S_{apc-AASHTO} = 6.22 \text{ ksi}$$

$$S_{apc-FDOT} = (0.7f'_c - 0.75f_{pe}) \text{ (FDOT (2019) compression driving stress limit)} \quad (\text{B.15})$$

$$S_{apc-FDOT} = 5.20 \text{ ksi}$$

The maximum allowable driving stresses (tension stress limits):

$$S_{apt-AASHTO} = 0.095\sqrt{f'_c} + f_{pe} \text{ (AASHTO (2017) tension driving stress limit in normal environment, ksi)} = 1.29 \text{ ksi} \quad (\text{B.16})$$

$$S_{apt-AASHTO} = f_{pe} \text{ (AASHTO (2017) tension driving stress limit in corrosive environment, ksi)} = 1.02 \text{ ksi} \quad (\text{B.17})$$

$$S_{apt-FDOT} = 6.5(f'_c)^{0.5} + 1.05f_{pe} \text{ (FDOT (2019) tension driving stress limit in psi)} \quad (\text{B.18})$$

where

$$S_{apt-FDOT} = 1.65 \text{ ksi}$$

Equivalent force for the maximum allowable driving stresses (Compression stress limits):

$$P_{\text{AASHTO}} = S_{\text{apc-AASHTO}} \times A_g = 3571 \text{ kips}$$

$$P_{\text{FDOT}} = S_{\text{apc-FDOT}} \times A_g = 2983 \text{ kips}$$

B.5. Calculations for Shear Capacity of Transverse Reinforcement

The nominal shear resistance, V_n :

$$V_n = \min \left((V_c + V_s + V_p), (0.25f'_c b_v d_v + V_p) \right) \quad (\text{B.19})$$

where

V_c = concrete contribution to nominal shear resistance

V_s = transverse reinforcement contribution to nominal shear resistance

V_p = nominal shear resistance from prestressing (= 0 for straight strands)

d_v = effective shear depth = $\max \left(d_e - \frac{a}{2}, 0.9d_e, 0.72h \right)$

$d_v = \max(9.18 \text{ in.}, 10.8 \text{ in.}, 17.3 \text{ in.})$

$$d_e = \frac{A_s f_y d_p + A_{sp} f_{sp} d_p}{A_s f_y + A_{sp} f_{sp}}$$

Note: $A_s f_y$ applies to non-prestressed steel reinforcement, which is taken as zero in this calculation.

b_v = effective width = b_w

$f'_c = 8.5 \text{ ksi}$

Concrete contribution to nominal shear resistance, V_c :

$$V_c = \min (V_{ci}, V_{cw}) \text{ (Hawkins et al. (2005))} \quad (\text{B.20})$$

where

V_{ci} = nominal shear resistance provided by concrete when inclined cracking results from combined shear and moment (flexure shear) = $0.02\sqrt{f'_c}b_vd_v + V_d + \frac{V_iM_{cr}}{M_{max}}$

V_{cw} = nominal shear resistance provided by concrete when inclined cracking results from excessive principal tensions in web (web shear) = $(0.06\sqrt{f'_c} + 0.30f_{pc})b_vd_v + V_p$

V_d = shear force at section due to unfactored dead load

V_i = factored shear force at section due to externally applied loads occurring simultaneously with M_{max}

M_{cr} = moment causing flexural cracking at section due to externally applied loads

M_{max} = maximum factored moment at section due to externally applied loads

f_{pc} = compressive stress in concrete after allowance for all prestress losses at centroid of cross section

$V_c = 85.19$ kips

Transverse reinforcement contribution to nominal shear resistance, V_s :

The following shows the calculation of V_s for a steel spiral in a standard 24-inch square prestressed concrete pile.

$$V_s = \frac{A_v f_y d_v \cot(\theta)}{s} \text{ (Equation C5.8.3.3-1 of AASHTO (2012))} \quad (\text{B.21})$$

where

s = spacing of transverse reinforcement (taken at largest spacing along the pile) = 6 in

A_v = area of all vertical legs of stirrup = $2 \times$ area of transverse reinforcement = $2 \times 0.034 = 0.068 \text{ in.}^2$

θ = angle of inclination for diagonal compressive stresses

$$\cot(\theta) = \min \left[1 + 3 \left(\frac{f_{pc}}{\sqrt{f'_c}} \right), 1.8 \right] \text{ if } V_{ci} > V_{cw}, \cot(\theta) = 1 \text{ } V_{ci} < V_{cw} \text{ (Article 5.8.3.4.3 of}$$

AASHTO (2012))

From excel calculations $V_{ci} < V_{cw}$

$V_s = 13.71$ kips

Therefore $V_n = V_c + V_s = 87.15$ kips (for pile with steel spiral)

Selection of GFRP transverse reinforcement

The aim here is to determine which GFRP rebar provides similar shear resistance to the shear resistance calculated for the steel spiral as described above.

Trial #1

Try #2 GFRP rebar.

Bar diameter, $d_b = 0.25$ in.

Area of FRP bar, $A_f = 0.049$ in.²

Area of shear reinforcement, $A_{fv} = 2 \times A_f = 0.098$ in.²

The guaranteed ultimate tensile load, $F_{fu}^* = 6.10$ kips (FDOT (2019))

The guaranteed ultimate tensile strength, $f_{fu}^* = 124.49$ ksi

Modulus of elasticity, $E_{GFRP} = 6500$ ksi (ASTM D7957-17)

Design material properties:

Environmental reduction factor, $C_E = 0.7$ (Table 6.2, ACI 440.1R-15)

Design tensile strength, $f_{fu} = C_E \times f_{fu}^* = 87.14$ ksi

Assumed curvature of bent stirrup bars, $\frac{r_b}{d_b} = 4.0$

r_b = bend radius of the bar

d_v = effective depth = 17.28 in.

Determine design tensile stress in transverse reinforcement.

- a. Based on tensile strength of bent bars, $f_{fb} = \left(0.05 \frac{r_b}{d_b} + 0.3\right) f_{fu} \leq f_{fu}$ (ACI 440.1R-15)

$$f_{fb} = 43.57 \text{ ksi}$$

- b. Tensile strength based on a tensile strain limit (0.004) for a conservative prediction of tensile strength (ACI 440.1R-15)

$$f_{fv} = 0.004 E_{GFRP} \leq f_{fu}$$

$$f_{fv} = 26 \text{ ksi}$$

Determine shear resistance.

For FRP rectangular spirals, the shear contribution, $V_f = \frac{A_{fv} f_{fv} d_v \cot(\theta)}{s}$ (CSA-806)

s = spiral pitch (taken at largest spacing along the pile) = 6 in

- a. Based on tensile strength of bent bars, f_{fb}

$$V_{fb} = \frac{A_{fv} f_{fb} d_v \cot(\theta)}{s} = 12.30 \text{ kips}$$

- b. Based on tensile strain limit (0.004)

$$V_f = \frac{A_{fv} f_{fv} d_v \cot(\theta)}{s} = 7.34 \text{ kips}$$

V_{fb} and V_f are less than $V_s = 13.71$, #2 GFRP rebar is inadequate.

Trial #2

Try #3 GFRP rebar.

Bar diameter, $d_b = 0.375$ in.

Area of FRP bar, $A_f = 0.11$ in.²

Area of shear reinforcement, $A_{fv} = 2 \times A_f = 0.22$ in.²

The guaranteed ultimate tensile load, $F_{fu}^* = 13.20$ kips (FDOT (2019))

The guaranteed ultimate tensile strength, $f_{fu}^* = 120$ ksi

Modulus of elasticity, $E_{GFRP} = 6500$ ksi (ASTM D7957-17)

Design material properties:

Environmental reduction factor, $C_E = 0.7$ (Table 6.2, ACI 440.1R-15)

Design tensile strength, $f_{fu} = C_E \times f_{fu}^* = 84$ ksi

Assumed curvature of bent stirrup bars, $\frac{r_b}{d_b} = 4.0$

r_b = bend radius of the bar

d_v = effective depth = 17.28 in.

Determine design tensile stress in transverse reinforcement

- a. Based on tensile strength of bent bars, $f_{fb} = \left(0.05 \frac{r_b}{d_b} + 0.3\right) f_{fu} \leq f_{fu}$ (ACI 440.1R-15)

$$f_{fb} = 42 \text{ ksi}$$

- b. Tensile strength based on a tensile strain limit (0.004) for a conservative prediction of tensile strength (ACI 440.1R-15)

$$f_{fv} = 0.004 E_{GFRP} \leq f_{fu}$$

$$f_{fv} = 26 \text{ ksi}$$

Determine shear resistance.

For FRP rectangular spirals, the shear contribution, $V_f = \frac{A_{fv} f_{fv} d_v \cot(\theta)}{s}$ (CSA-806)

s = spiral pitch (taken at largest spacing along the pile) = 6 in.

θ = angle of inclination of diagonal compressive stresses

a. Based on tensile strength of bent bars, f_{fb}

$$V_{fb} = \frac{A_{fv} f_{fb} d_v \cot(\theta)}{s} = 26.61 \text{ kips}$$

b. Based on tensile strain limit (0.004)

$$V_f = \frac{A_{fv} f_{fv} d_v \cot(\theta)}{s} = 16.47 \text{ kips}$$

V_f and V_{fb} are greater than $V_s = 13.71$ kips, #3 GFRP rebar is adequate.

Shear contribution from the 0.2"-diameter CFRP spiral from Roddenberry et al. (2014)

Bar diameter, $d_b = 0.2$ in.

Area of FRP bar, $A_f = 0.0236$ in.²

Area of shear reinforcement, $A_{fv} = 2 \times A_f = 0.0472$ in.²

The guaranteed ultimate tensile load, $F_{fu}^* = 8.54$ kips

The guaranteed ultimate tensile strength, $f_{fu}^* = 361.9$ ksi

Modulus of elasticity, $E_{CFRP} = 22400$ ksi (requirements in FDOT (2023))

Design material properties:

Environmental reduction factor, $C_E = 1$ (AASHTO, 2018)

Design tensile strength, $f_{fu} = C_E \times f_{fu}^* = 361.9$ ksi

Assumed curvature of bent stirrup bars, $\frac{r_b}{d_b} = 4.0$

r_b = bend radius of the bar

d_v = effective depth = 17.28 in.

Determine design tensile stress in shear reinforcement.

- a. Tensile strength based on a tensile strain limit (0.004) for a conservative prediction of tensile strength (ACI 440.1R-15)

$$f_{fv} = 0.004E_{GFRP} \leq f_{fu}$$

$$f_{fv} = 89.6 \text{ ksi}$$

- b. Based on tensile strength of bent bars, $f_{fb} = \left(0.05 \frac{r_b}{d_b} + 0.3\right) f_{fu} \leq f_{fu}$ (ACI 440.1R-15)

$$f_{fb} = 180.93 \text{ ksi}$$

Determine shear resistance.

For continuous FRP rectangular spirals, the shear contribution of FRP spirals, $V_f = \frac{A_{fv} f_{fv} d_v \cot(\theta)}{s}$

(CSA 806)

s = spiral pitch (taken at largest spacing along the pile) = 6 in

θ = angle of inclination for diagonal compressive stresses

Conservative prediction based on tensile strain limit (0.004)

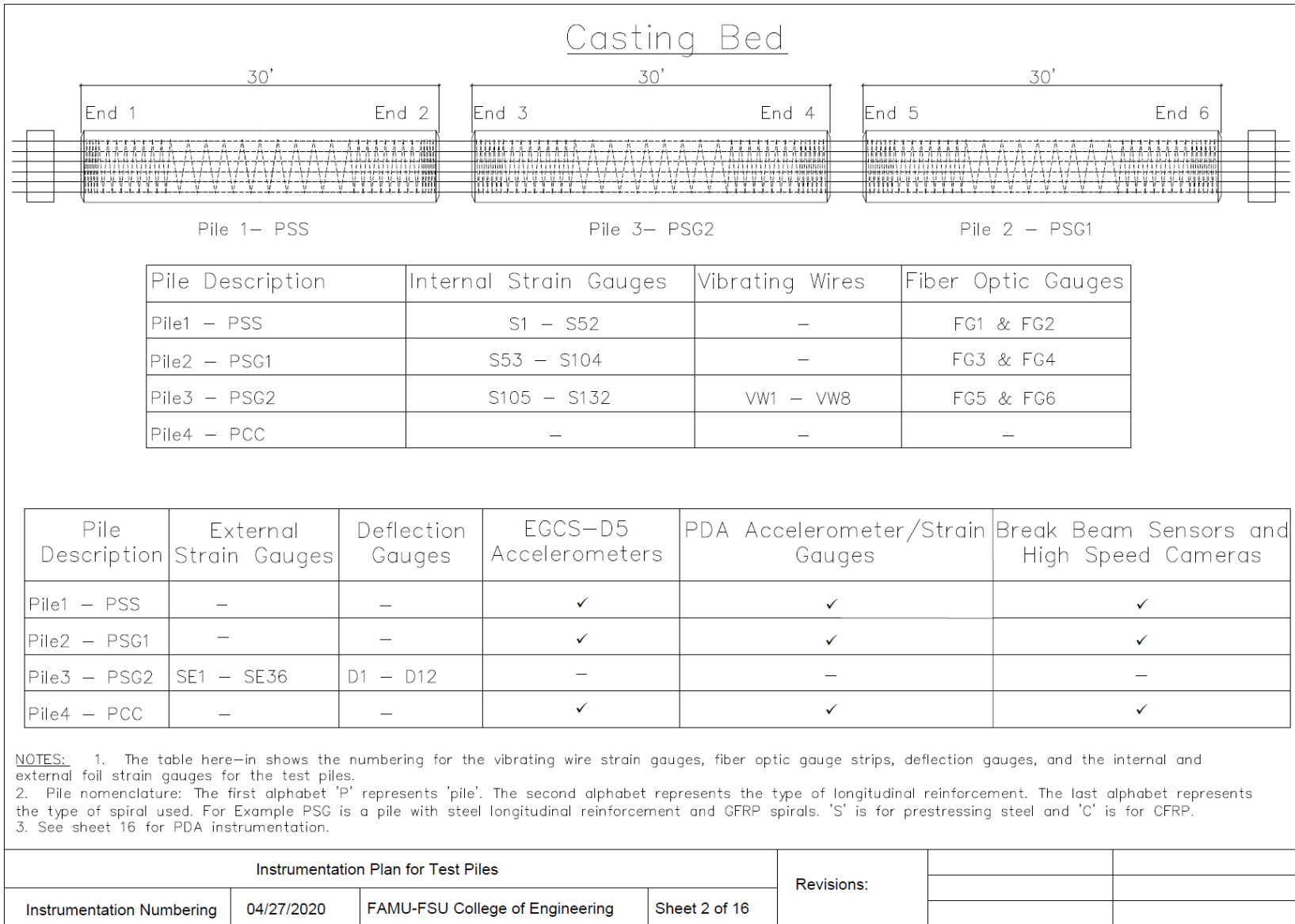
$$V_f = \frac{A_{fv} f_{fv} d_v \cot(\theta)}{s} = 9.13 \text{ kips}$$

- c. Based on tensile strength of bent bars, f_{fb}

$$V_{fb} = \frac{A_{fv} f_{fb} d_v \cot(\theta)}{s} = 18.45 \text{ kips}$$

V_{fb} is greater than $V_s = 13.71$ kips, while V_f is less than V_s .

C.2. Tests and Sensors Monitored



Tests and Sensors Being Monitored

For the tests number 1 to 4, the gauges are accompanied by green circles while the inactive gauges are accompanied by red circles.

1. Strand Detensioning: Fiber optic gauges in PSS, PSG1 and PSG2 will be monitored during the detensioning process.

Pile Description	Internal Strain Gauges	Vibrating Wires	Fiber Optic Gauges
Pile1 – PSS	S1 – S52 ●	–	FG1 & FG2 ●
Pile2 – PSG1	S53 – S104 ●	–	FG3 & FG4 ●
Pile3 – PSG2	S105 – S132 ●	VW1 – VW8 ●	FG5 & FG6 ●
Pile4 – PCC	–	–	–

Pile Description	External Strain Gauges	Deflection Gauges	EGCS–D5 Accelerometers	PDA Accelerometer/Strain Gauges	Break Beam Sensors and High Speed Cameras
Pile1 – PSS	–	–	✓ ●	✓ ●	✓ ●
Pile2 – PSG1	–	–	✓ ●	✓ ●	✓ ●
Pile3 – PSG2	SE1 – SE36 ●	D1 – D12 ●	–	–	–
Pile4 – PCC	–	–	✓ ●	✓ ●	✓ ●

Instrumentation Plan for Test Piles				Revisions:		
Tests and Sensors Monitored	04/27/2020	FAMU-FSU College of Engineering	Sheet 3 of 16			

Tests and Sensors Being Monitored

For the tests number 1 to 4, the gauges are accompanied by green circles while the inactive gauges are accompanied by red circles.

2. Impact Tests: Specimens PSS, PSG1 and PCC will be subjected to impact tests. In addition to the active gauges indicated, the accelerometer mounted on the impactor and PDA instrumentation on the piles will be monitored.

PILE DESCRIPTION	INTERNAL STRAIN GAUGES	VIBRATING WIRES	FIBER OPTIC GAUGES
Pile1 – PSS	S1 – S52 ●	–	FG1 & FG2 ●
Pile2 – PSG1	S53 – S104 ●	–	FG3 & FG4 ●
Pile3 – PSG2	S105 – S132 ●	VW1 – VW8 ●	FG5 & FG6 ●
Pile4 – PCC	–	–	–

PILE DESCRIPTION	EXTERNAL STRAIN GAUGES	DEFLECTION GAUGES	EGCS–D5 ACCELEROMETERS	PDA ACCELEROMETER/STRAIN GAUGES	BREAK BEAM SENSORS AND HIGH SPEED CAMERAS
Pile1 – PSS	–	–	✓ ●	✓ ●	✓ ●
Pile2 – PSG1	–	–	✓ ●	✓ ●	✓ ●
Pile3 – PSG2	SE1 – SE36 ●	D1 – D12 ●	–	–	–
Pile4 – PCC	–	–	✓ ●	✓ ●	✓ ●

Instrumentation Plan for Test Piles				Revisions:		
Tests and Sensors Monitored	04/27/2020	FAMU-FSU College of Engineering	Sheet 4 of 16			

Tests and Sensors Being Monitored

For the tests number 1 to 4, the gauges are accompanied by green circles while the inactive gauges are accompanied by red circles.

3. Flexural Test: Specimen PSG2 will be tested under flexure.

Pile Description	Internal Strain Gauges	Vibrating Wires	Fiber Optic Gauges
Pile1 – PSS	S1 – S52 ●	–	FG1 & FG2 ●
Pile2 – PSG1	S53 – S104 ●	–	FG3 & FG4 ●
Pile3 – PSG2	S105 – S132 ●	VW1 – VW8 ●	FG5 & FG6 ●
Pile4 – PCC	–	–	–

Pile Description	External Strain Gauges	Deflection Gauges	EGCS–D5 Accelerometers	PDA Accelerometer/Strain Gauges	Break Beam Sensors and High Speed Cameras
Pile1 – PSS	–	–	✓ ●	✓ ●	✓ ●
Pile2 – PSG1	–	–	✓ ●	✓ ●	✓ ●
Pile3 – PSG2	SE1 – SE36 ●	D1 – D12 ●	–	–	–
Pile4 – PCC	–	–	✓ ●	✓ ●	✓ ●

Instrumentation Plan for Test Piles				Revisions:		
Tests and Sensors Monitored	04/27/2020	FAMU-FSU College of Engineering	Sheet 5 of 16			

Tests and Sensors Being Monitored

For the tests number 1 to 4, the gauges are accompanied by green circles while the inactive gauges are accompanied by red circles.

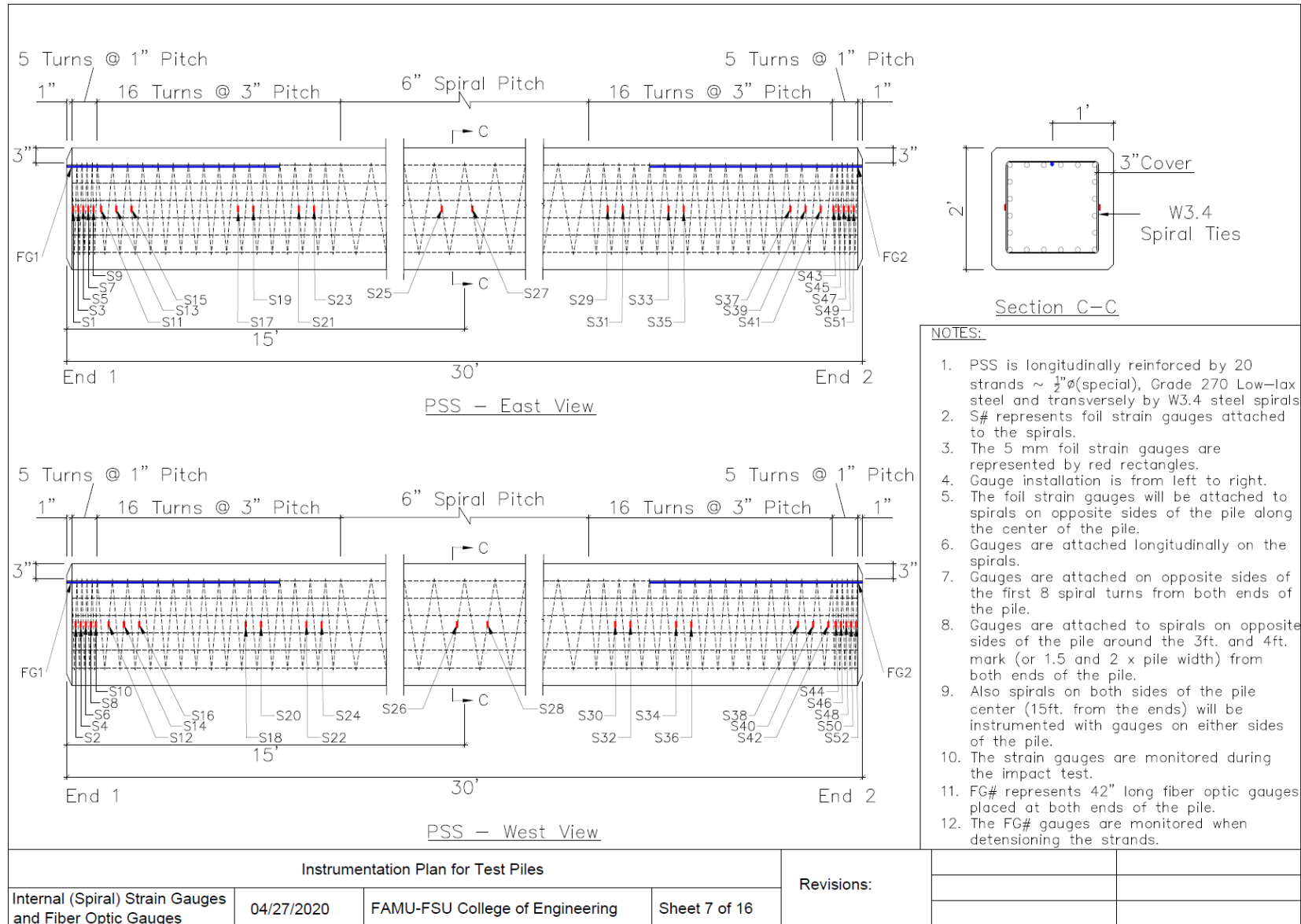
4. Axial Test: Part of specimen PSG2 will be utilized for the axial test.

Pile Description	Internal Strain Gauges	Vibrating Wires	Fiber Optic Gauges
Pile1 – PSS	S1 – S52 ●	–	FG1 & FG2 ●
Pile2 – PSG1	S53 – S104 ●	–	FG3 & FG4 ●
Pile3 – PSG2	S105 – S132 ●	VW1 – VW8 ●	FG5 & FG6 ●
Pile4 – PCC	–	–	–

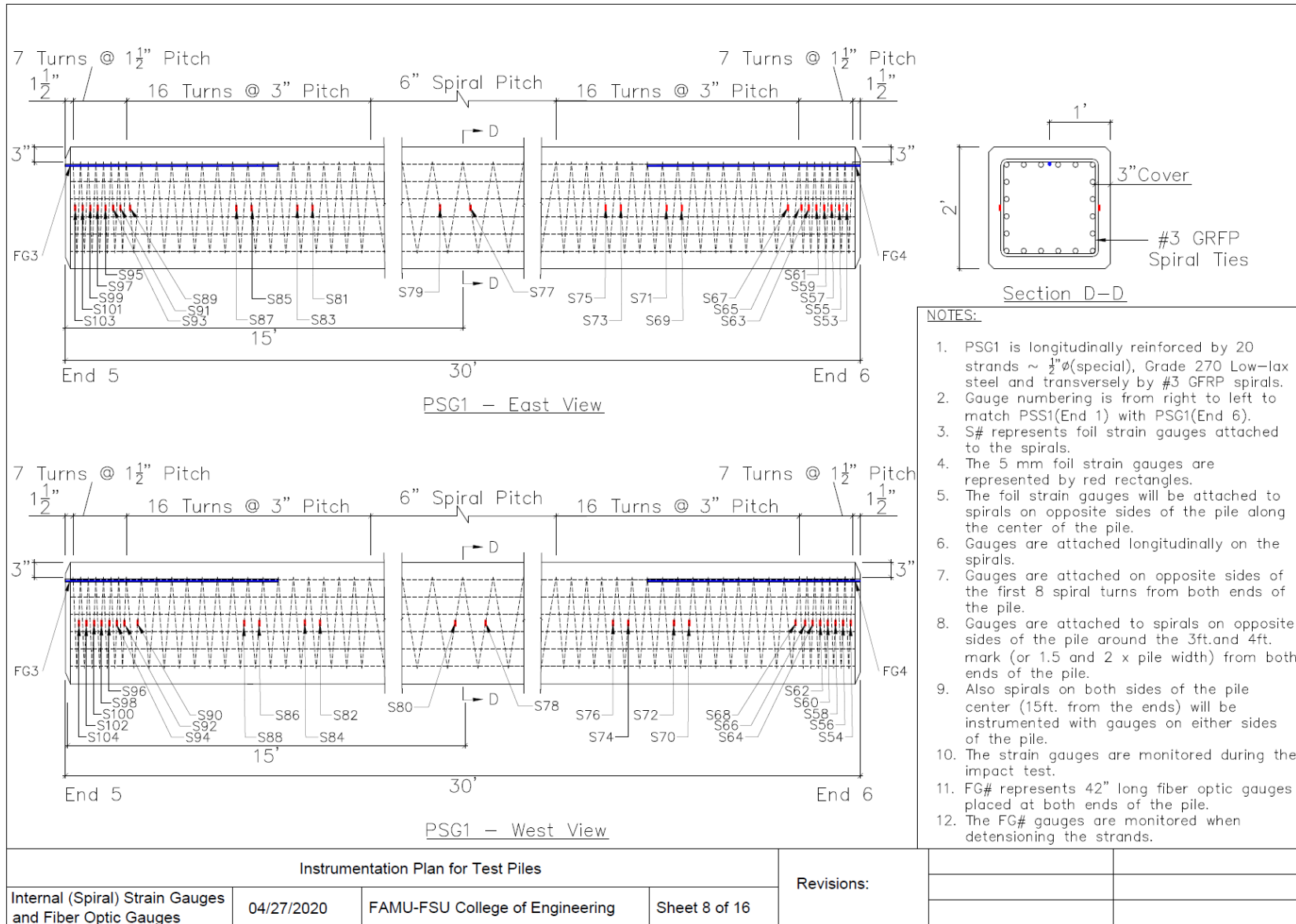
Pile Description	External Strain Gauges	Deflection Gauges	EGCS–D5 Accelerometers	PDA Accelerometer/Strain Gauges	Break Beam Sensors and High Speed Cameras
Pile1 – PSS	–	–	✓ ●	✓ ●	✓ ●
Pile2 – PSG1	–	–	✓ ●	✓ ●	✓ ●
Pile3 – PSG2	SE1 – SE36 ●	D1 – D12 ●	–	–	–
Pile4 – PCC	–	–	✓ ●	✓ ●	✓ ●

Instrumentation Plan for Test Piles				Revisions:		
Tests and Sensors Monitored	04/27/2020	FAMU-FSU College of Engineering	Sheet 6 of 16			

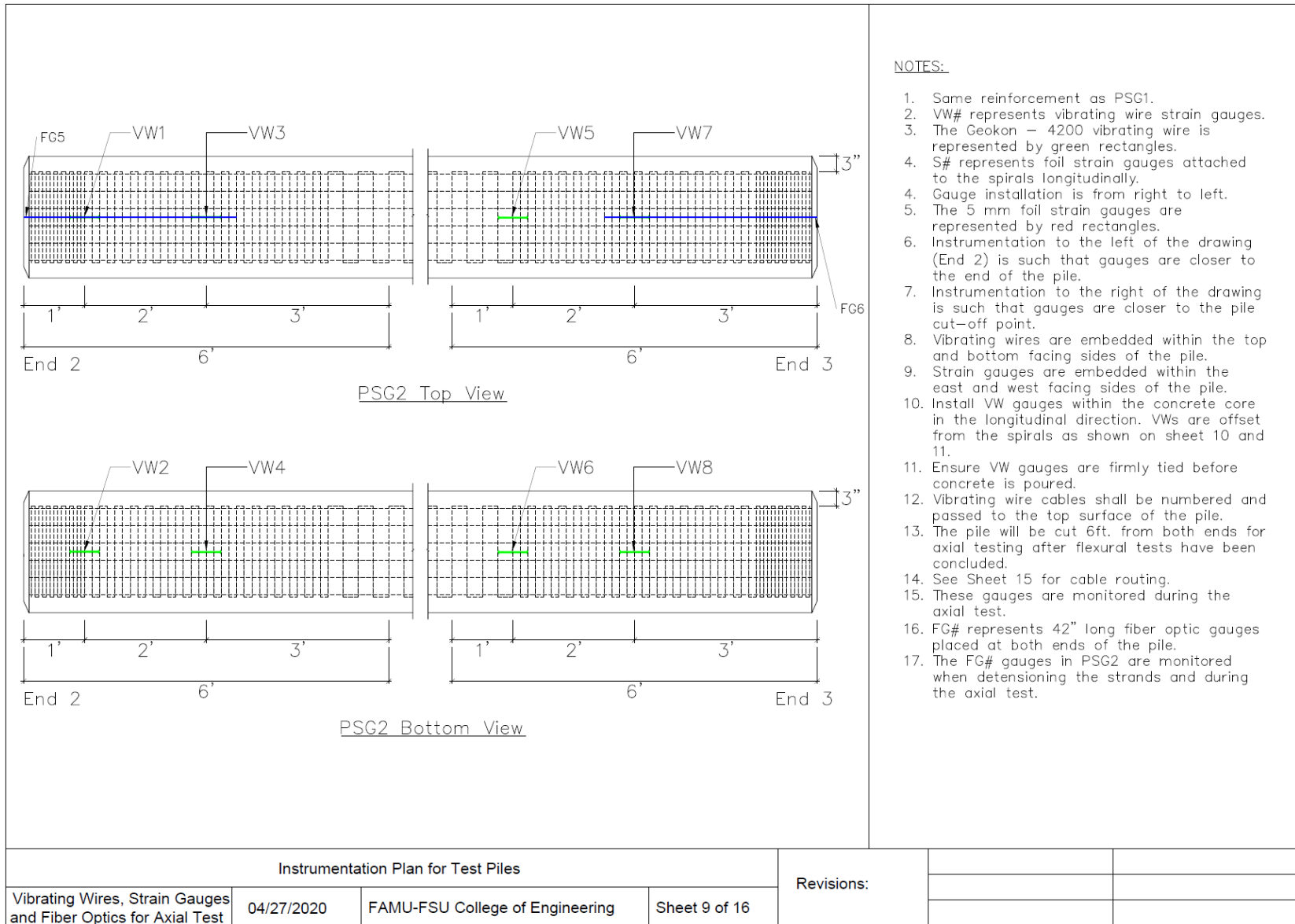
C.3. Internal (Spiral) Strain Gauge and Fiber Optic Gauge Instrumentation for PSS

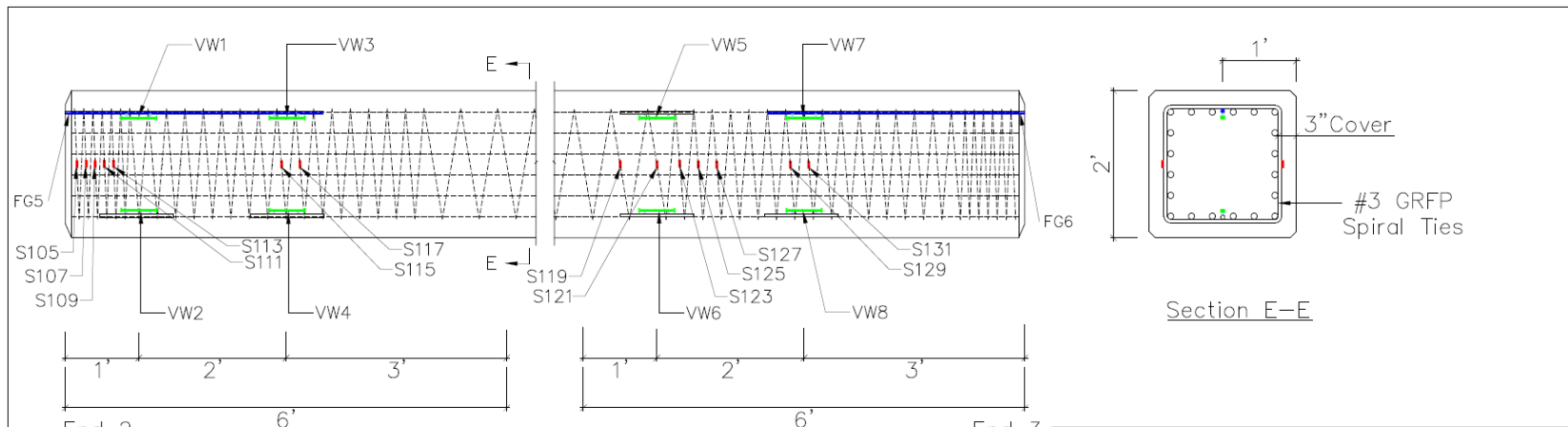


C.4. Internal (Spiral) Strain Gauge and Fiber Optic Gauge Instrumentation for PSG1



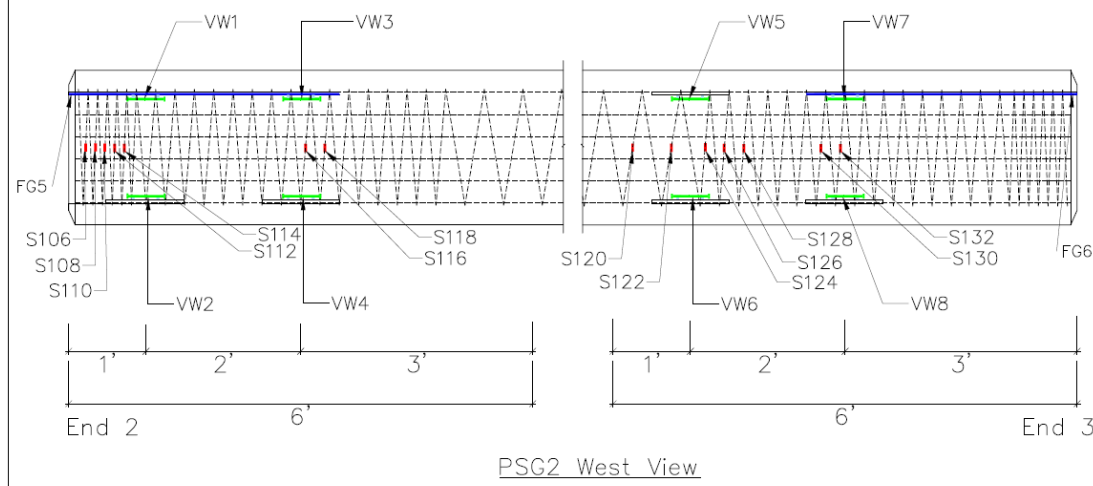
C.5. Internal (Spiral) Strain Gauge, Fiber Optic Gauge, and Vibrating Wire Instrumentation for PSG2





PSG2 East View

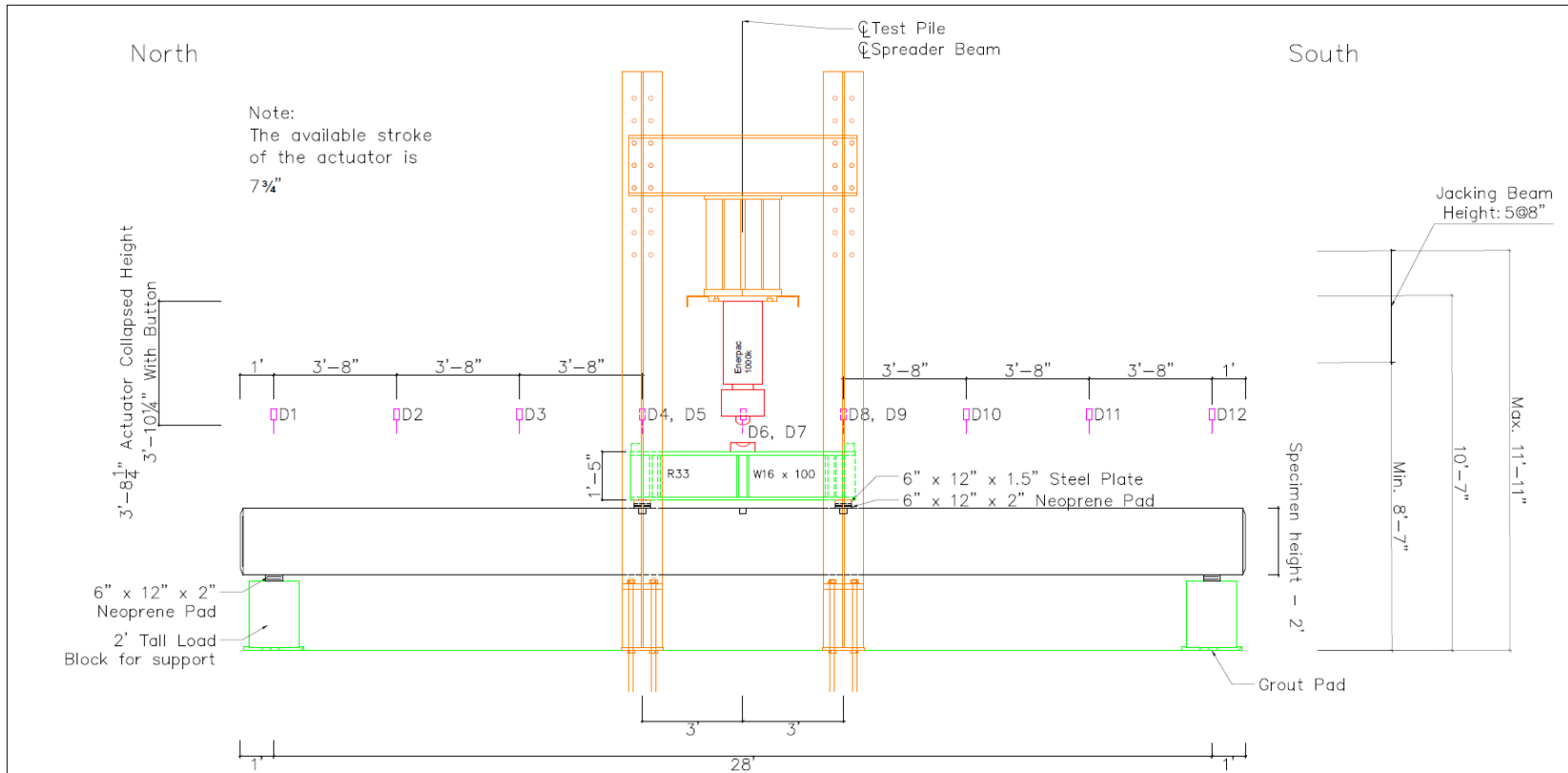
NOTE:
Same as previous sheet



PSG2 West View

Instrumentation Plan for Test Piles				Revisions:		
Vibrating Wires and Strain Gauges for Axial Test	04/27/2020	FAMU-FSU College of Engineering	Sheet 10 of 16			

C.6. Flexural Test Setup and Instrumentation

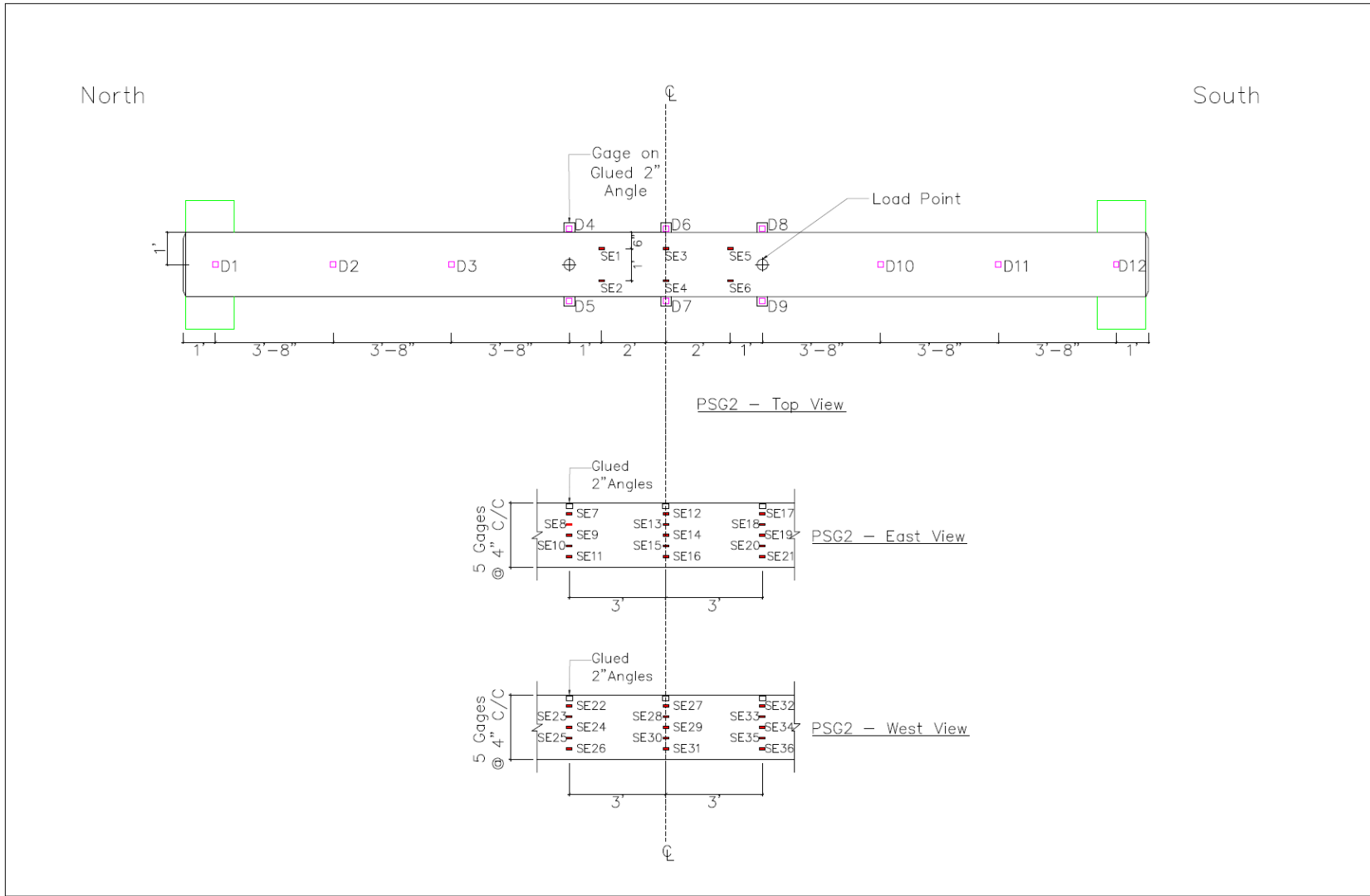


NOTE:

1. D# represents laser deflection gauges. Dimension shown are center to center of deflection gauges.
2. SE# represent 60 mm external strain gauges. Dimension shown on Sheet 14 are center to center of strain gages.
3. As shown on sheet 14 gauges D4, D5, D6, D7, D8 and D9 need 2 in. angles glued to the top side of the specimen to avoid interference with the spreader beam.

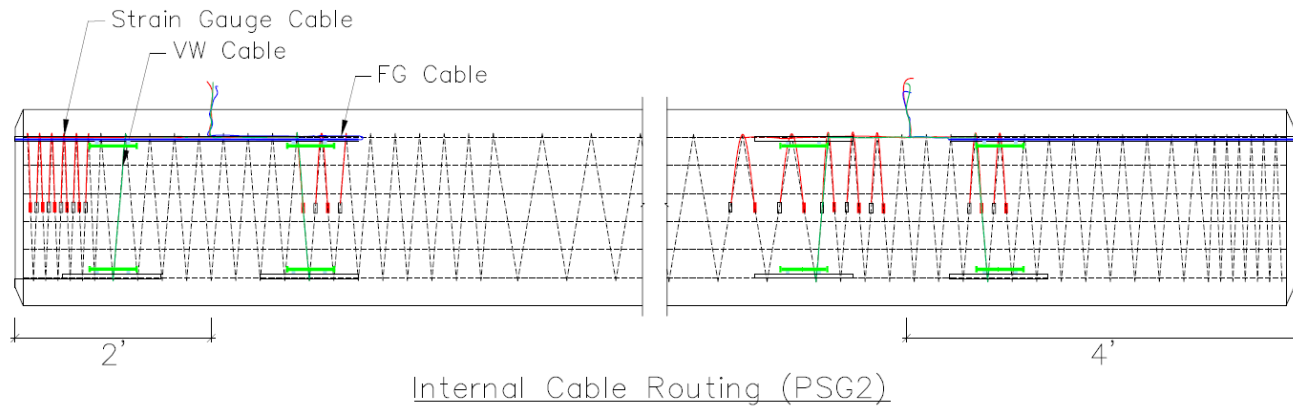
Load Rate:	250 lb/sec, then 200 lb/sec after the first flexural crack
Recording Rate:	10 Hz.
Predicted Load at Cracking :	33 kips (due to actuator)
Predicted Load at Flexural Failure:	103 kips
Predicted Deflection:	3.88 in.(when the actuator load=103 kips)

Instrumentation Plan for Test Piles				Revisions:		
Flexural Test Instrumentation	04/27/2020	FAMU-FSU College of Engineering	Sheet 13 of 16			

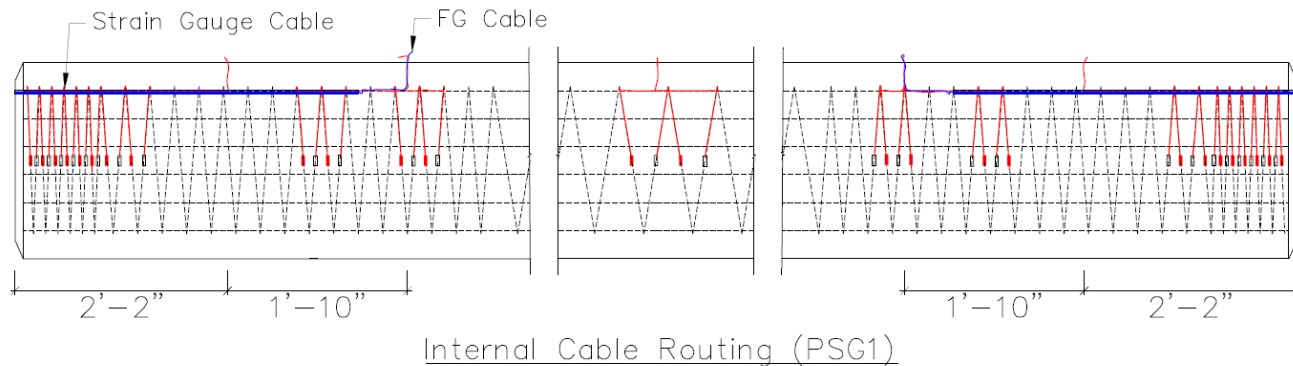


Instrumentation Plan for Test Piles				Revisions:		
Flexural Test Instrumentation	04/27/2020	FAMU-FSU College of Engineering	Sheet 14 of 16			

C.7. Cable Routing for Internal Instrumentation



Internal Cable Routing (PSG2)

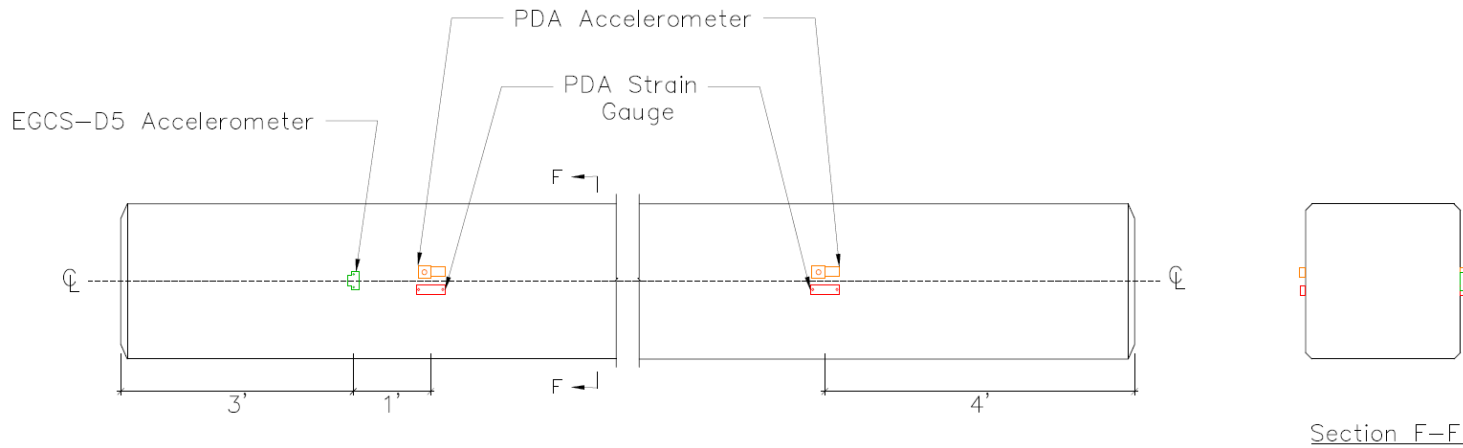


Internal Cable Routing (PSG1)

- NOTE:
1. Cable routing for PSS follows a similar pattern to PSG1.
 2. Red lines represent strain gauge cables.
 3. Green lines represent vibrating wire cables.
 4. Blue lines represent fiber optic gauge cables.

Instrumentation Plan for Test Piles				Revisions:		
Cable Routing	04/27/2020	FAMU-FSU College of Engineering	Sheet 15 of 16			

C.8. PDA Instrumentation



Side View and Cross Section of Instrumented Pile Showing the Layout of PDA Sensors and EGCS-D5 Accelerometer

NOTE:

1. PDA instrumentation is applicable to PSS, PSG1 and PCC.
2. EGCS-D5 is an accelerometer provided by the project team in order to obtain additional measurement at another point on the pile.

Instrumentation Plan for Test Piles				Revisions:		
PDA Instrumentation	04/27/2020	FAMU-FSU College of Engineering	Sheet 16 of 16			

Appendix D. Data Sheet for EGCS-D5 Accelerometer



MODEL EGCS-D5 ACCELEROMETER

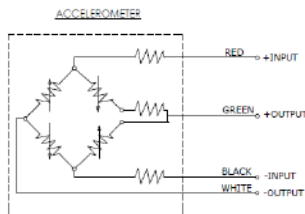
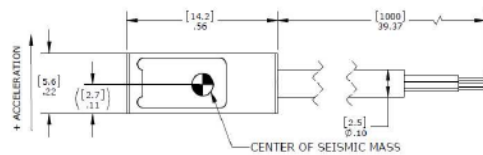
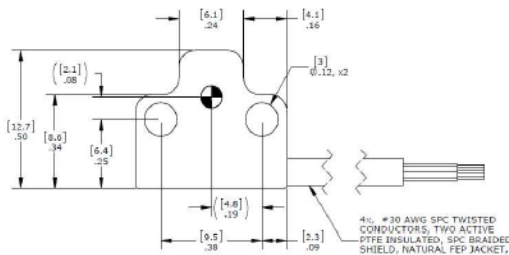
SPECIFICATIONS

- Rugged Piezoresistive Design
- DC Response, Critically Damped
- $\pm 50g$ to $\pm 10,000g$ Range
- DC to 10kHz Response
- Fits Popular Shock Accelerometer Mounting Bolt Pattern

The Model EGCS-D5 accelerometer is critically damped with built-in over-range stops that are set to protect the unit against up to 20,000g shocks. This is ideal for applications which may experience rough handling or in situations where the accelerometer must survive a high initial overload in order to make a low g measurement. These units feature a Wheatstone Bridge output with compensated temperature range of +20 to +80°C. An inline amplifier option is available for superior signal to noise performance.



dimensions



FEATURES

- $\pm 50g$ to $\pm 10,000g$ Dynamic Range
- Heavy Duty, Rugged
- Static and Dynamic Measurement
- DC to 10,000Hz Frequency Response
- $\pm 1\%$ Non-Linearity
- -40°C to +100°C Temperature Range
- Inline Amplifier Option

APPLICATIONS

- Metal-to-Metal Mechanical Shock
- Impact Testing
- Building Construction
- Pile Driving
- Weapons Testing

MODEL EGCS-D5 ACCELEROMETER

PERFORMANCE SPECIFICATIONS

All values are typical at +24°C, 80Hz and 15Vdc excitation unless otherwise stated. Measurement Specialties reserves the right to update and change these specifications without notice.

Parameters									Notes
DYNAMIC									
Range (g)	±50	±100	±250	±500	±1000	±2500	±5000	±10000	
Sensitivity (mV/g) ¹	4	2	0.8	0.4	0.2	0.08	0.04	0.016	
Frequency Response (Hz)	0-360	0-540	0-780	0-1050	0-1500	0-2100	0-2400	0-5000	+3%/-8%
Frequency Response (Hz)	0-600	0-900	0-1300	0-1750	0-2500	0-3500	0-4000	0-10000	+3%/-18%
Natural Frequency (Hz)	1200	1800	2600	3500	5000	7000	8000	16000	
Non-Linearity (%FSO)	±1	±1	±1	±1	±1	±1	±1	±1	
Transverse Sensitivity (%)	<3	<3	<3	<3	<3	<3	<3	<3	
Damping Ratio	0.7	0.7	0.7	0.7	0.7	0.7	0.7	0.7	Nominal
Shock Limit (g)	5000	10000	10000	10000	10000	10000	20000	20000	

ELECTRICAL

Zero Acceleration Output (mV)	±20 Differential
Excitation Voltage (Vdc)	15 (can be used from 2 to 15Vdc but lower excitation voltage will decrease sensitivity accordingly)
Input Resistance (Ω)	2000 Nominal
Output Resistance (Ω)	1000 Nominal
Insulation Resistance (MΩ)	>100 @50Vdc
Ground Isolation	Isolated from Mounting Surface

ENVIRONMENTAL

Thermal Zero Shift	±2.0mV / 50°C (±2.0mV / 100°F)
Thermal Sensitivity Shift	±2.5% / 50°C (±2.5% / 100°F)
Operating Temperature	-40 to +100°C (-40 to +212°F)
Compensated Temperature	+20 to +80°C (+70 to +170°F), contact factory for other temperature compensation options
Storage Temperature	-40 to +100°C (-40 to +212°F)
Humidity	Epoxy Sealed, IP65

PHYSICAL

Case Material	Stainless Steel
Cable	4x #30 AWG Leads, PTFE Insulated, Braided Shield, FEP Jacket
Weight	8 grams
Mounting	Screw Mount, 2x #4-40 Socket Head Cap Screws

¹ Output is ratiometric to excitation voltage

Calibration supplied: CS-FREQ-0100 NIST Traceable Amplitude Calibration from 20Hz to Frequency Response Limit

Optional accessories: AC-D05201 Triaxial Mounting Block
 121 3-Channel Precision Low Noise DC Amplifier
 140A Auto-zero Inline Amplifier
 145 Dedicated Inline Amplifier (see next page)



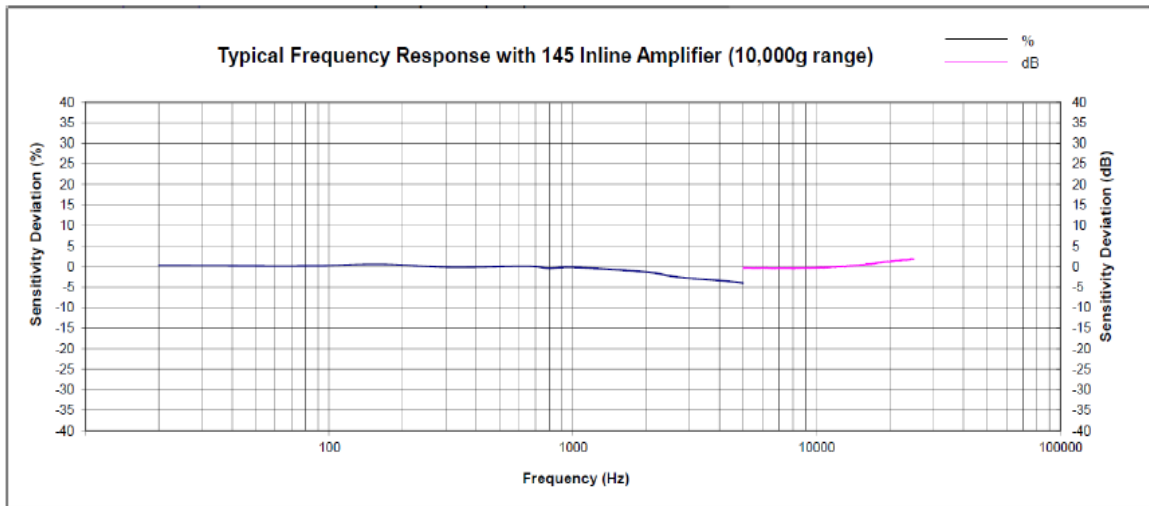
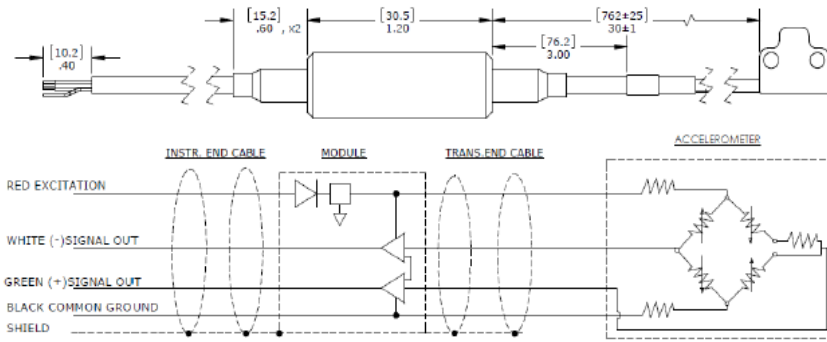
Optional 145 Inline Amplifier Module

The information in this sheet has been carefully reviewed and is believed to be accurate; however, no responsibility is assumed for inaccuracies. Furthermore, this information does not convey to the purchaser of such devices any license under the patent rights to the manufacturer. Measurement Specialties, Inc. reserves the right to make changes without further notice to any product herein. Measurement Specialties, Inc. makes no warranty, representation or guarantee regarding the suitability of its product for any particular purpose, nor does Measurement Specialties, Inc. assume any liability arising out of the application or use of any product or circuit and specifically disclaims any and all liability, including without limitation consequential or incidental damages. Typical parameters can and do vary in different applications. All operating parameters must be validated for each customer application by customer's technical experts. Measurement Specialties, Inc. does not convey any license under its patent rights nor the rights of others.

MODEL EGCS-D5 ACCELEROMETER

Unit with model 145 Inline Amplifier can be powered with 8-20Vdc. The sensor is supplied with regulated 5Vdc from the amplifier. The output is differential with a 2.5Vdc common mode. The amplifier has a 30x gain and a 20kHz low-pass filter and is intended for high-g ranges.

145 AMP OPTION



MODEL EGCS-D5 ACCELEROMETER

ORDERING INFO

EGCS-D5L-100-Z1/L2M/145

Options, otherwise leave blank
Range (100 is 100g)

Sensitive axis rotated 90°, otherwise blank

Compensated Temp Ranges: Standard = +20 to +80°C (+70 to +170°F)

Z* = Non standard, contact factory

Standard = 15Vdc

Excitation Voltage:

V* = Non standard, contact factory

Special Cable Length:

L00F = Replace "00" with length in feet

L00M = Replace "00" with length in meter

Standard Unit with 145 Amplifier: 145

= Inline amplifier added

Example: EGCS-D5-10000-L2M

Model EGCS-D5, 10,000g Range, 2 Meter Cable Length

NORTH AMERICA

Measurement Specialties, Inc.,
a TE Connectivity Company
Phone: 800-522-6752
Email: customercare.hmpt@te.com

EUROPE

MEAS Deutschland GmbH(Europe)
a TE Connectivity Company
Phone: 800-440-5100
Email: customercare.lcsb@te.com

ASIA

Measurement Specialties (China), Ltd.,
a TE Connectivity Company
Phone: 0400-820-6015
Email: customercare.shzn@te.com

TE.com/sensorsolutions

Measurement Specialties, Inc., a TE Connectivity company.

Acoustic, American Sensor Technologies, AST, ATEXIS, DEUTSCH, IdentCal, TruBlue, KPSI, Krystal Bond, Microfused, UltraStable, Measurement Specialties, MEAS, Schaevitz, TE Connectivity, TE, and the TE connectivity (logo) are trademarks of the TE Connectivity Ltd. family of companies. Other logos, product and company names mentioned herein may be trademarks of their respective owners.

The information given herein, including drawings, illustrations and schematics which are intended for illustration purposes only, is believed to be reliable. However, TE Connectivity makes no warranties as to its accuracy or completeness and disclaims any liability in connection with its use. TE Connectivity's obligations shall only be as set forth in TE Connectivity's Standard Terms and Conditions of Sale for this product and in no case will TE Connectivity be liable for any incidental, indirect or consequential damages arising out of the sale, use or misuse of the product. Users of TE Connectivity products should make their own evaluation to determine the suitability of each such product for the specific application.

Appendix E. PDA Measurements (Phase 1 Impact Tests)

E.1. PDA Strain Gauge Measurements

E.1.1. PDA Strain Gauge Measurement (PSS)

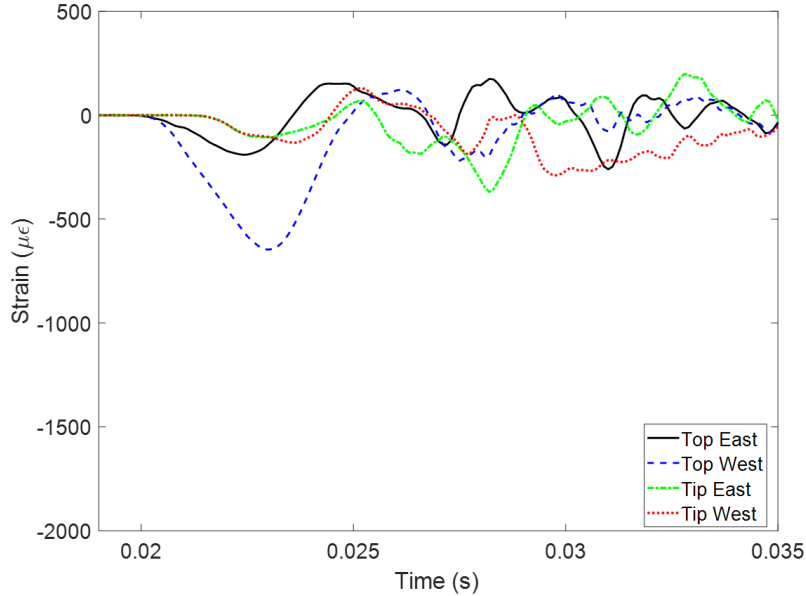


Figure E.1: Top and tip strains from PDA strain gauges at impact drop height of 7 ft (PSS)

E.1.2. PDA Strain Gauge Measurements (PSG1)

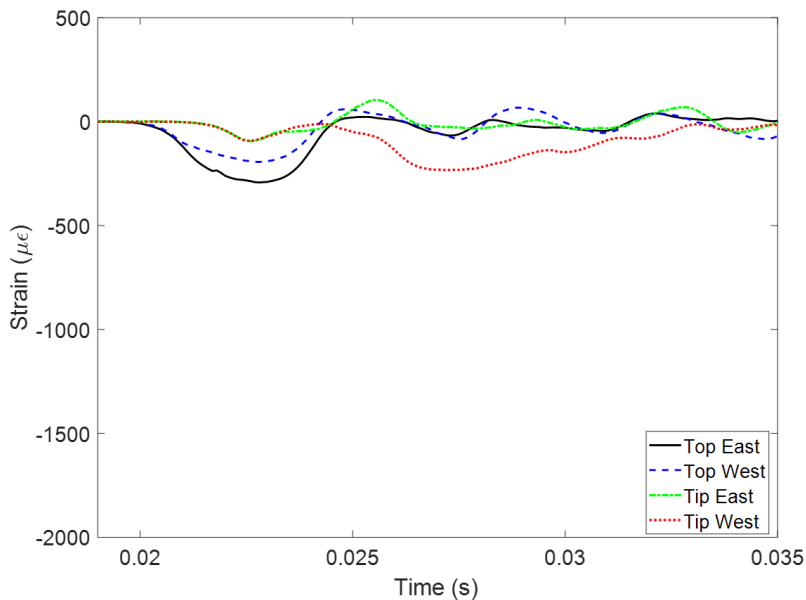


Figure E.2: Top and tip strains from PDA strain gauges at impact drop height of 4 ft (PSG1)

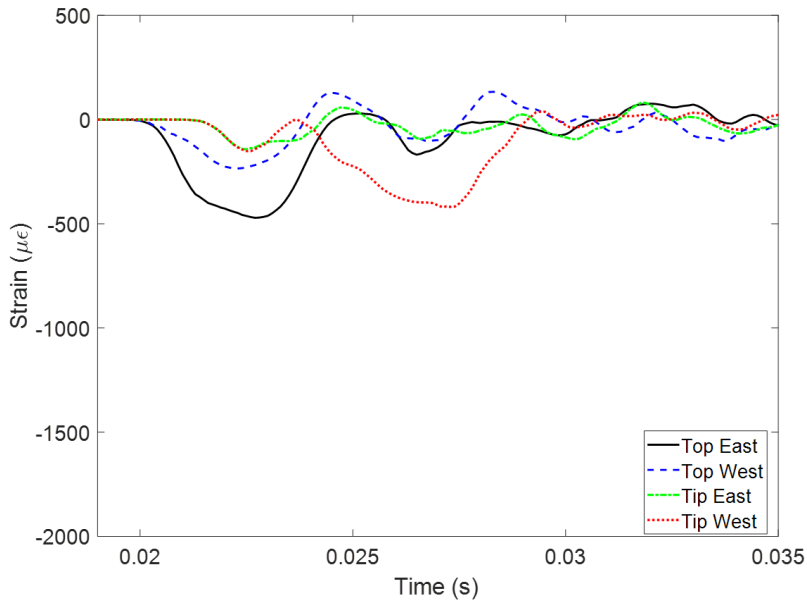


Figure E.3: Top and tip strains from PDA strain gauges at impact drop height of 7 ft (PSG1)

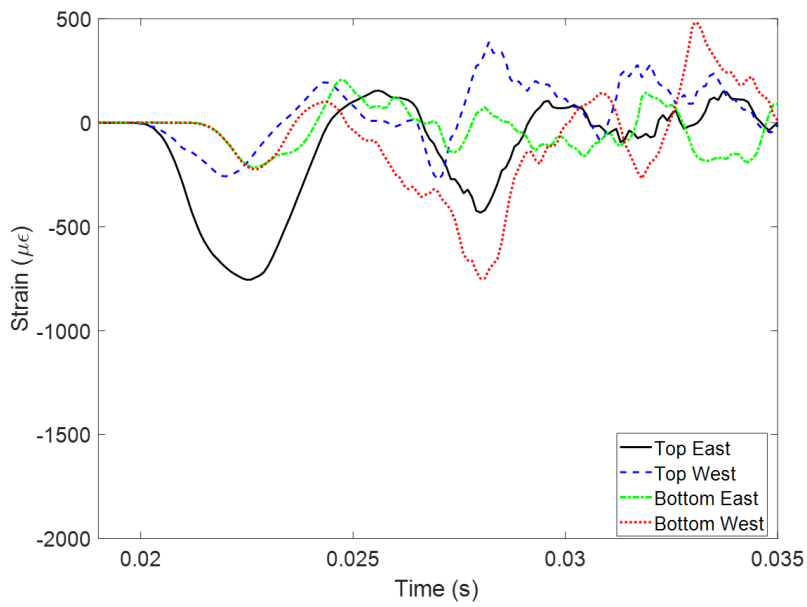


Figure E.4: Top and tip strains from PDA strain gauges at impact drop height of 10 ft (PSG1)

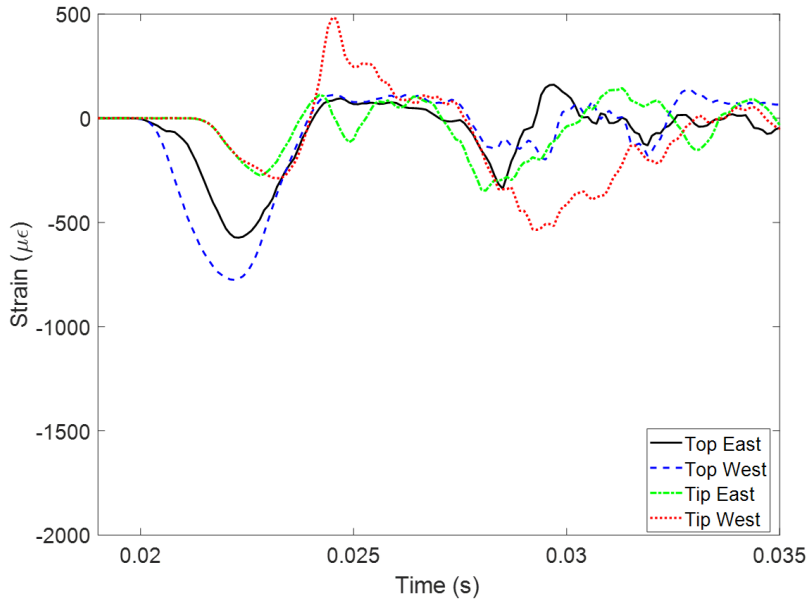


Figure E.5: Top and tip strains from PDA strain gauges at impact drop height of 15 ft (PSG1)

E.1.3. PDA Strain Gauge Measurements (PCC)

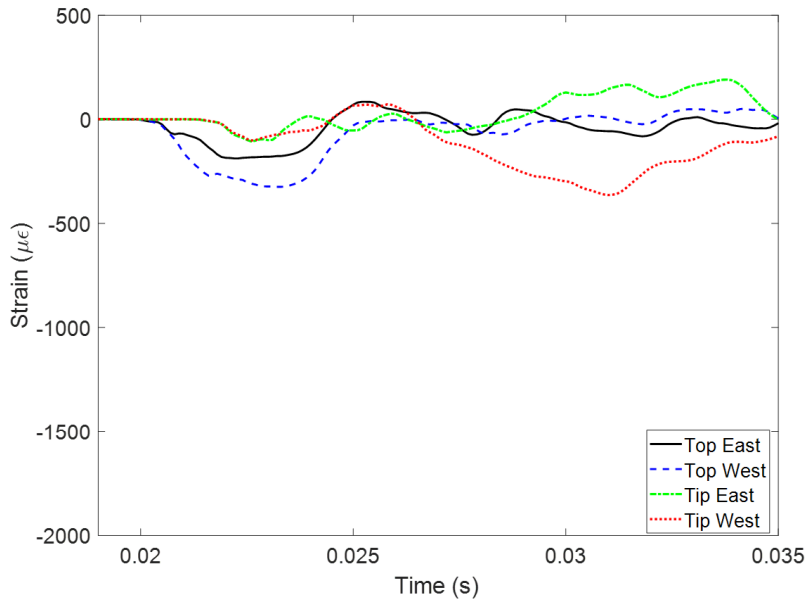


Figure E.6: Top and tip strains from PDA strain gauges at impact drop height of 4 ft (PCC)

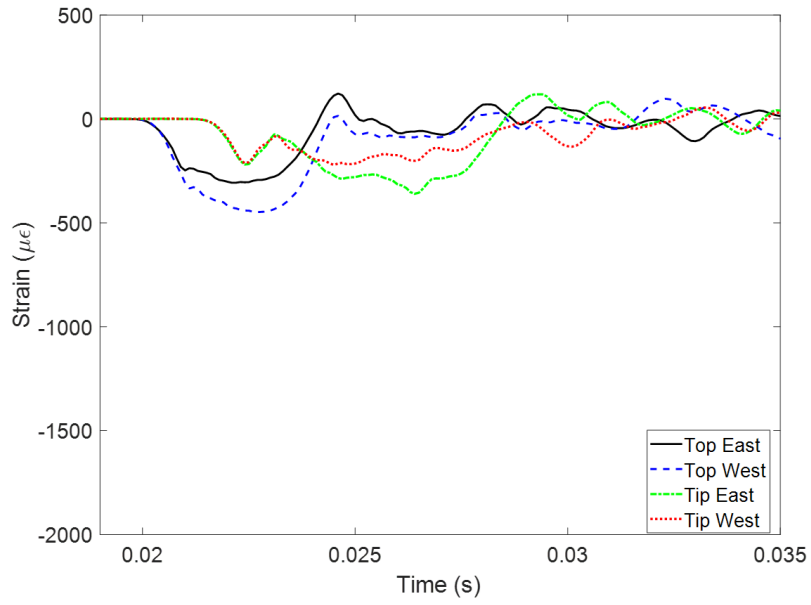


Figure E.7: Top and tip strains from PDA strain gauges at impact drop height of 7 ft (PCC)

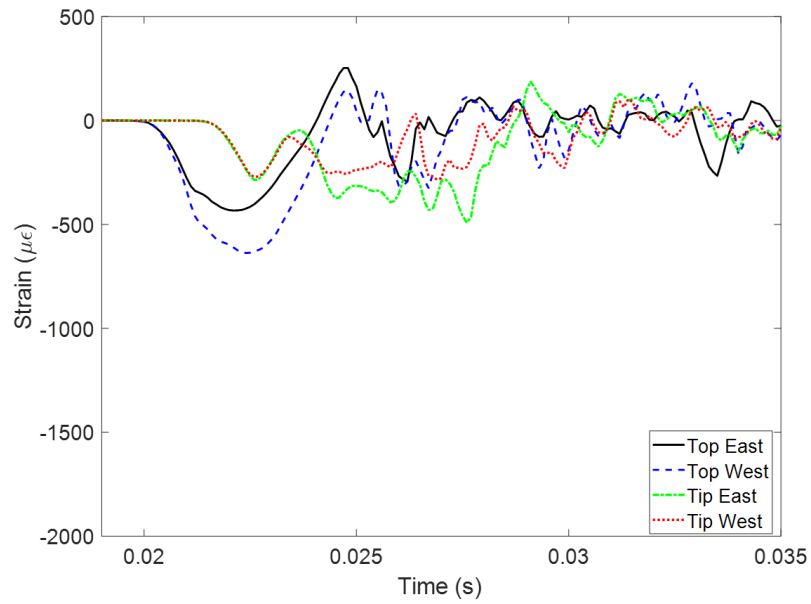


Figure E.8: Top and tip strains from PDA strain gauges at impact drop height of 10 ft (PCC)

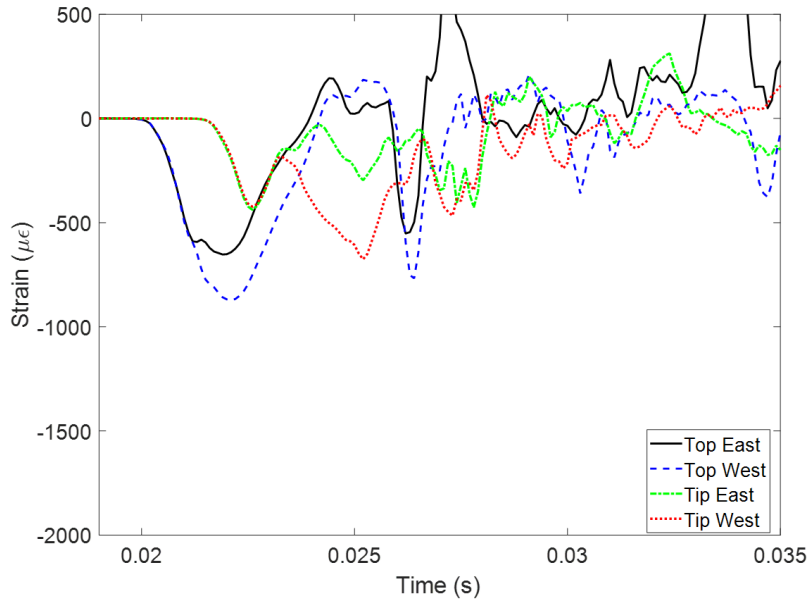


Figure E.9: Top and tip strains from PDA strain gauges at impact drop height of 15 ft (PCC)

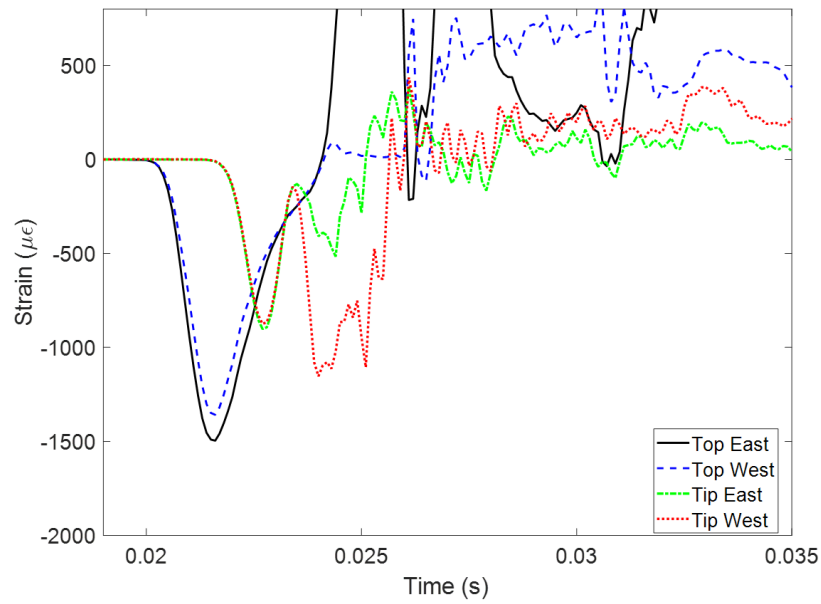


Figure E.10: Top and tip strains from PDA strain gauges at impact drop height of 25 ft (PCC)

E.2. PDA Acceleration Measurements

E.2.1. PDA Acceleration Measurement (PSS)

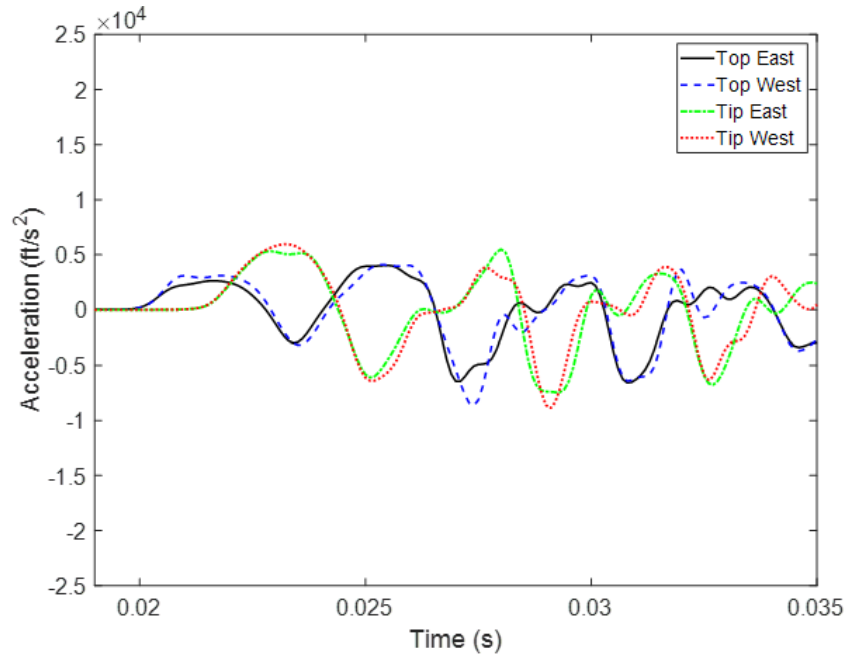


Figure E.11: PDA measured acceleration at pile top and tip at a drop height of 7 ft (PSS)

E.2.2. PDA Acceleration Measurements (PSG1)

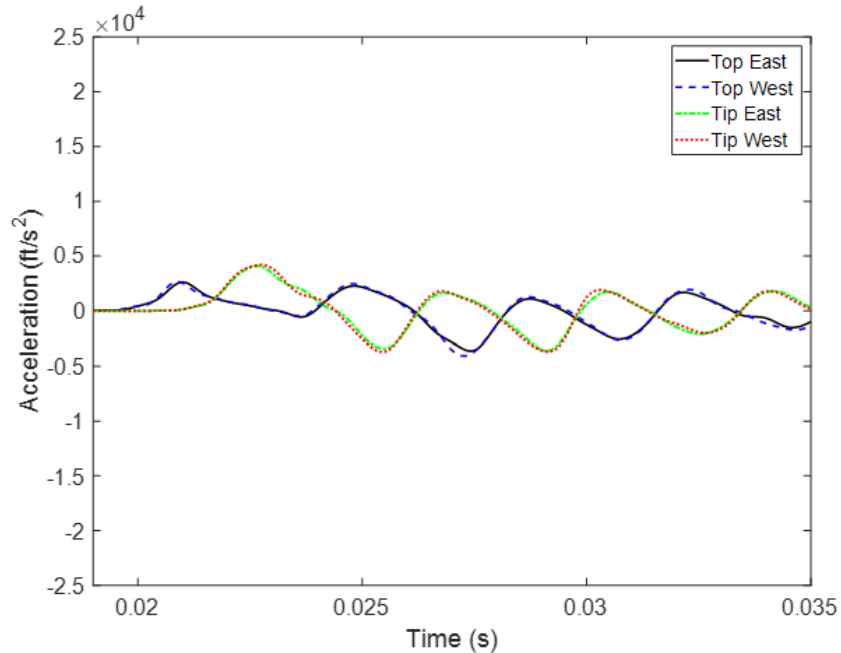


Figure E.12: PDA measured acceleration at pile top and tip at a drop height of 4 ft (PSG1)

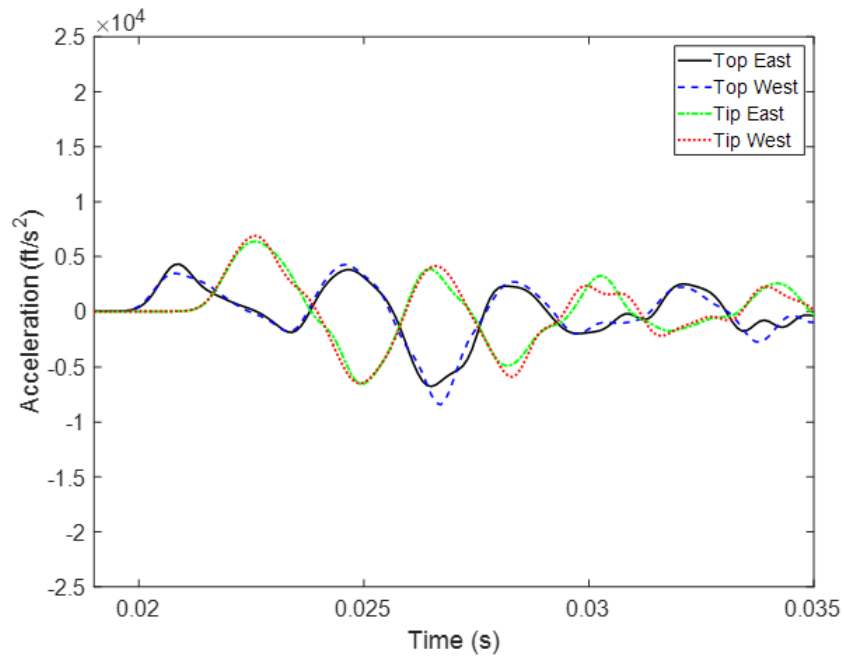


Figure E.13: PDA measured acceleration at pile top and tip at a drop height of 7 ft (PSG1)

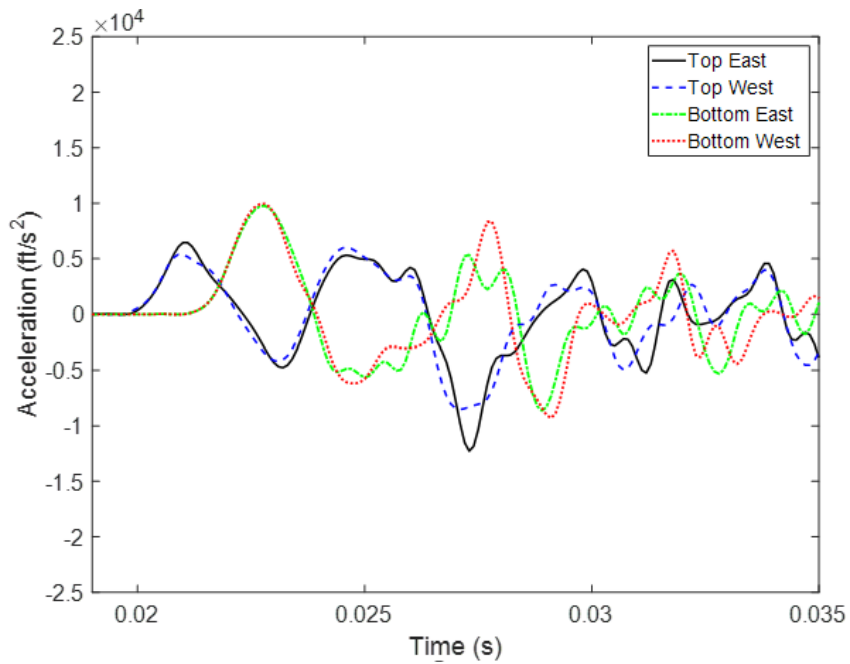


Figure E.14: PDA measured acceleration at pile top and tip at a drop height of 10 ft (PSG1)

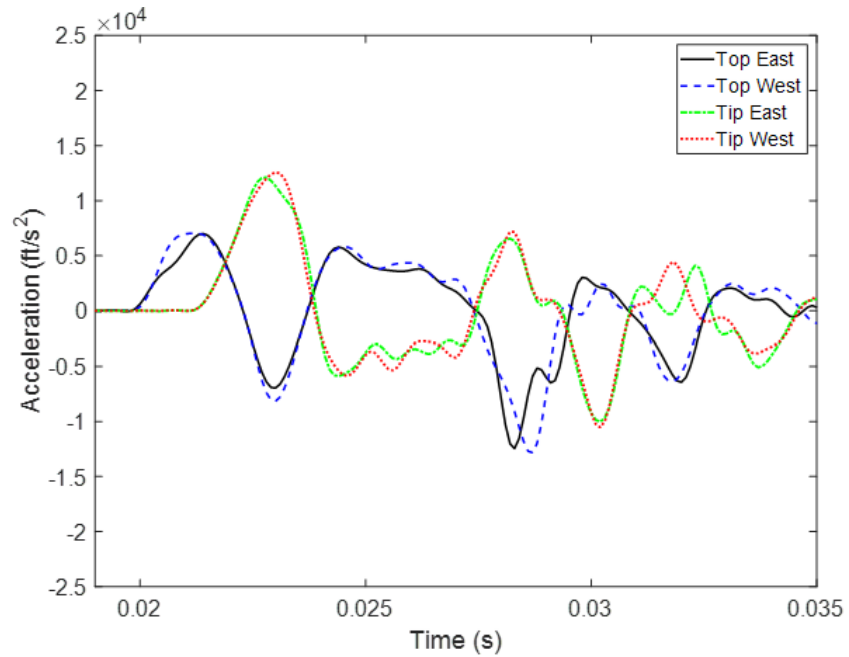


Figure E.15: PDA measured acceleration at pile top and tip at a drop height of 15 ft (PSG1)

E.2.3. PDA Acceleration Measurements (PCC)

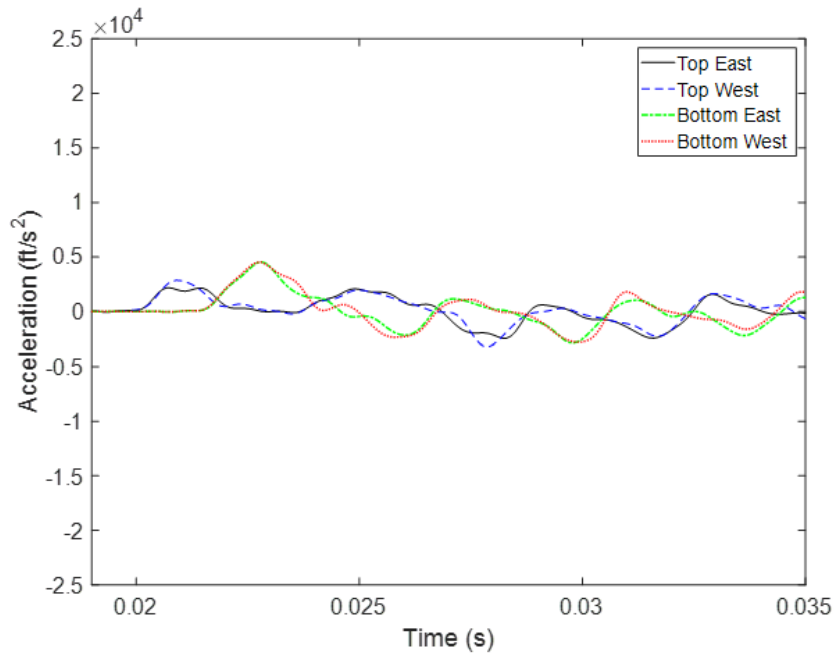


Figure E.16: PDA measured acceleration at pile top and tip at a drop height of 4 ft (PCC)

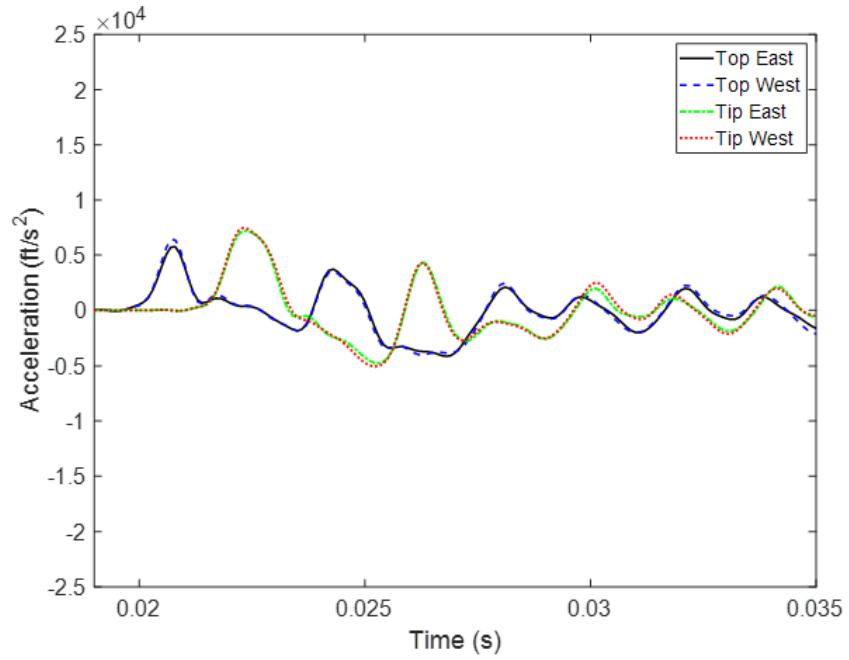


Figure E.17: PDA measured acceleration at pile top and tip at a drop height of 7 ft (PCC)

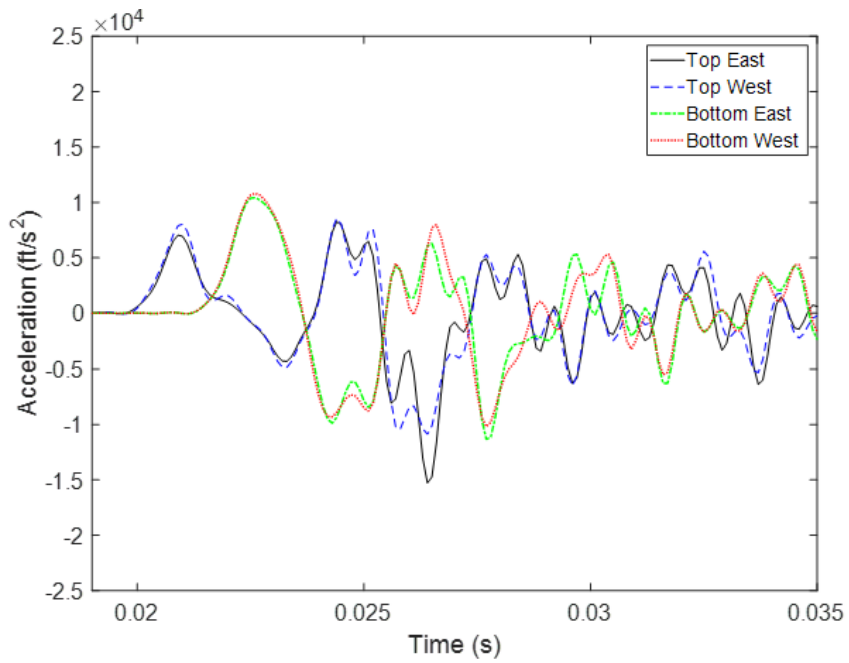


Figure E.18: PDA measured acceleration at pile top and tip at a drop height of 10 ft (PCC)

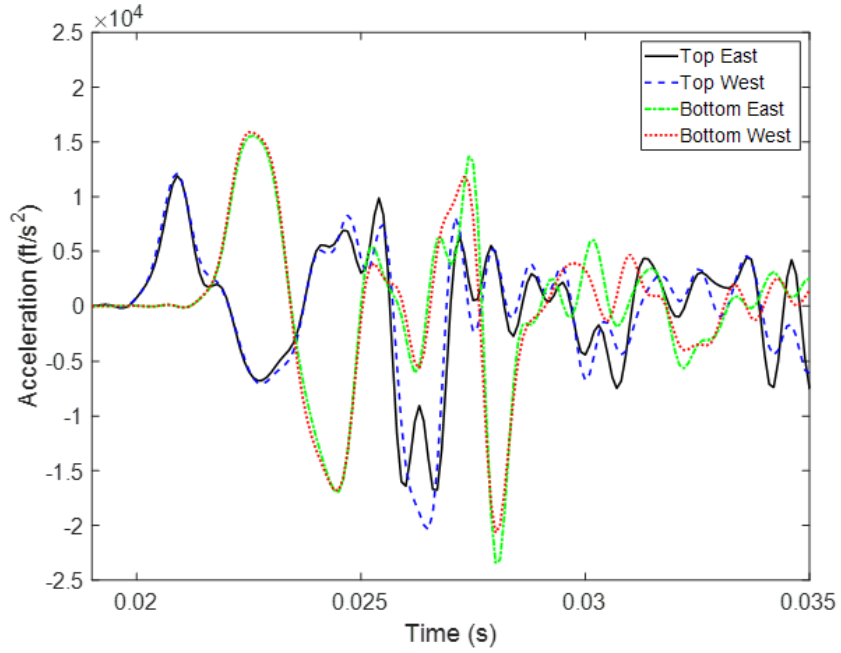


Figure E.19: PDA measured acceleration at pile top and tip at a drop height of 15 ft (PCC)

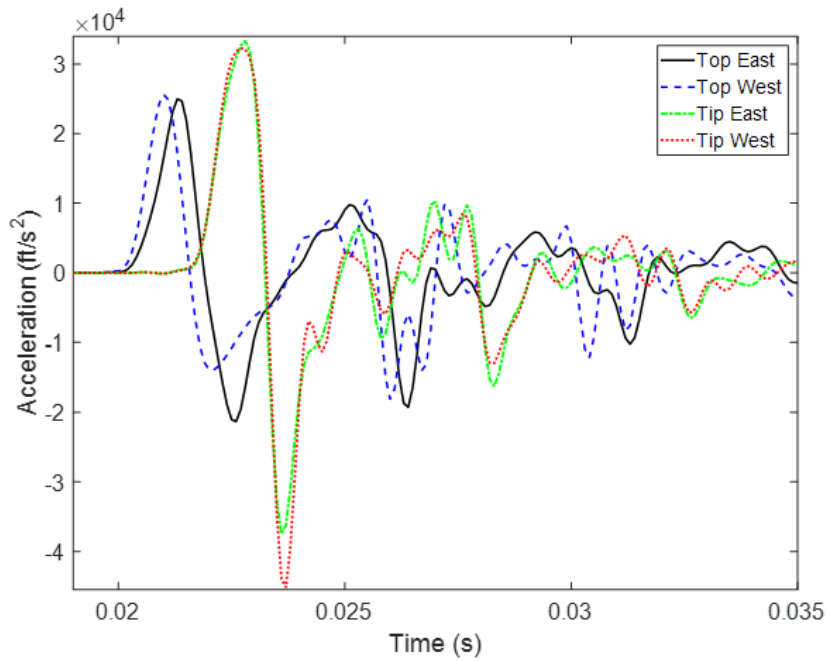


Figure E.20: PDA measured acceleration at pile top and tip at a drop height of 25 ft (PCC)

E.3. Pile Force Traces from PDA

E.3.1. Pile Force Traces from PDA (PSS)

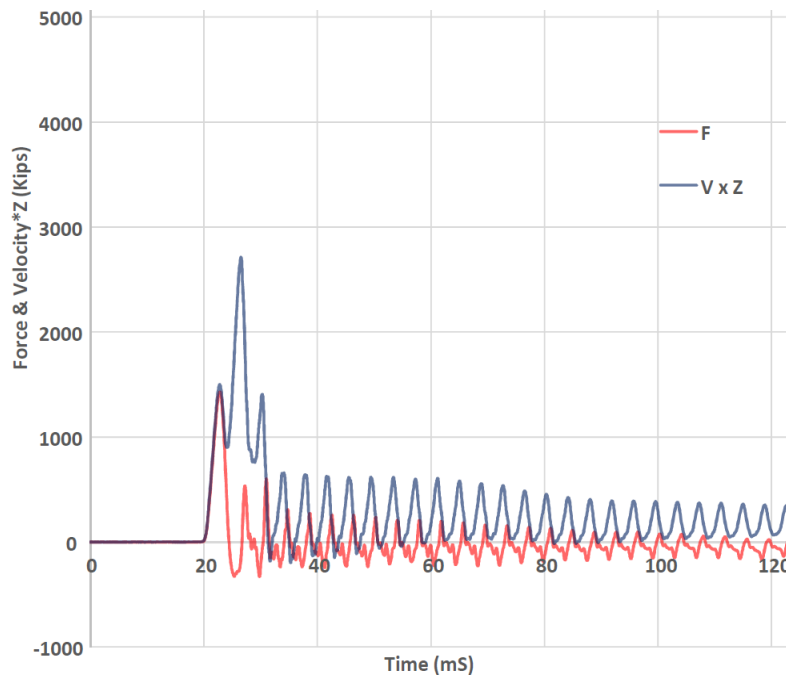


Figure E.21: Pile force traces from PDA resulting from impact drop height of 7 ft (PSS)

E.3.2. Pile Force Traces from PDA (PSG1)

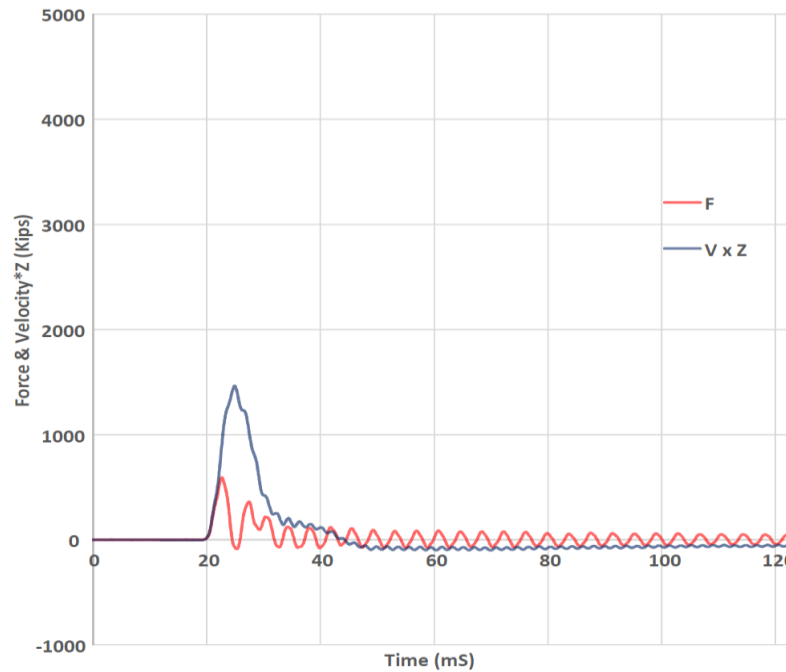


Figure E.22: Pile force traces from PDA resulting from impact drop height of 4 ft (PSG1)

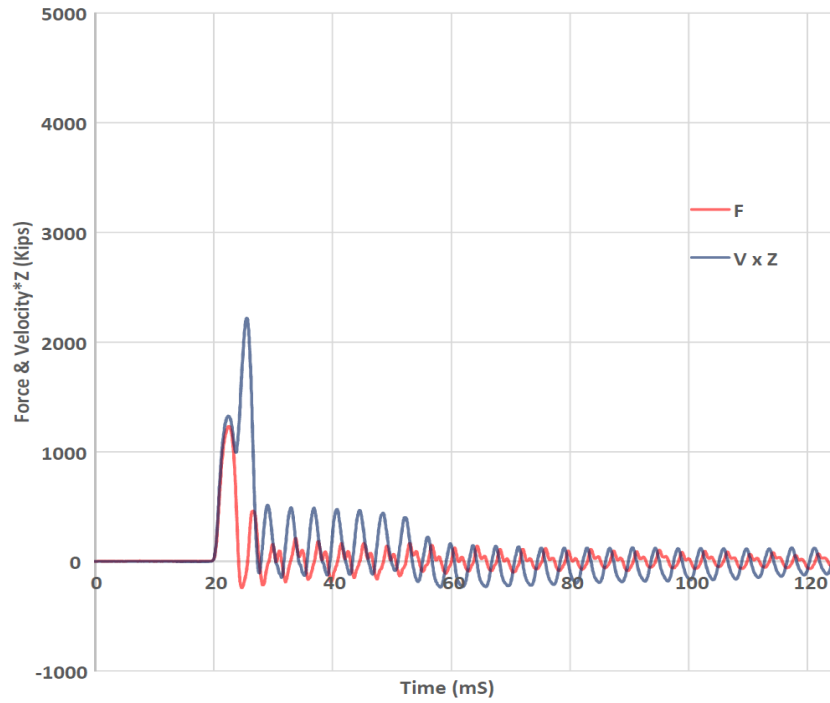


Figure E.23: Pile force traces from PDA resulting from impact drop height of 7 ft (PSG1)

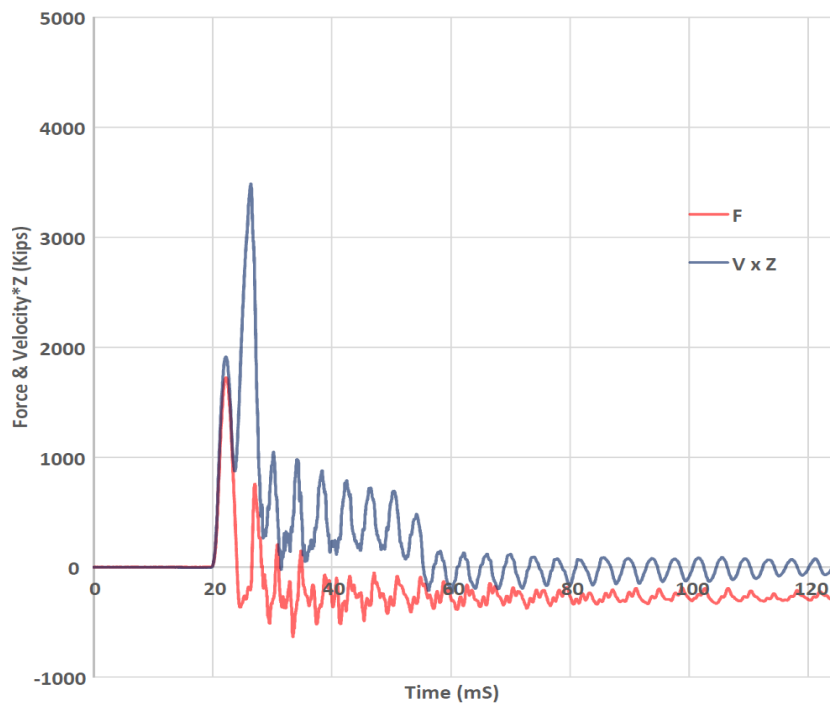


Figure E.24: Pile force traces from PDA resulting from impact drop height of 10 ft (PSG1)

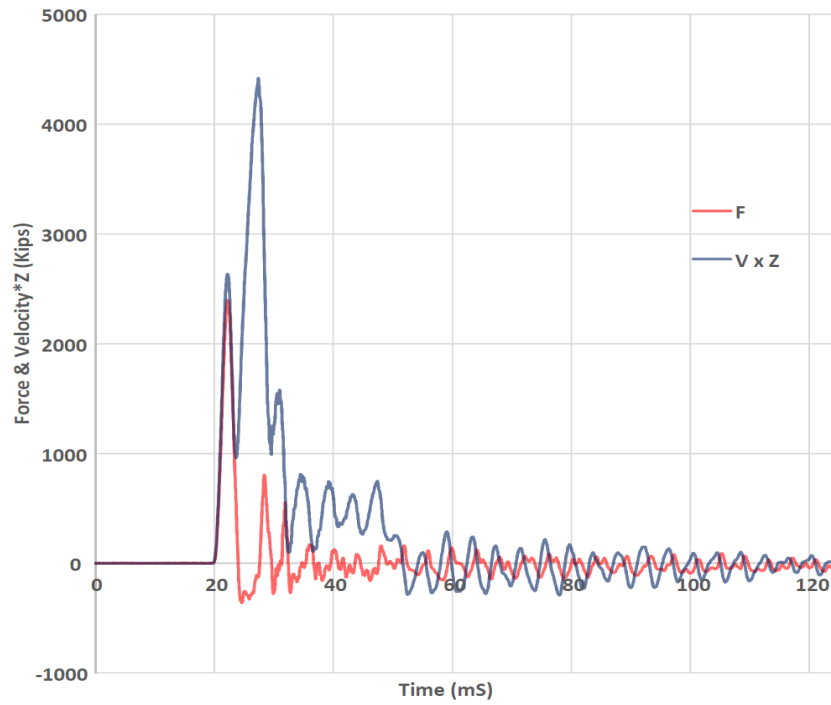


Figure E.25: Pile force traces from PDA resulting from impact drop height of 15 ft (PSG1)

E.3.3. Pile Force Traces from PDA (PCC)

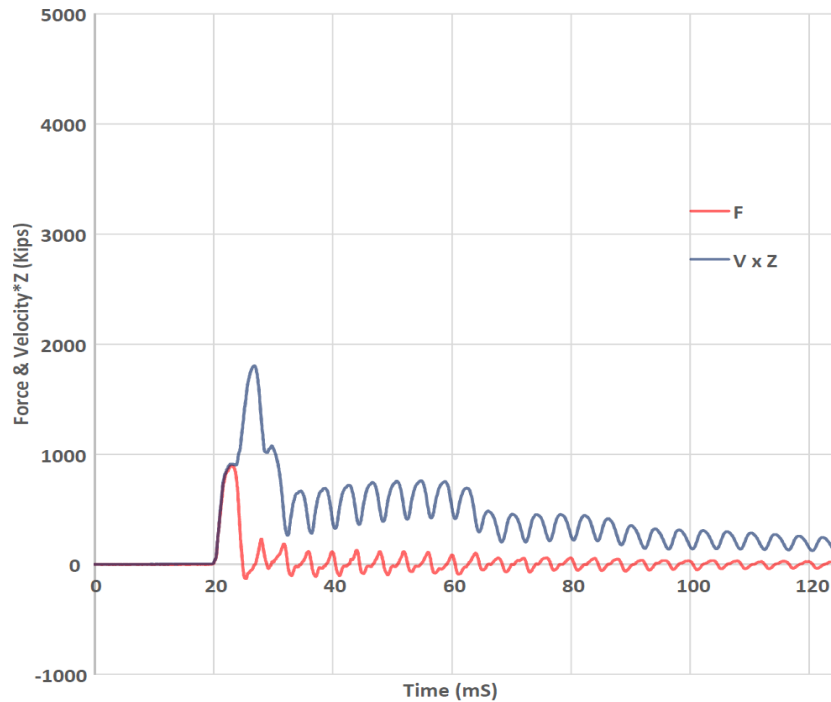


Figure E.26: Pile force traces from PDA resulting from impact drop height of 4 ft (PCC)

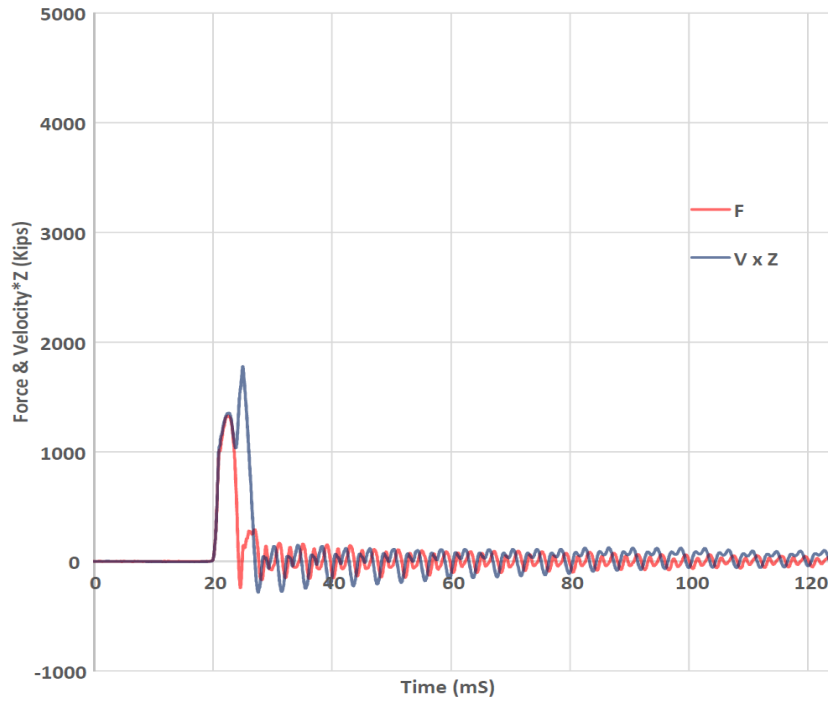


Figure E.27: Pile force traces from PDA resulting from impact drop height of 7 ft (PCC)

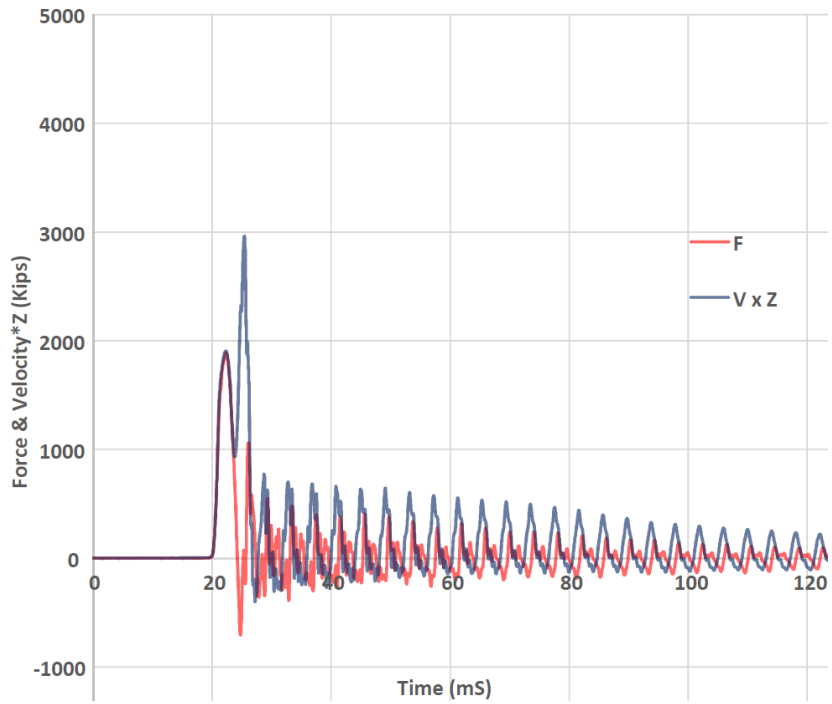


Figure E.28: Pile force traces from PDA resulting from impact drop height of 10 ft (PCC)

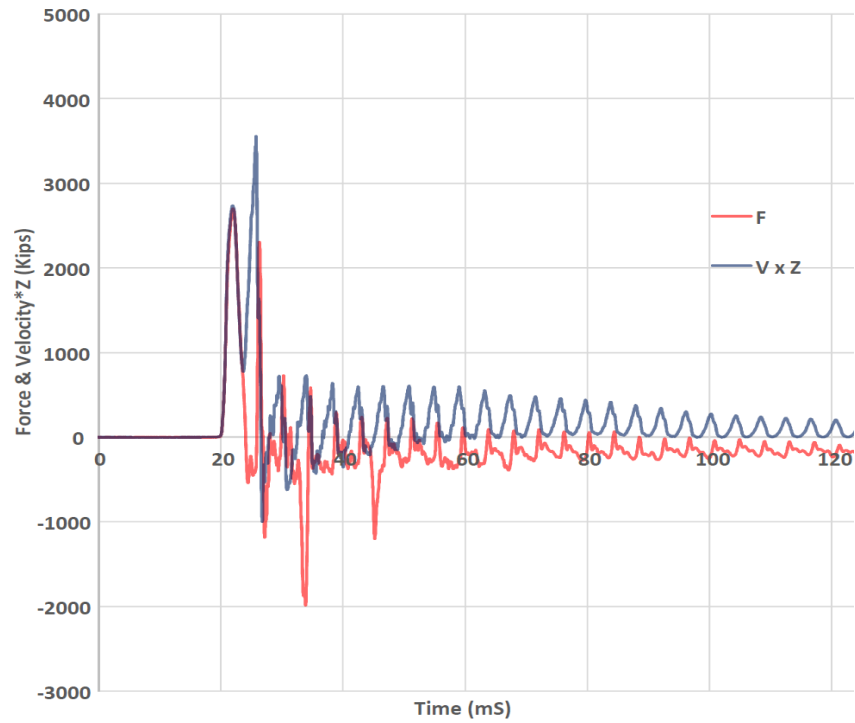


Figure E.29: Pile force traces from PDA resulting from impact drop height of 15 ft (PCC)

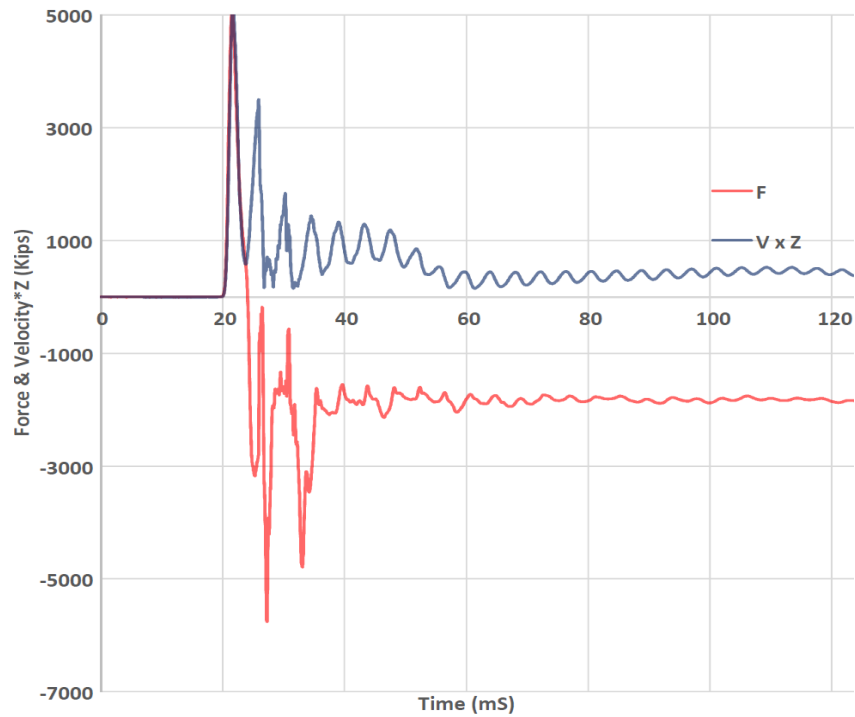


Figure E.30: Pile force traces from PDA resulting from impact drop height of 25 ft (PCC)

E.4. Peak Tensile Stress (TSX) and Its Location along the Pile.

E.4.1. Peak Tensile Stress (TSX) and its Location along the Pile (PSS)

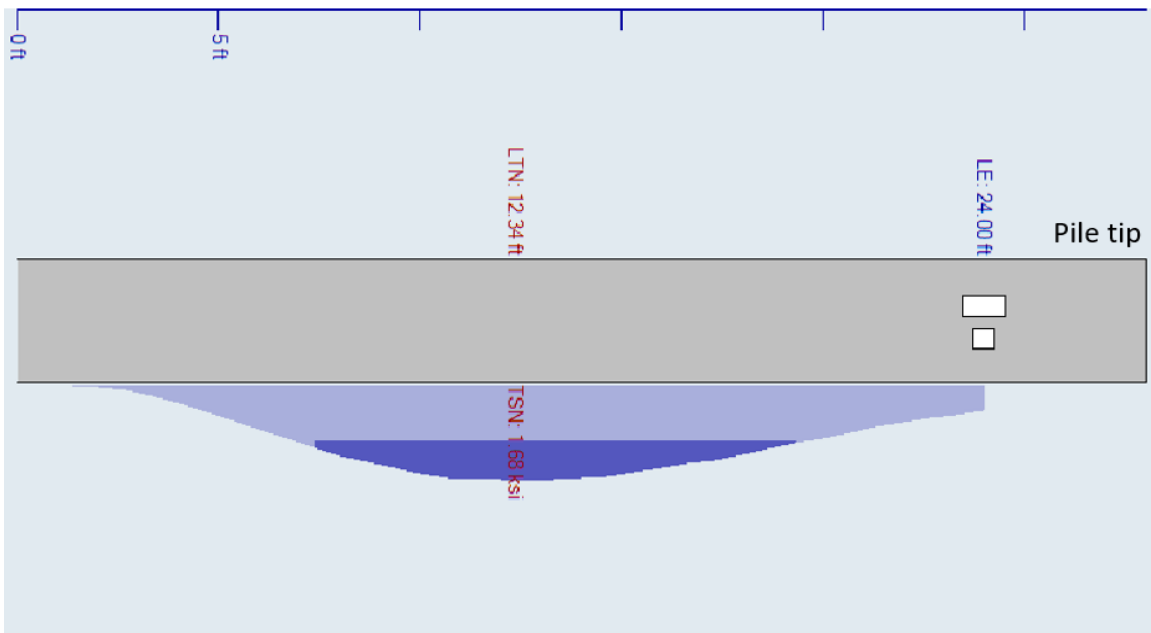


Figure E.31: Peak tensile stress (TSX) resulting from impact drop height of 7 ft (PSS) and its location along the pile

E.4.2. Peak Tensile Stress (TSX) and its Location along the Pile (PSG1)

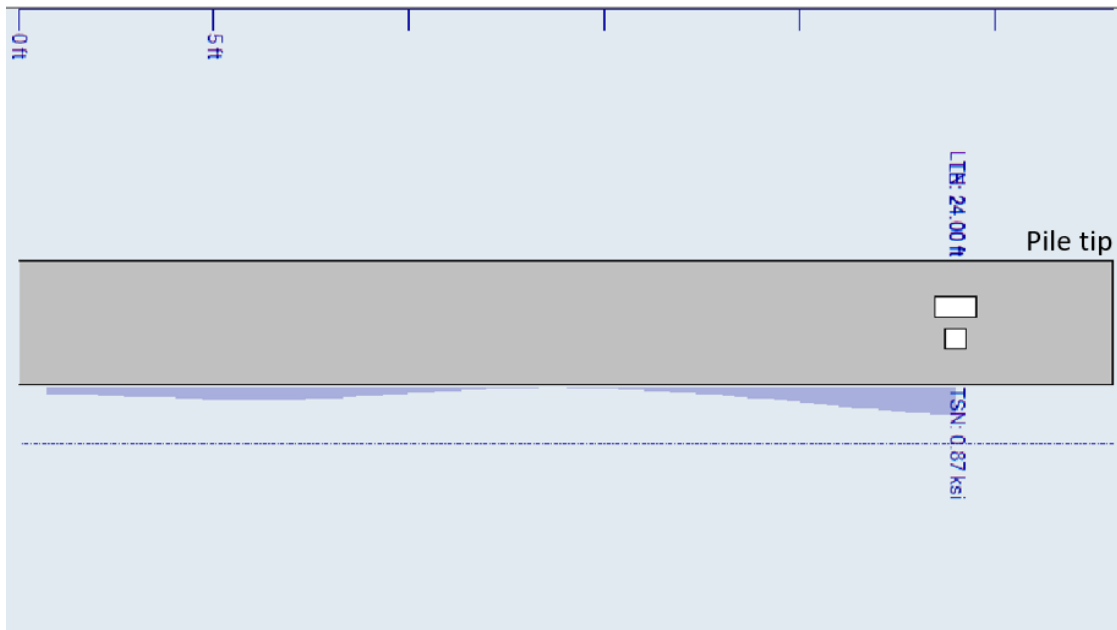


Figure E.32: Peak tensile stress (TSX) resulting from impact drop height of 4 ft (PSG1) and its location along the pile

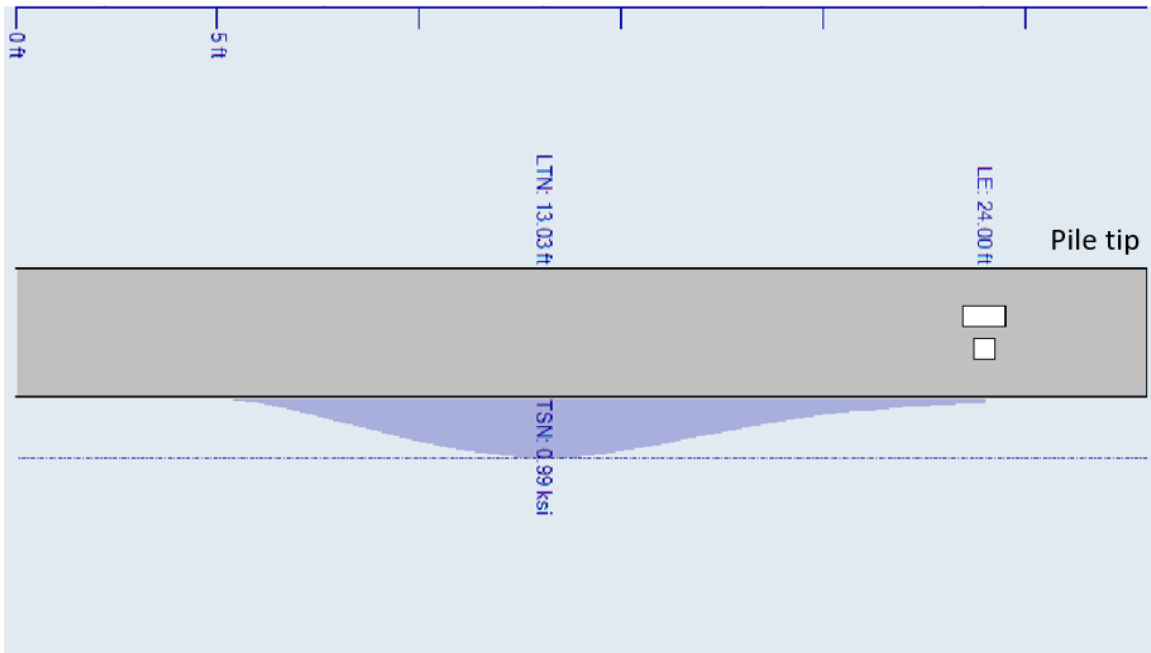


Figure E.33: Peak tensile stress (TSX) resulting from impact drop height of 7 ft (PSG1) and its location along the pile

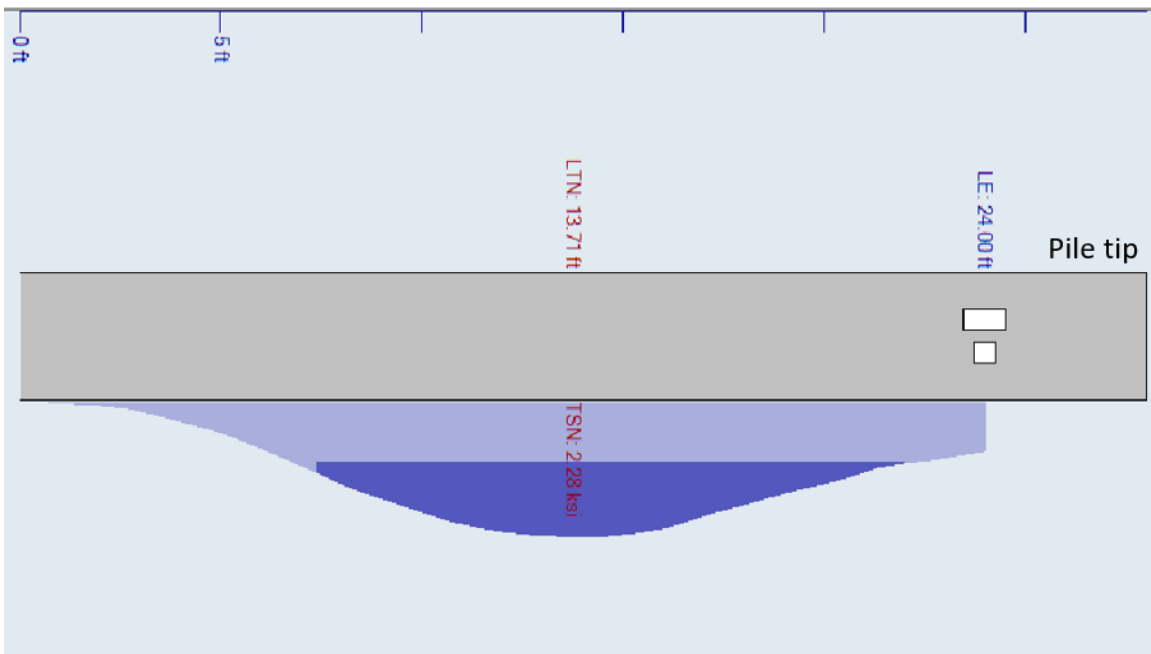


Figure E.34: Peak tensile stress (TSX) resulting from impact drop height of 10 ft (PSG1) and its location along the pile

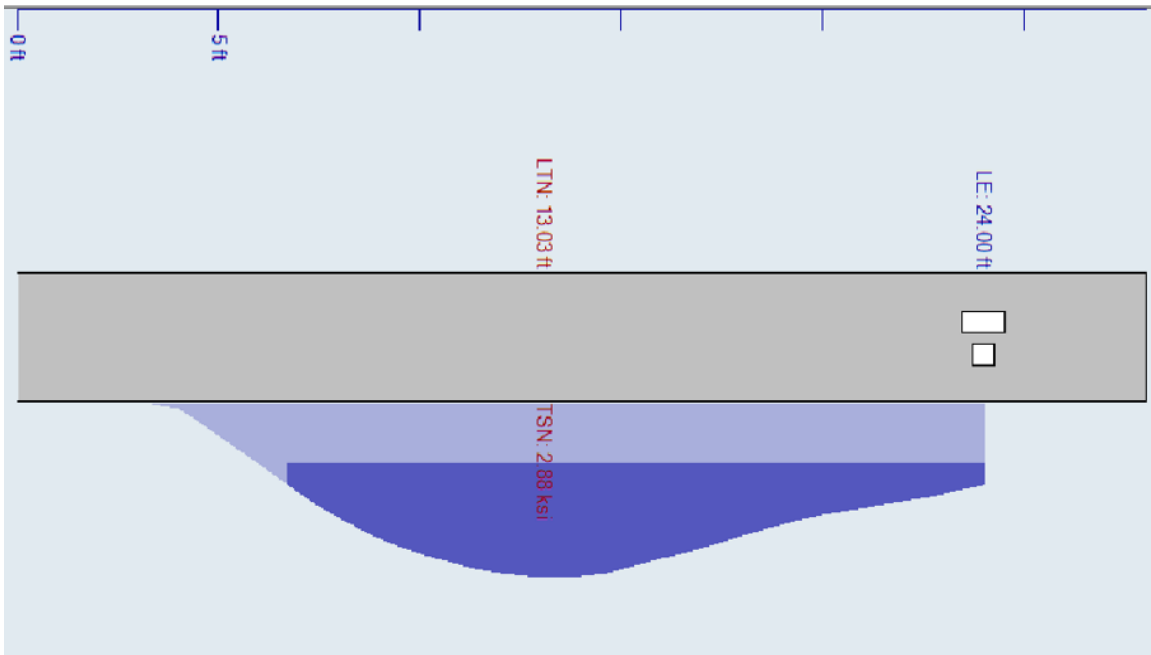


Figure E.35: Peak tensile stress (TSX) resulting from impact drop height of 15 ft (PSG1) and its location along the pile

E.4.3. Peak Tensile Stress (TSX) and its Location along the Pile (PCC)

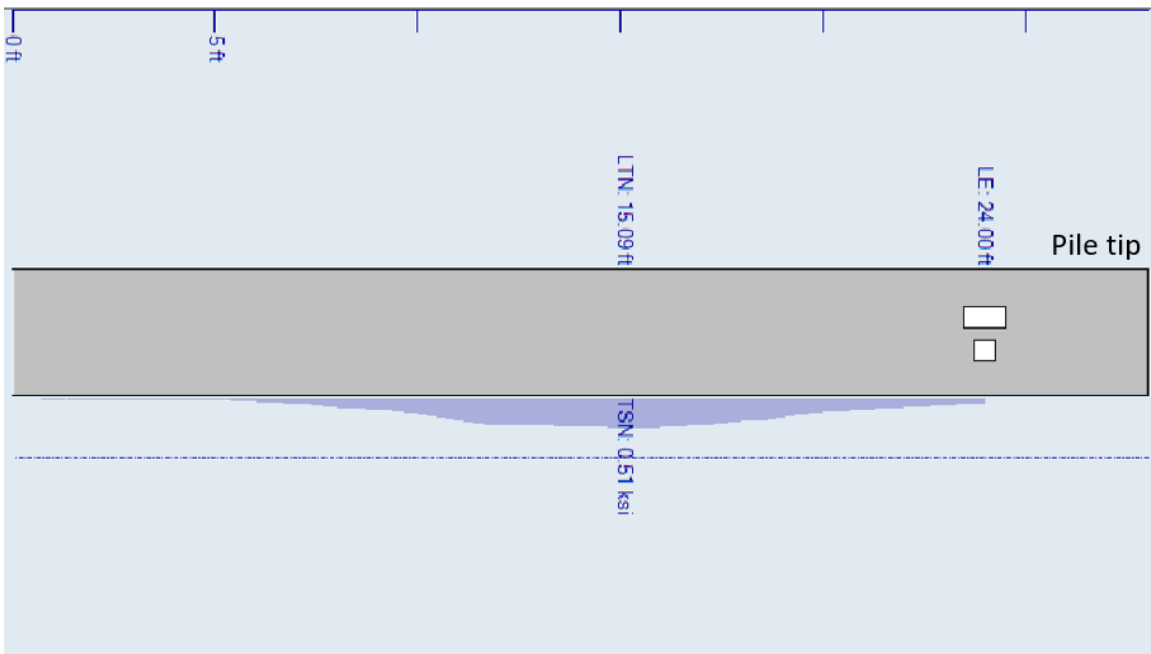


Figure E.36: Peak tensile stress (TSX) resulting from impact drop height of 4 ft (PCC) and its location along the pile

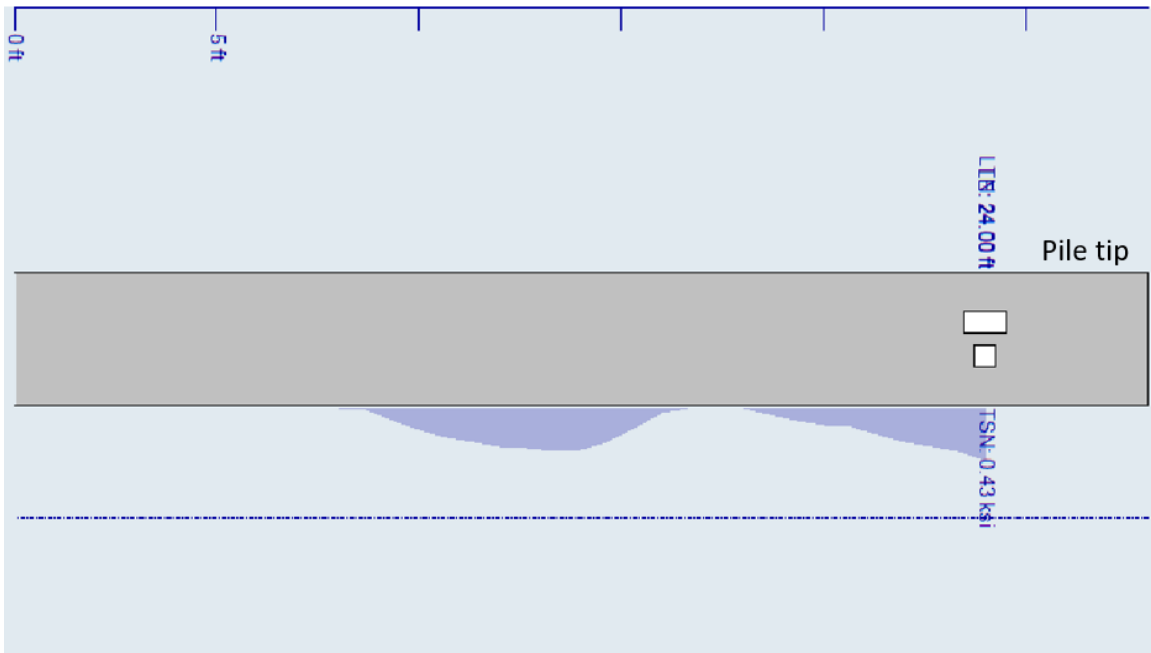


Figure E.37: Peak tensile stress (TSX) resulting from impact drop height of 7 ft (PCC) and its location along the pile

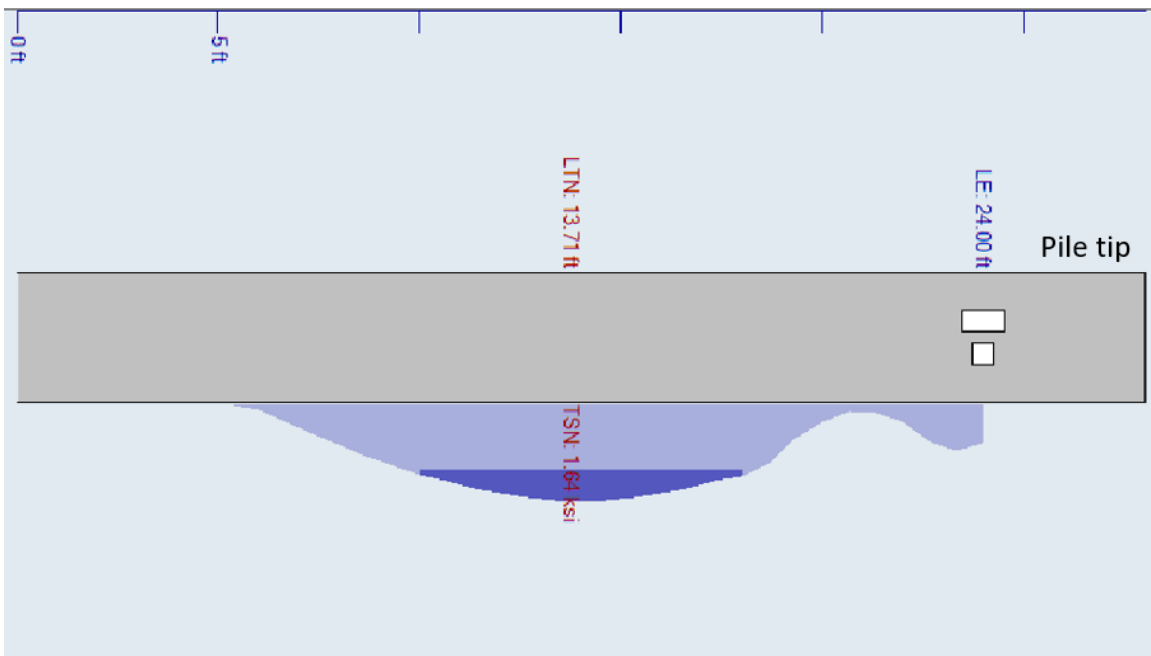


Figure E.38: Peak tensile stress (TSX) resulting from impact drop height of 10 ft (PCC) and its location along the pile

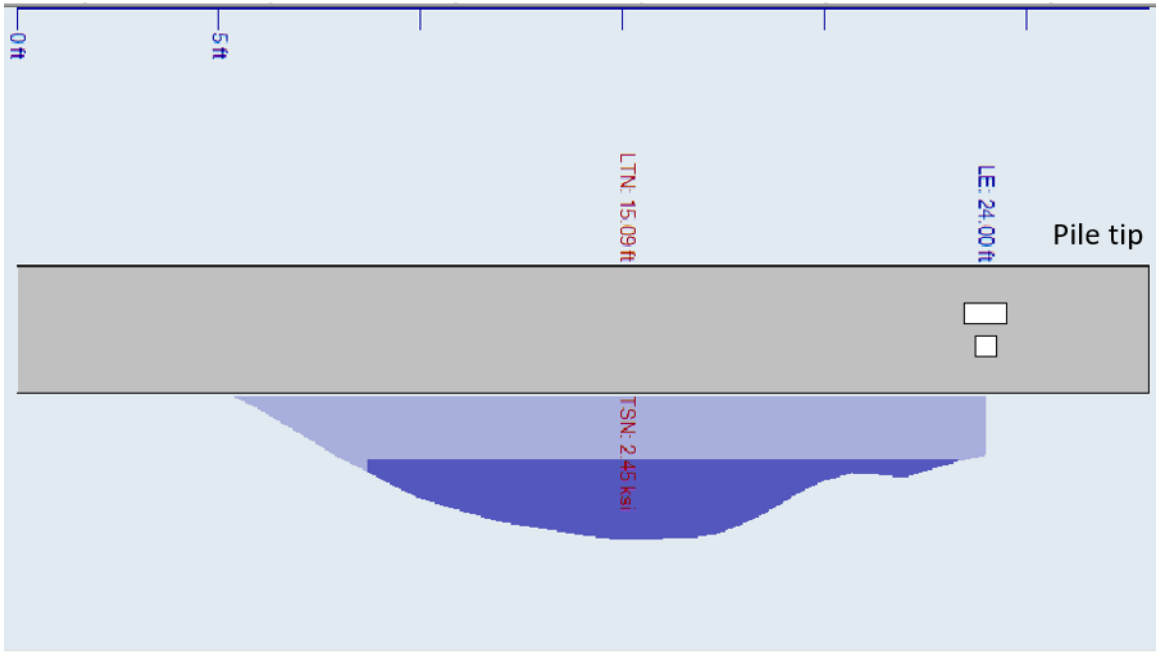


Figure E.39: Peak tensile stress (TSX) resulting from impact drop height of 15 ft (PCC) and its location along the pile

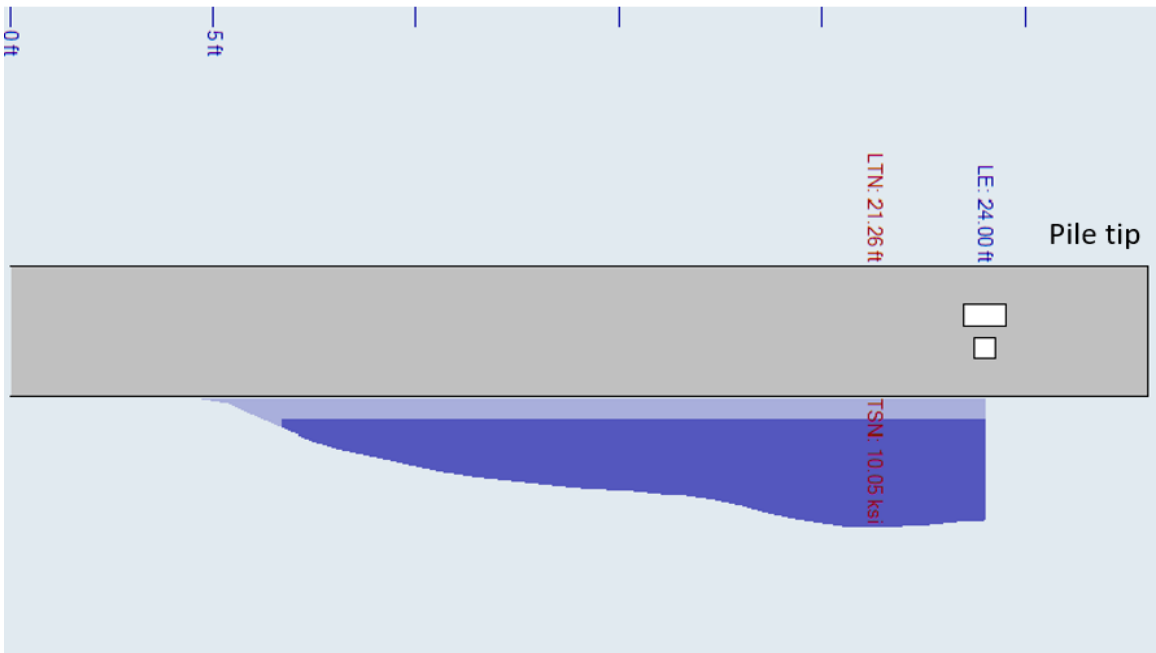


Figure E.40: Peak tensile stress (TSX) resulting from impact drop height of 25 ft (PCC) and its location along the pile

E.5. Spiral Strain under Impact Loading

E.5.1. Spiral Strain (PSS)

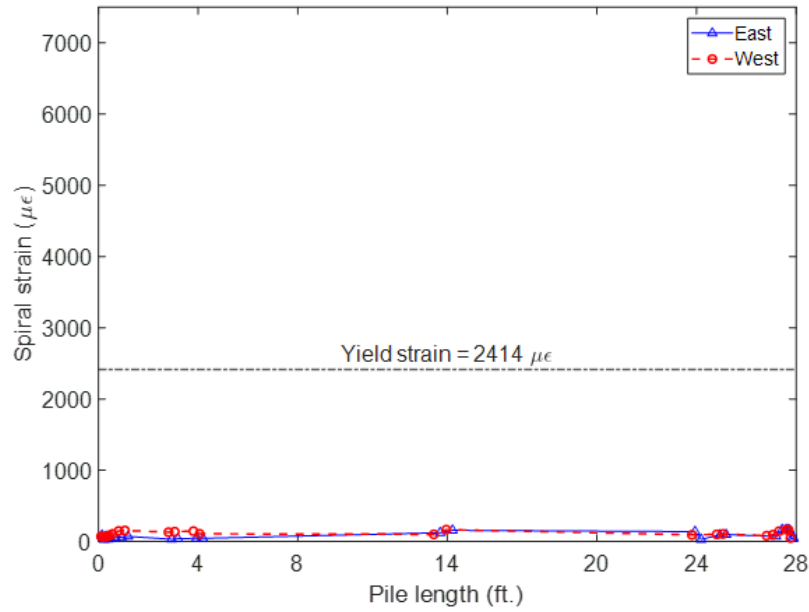


Figure E.41: Steel spiral strain PSS (7-ft drop height)

E.5.2. Spiral Strain (PSG1)

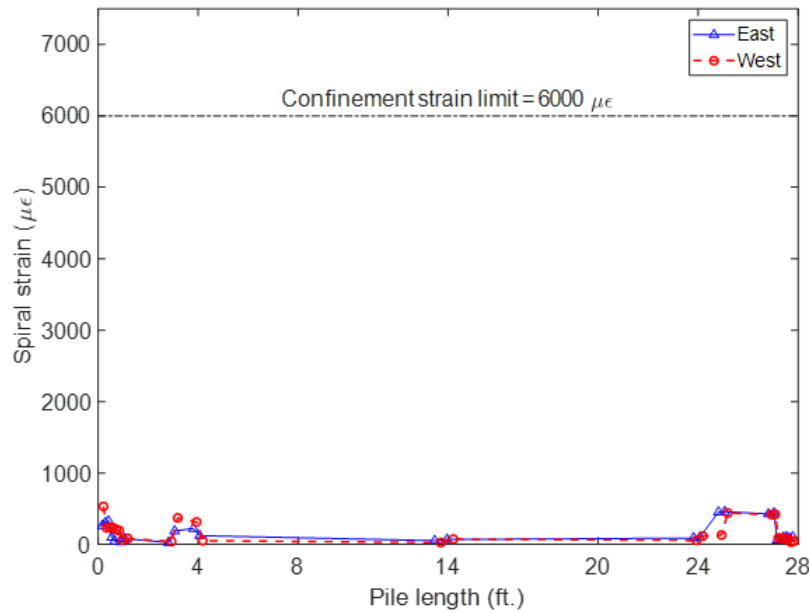


Figure E.42: GFRP spiral strain PSG1 (4-ft drop height)

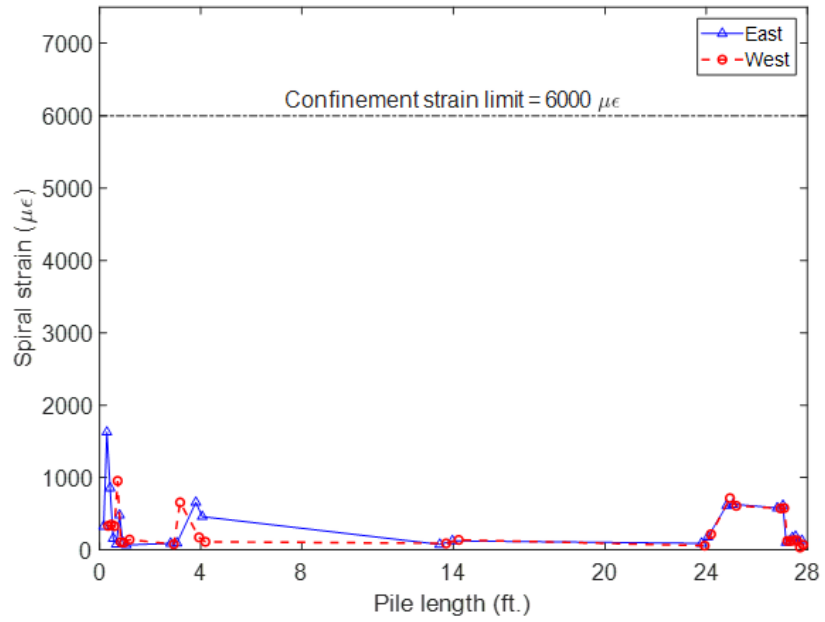


Figure E.43: GFRP spiral strain PSG1 (7-ft drop height)

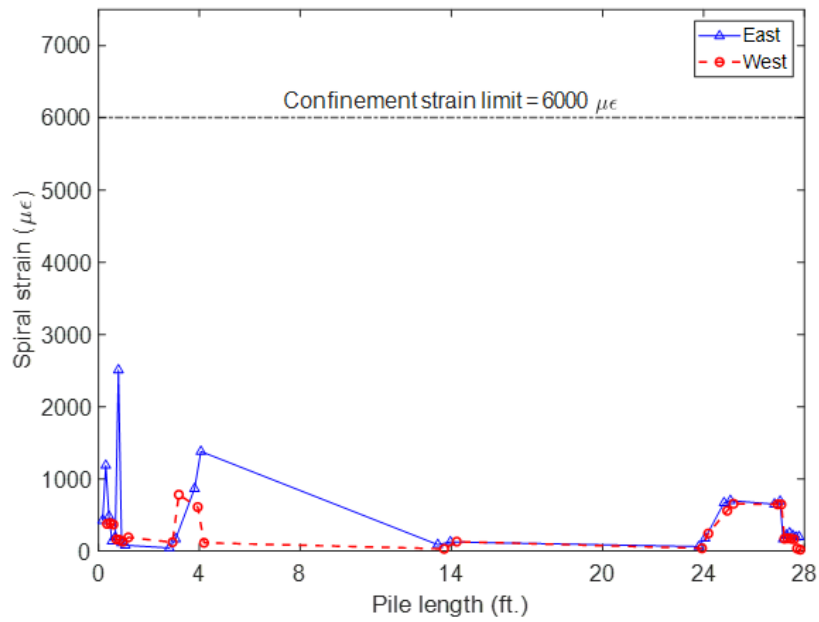


Figure E.44: GFRP spiral strain PSG1 (10-ft drop height)

E.6. Summary of All Test Results

Pile No.	Strike No.	Drop Height (ft)	Max. Top (ksi)	CSI Tip (ksi)	Avg. Top (ksi)	CSX Tip (ksi)	Max. TSX (ksi)
PSS	1	7	3.70	2.12	2.31	1.25	1.61
PSS	2	15	7.04	3.98	5.03	2.94	2.84
PSG1	1	4	2.64	1.19	1.51	0.64	1.09
PSG1	2	4	1.68	1.34	1.39	0.75	0.61
PSG1	3	7	2.70	2.41	1.98	1.41	0.95
PSG1	4	10	4.33	4.29	2.78	2.09	2.19
PSG1	5	15	4.44	3.07	3.86	2.09	2.85
PSG1	6	20	5.67	3.15	5.63	2.84	3.53
PCC	1	4	2.00	2.24	1.55	0.74	0.51
PCC	2	7	2.77	2.22	2.30	1.73	0.46
PCC	3	10	3.93	3.03	3.28	2.20	1.64
PCC	4	15	5.37	4.17	4.69	3.00	3.43
PCC	5	20	7.73	5.61	6.72	4.96	10.04
PCC	6	25	9.23	7.11	8.80	5.48	10.05

Appendix F. Construction Documents from CDS Manufacturing Inc. for Phase 2 Test Piles

CDS Manufacturing, Inc.				
QUALITY CONTROL - PRE/POST POUR INSPECTION REPORT - PILES				
Pre Pour Inspector: <i>GONYEA</i>		Date: 5/22/2023	Date: <i>5-24-23</i> <i>GONYEA</i>	
MAC Sample Number: <i>FSU</i>				
I.	FIN ID Number			
	Project Name	FSU/FAMU	FSU/FAMU	
D.	Lot / Pour Number	<i>FSU1</i>	<i>FSU1</i>	
	Piece Mark	FSU-24-001	FSU-24-002	
	Bed Location	1	2	
	Bed Identification	24" Pile Form	24" Pile Form	
P	Form Condition	<input checked="" type="checkbox"/>	<input checked="" type="checkbox"/>	
R	Form Cleanliness	<input checked="" type="checkbox"/>	<input checked="" type="checkbox"/>	
E	Length	28'	28'	
	Width	24"	24"	
P	Depth	24"	24"	
O	Squareness	<input checked="" type="checkbox"/>	<input checked="" type="checkbox"/>	
U	Strand Size	.6" CFCC	.6" CFCC	
R	Strand Placement	<input checked="" type="checkbox"/>	<input checked="" type="checkbox"/>	
	Reinforcing Size	<input checked="" type="checkbox"/>	<input checked="" type="checkbox"/>	
	Reinforcing Placement	<input checked="" type="checkbox"/>	<input checked="" type="checkbox"/>	
	Inserts / pipe sleeves	n/a	n/a	
	Lifting Apparatus	<input checked="" type="checkbox"/>	<input checked="" type="checkbox"/>	
	Chamfers	<input checked="" type="checkbox"/>	<input checked="" type="checkbox"/>	
P	Length	28'	28'	
O	Width	24"	24"	
S	Depth	24"	24"	
T	Squareness	<input checked="" type="checkbox"/>	<input checked="" type="checkbox"/>	
	Strand Placement	.6" CFCC	.6" CFCC	
P	Blockouts/Opening	<input checked="" type="checkbox"/>	<input checked="" type="checkbox"/>	
O	Plates	<input checked="" type="checkbox"/>	<input checked="" type="checkbox"/>	
U	Inserts / pipe sleeves	<input checked="" type="checkbox"/>	<input checked="" type="checkbox"/>	
R	Lifting Apparatus	n/a	n/a	
	Chamfers	<input checked="" type="checkbox"/>	<input checked="" type="checkbox"/>	
	Overall Finish	<input checked="" type="checkbox"/>	<input checked="" type="checkbox"/>	
	Surface Texture	<input checked="" type="checkbox"/>	<input checked="" type="checkbox"/>	
	Sprayed Finish	<input checked="" type="checkbox"/>	<input checked="" type="checkbox"/>	
	Sweep	n/a	n/a	
	Bowing	<input checked="" type="checkbox"/>	<input checked="" type="checkbox"/>	
	Cracks Or Spalls	<input checked="" type="checkbox"/>	<input checked="" type="checkbox"/>	
	Blocking/Dunnage	<input checked="" type="checkbox"/>	<input checked="" type="checkbox"/>	
COMMENTS:				

*Adjusted spiral
FSU present at
pre-pour*

*Minor bughdes
Minor tarp
lines*

CDS Manufacturing Inc.
Tensioning Report - Fixed Abutment Bed (non-self stressing)

Project: FSU/FAMU
 DATE: 5/19/23

STRAND LENGTH	.6 STEEL	DESIGN FORCE	PRELOAD	BASIC ELONGATION
2318				
816	CFCC	42,000	5,000	22.92

Gross Elongation Calcs.	DESIGN BASIC ELONGATION	22.92
	DEAD END SLIP (average)	0.13
	LIVE END SLIP (average)	0.34
	ABUTMENT ROTATION	0.125
	TOTAL GROSS ELONGATION	23.42
	PLUS 5%	24.59
	MINUS 5%	22.25
Adj. Force Calcs.	FORCE ADJUSTMENTS	
	DESIGN FORCE	42,000
	LIVE END SEATING ADJUSTED FORCE (lbs)	404
	ABUTMENT ROTATION ADJUSTED FORCE (lbs)	202
	ADJUSTED DESIGN FORCE	42,605
	ADJUSTED DESIGN FORCE plus 5%	44,736
ADJUSTED DESIGN FORCE minus 5%	40,475	
Net Elongation	GROSS ELONGATION	23.42
	LIVE END SEATING (deduct live end seating from gross along.)	0.25
	CFCC Anchor Slip	2.25
	NET ELONGATION	25.42
	PLUS 5%	26.69
	MINUS 5%	24.15

CFCC			
P	L		
37,000	816		CFCC Elongation
A	E		7.49646
0.1790	22,500,000		
.600 Strand			
P	L		
42,000	2316		.600 Elongation
A	E		15.4224
0.2100	28,800,000		
			Total Elongation
			22.91883625

Prestressing Strand information (per manufacturer certifications)

CFCC	.6 STEEL
AREA OF STRAND	0.1790
MODULUS OF ELASTICITY	22,500,000
AREA OF STRAND	0.1150
MODULUS OF ELASTICITY	28,800,000
AASHTO Limitation of force (lbs):	45,000
(not to exceed)	

Summary	
GROSS ELONGATION	23.42
NET ELONGATION	25.42
	26 3 / 8
NET ELONGATION plus 5%	26.69 26 5 / 8
NET ELONGATION minus 5%	24.15 24 1 / 8
ADJUSTED FORCE	42,605
ADJUSTED FORCE plus 5%	44,736
ADJUSTED FORCE minus 5%	40,475

5	0	0	0	0	0
4	0				0
3	0				0
2	0				0
1	0	0	0	0	0
	A	B	C	D	E

Jack No. CHAD
 Strand Size .600
 Roil / Pack No's. Sumiden/ TOKYO ROPE
RO21713-2
 Operators Name GOV YEA
 Weather 70° Clear
 Time Start 10 AM
 Time Finish 10:35 AM
 Comments: _____

Abutment Rotation (measured following stressing)

End 1: 0
 End 2: _____
 Total: _____

Live End Seating

1 1/4
 2 1/4
 3 1/4 1/4
 4 1/4 1/4
 Average: _____

Dead End Seating

1 1/2
 2 1/2
 3 1/2
 4 1/2
 Average: _____

Target Elongation (NET) (inches)	25.42		
		25	3 / 8
Elongation plus 5%	26.69		
		26	5 / 8
Elongation minus 5%	24.15		
		24	1 / 8
AASHTO Limit (Not to Exceed)	45,000		
Adjusted Force	42,605		
Adjusted Force plus 5%	44,736		
Adjusted Force Minus 5%	40,475		
<i>**if adjusted force plus 5% exceeds AASHTO Limit - use AASHTO limit as the maximum force. Do not Exceed AASHTO Limit</i>			

STRAND No.	NET ELONG.	GAUGE READING
1A	24 3/4	42.6
B	24 3/4	↓
C	24 3/4	↓
D	24 3/4	↓
E	24 3/4	↓
2A	24 5/8	42.6
E	24 5/8	42.6
3A	24 3/4	42.6
E	24 3/4	42.6
4A	24 3/4	42.6
E	24 3/4	42.6
5A	24 3/4	↑
B	24 3/4	↑
C	24 3/4	↑
D	24 3/4	↑
E	24 3/4	42.6

CDS

Manufacturing, Inc.

106 Charles Hayes St. Drive
Gretna, FL 32332

Phone: (850) 627-3035 • Fax: (850) 627-3904

01

05/22/2023

CDS GRETNA

52683

FSU/FAMU

24" PILES

INITIAL
ACCEPT

Plant No. CD502	DOT Class 8500-psi	DOT Mix No. 03-2343	Cubic Yards This Load	Chloride Test Results
Truck No.	Water Added 2gal	Time Loaded 1:27 PM	Cubic Yards Total Today	Chloride Test Date
Cement		Fly Ash or Slag		
Source ASH	Type IL (13)	Amount	Source ECO	Type F
Coarse Agg. GA553 / 30-267		Air Entertainment Admixtures		
Pt Num.	% Moisture	Amount	Source BASF	Brand AE-90
Fine Agg. 50-471		Admixture		
Pt Num.	% Moisture	Amount	Source BASF	Brand 961-R
Batch Water (gals. Or lbs.)		Admixture		
		Source BASF		
		Brand 7920		
		Type F		

Truck	Driver	User	Disp Ticket Num	Ticket ID	Time Date
CD502		user		52683	13:29 5/22/2
Load Size	Mix Code	Returned	Qty	Mix Age	Seq
9.00 yd	03-2343				W
					Load ID
					53204

Material	Design Qty	Required	Batched	% Var	% Moisture	Actual	Wat	Trim
CEMENT	736.0 lb	6624.0 lb	6615.0 lb	-0.14%				
FLYASH	164.0 lb	1476.0 lb	1475.0 lb	-0.07%				
#67 Granite	1588 lb	14432 lb	14410 lb	-0.15%	0.98% M	17 gl		
SAND	1270 lb	11636 lb	11600 lb	-0.31%	1.80% M	25 gl		
AE-90	50 oz	4.50 oz	4.75 oz	5.56%				
R 961	7.00 oz	63.00 oz	63.00 oz	0.00%				
GLENIUM 79:	60.00 oz	540.00 oz	537.00 oz	-0.56%				
WATER	33.60 gl	193.46 gl	193.00 gl	-0.24%		193.00 gl		-7.50 gl

u/w = 25
8.55
46.0

Actual Issuance of this ticket constitutes certification that the concrete batched was produced and information recorded in compliance with Department
Load Specification and other Contract Document requirements for Structural Concrete. 302.4 gl Actual 234.3 gl To Add: 68
Slump: 3.00 in Water in Truck: 0.0 gl Adjust Water: 0.0 gl / Load Trim Water: 7.5 gl / yd

Robbie Harris

CTQP Technical Identification Number

Signature of Batch Plant Operator

MIXER	B: 1 Mixed	80 of	80 Sec.	Initial Concrete Temp.	Initial w/c Ratio
MIXER	B: 2 Mixed	80 of	80 Sec.	87°F	.24
MIXER	B: 3 Mixed	80 of	80 Sec.	Acceptance Concrete Temp.	Acceptance w/c Ratio
	Acceptance Slump/Spread	Acceptance Air		88°F	.24

Issuance of this ticket constitutes certification that the maximum specified water cementitious ratio was not exceeded and the batch was delivered and placed in compliance with Department Specification and other Contract Document requirements.

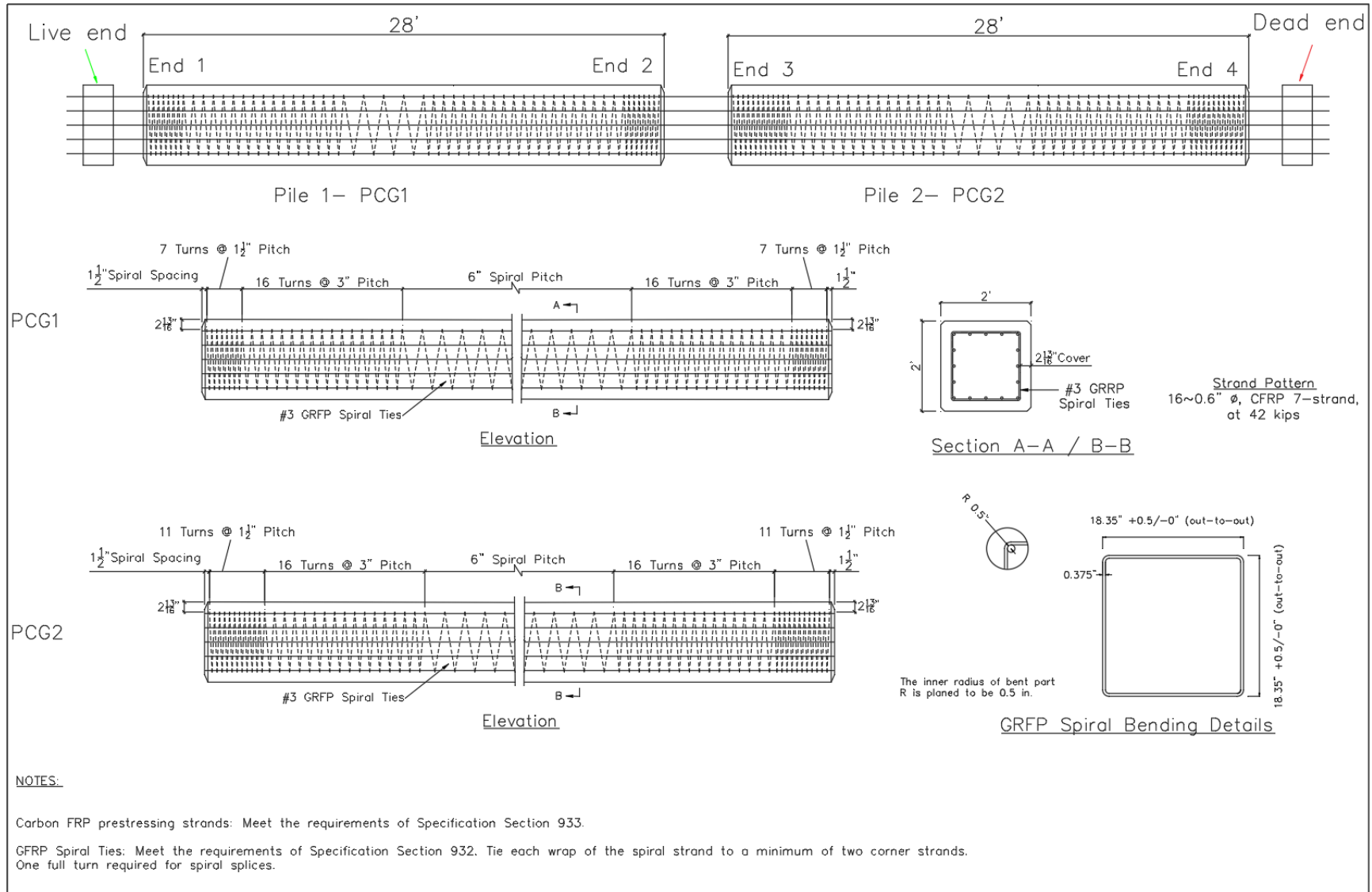
CTQP Technical Identification Number

Signature of Contractor's Representative

M36210397

CM

Appendix G. As-built Drawing of Phase 2 Test Piles



Appendix H. PDA Measurements (Phase 2 Impact Tests)

H.1. PDA Measurements (PCG1)

H.1.1. PDA Strain Gauge Measurement (PCG1)

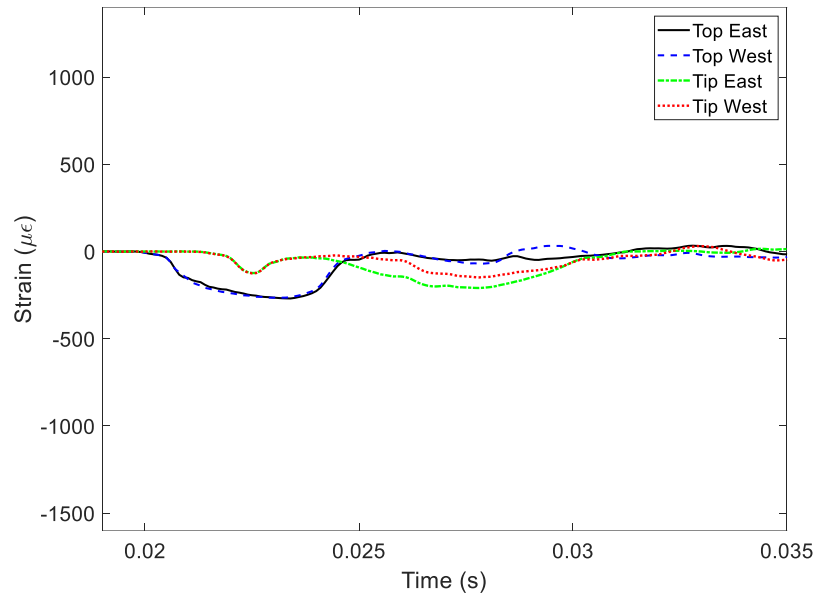


Figure H.1: Top and tip strains from PDA strain gauges at impact drop height of 5 ft (PCG1)

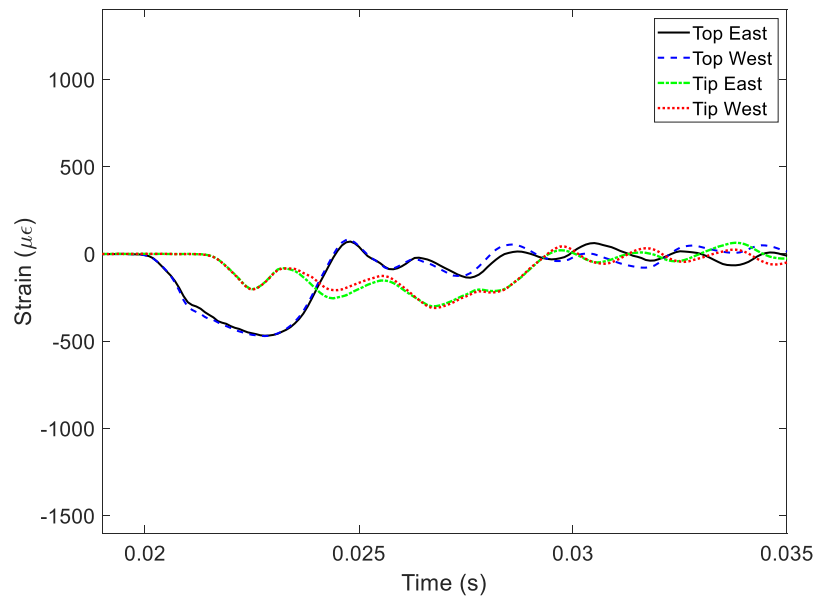


Figure H.2: Top and tip strains from PDA strain gauges at impact drop height of 10 ft (PCG1)

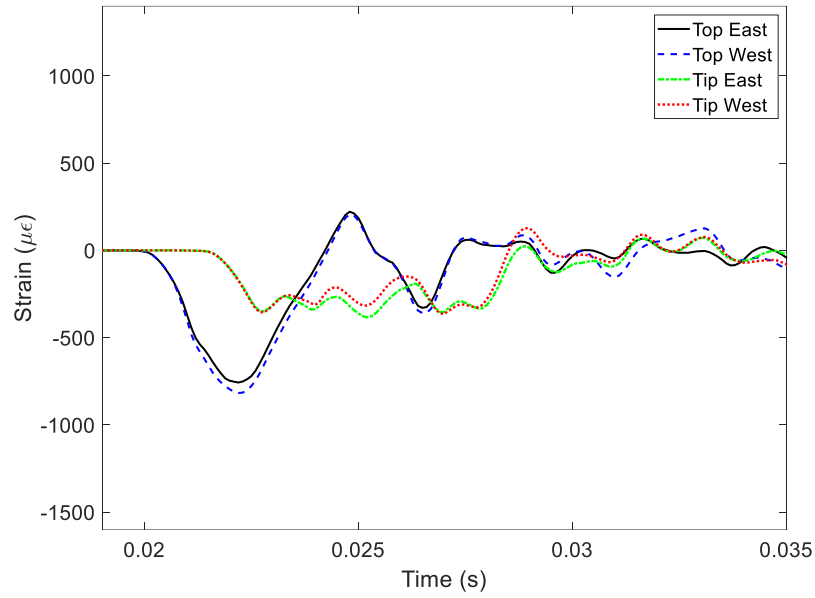


Figure H.3: Top and tip strains from PDA strain gauges at impact drop height of 15 ft (PCG1)

H.1.2. PDA Acceleration Measurement (PCG1)

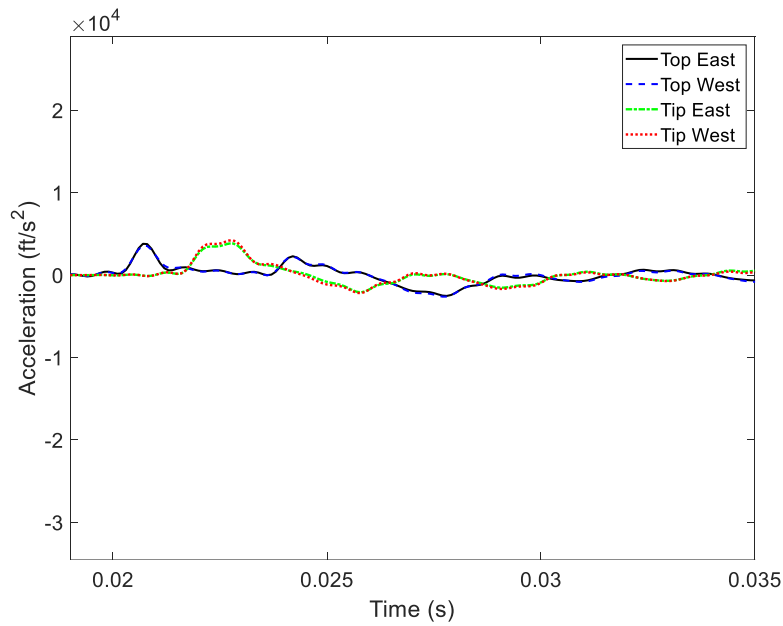


Figure H.4: PDA measured acceleration at pile top and tip at a drop height of 5 ft (PCG1)

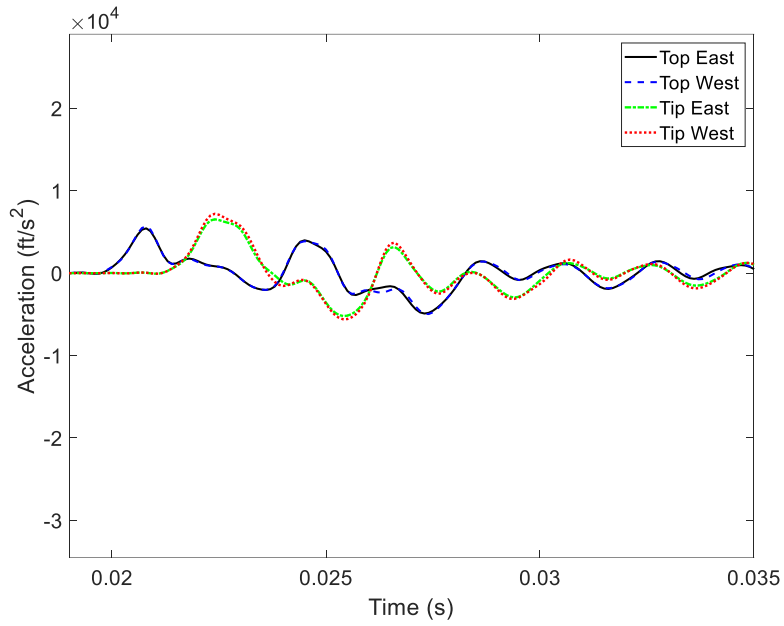


Figure H.5: PDA measured acceleration at pile top and tip at a drop height of 10 ft (PCG1)

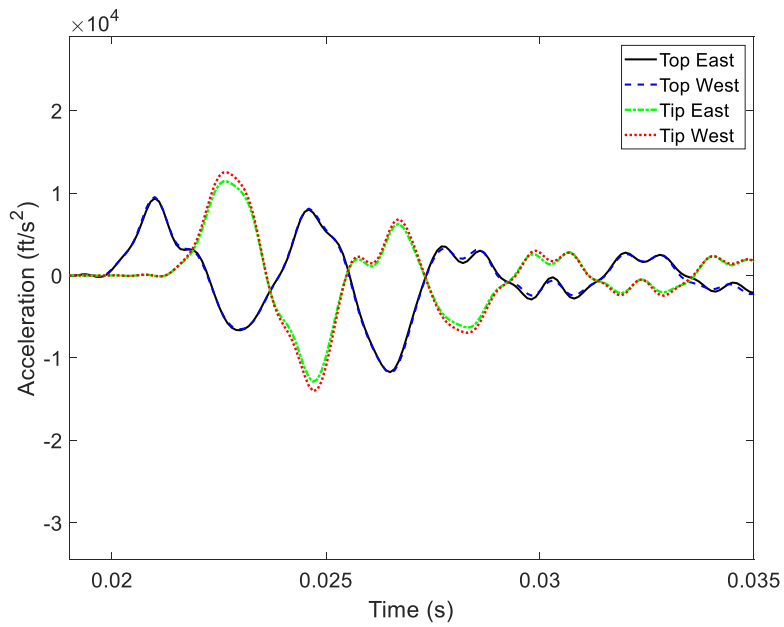


Figure H.6: PDA measured acceleration at pile top and tip at a drop height of 15 ft (PCG1)

H.2. PDA Measurements (PCG2)

H.2.1. PDA Strain Gauge Measurement (PCG2)

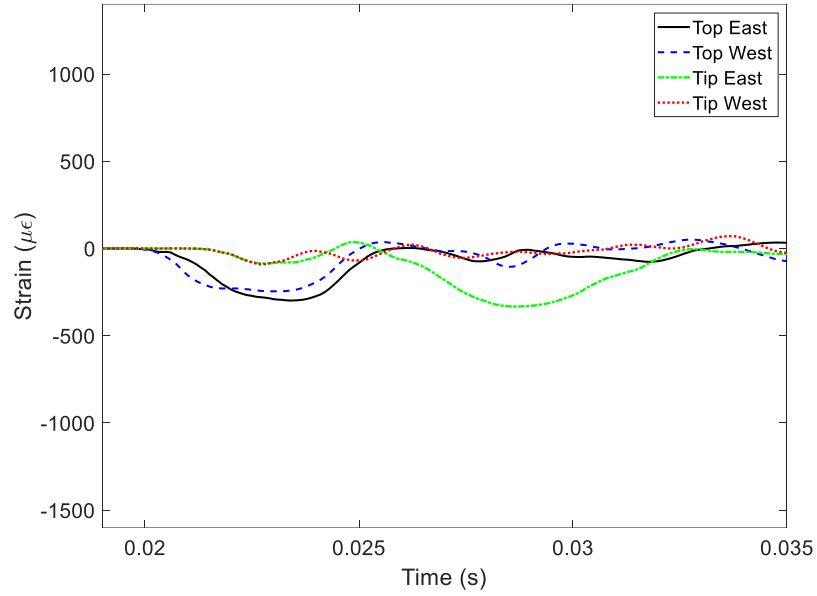


Figure H.7: Top and tip strains from PDA strain gauges at impact drop height of 5 ft (PCG2)

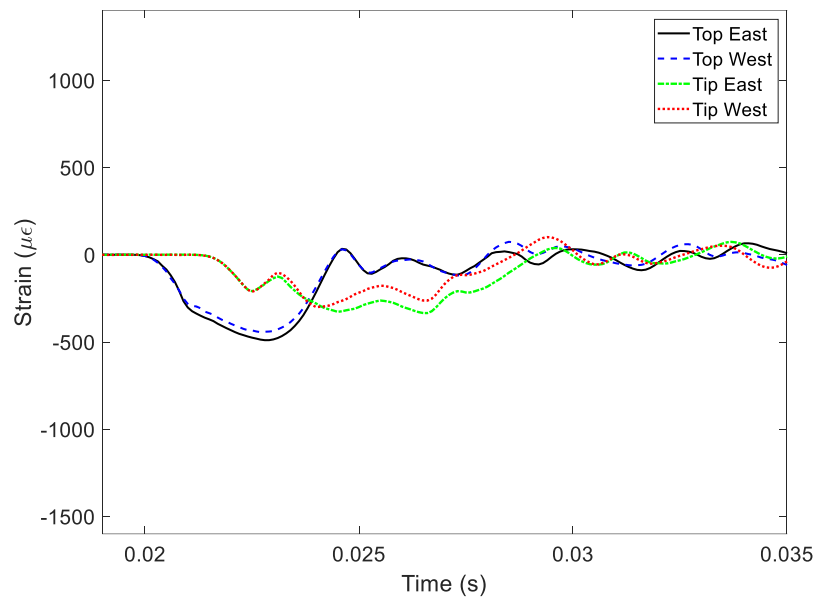


Figure H.8: PDA measured acceleration at pile top and tip at a drop height of 10 ft (PCG2)

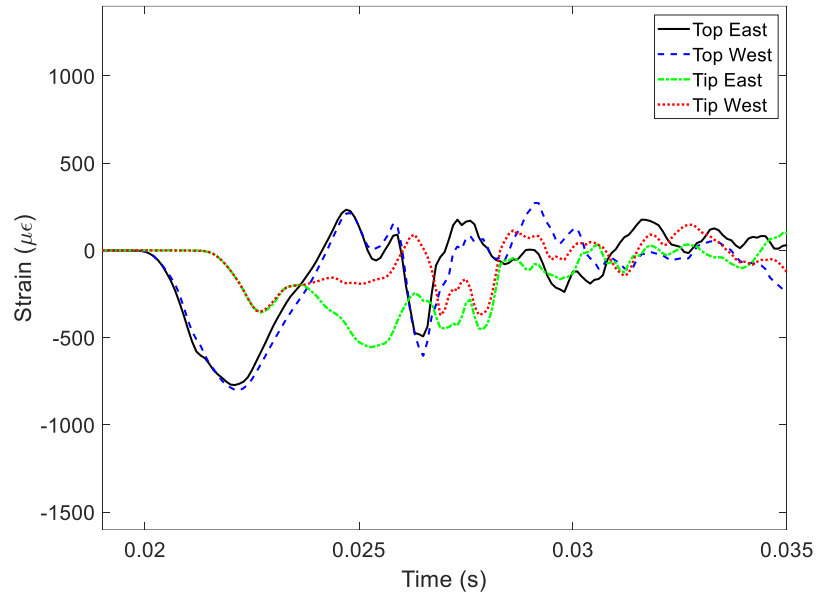


Figure H.9: PDA measured acceleration at pile top and tip at a drop height of 15 ft (PCG2)

H.2.1. PDA Acceleration Measurement (PCG2)

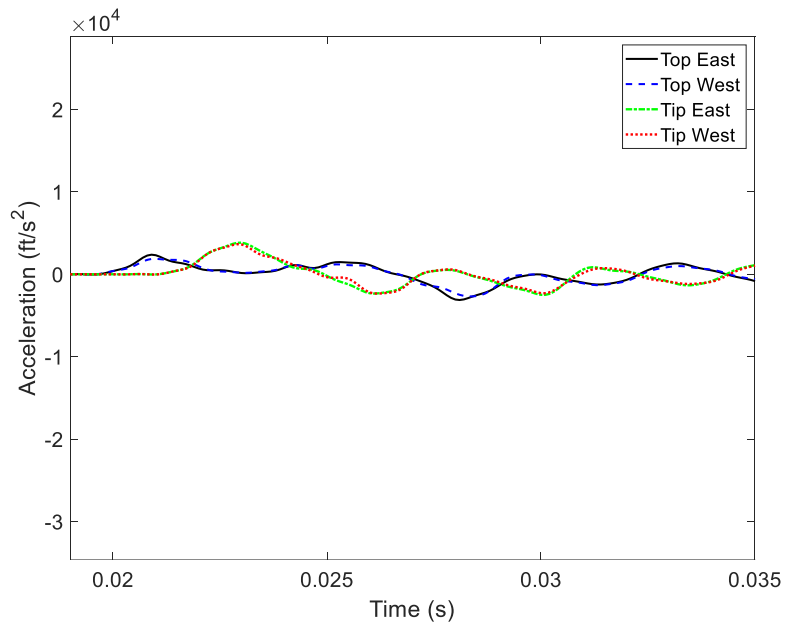


Figure H.10: PDA measured acceleration at pile top and tip at a drop height of 5 ft (PCG2)

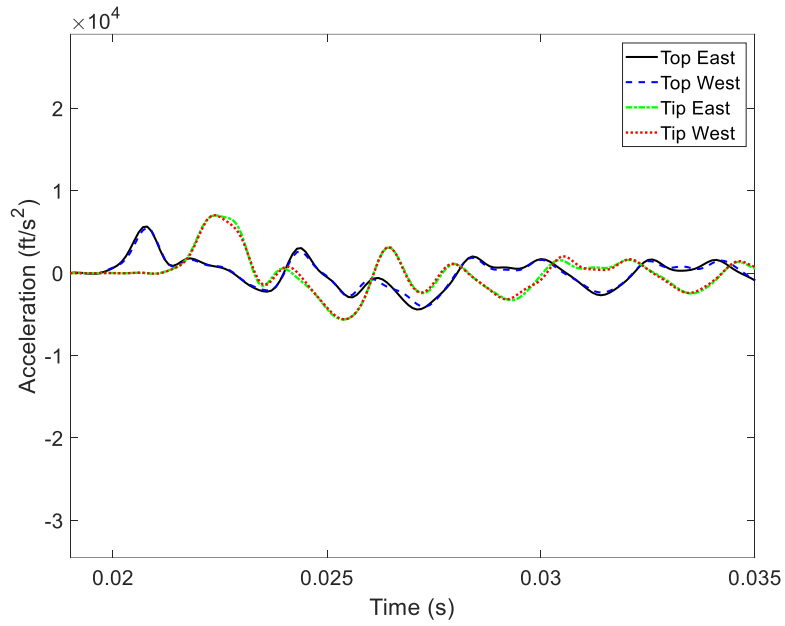


Figure H.11: PDA measured acceleration at pile top and tip at a drop height of 10 ft (PCG2)

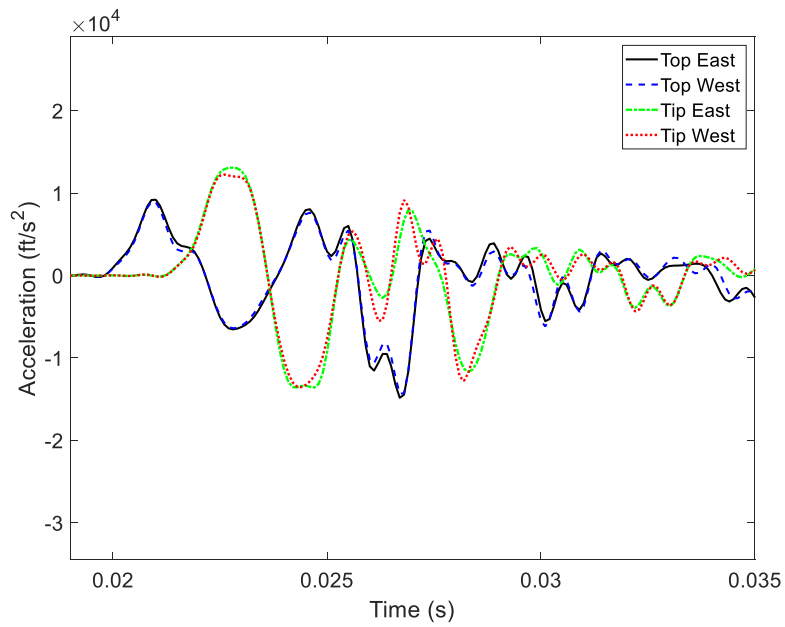


Figure H.12: PDA measured acceleration at pile top and tip at a drop height of 15 ft (PCG2)

H.3. Pile Force Traces from PDA

H.3.1. Pile Force Traces from PDA (PCG1)

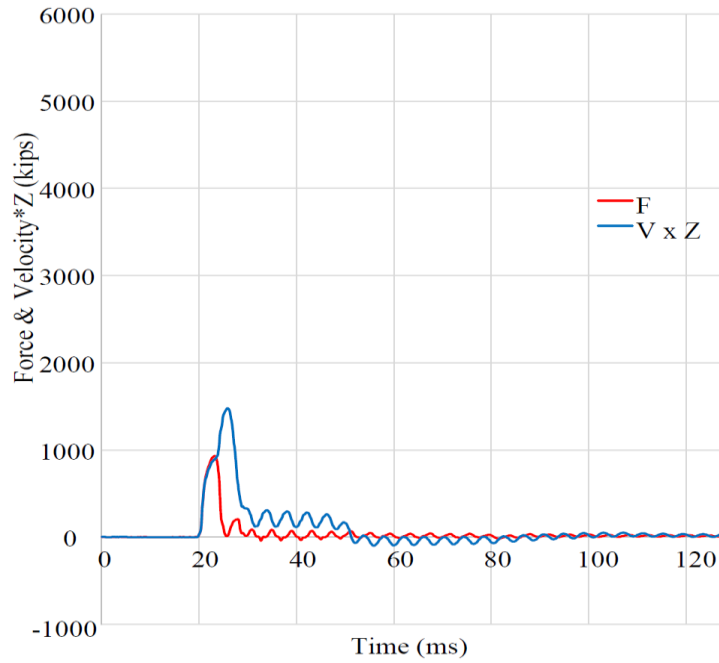


Figure H.13: Pile force traces from PDA resulting from impact drop height of 5 ft (PCG1). (Compressive force is positive in this figure which was produced by Terracon)

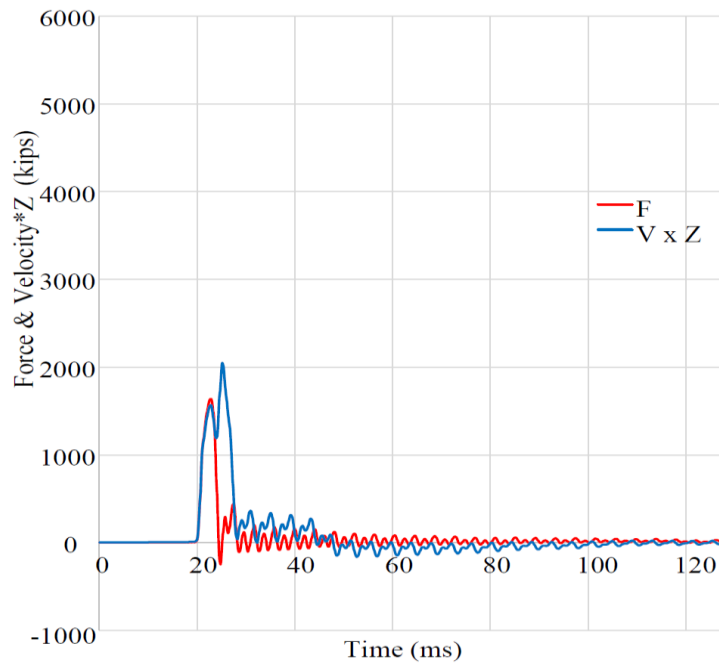


Figure H.14: Pile force traces from PDA resulting from impact drop height of 10 ft (PCG1). (Compressive force is positive in this figure which was produced by Terracon)

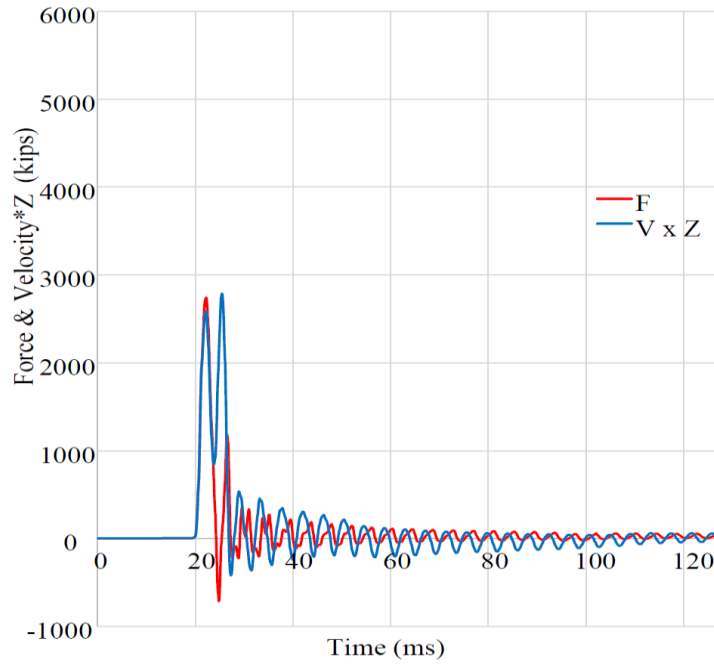


Figure H.15: Pile force traces from PDA resulting from impact drop height of 15 ft (PCG1).
(Compressive force is positive in this figure which was produced by Terracon)

H.3.2. Pile Force Traces from PDA (PCG1)

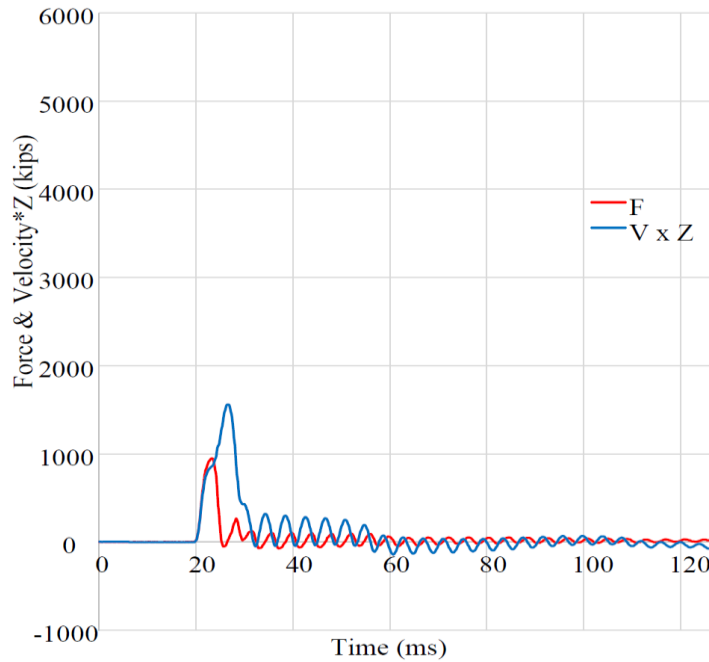


Figure H.16: Pile force traces from PDA resulting from impact drop height of 5 ft (PCG2).
(Compressive force is positive in this figure which was produced by Terracon)

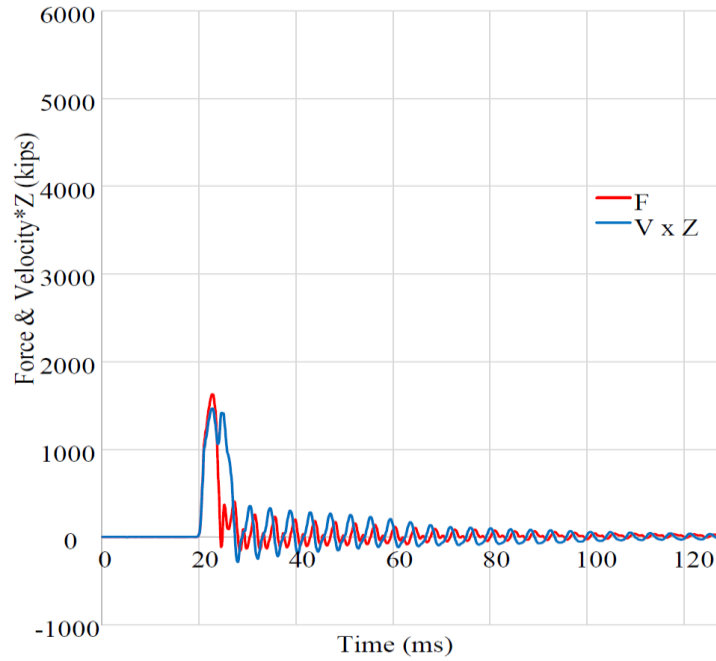


Figure H.17: Pile force traces from PDA resulting from impact drop height of 10 ft (PCG2). (Compressive force is positive in this figure which was produced by Terracon)

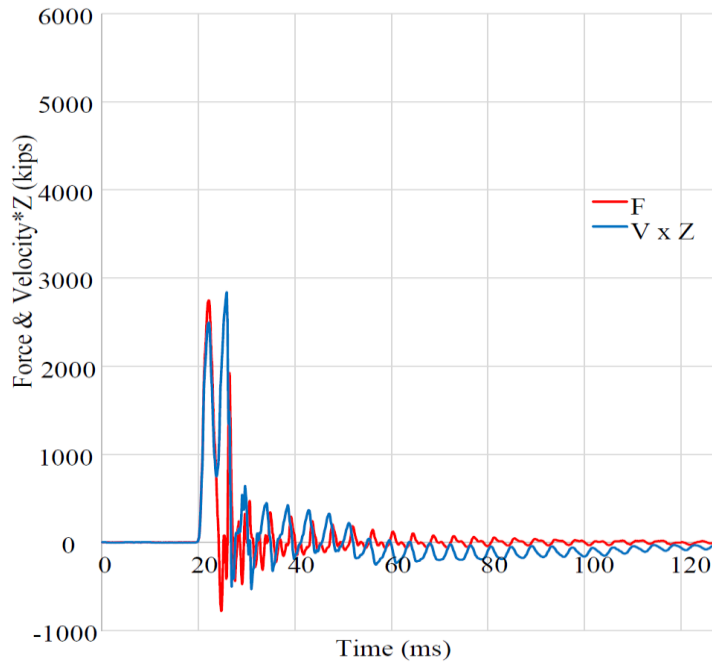


Figure H.18: Pile force traces from PDA resulting from impact drop height of 15 ft (PCG2). (Compressive force is positive in this figure which was produced by Terracon)

H.4. Peak Tensile Stress (TSX) and Its Location along the Pile.

H.4.1. Peak Tensile Stress (TSX) and its Location along the Pile (PCG1)

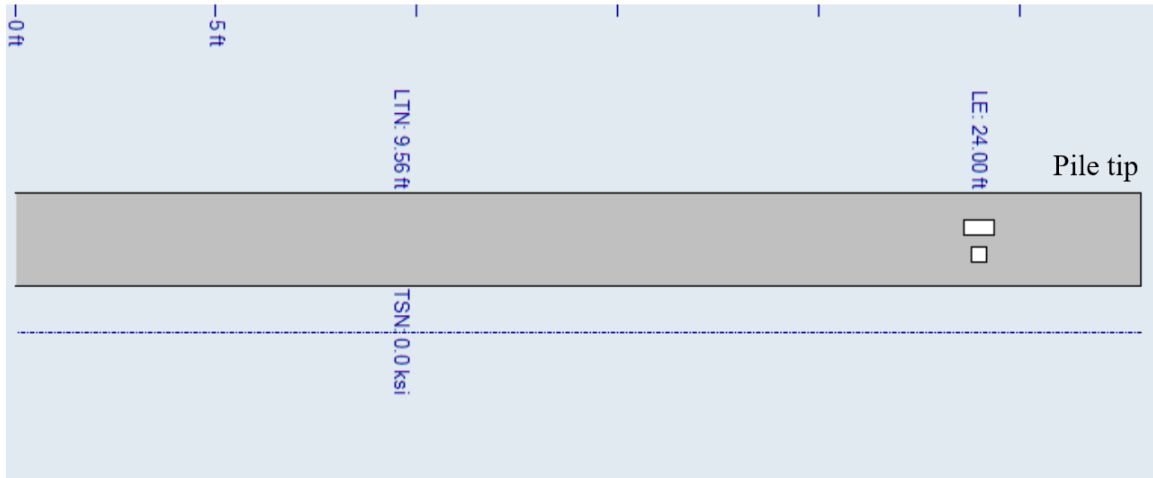


Figure H.19: Peak tensile stress (TSX) resulting from impact drop height of 5 ft (PCG1) and its location along the pile. (This figure was produced by Terracon)

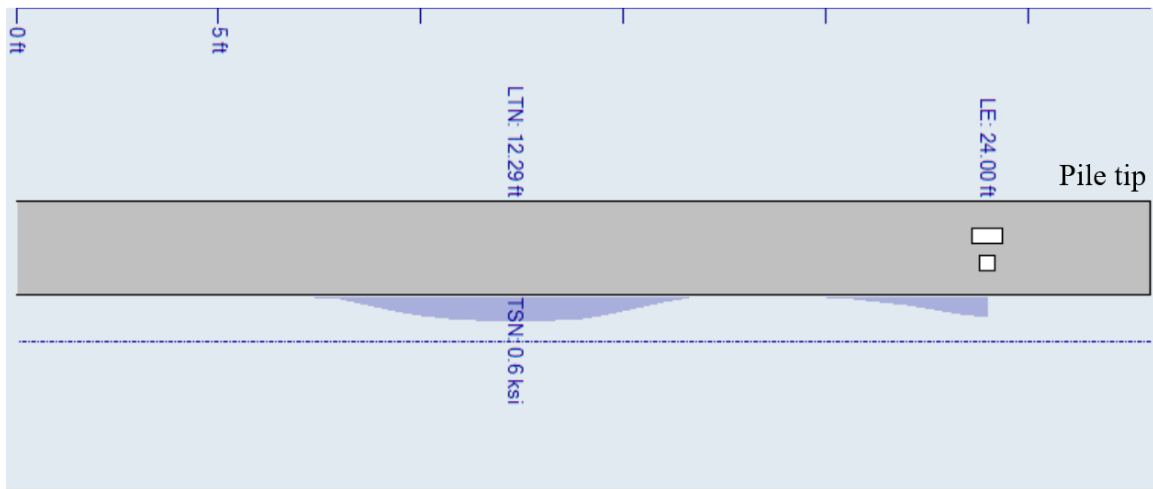


Figure H.20: Peak tensile stress (TSX) resulting from impact drop height of 10 ft (PCG1) and its location along the pile. (This figure was produced by Terracon)

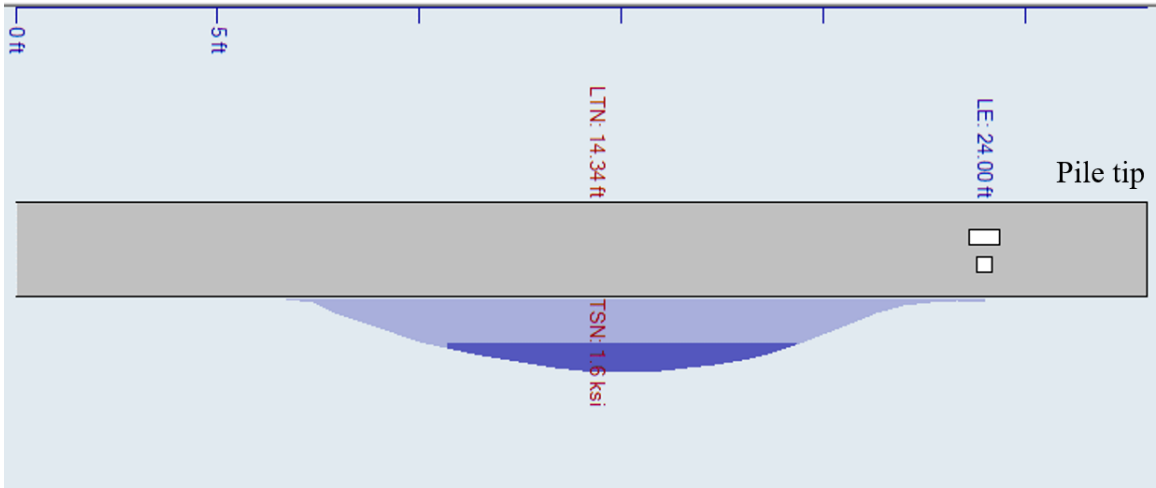


Figure H.21: Peak tensile stress (TSX) resulting from impact drop height of 15 ft (PCG1) and its location along the pile. (This figure was produced by Terracon)

H.4.2. Peak Tensile Stress (TSX) and its Location along the Pile (PCG1)

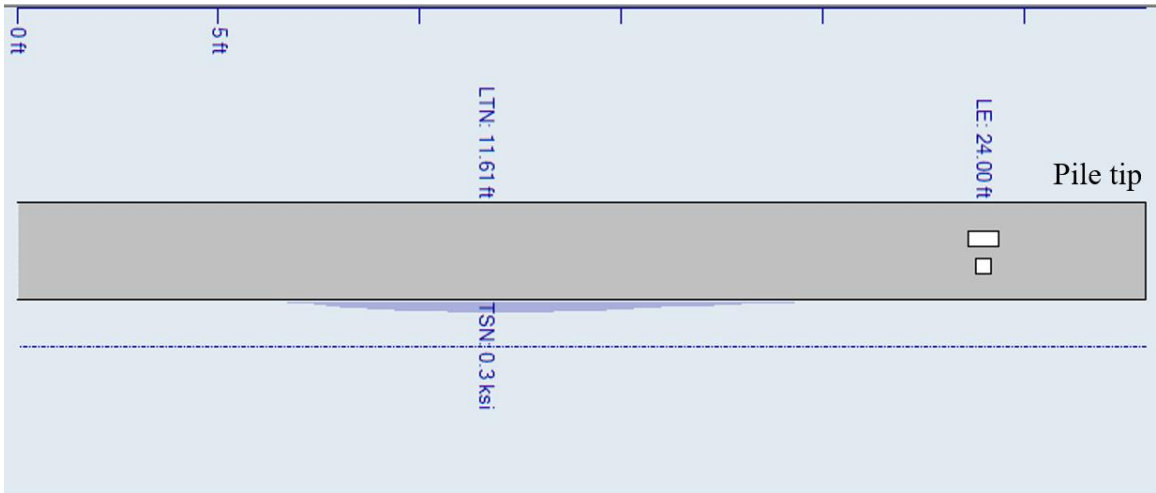


Figure H.22: Peak tensile stress (TSX) resulting from impact drop height of 5 ft (PCG2) and its location along the pile. (This figure was produced by Terracon)

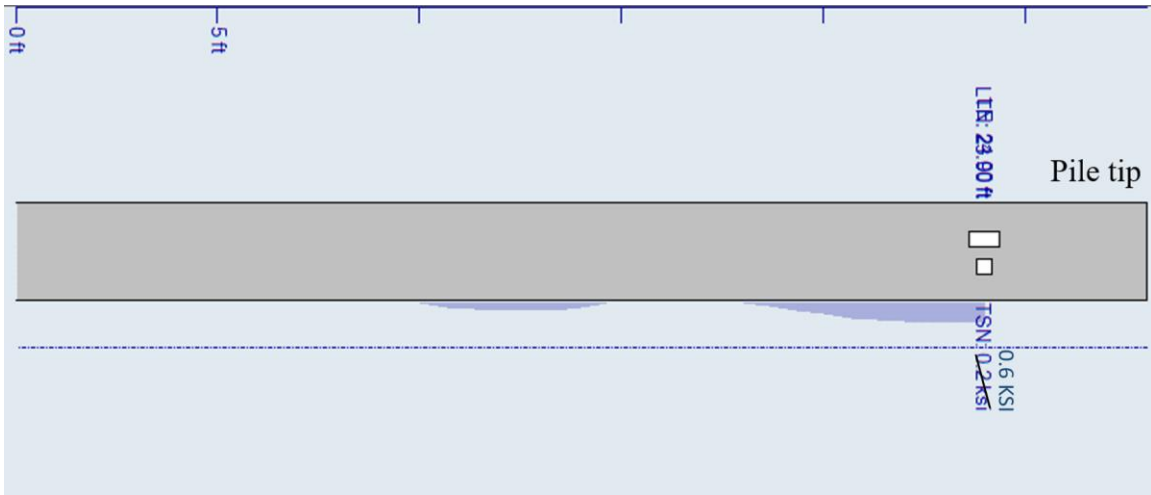


Figure H.23: Peak tensile stress (TSX) resulting from impact drop height of 10 ft (PCG2) and its location along the pile. (This figure was produced by Terracon)

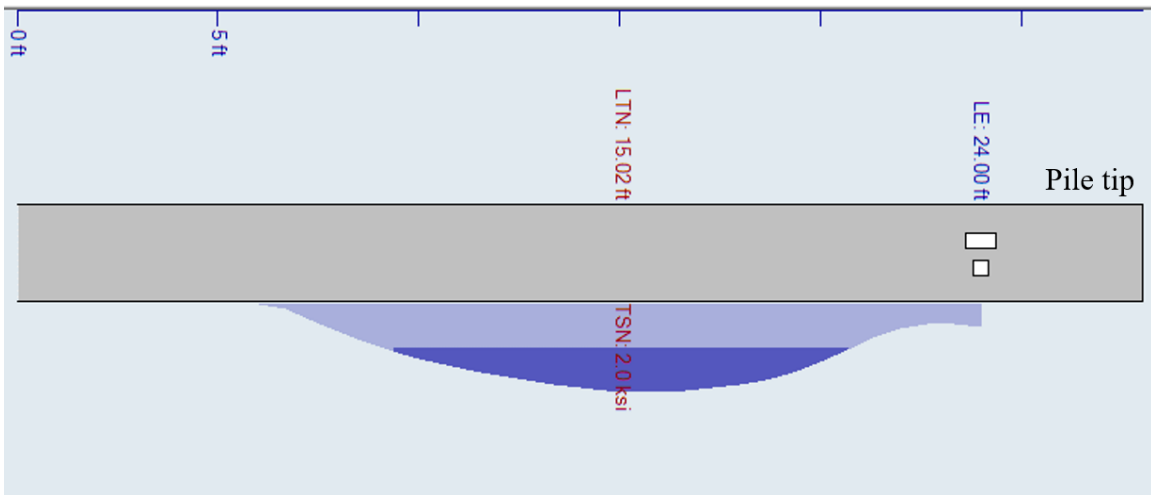


Figure H.24: Peak tensile stress (TSX) resulting from impact drop height of 15 ft (PCG2) and its location along the pile. (This figure was produced by Terracon)

H.5. Spiral Strain under Impact Loading

H.5.1. Spiral Strain (PCG1)

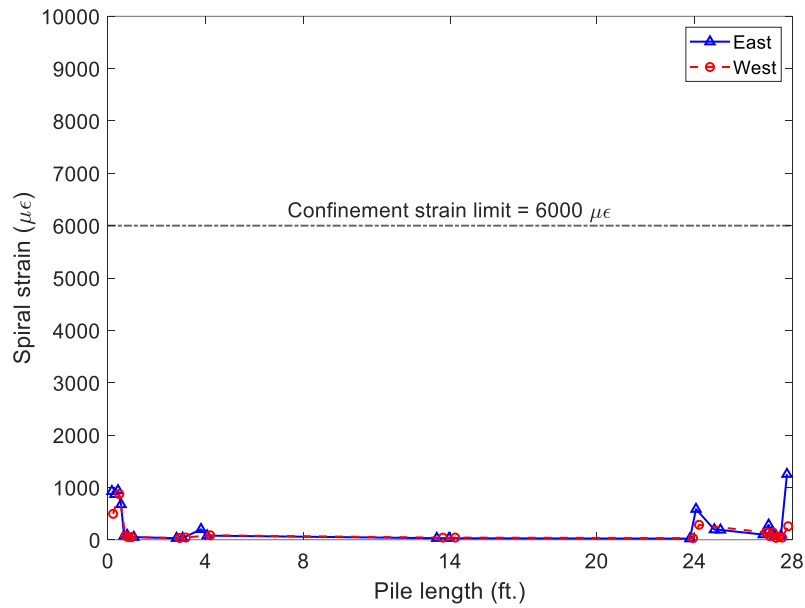


Figure H.25: PCG1 spiral strain (5-ft drop height)

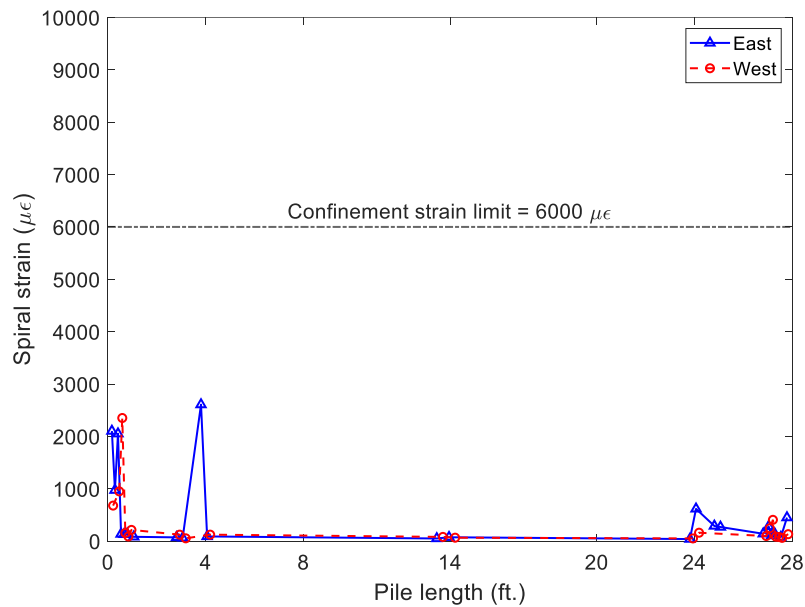


Figure H.26: PCG1 spiral strain (10-ft drop height)

H.5.2. Spiral Strain (PCG2)

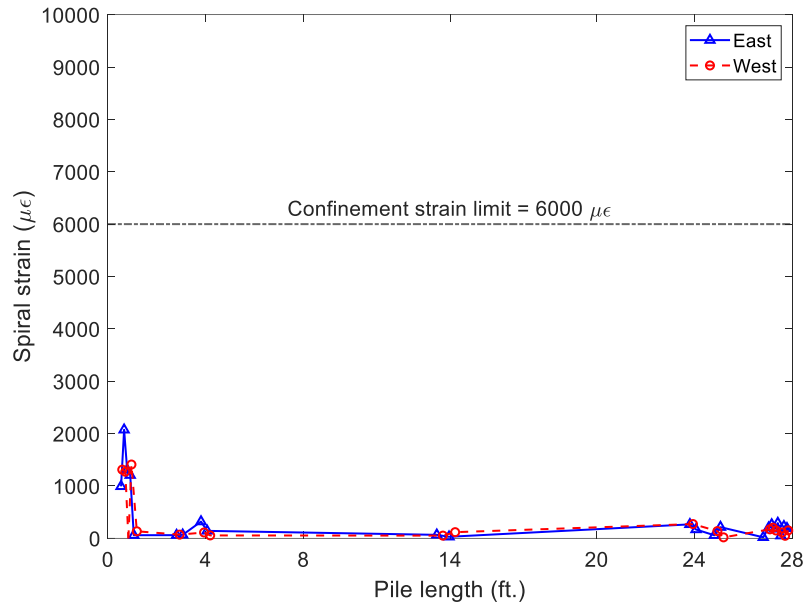


Figure H.27: PCG2 spiral strain (5-ft drop height)

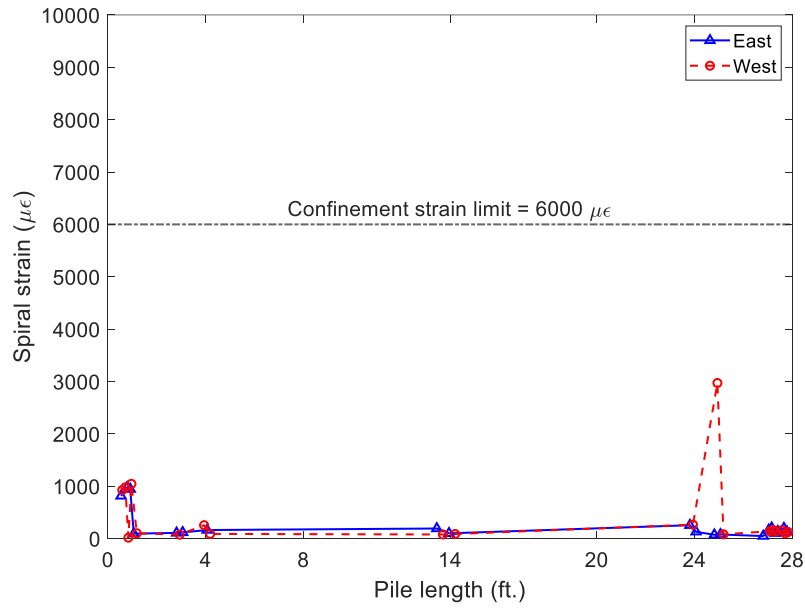


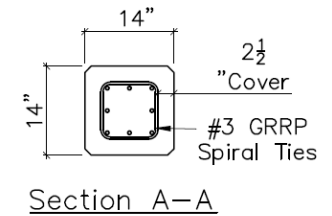
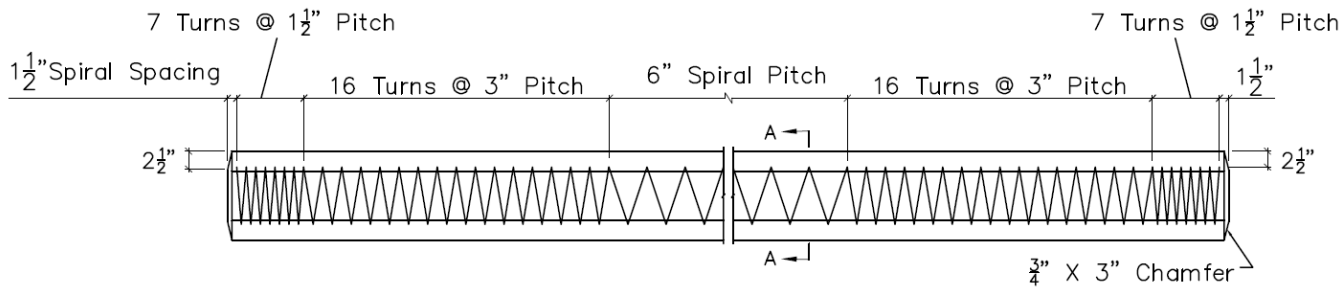
Figure H.28: PCG2 spiral strain (10-ft drop height)

H.6. Summary of All Test Results

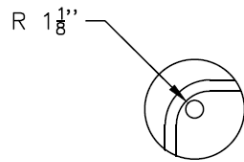
Pile No.	Strike No.	Drop Height (ft.)	Max. Top (ksi)	CSI Tip (ksi)	Avg. Top (ksi)	CSX Tip (ksi)	Max. TSX (ksi)
PCG1	1	5	1.63	1.27	1.62	1.08	0.07
PCG1	2	10	2.85	1.87	2.85	1.84	0.55
PCG1	3	15	4.95	2.31	4.77	2.14	1.65
PCG1	4	20	7.24	5.13	7.20	5.01	3.21
PCG1	5	25	9.28	5.23	8.85	5.19	6.15
PCG2	1	5	1.82	2.03	1.65	1.08	0.32
PCG2	2	10	2.98	2.03	2.83	1.83	0.62
PCG2	3	15	4.87	3.37	4.77	2.49	1.99
PCG2	4	20	7.35	4.27	6.78	3.83	3.06
PCG2	5	25	9.44	6.16	8.52	4.78	3.96

Appendix I. Final Drawings for Piles with CFRP Strands and GFRP Spirals

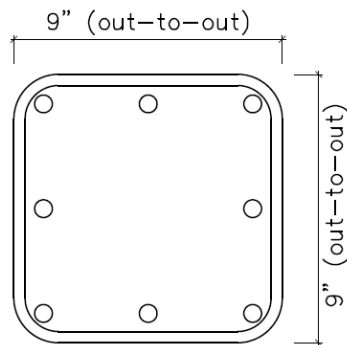
Note: FDOT review of the draft final report recommended a larger radius for the inner bent part. The final drawings below incorporated the recommendation, and therefore, are slightly different from the earlier drawings representing the test specimens.



Elevation



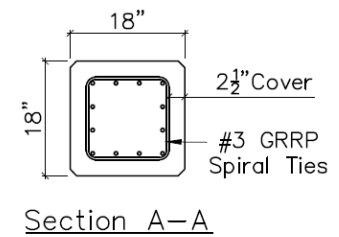
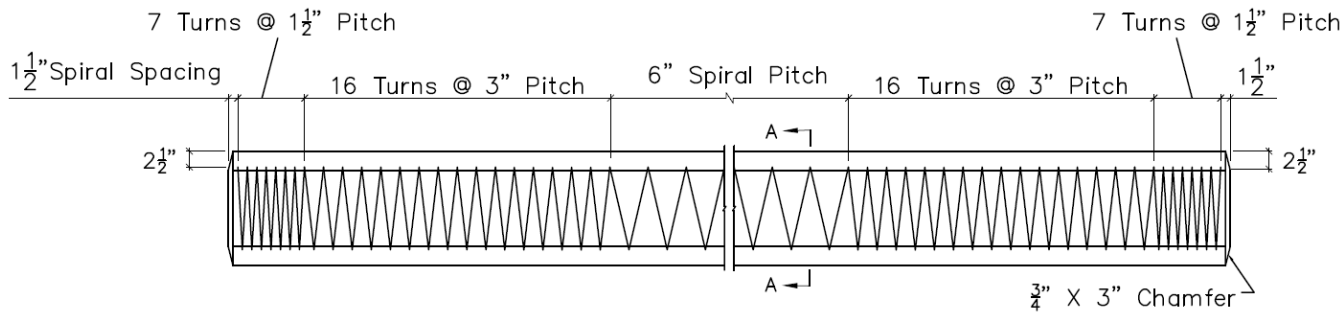
The inner radius of bent part
R is 1.125 in.



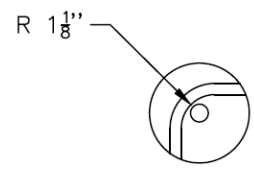
Strand Pattern
8~0.6" ϕ , CFRP 7-strand at 31.5 kips

GFRP Spiral Bending Details

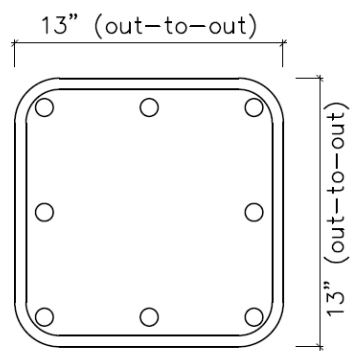
14" Square Prestressed Concrete Pile with CFRP Strands and GFRP Spiral				Revisions:	12-16-2023	
	6-23-2023	FAMU-FSU College of Engineering	Sheet 1 of 4			



Elevation



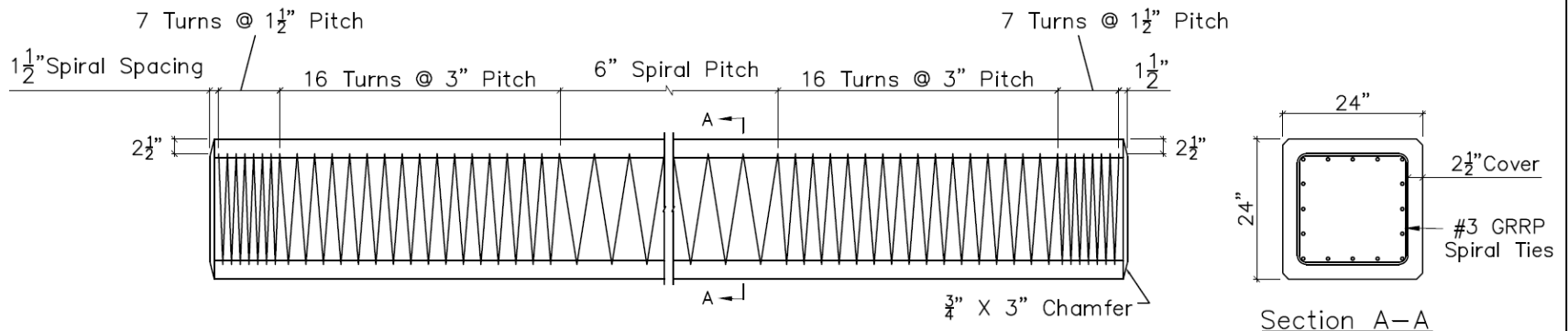
The inner radius of bent part
R is 1.125 in.



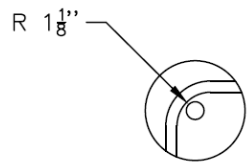
GRFP Spiral Bending Details

Strand Pattern
12~0.6" ϕ , CFRP 7-strand at 34 kips

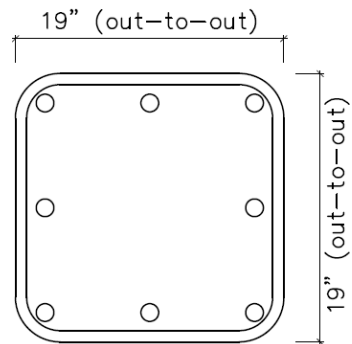
18" Square Prestressed Concrete Pile with CFRP Strands and GFRP Spiral				Revisions:	12-16-2023	
	6-23-2023	FAMU-FSU College of Engineering	Sheet 2 of 4			



Elevation



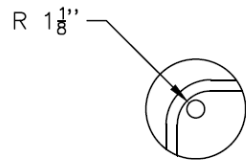
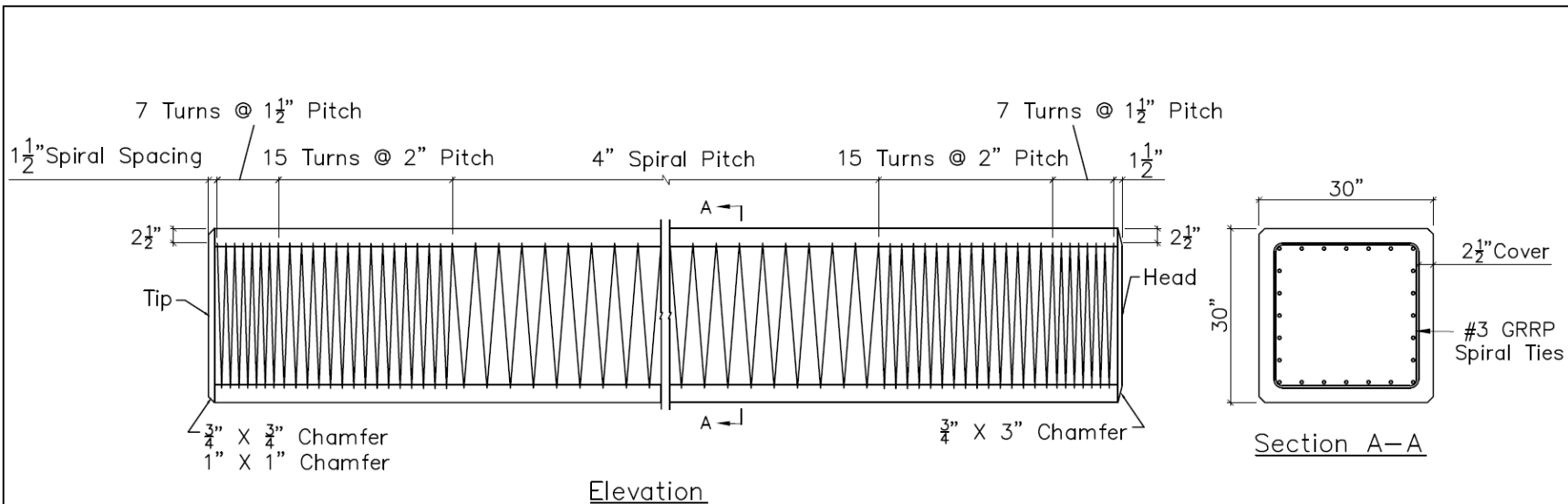
The inner radius of bent part
R is 1.125 in.



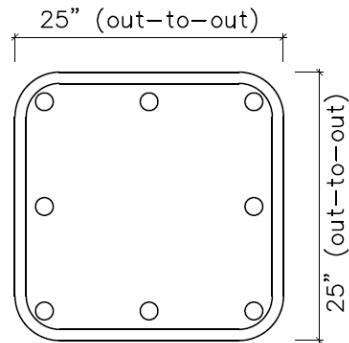
Strand Pattern
16~0.6" ϕ , CFRP 7-strand at 42 kips

GRFP Spiral Bending Details

24" Square Prestressed Concrete Pile with CFRP Strands and GFRP Spiral				Revisions:	12-16-2023	
	6-23-2023	FAMU-FSU College of Engineering	Sheet 3 of 4			



The inner radius of bent part
 R is 1.125 in.



Strand Pattern
 20~0.6" ϕ , CFRP 7-strand at 38 kips

Note: only spiral and strand details shown

GRRP Spiral Bending Details

30" Square Prestressed Concrete Pile with CFRP Strands and GFRP Spiral				Revisions:	12-16-2023	
	6-23-2023	FAMU-FSU College of Engineering	Sheet 4 of 4			